

**Preparing for gravitational wave astronomy:  
A verification of the GEO 600 detection  
chain by generation, injection, and  
extraction of continuous signals**

Dipl.-Phys. Uta Weiland

2004



**Preparing for gravitational wave astronomy:  
A verification of the GEO 600 detection  
chain by generation, injection, and  
extraction of continuous signals**

Vom Fachbereich Physik der Universität Hannover und  
der Faculty of Physical Sciences der Universität Glasgow  
zur Erlangung des gemeinsamen Grades

**Doktorin der Naturwissenschaften<sup>1</sup>  
-Dr. rer. nat.-**

genehmigte Dissertation von

**Dipl.-Phys. Uta Weiland**

geboren am 14. Juni 1974 in Hannover

©Uta Weiland Dezember 2004

---

<sup>1</sup>Dieser Grad ist dem Grad **Doctor of Philosophy by Research (Ph.D.)** der Universität Glasgow äquivalent.

**Preparing for gravitational wave astronomy:  
A verification of the GEO 600 detection  
chain by generation, injection, and  
extraction of continuous signals**

Thesis by Uta Weiland, accepted by  
the Fachbereich Physik of the University of Hannover and  
the Faculty of Physical Sciences at the University of Glasgow  
for the jointly awarded degree

**Doktorin der Naturwissenschaften<sup>2</sup>  
-Dr. rer. nat.-**

©Uta Weiland December 2004

Referent:	Prof. K. Danzmann
Korreferent:	Prof. K.A. Strain
External examiner (appointed by the University of Glasgow):	Prof. E. Riis
Tag der Promotion:	23. November 2004

---

<sup>2</sup>This degree is equivalent to the degree **Doctor of Philosophy by Research (Ph.D.)** of the University of Glasgow.

## Abstract

Promising sources of gravitational waves are spinning neutron stars with a non-zero quadrupole moment. If the position and spin-down parameters of the neutron stars are known (such as for pulsars), the signal waveform of the emitted gravitational wave is well understood for a certain emission mechanism except for four remaining parameters. To search for gravitational waves of such sources, a time-domain search algorithm has been developed at the University of Glasgow. The algorithm can identify a continuous gravitational wave signal emitted by a known pulsar in the output of a gravitational wave detector which contains the signal and detector noise.

The British-German laser-interferometric gravitational wave detector GEO 600 is one of a worldwide network of earth-bound gravitational wave detectors. To test the detection chain for continuous gravitational waves, a simulated, continuous gravitational wave signal has been injected into the detector hardware of GEO 600 and successfully recovered from the data using the time-domain search algorithm. In particular, the amplitude and the phase were recovered with values consistent with the parameters of the injected signal, thus proving the full detection chain for continuous gravitational waves at GEO 600. For a reliable test, the injected signal needs high phase and amplitude accuracy. An instrument has been developed that generates a simulated, continuous gravitational wave signal with a phase error of less than 1% of  $2\pi$ . The signal has been measured to be stable over several months and autonomously recovers from interruptions, such as data-transfer failures. The key component of the instrument is a microcontroller operated as a direct digital frequency synthesiser to generate the signal in an analog electronic form. A digital phase-locked loop running on a control computer controls the phase accumulator of the microcontroller via its phase increment register. The absolute timing of the injected signal is controlled by locking the microcontroller to GPS time. The signal to be injected is calculated by means of the LIGO/LSC Algorithm Library on the control computer.

After the first detections of gravitational waves, the network of detectors will start a new type of astronomy: gravitational wave astronomy. For this purpose the best possible calibration accuracy is desirable. The theoretical accuracy of a photon pressure actuator, that excites a main interferometer mirror by the radiation pressure of laser light, is investigated. First measurements with a photon pressure actuator installed at the GEO 600 interferometer are presented. An advanced setup is proposed along with the necessary steps to obtain an accuracy of a few percent.

**Keywords:** Gravitational wave detector, pulsar, signal generation, hardware signal injection, photon pressure actuator, calibration accuracy.



## Zusammenfassung

Vielversprechende Quellen für Gravitationswellen sind rotierende Neutronensterne mit einem nicht verschwindenden Quadrupolmoment. Wenn die Position und die Spin-Down Parameter des Neutronensterns bekannt sind (wie im Fall von Pulsaren), ist die Signalform der emittierten Gravitationswelle bei einem bestimmten Emissionsmechanismus bis auf vier verbleibende Parameter bekannt. Zur Suche nach solchen Gravitationswellensignalen wurde an der Universität Glasgow ein Suchalgorithmus in der Zeitdomäne entwickelt. Dieser Suchalgorithmus kann ein kontinuierliches Gravitationswellensignal, wie es von einem bekannten Pulsar emittiert wird, aus dem von Rauschen dominierten Detektorsignal extrahieren.

Der britisch-deutsche Gravitationswellendetektor GEO 600 ist Teil eines weltweiten Netzwerks erdgebundener Gravitationswellendetektoren. Um alle Elemente, die an der Detektion von kontinuierlichen Gravitationswellen beteiligt sind, als Einheit im realen Betrieb zu testen, wurde ein simuliertes Signal in den Detektor GEO 600 eingespeist und erfolgreich im Ausgangssignal des Detektors mit Hilfe des Suchalgorithmus nachgewiesen. Insbesondere stimmten dabei die Werte der Amplitude und der Phase des extrahierten Signals mit den Parametern überein, die für die Signalerzeugung benutzt worden waren. Auf diese Weise wurden alle Detektionselemente für kontinuierliche Gravitationswellensignale bei GEO 600 erfolgreich getestet. Für einen aussagekräftigen Test muß das für die Einspeisung verwendete Signal eine hohe Phasen- und Amplitudengenauigkeit besitzen. Hierfür wurde ein spezieller Signalgenerator entwickelt, der ein simuliertes, kontinuierliches Gravitationswellensignal mit einer Phasengenauigkeit besser als 1 % (von  $2\pi$ ) erzeugt. Das Signal hat sich über mehrere Monate als stabil erwiesen und stabilisiert sich nach Störungen, wie z.B. Ausfällen in der Datenübertragung, wieder selbst. Die Hauptkomponente des Signalgenerators ist ein Microcontroller, der als digitaler Frequenzgenerator betrieben wird, um das Signal in analoger elektronischer Form zu produzieren. Ein digitaler Phasenregelkreis (PLL) läuft auf einem Kontrollrechner, der den Phasenakkumulator des Microcontrollers mittels des Phaseninkrementregisters regelt. Alle zeitlichen Taktungen des Microcontrollers sind mit Signalen synchronisiert, die von einem GPS Empfänger abgeleitet sind. Das eingespeiste Signal wird mit Hilfe der „LIGO/LSC Algorithm Library“ auf dem Kontrollrechner bestimmt.

Sobald die ersten Detektionen von Gravitationswellen erfolgt sind, wird das Netzwerk von Gravitationswellendetektoren zu einer neuen Form der Astronomie übergehen: Gravitationswellenastronomie. Um Gravitationswellenastronomie zu betreiben, ist eine möglichst genaue Kalibrierung des Detektors anzustreben. Die theoretisch erreichbare Genauigkeit eines Strahlungsdruckaktuators wird untersucht, der die Hauptspiegel des Interferometers mit dem Strahlungsdruck eines Lasers auslenkt. Erste Messungen mit einem Strahlungsdruckaktor am Hauptinterferometer von GEO 600 werden vorgestellt. Ein verbesserter Aufbau für einen Strahlungsdruckaktor wird vorgeschlagen, mit dem eine Genauigkeit von wenigen Prozent erreicht werden kann.

**Stichwörter:** Gravitationswellendetektor, Pulsar, Signalerzeugung, Signaleinspeisung, Strahlungsdruckaktor, Kalibrationsgenauigkeit.





# Contents

<b>Abstract</b>	<b>v</b>
<b>Zusammenfassung</b>	<b>vii</b>
<b>Contents</b>	<b>ix</b>
<b>List of Figures</b>	<b>xiii</b>
<b>List of Tables</b>	<b>xvii</b>
<b>Glossary</b>	<b>xix</b>
<b>1 Gravitational waves</b>	<b>1</b>
1.1 Introduction . . . . .	1
1.1.1 Detection Principle . . . . .	4
1.1.2 Gravitational wave sources . . . . .	4
1.2 Continuous gravitational wave signals . . . . .	6
1.2.1 Radiation mechanisms for continuous gravitational wave signals . . . . .	6
1.2.2 Derivation of the signal . . . . .	9
<b>2 Production of a simulated, continuous gravitational wave signal</b>	<b>19</b>
2.1 Signal generation software . . . . .	20
2.1.1 Calculating the phase . . . . .	20
2.1.2 Mapping the amplitude envelope . . . . .	24
2.1.3 Software comparison of the time-domain search algorithm and the hardware injection code . . . . .	27
2.2 Signal production hardware . . . . .	31
2.2.1 Operating mode of a direct digital synthesiser . . . . .	32
2.2.2 The use of the microcontroller . . . . .	33
<b>3 Hardware signal injection</b>	<b>45</b>
3.1 The simulated, continuous gravitational wave signal generated at the GEO 600 site . . . . .	45
3.1.1 Timing issues of the DDS output . . . . .	46
3.1.2 Test of the DDS output . . . . .	49
3.2 Actuators for the hardware signal injection . . . . .	57
3.2.1 Electrostatic drive . . . . .	61
3.2.2 Photon pressure actuator . . . . .	64

3.2.3	Implications of the actuator transfer functions on the hardware signal injection . . . . .	64
3.2.4	Noise of the microcontroller on the analog simulated gravitational wave signal . . . . .	65
3.3	Amplitude of the injected simulated, continuous gravitational wave signal	65
3.3.1	Signal amplitude of 11-12 June 2004 injection . . . . .	68
<b>4</b>	<b>Results of the hardware injection experiment</b>	<b>69</b>
4.1	The time-domain search algorithm . . . . .	69
4.2	Noise . . . . .	71
4.2.1	Line noise . . . . .	71
4.2.2	Blind test . . . . .	72
4.3	Extraction of the continuous gravitational wave signal . . . . .	74
<b>5</b>	<b>Increasing the calibration accuracy - A photon pressure actuator</b>	<b>79</b>
5.1	Power needed for online calibration . . . . .	80
5.2	Theoretical accuracy . . . . .	81
5.2.1	Pendulum transfer function . . . . .	83
5.2.2	Absolute intensity measurement . . . . .	83
5.2.3	Determining the amount of reflected power . . . . .	87
5.2.4	Mirror mass . . . . .	87
5.2.5	Effect of mirror rotation on the mirror's longitudinal displacement	87
5.2.6	Temperature distribution in a mirror illuminated by a modulated laser beam . . . . .	90
5.2.7	Quantitative comparison of photon pressure actuator accuracy .	93
5.3	Current photon pressure actuator . . . . .	94
5.3.1	Accuracy of the current photon pressure actuator . . . . .	94
5.3.2	First Measurements with the photon pressure actuator . . . . .	97
5.3.3	Conclusion . . . . .	99
5.4	Possible setup for an advanced photon pressure actuator . . . . .	104
	<b>Appendix</b>	<b>107</b>
	<b>A Gravitational waves emitted by a spinning neutron star</b>	<b>107</b>
	<b>B Coordinate systems</b>	<b>111</b>
B.1	Celestial equatorial coordinate system . . . . .	111
B.2	Cardinal coordinate system . . . . .	112
B.3	Detector proper reference frame coordinate system . . . . .	113
	<b>C Power spectral densities</b>	<b>115</b>
C.1	Normalisation . . . . .	115
C.1.1	Normalised power spectral density . . . . .	115
C.1.2	Normalised power spectrum . . . . .	116
C.2	Vocabulary . . . . .	116

<b>D Matlab script to determine power needed for online calibration with a photon pressure actuator</b>	<b>119</b>
<b>E Reflectivity of viewport</b>	<b>121</b>
<b>F Transformation between transfer function notations</b>	<b>123</b>
F.1 Notations . . . . .	123
F.1.1 Single-complex zero pole notation . . . . .	123
F.1.2 Frequency/Q-value notation . . . . .	123
F.2 Transformation between the two notations . . . . .	124
F.2.1 Transformation from single-complex zero pole notation to f/Q-value notation . . . . .	124
F.2.2 Transformation from f/Q-value notation to single-complex zero pole notation . . . . .	125
F.3 Example . . . . .	125
<b>G Optical layout of GEO 600</b>	<b>127</b>
<b>H The electrostatic drive</b>	<b>131</b>
<b>I Electronics</b>	<b>133</b>
<b>Bibliography</b>	<b>145</b>
<b>Acknowledgements</b>	<b>151</b>
<b>Curriculum Vitae</b>	<b>153</b>
<b>List of publications</b>	<b>155</b>



## List of Figures

1.1	Effect of a gravitational wave on test masses arranged in a circle . . . . .	5
1.2	Position of a neutron star in celestial equatorial coordinates expressed in right ascension and declination . . . . .	10
1.3	Transformation of the celestial equatorial coordinate system into the solar system barycentre reference frame . . . . .	11
1.4	Euler angles to transform the celestial equatorial coordinate system to the gravitational wave coordinate system . . . . .	14
1.5	Transformation from the celestial equatorial coordinate system to the cardinal coordinate system . . . . .	16
1.6	Transformation from the cardinal coordinate system to the detector proper reference frame coordinate system . . . . .	17
2.1	Behaviour of the C function <code>atan2</code> . . . . .	21
2.2	Annual Doppler shift . . . . .	24
2.3	Diurnal Doppler shift . . . . .	25
2.4	Mapping the amplitude envelope . . . . .	26
2.5	Signal amplitude envelopes of neutron stars with different parameters . . . . .	28
2.6	Software test for 31 December 2003 . . . . .	29
2.7	Software comparison . . . . .	30
2.8	Schematic of the hardware signal injection setup . . . . .	31
2.9	DDS schematic . . . . .	32
2.10	Graphical illustration of a sine look-up table . . . . .	33
2.11	PLL schematic . . . . .	35
2.12	Timing of the PLL . . . . .	36
2.13	PLL performance on 1 January 2004 . . . . .	37
2.14	Settling of the PLL after a phase shift introduced due to the discretisation of the ephemeris data . . . . .	38
2.15	PLL open-loop transfer function . . . . .	40
2.16	Microcontroller and control computer setup . . . . .	41
2.17	Measured transfer function of the analog bandpass filter behind the multiplication of the two D/A converter signals. . . . .	42
3.1	Measurement of the time delay with which the phase accumulator of the microcontroller is read out . . . . .	49
3.2	Frequency domain comparison of the phase of the DDS output and the simulated signal generated in software . . . . .	51
3.3	Frequency domain comparison of the amplitude envelope of the DDS output and simulated signal generated in software . . . . .	52

3.4	Phase error of a sinusoidal signal at a zero crossing introduced by a DC offset in the amplitude . . . . .	54
3.5	Direct comparison of the DDS output and simulated signal generated in software . . . . .	55
3.6	Amplitude error between the DDS output and software generated signal	56
3.7	Schematic of the inboard and far end mirror suspensions and their actuators	58
3.8	Schematic of a mirror suspended as a pendulum . . . . .	59
3.9	Bode plot of a pendulum transfer function . . . . .	60
3.10	Schematic of a main mirror . . . . .	61
3.11	Mechanism of the electrostatic drive . . . . .	62
3.12	Amplitude spectral density of the microcontroller signal . . . . .	66
4.1	Blind test of hardware signal injection . . . . .	73
4.2	Amplitude spectral density of $h(t)$ during hardware injection . . . . .	75
4.3	Probability density functions of the hardware injection for the injected signal parameters $h_0$ , $\phi_0$ , $\cos \iota$ , and $\psi$ . . . . .	76
4.4	Probability density functions for the parameters $(h_0, \phi_0)$ , $(h_0, \psi)$ , and $(h_0, \cos \iota)$ . . . . .	77
5.1	Graphical display of the investigation on the approximated pendulum transfer function accuracy . . . . .	82
5.2	Response of a photodiode over its active area . . . . .	85
5.3	Difference between the expected measured power at a fixed position and varied positions of a laser beam on the active area of a photodiode . . . . .	86
5.4	Effect of rotation on the longitudinal displacement of a cylindrical mirror	88
5.5	Plot of apparent longitudinal displacement of a main mirror as a function of its rotation . . . . .	89
5.6	Temperature change in a main mirror induced by a modulated laser beam traversing the main mirror . . . . .	91
5.7	Illumination of a main mirror by the photon pressure actuator . . . . .	93
5.8	Current setup of the photon pressure actuator measurement . . . . .	96
5.9	Positions of the laser beam of the photon pressure actuator on the viewport	98
5.10	Amplitude spectrum of the Michelson differential error point during photon pressure actuator measurements . . . . .	99
5.11	Graphical display of the first photon pressure actuator measurements . . . . .	102
5.12	Graphical comparison of all photon pressure actuator measurements . . . . .	103
5.13	Suggested setup for an advanced photon pressure actuator . . . . .	104
5.14	Laser beam radius of the suggested advanced photon pressure actuator . . . . .	105
A.1	Geometry of a non-axisymmetric non-precressing spinning neutron star . . . . .	108
A.2	Neutron star's and observer's reference frame system . . . . .	109
B.1	Schematic of the celestial equatorial coordinate system . . . . .	112
B.2	Schematic of the cardinal coordinate system . . . . .	112

E.1	Graphical display of the measured reflectivity of a coated viewport under normal incidence . . . . .	121
F.1	Bode plot of a transfer function with parameters given in LISO and single-complex zero pole notation . . . . .	126
G.1	Inboard mirrors of the optical layout of GEO 600 . . . . .	127
G.2	Optical layout of GEO 600 . . . . .	128
G.3	Mirror far north of the optical layout of GEO 600 . . . . .	129
H.1	Schematic of the electrostatic drive . . . . .	131
I.1	Connectors and power supply of the microcontroller electronics . . . . .	134
I.2	Reprogramming switch of the microcontroller electronics . . . . .	135
I.3	Data acquisition inputs on the microcontroller electronics . . . . .	136
I.4	Opto-isolated serial interface of the microcontroller electronics . . . . .	137
I.5	Signal output of the microcontroller electronics . . . . .	138
I.6	Power supplies of the microcontroller electronics . . . . .	139
I.7	Electronics to quadruplicate the $2^{22}$ Hz signal of the data acquisition system	140
I.8	Electronics of the electro static drive for the auto alignment quadrant driver	141
I.9	Electronics of the MCE electro static drive quadrant driver . . . . .	142
I.10	Electronics of the MCN electro static drive quadrant driver . . . . .	143





## List of Tables

2.1	Mapping of the amplitude $a(t)$ . . . . .	27
2.2	Pulsar parameters used for the hardware injection . . . . .	31
2.3	Sine look-up table with 3-bit resolution . . . . .	34
2.4	Taps of the IIR filter in the PLL . . . . .	39
2.5	List of possible commands from the control computer to the microcontroller	42
2.6	All characters used between the control computer and microcontroller .	43
3.1	Timing inaccuracies of the recorded DDS output at the GEO 600 site . .	50
4.1	Hardware injection parameters and best fits . . . . .	74
5.1	Material properties of main mirrors . . . . .	90
5.2	Geometric properties and mass of main mirrors . . . . .	94
5.3	Quantitative comparison of the effects that lead to longitudinal displacement and apparent longitudinal displacement . . . . .	95
5.4	Results of first photon pressure actuator measurements . . . . .	100
5.5	Comparison of photon pressure actuator and electrostatic drive of the measurement on 17 February 2004 . . . . .	101
5.6	Comparison of photon pressure actuator and electrostatic drive of the measurements on 19 February 2004 . . . . .	101
C.1	Vocabular of spectral densities and spectra . . . . .	117



# Glossary

---

## Mathematical and physical constants

$\epsilon_0$	$8.8544 \times 10^{-12}$	$[\text{C}^2\text{N}^{-1}\text{m}^{-2}]$	dielectric constant of vacuum
$\pi$	$\cong 3.141592654$	[1]	circular constant
$c$	$2.998 \times 10^8$	$[\text{m s}^{-1}]$	speed of light
$e$	$\cong 2.718281828$	[1]	base of natural logarithm
$G$	$6.673 \times 10^{-11}$	$[\text{m}^3\text{kg}^{-1}\text{s}^{-2}]$	gravitational constant
$g$	9.81	$[\text{m s}^{-2}]$	Earth's acceleration
$h$	$6.6256 \times 10^{-34}$	[J s]	Planck's constant
$i$	$i \cdot i = -1$	[1]	imaginary unit
$v_{\oplus\text{rot}}$	465	$[\text{m s}^{-1}]$	maximum velocity on the Earth surface due to the Earth rotation
$v_{\oplus\text{orb}}$	30290	$[\text{m s}^{-1}]$	maximum orbital velocity of the Earth

---

## Symbols for physical variables

$\alpha$	[rad]	right ascension (R.A.)
$\alpha_{\text{ab}}$	[ppm $\text{cm}^{-1}$ ]	absorption coefficient
$\alpha_{\text{ex}}$	$[\text{K}^{-1}]$	expansion coefficient
$\alpha_{\text{vp}}$	[1]	losses at vacuum viewport
$\gamma$	[rad]	angle measured counterclockwise from East to the bisector of Michelson interferometer arms (chapter 1)
$\gamma$	$[\text{kg s}^{-1}]$	coefficient of friction for viscous damping for a swinging pendulum (chapter 3)
$\gamma$	$[\text{kg m}^2 \text{s}^{-1}]$	coefficient of friction for viscous damping for a torsion pendulum (chapter 3)
$\Delta_{E\odot}$	[s]	solar system Einstein time delay
$\Delta_{S\odot}$	[s]	solar system Shapiro time delay
$\delta$	[rad]	declination (DEC)
$\epsilon$	[1]	ellipticity
$\epsilon_r$	[1]	relative dielectric constant
$\varepsilon$	[rad]	angle between the ecliptic and the Earth's equatorial plane
$\zeta$	[rad]	angle between Michelson interferometer arms
$\theta$	[rad]	excursion angle of a pendulum (chapter 3)

$\theta$	[rad]	mirror rotation
$\iota$	[rad]	angle between a neutron star's angular momentum and the propagation direction of its emitted gravitational wave
$\kappa$	[N m]	torque constant of a pendulum (chapter 3)
$\kappa$	[W mK <sup>-1</sup> ]	thermal conductivity (chapter 5)
$\lambda$	[rad]	latitude of a detector site (chapter 1, chapter 2)
$\lambda$	[nm]	wave length (chapter 3)
$\rho$	[kg m <sup>-3</sup> ]	density
$\tau$	[s]	error in the travel time of a continuous gravitational wave signal from the solar system barycentre to a detector
$\phi(t)$	[rad]	phase evolution of a Doppler shifted neutron star signal
$\phi_0$	[rad]	phase of a Doppler shifted neutron star signal at a fiducial time
$\phi_r$	[rad]	deterministic phase which defines the position of the Earth in its diurnal motion at a fixed time
$\Delta\phi$	[rad]	phase error
$\varphi(t)$	[rad]	combined phase of both polarisations ( $F_+$ , $F_\times$ ) of a gravitational wave neutron star signal
$\varphi_{\text{ACC}}(t)$	[rad]	phase accumulator value
$\Delta\varphi$	[rad]	phase offset
$\psi$	[rad]	polarisation angle of a gravitational wave emitted by a neutron star
$\Omega_0$	[rad s <sup>-1</sup> ]	orbital angular velocity of the Earth
$\Omega_r$	[rad s <sup>-1</sup> ]	rotational angular velocity of the Earth
$\omega$	[rad s <sup>-1</sup> ]	angular frequency
$\omega_0$	[rad s <sup>-1</sup> ]	resonance frequency
$\omega_m$	[rad s <sup>-1</sup> ]	modulation frequency of photon pressure actuator
$\omega_s$	[rad s <sup>-1</sup> ]	critical frequency beyond which accretion can no longer spin-up a neutron star as its spin-down torque is balanced with the spin-up accretion torque
$A$	[m <sup>2</sup> ]	geometric factor of a plate capacitor
$\Delta A$	[1]	amplitude offset
$a$	[cm]	$1/e^2$ radius of a Gaussian laser beam
$a(t)$	[1]	combined amplitude of both polarisations ( $F_+$ , $F_\times$ ) of a gravitational wave neutron star signal
$C$	[J kg <sup>-1</sup> K <sup>-1</sup> ]	specific heat capacity
$d$	[cm]	mirror thickness
$d_c$	[cm]	distance from mirror centre
$E$	[N C <sup>-1</sup> ]	electric field
$F_+(t, \psi)$	[1]	antenna response or beam pattern function of the plus-polarisation
$F_\times(t, \psi)$	[1]	antenna response or beam pattern function of the cross-polarisation
$F$	[N]	force

---

$F_{\text{bp}}$	[1]	factor for determining the amplitude of the injected simulated continuous gravitational wave signal taking account of the inclination of the neutron star and the beam pattern function of the detector
$F_{\text{ex}}$	[N]	externally applied force
$F_{\text{hv}}$	[1]	calibration factor of the high-voltage path of the electrostatic drive
$F_{\text{r}}$	[N]	restoring force
$f$	[Hz]	frequency
$f_0$	[Hz]	neutron star spin frequency (chapter 1, chapter 2)
$f_0$	[Hz]	pendulum resonance frequency (chapter 3, chapter 5)
$f_{\text{CL}}$	[Hz]	frequency of the external clock applied to the DDS
$f_{\text{DDS}}$	[Hz]	fundamental frequency of the signal produced by a direct digital synthesiser
$f_{\text{P}}$	[Hz]	frequency of a pole in the $f/Q$ -value or LISO transfer function notation
$f_{\text{SSB}}$	[Hz]	gravitational wave signal frequency at the solar system barycentre
$f_{\text{Z}}$	[Hz]	frequency of a zero in the $f/Q$ -value or LISO transfer function notation
$\Delta f$	[Hz]	frequency difference
$h$	[1]	gravitational wave strain
$h(t)$	[1]	time dependant gravitational wave strain
$h_0$	[1]	gravitational wave strain amplitude
$h_+(t)$	[1]	time dependant gravitational wave plus-polarisation
$h_{\times}(t)$	[1]	time dependant gravitational wave cross-polarisation
$I$	[kg m <sup>2</sup> ]	moment of inertia
$I_y$	[kg m <sup>2</sup> ]	mirror moment of inertia around $y$ -axis
$I_z$	[kg m <sup>2</sup> ]	mirror moment of inertia around $z$ -axis
$I_{xx}$	[kg m <sup>2</sup> ]	neutron star moment of inertia around $x$ -axis
$I_{yy}$	[kg m <sup>2</sup> ]	neutron star moment of inertia around $y$ -axis
$I_{zz}$	[kg m <sup>2</sup> ]	neutron star moment of inertia around $z$ -axis
$I_{\text{in}}$	[W]	light power of the photon pressure actuator entering the vacuum
$I_{\text{out}}$	[W]	light power of the photon pressure actuator leaving the vacuum
$k$	[m <sup>2</sup> s <sup>-1</sup> ]	thermal diffusivity
$k_{\text{DB}}$	[1]	gain factor of transfer functions in the GEO 600 database notation
$k_{\text{LISO}}$	[1]	gain factor in the LISO transfer function notation
$L$	[m]	distance between two points
$\Delta L$	[m]	change of distance $L$
$\Delta L$	[m]	length change of mirror due to thermal expansion (subsection 5.2.6)
$l$	[m]	pendulum length

$l_{\text{th}}$	[m]	effective thermal length
$\dot{M}$	[kg s <sup>-1</sup> ]	accretion rate of a neutron star
$m$	[kg]	mirror mass
$N$	[1]	length of a data segment
$p$	[Hz]	a zero in a transfer function
$p_{\text{CP}}$	[Hz]	a complex pole in a transfer function
$p_{\text{SG}}$	[Hz]	a single pole in a transfer function
$Q$	[kg m <sup>2</sup> ]	quadrupole moment of a neutron star (chapter 1)
$Q$	[1]	quality factor (chapter 3, subsection 5.2.1)
$Q$	[J m <sup>-3</sup> s <sup>-1</sup> ]	heat deposited per unit volume and time in an absorbing medium (subsection 5.2.6)
$q$	[C]	charge
$R$	[pc]	distance of the neutron star to the detector
$R_{SE}$	[m]	distance from the SSB to the Earth's centre
$R_{ED}$	[m]	distance from the Earth's centre to the detector
$R_{lh}$	[1]	ratio between the low and high-voltage paths of the electrostatic drive
$r$	[cm]	mirror radius
$S/N$	[1]	signal-to-noise ratio
SR	[Hz]	sample rate
$s$	[m]	longitudinal displacement of a mirror suspended as a pendulum on the circle described by the pendulum (chapter 3)
$s$	[Hz]	complex angular frequency (chapter 2, Appendix F)
$s_{\text{LAL}}(t)$	[1]	simulated gravitational wave signal produced with the time-domain search algorithm
$s_{\text{DDS}}(t)$	[1]	DDS output
$T$	[s]	integration time (chapter 1)
$T$	[K]	temperature (chapter 5)
$T_0$	[s]	fiducial time for which a pulsar frequency and the pulsar spin down parameters are given; also called epoch
$\Delta T$	[K]	temperature difference
$t$	[s]	time
$U$	[V]	voltage
$V_{\text{max}}$	[V]	maximum voltage of the signal produced by the microcontroller
$v$	[m s <sup>-1</sup> ]	maximum velocity of a detector within the SSB reference frame
$\text{win}_n$	[1]	discrete window function applied to data segment over which an fft is performed
$x$	[m]	mirror displacement along the optical axis of a mirror (chapter 3)
$x_d$	[m]	apparent longitudinal displacement of a mirror centre along its optical axis due to rotation
$x_c$	[m]	apparent longitudinal displacement of a mirror at a distance away from its centre due to rotation

---

$z$	[m]	propagation direction of the laser beam (subsection 5.2.6)
$z$	[Hz]	a zero in a transfer function (subsection F.1.2)
$z_{CP}$	[Hz]	a complex zero in a transfer function
$z_{SG}$	[Hz]	a single zero in a transfer function

---



---

## Abbreviations

---

CCD	charge-coupled device
CD	cardinal coordinate system
CS	celestial equatorial coordinate system
D/A	digital analog
DDS	direct digital frequency synthesiser
DT	detector proper reference frame coordinate system
DEC	declination $\delta$
ESD	electrostatic drive
fft	fast Fourier transform
GEO 600	British-German earth-bound gravitational wave observatory
GPS	global positioning system
GW	gravitational wave coordinate system
IIR	infinite impulse response
LAL	LIGO/LSC algorithm library
LIGO	laser interferometric gravitational wave observatory
LMXB	low-mass X-ray binary
LSC	LIGO scientific collaboration
MCE	mirror central East
MCN	mirror central North
MFE	mirror far East
MFN	mirror far North
NA	numerical aperture
NCO	numerically-controlled oscillator
NPS	normalised power spectrum
PC	personal computer
PIR	phase increment register
PLL	phase locked loop
PPA	photon pressure actuator
PPS	pulse per second
PSD	power spectral density
PTB	Physikalisch-Technische Bundesanstalt (German national metrology institute)
pk	peak

## Glossary

---

pp	peak-to-peak
ppm	parts per million
R.A.	right ascension $\alpha$
S2	science run 2 (2003-02-14 - 2003-04-14)
S3 I	science run 3 part I (2003-11-05 13:30:00 UTC - 2003-11-12 15:00:00 UTC)
S3 II	science run 3 part II (2003-12-30 15:00:00 UTC - 2004-01-13 16:00:00 UTC)
SBDFT	single-bin discrete Fourier transform
SNR	signal-to-noise ratio
SSB	solar system barycentre

---



# Chapter 1

## Gravitational waves

In the first part of this chapter an introduction to gravitational waves is given. Two different detection principles along with an overview of the existing earth-bound gravitational wave detectors and their sensitivity are presented. The detection principle of laser-interferometric gravitational wave detectors is summarised in more detail before an overview of possible gravitational wave sources for the described detectors is given. In the second part of this chapter continuous gravitational waves, which are emitted by fast spinning neutron stars, are discussed in more detail. The possible radiation mechanisms for spinning neutron stars are described. Then the gravitational wave signal for the special case of a non-axisymmetric, non-precessing, spinning neutron star is derived, which was used for the hardware injection described in the other chapters.

### 1.1 Introduction

Gravitational waves are a direct consequence of Einstein's General Theory of Relativity [1]. Already in Einstein's pioneering work the wave solution of his linearised field equations can be found at the beginning of the 20th century. Gravitational waves can be looked at as ripples in the fabric of space-time. According to the General Theory of Relativity gravitational waves are quadrupole waves and travel at the speed of light (higher moments than quadrupole are also possible). As space-time, the fabric in which these waves propagate, is very stiff, the effect of gravitational waves on space-time is very small; so small that Einstein never believed that the wave solution of his field equations would be of any relevance, as he thought the effect of these waves was undetectable. Forty years after Einstein's work on gravitational waves, Bondi proved that the effect of the emission of gravitational radiation should be physically observable, as gravitational waves carry energy, and that a system that emits gravitational waves should lose energy [2]. In 1993 Hulse and Taylor received the Nobel price for the discovery of the binary pulsar system PSR B1913+16, which had opened up new possibilities for the study of gravitation [3]. Within four years after the discovery it was shown that the loss of kinetic energy of the binary system agrees to within 0.5% with the assumption that the system emits gravitational waves as predicted by the General Theory of Relativity [4]. This was the first indirect proof of the existence of gravitational waves.

Technology has evolved over the last century at such a pace that today, at the beginning of the 21st century, the first direct detection of gravitational waves may occur in the next few years. Gravitational waves are produced by accelerated masses. For a detectable gravitational wave on Earth, only accelerated objects with very large and

dense masses, which can only be found on an astrophysical scale, are detectable realistic sources. Therefore the detection of gravitational waves is not only of great value providing confirmation of a basic prediction of the General Theory of Relativity, but also opens the prospect of using gravitational waves to probe the astrophysics of their sources. Thus the long term goal of the detection of gravitational waves is to conduct gravitational wave astronomy. This new type of astronomy would allow to directly observe astronomical objects and events which are very faint or even invisible in the electromagnetic spectrum, but at the same time involve very massive objects and events in which a lot of energy is released.

There are two basic methods to detect a gravitational wave. One is by measuring the energy deposited by the wave in a resonant massive body. Detectors based on this principle are so-called resonant-mass detectors. The other principle is by measuring the change in space-time via measuring the change in time it takes light to travel between two distinct points, typically with an interferometer. The detectors based on this principle are called laser-interferometric detectors. For a reasonable chance of making astronomical observations these detectors must be able to measure changes in its arm-length that are smaller than 1 part in  $10^{-21}$  [5].

One type of a resonant-mass detector is the so-called bar detector which consists of a cylindrical bar weighing approximately two tons. Worldwide there are currently five operating bar detectors, ALLEGRO [6], AURIGA [7], EXPLORER [8], NAUTILUS [9], and NIOBÉ [10]. These bar detectors are sensitive over a small frequency region of a few Hz with typically two resonance frequencies a few 10 Hz apart. An overview on the status of bar detectors can be found in [11].

**ALLEGRO** with resonance frequencies at 895 Hz and 920 Hz situated in Baton Rouge, Louisiana, USA has been running with a strain sensitivity of  $\sim 8 \times 10^{-22}/\sqrt{\text{Hz}}$ .

**AURIGA** with resonance frequencies at 911 Hz and 929 Hz situated in Padua, Italy has been running with a strain sensitivity of  $\sim 4 \times 10^{-22}/\sqrt{\text{Hz}}$ .

**EXPLORER** with resonance frequencies at 905 Hz and 921 Hz situated at CERN has been running with a strain sensitivity of  $\sim 3 \times 10^{-21}/\sqrt{\text{Hz}}$ .

**NAUTILUS** with originally resonance frequencies at 907 Hz and 922 Hz situated in Rome, Italy has been running with a strain sensitivity of  $\sim 4 \times 10^{-22}/\sqrt{\text{Hz}}$ . Recently the detector has been tuned to 935 Hz.

**NIOBÉ** with resonance frequencies at 695 Hz and 713 Hz situated in Perth, Australia has been running with a strain sensitivity of  $\sim 2 \times 10^{-21}/\sqrt{\text{Hz}}$ .

Current developments of so-called double-stage transducers broaden the resonances of the bar detectors over a few 10 Hz without loss of peak strain sensitivity.

Another development among the resonant-mass detectors are the so-called spherical detectors, consisting of a metal sphere. They operate in the kHz frequency region with a bandwidth of a few 100 Hz. In contrast to the bar detectors they are capable of detecting gravitational waves from all directions and polarisations. There are currently two projects under construction, the Dutch project MiniGRAIL [12] and the Brazilian project Schenberger [13]. MiniGRAIL's design sensitivity shows a minimal strain of  $\sim 6 \times 10^{-22}/\sqrt{\text{Hz}}$  at 3.1 kHz with 300 Hz bandwidth. It has currently been running with a strain sensitivity of  $\sim 1.5 \times 10^{-20}/\sqrt{\text{Hz}}$ . Schenberger's design sensitivity aims for a sensitivity better than  $\sim 10^{-21}/\sqrt{\text{Hz}}$  at 3.2 kHz with 400 Hz bandwidth. So far

the mechanical parts of the sphere have been assembled.

A totally new conceptual scheme for resonant-mass detectors, so-called dual detectors, would allow strain sensitivities of  $2 \times 10^{-23}/\sqrt{\text{Hz}}$  from 1 to 3 kHz. In the dual scheme one resonant body is nested into another [14].

The measurement technique of laser-interferometric gravitational wave detectors is based on an interferometric measurement with a Michelson interferometer operated with highly stabilised laser light. In contrast to the bar detectors the laser-interferometric detectors reach an astrophysically meaningful sensitivity over a broad frequency band, approximately from 100 Hz to 2 kHz. Currently there are worldwide four earth-based detector projects based on the laser-interferometric method. These are TAMA [15], GEO 600 [16], LIGO [17], and VIRGO [18].

**TAMA** is a Japanese detector with 300 m long arms situated near Tokyo. It has Fabry-Perot cavities in the arms and has implemented power recycling. It was the first large scale laser-interferometric gravitational wave detector to start taking scientific data in September 1999 [19]. The current sensitivity is  $\sim 3 \times 10^{-21}/\sqrt{\text{Hz}}$  around 1 kHz.

**GEO 600** is a British-German detector with 600 m long arms situated in Germany close to Hannover. The light is folded once in both arms increasing the light path to 1200 m in one arm. GEO 600 has implemented both power and signal recycling [20]. With the help of signal recycling the sensitivity can be increased in a frequency band of a few Hz allowing in particular searches of continuous gravitational waves. At GEO 600 first scientific data taking started in August 2002 along with LIGO [21]. The current sensitivity is  $\sim 2 \times 10^{-21}/\sqrt{\text{Hz}}$  around 1 kHz.

**LIGO** is an American project that consists of three detectors. One interferometer with 4 km long arms is situated in Louisiana and two with 4 km and 2 km arms, respectively, are included in a single vacuum system situated in Washington state. All three detectors have the same configuration, that is Fabry-Perot cavities in the arms and power recycling. The current setup of LIGO includes relatively easily controllable technology. From the very beginning, the interferometer infrastructures were designed to allow two major upgrades, leading to higher sensitivity [22]. The current detector design is called LIGO I. The two upgrades are called LIGO II and LIGO III, respectively. By making use of more advanced technology and interferometer configurations, such as fused silica suspensions, electrostatic actuation, high power stabilised lasers and signal recycling, an improvement of a factor of 10 is aimed at for LIGO II. As already stated, LIGO I started taking scientific data in August 2002. The best LIGO I detector is currently operating with a sensitivity of  $\sim 8 \times 10^{-23}/\sqrt{\text{Hz}}$  between approximately 100 and 200 Hz.

**VIRGO** is a French-Italian detector with 3 km long arms situated close to Pisa in Italy. Currently VIRGO is operating in its final commissioning state i.e. with no power recycling yet. In its final configuration VIRGO will operate as a Michelson interferometer with Fabry-Perot cavities in both arms and power recycling. Due to a very sophisticated suspension system seismic noise is reduced very effectively, dominating the overall noise only up to 3 Hz [23]. The design sensitivity is below  $10^{-21}/\sqrt{\text{Hz}}$  from 15 Hz to 20 kHz with a minimum of  $4 \times 10^{-23} / \sqrt{\text{Hz}}$  at 300 Hz.

This apparently vast amount of detectors is not competing with each other but in contrast forms a network of detectors. Apart from the fact that only a detection in at

least two detectors can be trusted, only a network of detectors is able to conduct useful gravitational wave astronomy. The full information of a gravitational wave consists of five quantities, that is the amplitudes of its two polarisations (see below for a description of these polarisations), the phase between the two polarisations, and the position of the source, expressible in two angles. To derive this information at least three detectors need to detect a gravitational wave yielding six quantities; each detector measures the combined amplitude of both polarisations at the detector site and between all of them three differences between the time of arrival of the wave at the detectors can be determined. Furthermore the various detectors complement each other by covering different polarisation directions and different sensitivities over the frequency detection range.

### 1.1.1 Detection Principle

The laser-interferometric gravitational wave detectors are based on measuring the change in time it takes light to travel between two test masses, which are freely falling<sup>1</sup> in space-time. In the flat space far field approximation of Einstein's field equations the effect of a gravitational wave is

$$\frac{h}{2} = \frac{\Delta L}{L}, \quad (1.1)$$

where  $h$  is the perturbation of space-time due to the gravitational wave,  $L$  the distance between two test masses and  $\Delta L$  their apparent change in optical pathlength. According to Equation 1.1 the effect of a gravitational wave can be looked at as a relative length change over a defined distance. In Figure 1.1 the effect of a gravitational wave on freely falling test masses arranged in a circle is illustrated. Plotted are the effects for the so-called plus-polarisation,  $h_+$ , and cross-polarisation,  $h_\times$ , at phases  $0$ ,  $\pi/2$ ,  $\pi$ , and  $3/2 \pi$  of the wave. In the picture it is assumed that the wave hits the drawing plane perpendicular.

In a Michelson interferometer, the effect of a gravitational wave with amplitude  $h$  passing the interferometer perpendicular is according to [25] section 1.2 equivalent to Equation 1.1, where then  $L$  is then length of one arm and  $\Delta L$  is the length change in one arm.

### 1.1.2 Gravitational wave sources

Gravitational wave sources can be divided by the types of gravitational wave signals which they produce. These types are classified by the predicted waveforms of the signals and the duration of the signals. Currently, one differentiates between four types of gravitational wave signals: Continuous, inspiral, and burst signals and the stochastic background. The knowledge about the waveform of the signals ranges from very accurate knowledge to complete ignorance. For a detailed overview of these signals and their predicted event rates see [26].

Sources for **continuous gravitational waves** are slightly deformed, spinning neutron stars. The waveforms of these signals are well known and emitted due to a

---

<sup>1</sup>So-called freely falling test masses cannot be realised at DC, but at frequencies within the measurement band. For the definition of freely falling see [24], in particular chapter 10.

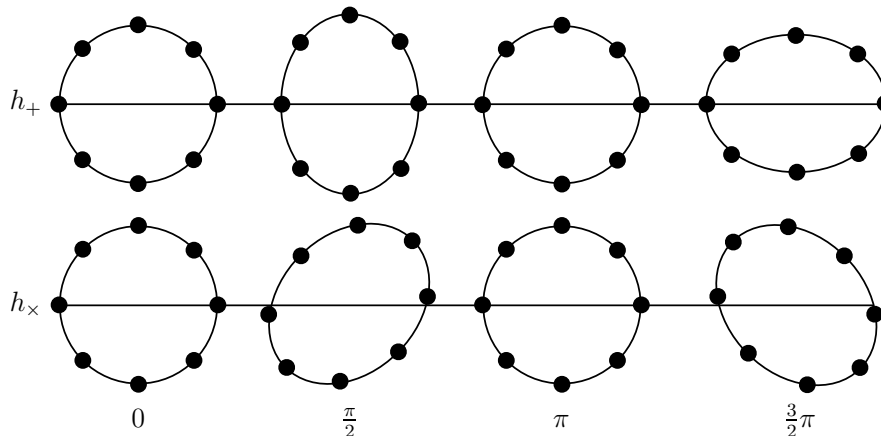


**Figure 1.1:** The effect of a gravitational wave impinging perpendicular the drawing plane on freely falling test masses arranged in a circle. Depicted are the two polarisations of the transverse quadrupole wave  $h_+$  and  $h_\times$ . The apparent differential length change is illustrated at phase  $0$ ,  $\pi/2$ ,  $\pi$ , and  $3/2\pi$ .

quadrupole moment of the spinning neutron star. Candidates are neutron stars in low-mass X-ray binaries, young pulsars, millisecond pulsars, and spinning neutron stars. Emission scenarios are a quadrupole moment due to accretion, r-mode ringing, toroidal B-fields, and precession. Continuous gravitational wave signals are continuously present. Depending on the emission mechanism they are expected to be coherent from over several days up to several years. The frequency region of continuous gravitational waves range from a few Hz up to a few kHz, the breakup frequency of neutron stars. In section 1.2 the various radiation mechanisms are presented in more detail.

Sources for **inspiral gravitational wave signals** are binary neutron star systems and binary black-hole systems in the last few minutes of their inspiral. Also a neutron star black-hole binary in the last few minutes of its inspiral when the neutron star is tidally disrupted by its black hole companion is a source for inspiral gravitational waves. The waveforms of the signal during the inspiraling and the vibrational ringdown after the merger are well known. The waveforms of signals emitted during the actual merging process, however, are hardly understood, yet. The observed inspiral wave signal will last between  $\sim 1000$  and  $\sim 10,000$  cycles depending on the binary masses. Depending on the masses of the involved objects the signal frequencies vary between mHz and kHz.

Sources for **burst like gravitational wave signals** are stellar core collapses in supernovae and the accretion induced collapse of white dwarfs. As the details of a stellar collapse are poorly understood, the waveforms of these signals are almost unknown. The signals are supposed to last a few ms. The frequency spectrum of the signals is expected to cover a broad band of frequencies.

Sources for a **stochastic gravitational wave background** are processes in the very early universe. Inflationary models and superstring theory along with a wide variety of postulated mechanisms predict various levels of stochastic gravitational wave background. Even though their detection with earth-bound interferometers is unlikely,

upper limits could be set that would rule out some of the suggested models. A stochastic gravitational background can also originate from unresolvable background noise. As one searches for a stochastic gravitational wave background by correlating the outputs of at least two detectors, the upper frequency limit for the detection band is given by the distance of the two detectors.

Besides all the known expected sources of gravitational waves there might be a large number of unknown sources, reflecting the current ignorance about the physics and astrophysics of gravitational waves.

Depending on the knowledge of the signal waveform, the application of matched filters can significantly increase the signal-to-noise ratio of a detection for a given sensitivity of a detector. In particular this applies for continuous gravitational wave signals emitted by spinning neutron stars [27], which emit sinusoidal signals. Matched filtering works by multiplying the output of the detector by a function of time that represents the expected waveform (called template) and integrating the result. The longer the time a signal is integrated over, the better the signal-to-noise ratio,  $S/N$ , gets, as the mean noise decreases inversely to the square root of the integration time while the signal is constant. This is described by the following relation

$$\frac{S}{N} \propto \sqrt{T}. \quad (1.2)$$

Equation 1.2 only holds if the used template is correct and its phase evolution is coherent over the full integration time. For a sinusoidal signal once the template is shifted by  $\pi/2$  the signal-to-noise ratio starts to decrease again. For the search of continuous gravitational wave signals integration times of the order of years are aimed at. This requires very good templates, in particular with a very accurate phase evolution.

## 1.2 Continuous gravitational wave signals

As described in the previous section, a very good signal template is required for matched filtering. In order to calculate such a signal, a good model of the emission mechanism is required. In the first part of this section different radiation mechanisms for continuous gravitational wave signals are introduced. In the second part the exact waveform for one of these mechanisms is derived. This signal is currently used as a template for the data analysis of continuous gravitational wave signals. This signal is therefore also used for the hardware injections, as the hardware injections were performed to test the search algorithms with real instrumental data.

### 1.2.1 Radiation mechanisms for continuous gravitational wave signals

In order to emit gravitational waves, a neutron star needs a non-zero second (or quadrupole) moment of its mass distribution around its rotation axis (see Appendix A). The frequencies at which it then can emit gravitational waves are at the rotation frequency, twice the rotation frequency, and the frequency bands around these two frequencies, depending on the emission mechanism. Promising continuous gravitational wave sources for earth-bound laser-interferometric gravitational wave detectors are therefore neutron

stars that spin at frequencies between a few 10 Hz up to several kHz. In the following, electromagnetic observations of spinning neutron stars in the relevant frequency region are summarised. The current observations show evidence that spinning neutron stars should emit gravitational waves. The evidence is presented and mechanisms that can lead to the emission of gravitational waves are introduced.

If a neutron star is a pulsar, it is relatively easy to observe its apparent spin frequency. A pulsar is a neutron star with a magnetic axis that is not aligned with the star's spin axis [28]. If the neutron star then rotates, electromagnetic radiation arises from charged particles above the neutron star which are accelerated in the moving magnetic field. If the magnetic poles point into the line of sight to an observer on the Earth during a cycle of the star, a pulse of electromagnetic radiation is periodically observed. Currently there are almost 1500 known pulsars [29]. These can be divided into two different populations, the normal pulsars and the millisecond pulsars [30].

Normal pulsars have spin periods of order one second and show spin-down rates of typically  $10^{-15}$  Hz/s. Their age is typically  $10^6$  years. The millisecond pulsars have spin periods primarily between 1.5 and 30 ms and show very low spin-down rates of  $\leq 10^{-19}$  Hz/s. They belong to an older population of pulsars with an age of  $10^9$  years and are believed to have spun up earlier by accretion during a low-mass X-ray binary (LMXB) phase [31]. There are approximately 100 known millisecond pulsars. The fastest known millisecond pulsar B1937+21 has a spin period of 0.001557806472448817 s (spin frequency  $\sim 642$  Hz) [32]. There are more than 90 pulsars found in binaries. Approximately 80 % of these pulsars in binaries are millisecond pulsars.

Another way to determine the spin frequencies of neutron stars is to infer them from millisecond oscillations in X-ray binaries [33]. Though no model valid to all observed phenomena exists yet, recent observations show a clear link between the so-called quasi-periodic oscillations in X-ray bursts from LMXB and the spin frequency of the accreting neutron star [34, 35].

Neutron star spin frequencies in LMXBs lie between 270 Hz and 619 Hz. From the distribution of this data it can be derived that with a 95 % confidence the spin frequency of neutron stars in LMXBs lies below 760 Hz [35]. General relativistic calculations on the contrast show that the spin-up of rotating neutron stars stops only when their spin frequency reaches at least 1180 Hz [36]. The discrepancy between observation and theory suggests that some mechanisms prevent further spin-up. One possible mechanism is that density or velocity fluctuations within the neutron star might lead to a quadrupole momentum producing gravitational radiation, reducing the star's angular momentum and hence limiting the spin frequency [37]. The neutron star will lose angular momentum at a rate  $\sim \omega^5$  where  $\omega$  is the angular spin frequency of the neutron star. According to [38, 39] balancing the spin-down torque with the spin-up accretion torque leads to a critical frequency  $\omega_s$  beyond which accretion can no longer spin-up the star. This critical frequency is given by

$$\omega_s \sim \dot{M}^{1/5} Q^{-2/5}, \quad (1.3)$$

where  $\dot{M}$  is the accretion rate and  $Q$  the quadrupole moment of the neutron star. The weak dependence of  $\omega_s$  on the critical values  $\dot{M}$  and  $Q$  lets expect very similar  $\omega_s$ . This is one of the strongest arguments that neutron stars should emit gravitational waves.

There have been three main possible physical mechanisms identified that can be responsible for continuous gravitational wave emission by neutron stars. These are neutron star spin precession, an excited neutron star oscillation mode, and small distortions of the neutron star's shape away from axisymmetry.

A possible emission mechanism of continuous gravitational waves is free precession of a neutron star. Let the angular momentum of the star be not aligned with any principal axis of its inertia tensor. Then the angular velocity vector rotates around the fixed angular momentum at the inertial precession frequency. The neutron star then emits gravitational waves at the inertial precession frequency which is nearly the rotation frequency of the neutron star. The dissipation time scale of the precession is orders of magnitude smaller than the typical lifetime of a millisecond pulsar [40]. Also no astrophysical pumping mechanisms are known that maintain the free precession. Therefore freely precessing neutron stars are not a very promising source for observable continuous gravitational waves.

Another possible emission mechanism of continuous gravitational waves are oscillation modes in neutron stars. The so-called r-modes are unstable due to the emission of gravitational waves [41, 42]. But as the saturation amplitude of the r-modes is quite small, gravitational waves emitted due to this mechanism are supposed to be too weak to be detected by the current gravitational wave detectors [43].

A third emission mechanism of continuous gravitational waves are small non-axisymmetries in the neutron star's shape, that is small ellipticities. If such a neutron star with a quadrupole moment due to the non-axisymmetries rotates, it will emit gravitational waves at twice its rotation frequency. The quadrupole moment can be generated in the crust due to electron capture. For LMXB lateral temperature variations of order  $\leq 5\%$  in the deep crust of the neutron star or 0.5% lateral variation in the charge-to-mass ratio can lead to quadrupole moments sufficient to balance the accretion torque by emission of gravitational waves [44]. Another mechanism that can lead to a neutron star not rotating about its axis of symmetry are neutron stars with large toroidal B-fields [45]. These fields can be generated during the neutron star formation by differential rotation. A toroidal B-field tends to distort a neutron star in a prolate shape. By dissipation the symmetry axis of the toroidal B-field is reorientated until it is perpendicular to the rotation axis, leading to maximal equatorial ellipticity.

At present the mechanism of distortions from axisymmetry is considered the most favourable source of detectable gravitational waves. Within the LIGO scientific collaboration (LSC) upper limits have been set for this particular mechanism [46]. In the following section the signal signature for neutron stars with small ellipticity is derived in detail for the special case that the neutron star is not precessing.



### 1.2.2 Derivation of the signal

The continuous gravitational wave signal from a non-axisymmetric, non-precessing, spinning neutron star (i.e. with a “wobble angle”<sup>2</sup> of  $\pi/2$ ) produces a strain

$$h(t) = F_+(t, \psi) h_+(t) + F_\times(t, \psi) h_\times(t) , \quad (1.4)$$

with

$$h_+(t) = \frac{1}{2} h_0 (1 + \cos^2 \iota) \cos 2\phi(t) , \quad (1.5)$$

$$h_\times(t) = h_0 \cos \iota \sin 2\phi(t) \quad (1.6)$$

at a detector on Earth [47]. Here  $h_+(t)$  and  $h_\times(t)$  are the two independent polarisations of the gravitational wave,  $h_0$  is the strain amplitude,  $\iota$  the angle between the neutron star’s angular momentum and the propagation direction of the gravitational wave,  $\phi(t)$  the phase evolution of the Doppler shifted star’s spin,  $F_+(t, \psi)$  and  $F_\times(t, \psi)$  are the antenna response functions of the detector to the plus- and cross-polarisations of the gravitational wave, and  $\psi$  is the polarisation angle of the wave. The amplitude  $h_0$  is given by [47]

$$h_0 = \frac{16\pi^2 G}{c^4} \frac{\epsilon I_{zz} f_0^2}{R} , \quad (1.7)$$

where  $f_0$  is the rotation frequency of the neutron star,  $I_{zz}$  is its principal moment of inertia with respect to the rotation axis,  $\epsilon$  is the ellipticity of the star given by  $\epsilon = (I_{yy} - I_{xx})/I_{zz}$ ,  $R$  the distance from the detector to the star,  $G$  the gravitational constant, and  $c$  the speed of light. Equation 1.5 to 1.7 are derived in Appendix A from the second moment of the mass distribution (or quadrupole moment) of a spinning ellipsoid. The gravitational wave signal frequency at the detector is constantly changing due to the spin-down of the neutron star and the Doppler shift caused by the detector’s motion relative to the solar system barycentre. This phase evolution information is contained in  $\phi(t)$ . The antenna response functions  $F_+(t, \psi)$  and  $F_\times(t, \psi)$  describe the amplitude modulation of the gravitational wave signal due to the changing orientation of the detector towards the neutron star as the detector rotates with the Earth. A more detailed description of  $\psi$  is given below.

#### The phase evolution

The phase evolution of the pulsar can be described as a truncated Taylor series as follows [46]

$$\phi(t) = \phi_0 + 2\pi [f_0(T - T_0) + \frac{1}{2} \dot{f}_0(T - T_0)^2 + \frac{1}{6} \ddot{f}_0(T - T_0)^3] , \quad (1.8)$$

where  $\phi_0$  is the phase of the signal at a fiducial time  $T_0$ , the so-called epoch,  $f_0$  the rotation frequency of the neutron star at this fiducial time  $T_0$ ,  $\dot{f}_0$  and  $\ddot{f}_0$  are the first

<sup>2</sup>The wobble angle is the angle between the total angular momentum vector of the star and the star’s principal axis of symmetry.

and second time derivatives of  $f_0$  at  $T_0$ , the so-called spin-down parameters, and  $T$  is the time of arrival of a signal at the solar system barycentre (SSB) given by

$$T = t - \frac{\vec{r}_D \cdot \vec{e}_{\text{NS}}}{c} + \Delta_{E\odot} - \Delta_{S\odot}, \quad (1.9)$$

where  $t$  is the time of arrival of a signal at the detector,  $\vec{e}_{\text{NS}}$  is a constant unit vector pointing in the direction of the star in the SSB reference frame,  $\vec{r}_D$  the position of the detector in the SSB reference frame,  $\Delta_{E\odot}$  the solar system Einstein time delay and  $\Delta_{S\odot}$  the solar system Shapiro time delay. The latter two are relativistic corrections. The Einstein delay originates in the difference between the coordinate time  $T$  and the proper time  $t$  in the detector's reference frame. The difference is due to the combined effect of the gravitational redshift and the time dilation. The Shapiro delay is caused by propagation of the gravitational wave through the curved space-time of the solar system. For a more detailed discussion of the Einstein and Shapiro delay see [47]. Putting Equation 1.8 into Equations 1.4 to 1.6 one can see that the gravitational wave is emitted at twice the rotational frequency  $f_0$  of the neutron star.

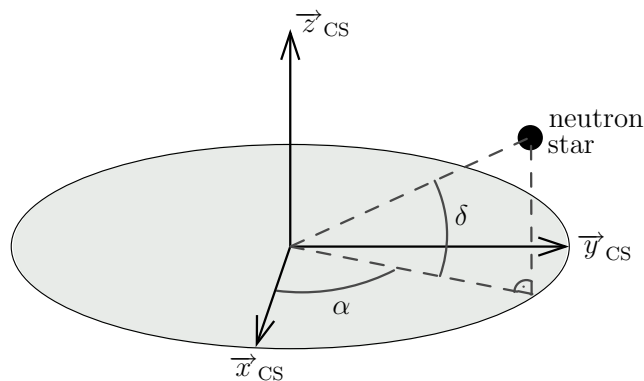


**Figure 1.2:** Position of a neutron star in celestial equatorial coordinates expressed in right ascension  $\alpha$  and declination  $\delta$ . The light grey ellipse represents the plane spanned by the vectors  $\vec{x}_{\text{CS}}$  and  $\vec{y}_{\text{CS}}$ . It corresponds to the Earth's equatorial plane.

In the following paragraphs, the vector  $\vec{e}_{\text{NS}}$  is derived. As mentioned before  $\vec{e}_{\text{NS}}$  is a constant unit vector pointing in the direction of the star in the SSB reference frame. To determine  $\vec{e}_{\text{NS}}$  first the position of the neutron star is determined in the celestial equatorial coordinate system<sup>3</sup>. From Figure 1.2 the position of the neutron star in the celestial equatorial coordinate system can be expressed in terms of its right ascension  $\alpha$  and declination  $\delta$ . It is given by the vector  $(\cos \alpha \cos \delta, \sin \alpha \cos \delta, \sin \delta)$ . Now only the matrix that transforms the celestial equatorial coordinate system to the SSB reference frame needs to be applied to this vector to yield  $\vec{e}_{\text{NS}}$ .

To determine a transformation matrix  $T$  of rotation from one Cartesian coordinate system  $(\vec{e}_{x'}, \vec{e}_{y'}, \vec{e}_{z'})$  to another  $(\vec{e}_{x''}, \vec{e}_{y''}, \vec{e}_{z''})$ , one needs to write the unit vectors

<sup>3</sup>For a description of the celestial equatorial coordinate system see Appendix B.

of  $(\vec{e}_{x''}, \vec{e}_{y''}, \vec{e}_{z''})$  in the coordinates of  $(\vec{e}_{x'}, \vec{e}_{y'}, \vec{e}_{z'})$  into the rows of  $T$  (Equation 4.2 [48])

$$T = \begin{pmatrix} \leftarrow & \vec{e}_{x''} & \rightarrow \\ \leftarrow & \vec{e}_{y''} & \rightarrow \\ \leftarrow & \vec{e}_{z''} & \rightarrow \end{pmatrix}. \quad (1.10)$$

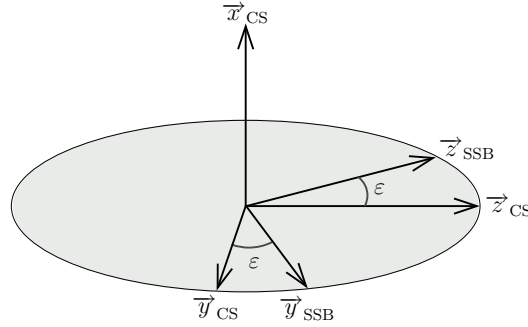


**Figure 1.3:** For the transformation of the celestial equatorial coordinate system into the solar system barycentre reference frame the celestial coordinate system needs to be rotated counterclockwise about its  $x$ -axis by the angle  $\varepsilon$ , which is the angle between the ecliptic and the Earth’s equatorial plane. This rotation is described by a simple matrix of rotation which can be read from the above figure. The grey ellipse spans a plane perpendicular to  $\vec{x}_{\text{CS}}$ , the vector of rotation. All vectors which end on the rim of that ellipse are situated in this plane. The transformation matrix giving the transformation from the celestial equatorial coordinate system to the SSB reference frame depends only on  $\varepsilon$ .

The unit vector  $\vec{e}_{\text{NS}}$  pointing in the SSB reference frame to the neutron star can be derived by multiplying the unit vector pointing in the celestial equatorial coordinate system to the neutron star with the matrix of rotation from the celestial equatorial coordinate system to the SSB reference frame. In the coordinate system of the SSB reference frame, the  $x$ -axis is parallel to the  $x_{\text{CS}}$ -axis of the celestial equatorial coordinate system; the  $z$ -axis of the SSB reference frame is perpendicular to the ecliptic and coincides with the orbital angular momentum vector of the Earth; the  $x$ -,  $y$ -, and  $z$ -axes of the SSB reference frame form a right-hand system. From Figure 1.3 the transformation matrix from the celestial equatorial coordinate system to the SSB reference frame can be read and applied to the position vector of the neutron star in the celestial equatorial coordinate system to yield

$$\vec{e}_{\text{NS}} = \begin{pmatrix} 1 & 0 & 0 \\ 0 & \cos \varepsilon & \sin \varepsilon \\ 0 & -\sin \varepsilon & \cos \varepsilon \end{pmatrix} \begin{pmatrix} \cos \alpha \cos \delta \\ \sin \alpha \cos \delta \\ \sin \delta \end{pmatrix}, \quad (1.11)$$

where  $\varepsilon$  is the angle between the ecliptic and the Earth’s equatorial plane,  $\delta$  the declination, and  $\alpha$  the right ascension of the position of the neutron star in the celestial equatorial coordinate system.

The position vector of the detector in the SSB reference frame,  $\vec{r}_D$ , is given by the sum of the vector pointing from the SSB to the Earth centre and the vector pointing

from the Earth centre to the detector, both in the SSB reference frame. As the SSB and the Earth centre lie by definition in one plane in the SSB reference frame, the unit vector,  $\vec{e}_{SE}$ , pointing from the SSB to the Earth centre in the SSB reference frame is

$$\vec{e}_{SE} = \begin{pmatrix} \cos(\phi_0 + \Omega_0 t) \\ \sin(\phi_0 + \Omega_0 t) \\ 0 \end{pmatrix}. \quad (1.12)$$

Here  $\Omega_0$  is the orbital angular velocity of the Earth and  $\phi_0$  is a deterministic phase which defines the position of the Earth in its orbital motion at  $t = 0$ . From picture III of Figure 1.5 (here  $\vec{e}_{ED}$  equals  $\vec{z}_{CD}$ ), the unit vector,  $\vec{e}_{ED}$ , pointing from the Earth centre to the detector in the celestial equatorial coordinate system can be found to be

$$\vec{e}_{ED} = \begin{pmatrix} \cos \lambda \cos(\phi_r + \Omega_r t) \\ \cos \lambda \sin(\phi_r + \Omega_r t) \\ \sin \lambda \end{pmatrix}. \quad (1.13)$$

Here  $\lambda$  is the latitude of the detector's site,  $\Omega_r$  the rotational angular velocity of the Earth in the SSB reference frame, and  $\phi_r$  is a deterministic phase which defines the position of the Earth in its diurnal motion at  $t = 0$ . To transform this vector into the SSB reference frame, it needs to be multiplied with the transformation matrix used in Equation 1.11. This yields the position of the detector in the SSB reference frame

$$\vec{r}_D = R_{SE} \begin{pmatrix} \cos(\phi_0 + \Omega_0 t) \\ \sin(\phi_0 + \Omega_0 t) \\ 0 \end{pmatrix} + R_{ED} \begin{pmatrix} 1 & 0 & 0 \\ 0 & \cos \varepsilon & \sin \varepsilon \\ 0 & -\sin \varepsilon & \cos \varepsilon \end{pmatrix} \begin{pmatrix} \cos \lambda \cos(\phi_r + \Omega_r t) \\ \cos \lambda \sin(\phi_r + \Omega_r t) \\ \sin \lambda \end{pmatrix}, \quad (1.14)$$

where  $R_{SE}$  is the distance from the SSB to the Earth centre, and  $R_{ED}$  is the distance from the Earth centre to the detector. Now it can be seen that the phase evolution is a function that depends on 13 parameters apart from the time  $t$ .

$$\phi(t) = \phi(t; f_0, \dot{f}_0, \ddot{f}_0, \alpha, \delta, \varepsilon, \phi_0, \Omega_0, \lambda, \phi_r, \Omega_r, R_{SE}, R_{ED}) \quad (1.15)$$

Due to the elliptic orbit of the Earth around the Sun the parameters  $R_{SE}$  and  $\Omega_0$  are time dependent. All other parameters of the function for the phase evolution are constant in time.

### The antenna response functions

As mentioned in subsection 1.2.2, the antenna response functions  $F_+(t, \psi)$  and  $F_\times(t, \psi)$  describe the signal amplitude modulation due to the changing orientation of the detector towards the neutron star as the detector rotates with the Earth. Because of this motion, the antenna response functions are periodic in time with a period of one sidereal day. In order to extract this explicit time dependence and express the antenna response  $F_+(t, \psi)$  and  $F_\times(t, \psi)$  as functions of the position of the neutron star, right ascension  $\alpha$  and declination  $\delta$ , and its polarisation angle  $\psi$ , one has to transform the gravitational wave signal from the gravitational wave coordinate system to the so-called ‘‘detector proper reference frame coordinates’’. This can be achieved through three transformations: first the transformation from the gravitational wave coordinate system to the

celestial equatorial coordinate system, second from the celestial equatorial coordinate system to the cardinal coordinate system located at the detector, and third from the cardinal coordinate system to the detector proper reference frame coordinate system<sup>4</sup>.

In the gravitational wave coordinate system, the gravitational wave propagates in the positive  $z$ -direction. Thus, the  $z$ -axis coincides with the line of sight from the neutron star to the Earth. The  $x$ -axis of the gravitational wave coordinate system lies in the gravitational wave plane; it is perpendicular to the  $z$ -axis and perpendicular to the star's rotation axis. The  $3 \times 3$  matrix  $H(t)$  of the spatial metric perturbation produced by the gravitational wave in the wave coordinate system has the form

$$H(t) = \begin{pmatrix} h_+(t) & h_\times(t) & 0 \\ h_\times(t) & -h_+(t) & 0 \\ 0 & 0 & 0 \end{pmatrix}. \quad (1.16)$$

To determine the  $3 \times 3$  matrix  $\tilde{H}(t)$  of the spatial metric perturbation produced by the gravitational wave in the detector proper reference frame coordinate system,  $H(t)$  needs to be transformed into the desired coordinate system via

$$\tilde{H}(t) = M(t) H(t) M(t)^T, \quad (1.17)$$

with

$$M = M_3 M_2 M_1. \quad (1.18)$$

$M_1$  is the matrix of transformation from the gravitational wave coordinate system to the celestial equatorial coordinate system,  $M_2$  is the matrix of transformation from the celestial equatorial coordinate system to the cardinal coordinate system located at the detector, and  $M_3$  is the matrix of transformation from the cardinal coordinate system to the detector proper reference frame coordinate system. In the following a detailed description of the three matrices is given. Most of the steps and description are taken from the publications<sup>5</sup> [47, 49, 50].

The matrix  $M_1$  is defined in terms of the position of the neutron star in the celestial equatorial coordinate system, i.e. by its declination,  $\delta$ , and right ascension,  $\alpha$ , and the polarisation angle  $\psi$ . The polarisation angle,  $\psi$ , is defined as the angle between lines  $a$  and  $b$  shown in picture III of Figure 1.4. Line  $a$  is the intersection of the gravitational wave plane (the plane transverse to the propagation direction) and the equatorial plane of the Earth. Line  $b$  is perpendicular to the neutron star's angular momentum and also lies in the gravitational wave plane. From these three angles ( $\alpha$ ,  $\delta$ , and  $\psi$ ) the Euler angles can be derived, which transform the celestial equatorial coordinate system to the gravitational wave coordinate system and yield  $M_1^T$ . Here the convention of the Euler angles as described in [50] will be applied.

In Figure 1.4 the three rotations for the coordinate system transformation are pictured. First, the celestial equatorial coordinate system  $(\vec{x}_{\text{CS}}, \vec{y}_{\text{CS}}, \vec{z}_{\text{CS}})$  is rotated counterclockwise about its  $\vec{z}_{\text{CS}}$ -axis by the angle  $\phi$ , where  $\phi$  equals  $(\alpha - \pi/2)$ . This leads to the intermediate coordinate system  $(\vec{x}', \vec{y}', \vec{z}')$  in which  $\vec{z}'$  corresponds to

<sup>4</sup>For a description of the celestial equatorial coordinate system, the cardinal coordinate system, and the detector proper reference frame coordinate system see Appendix B.

<sup>5</sup>Please be aware that Equation 8 of [47] contains a sign error and Figure 8 in [49] is misleading.

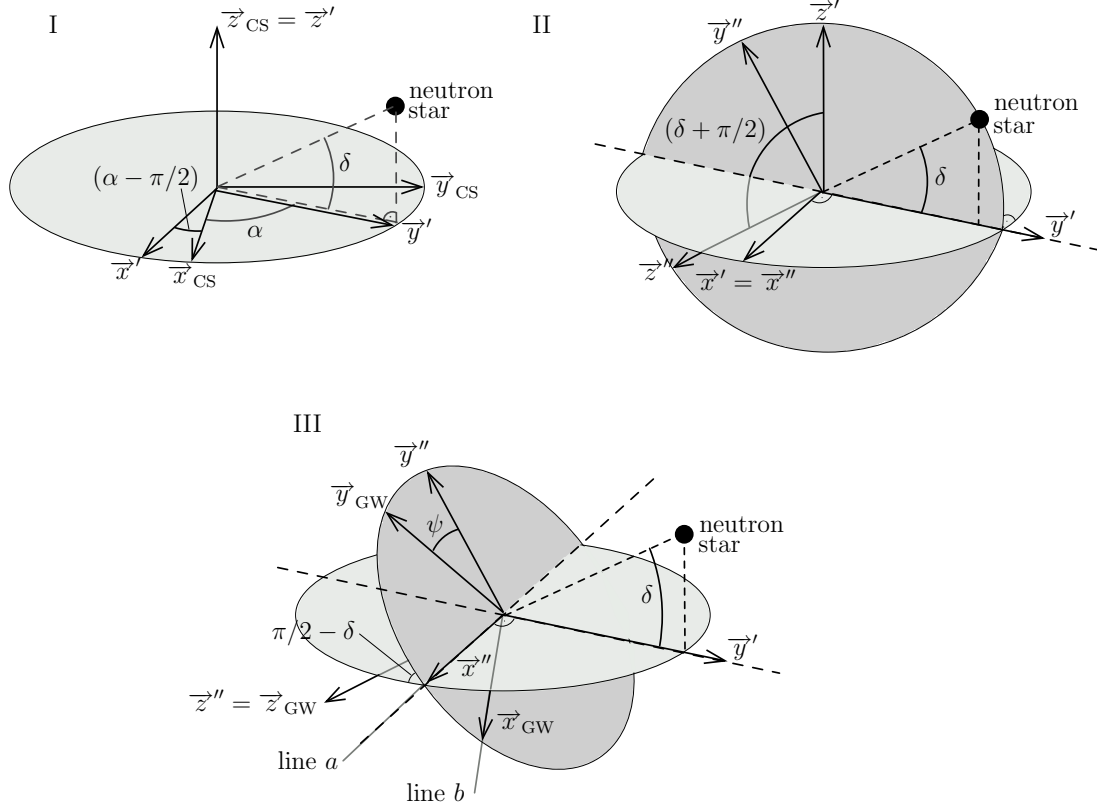


**Figure 1.4:** Euler angles to transform the celestial equatorial coordinate system to the gravitational wave coordinate system. The grey ellipses span a plane perpendicular to a vector of rotation. All vectors which end on the rim of an ellipse are situated in this plane. In I  $\vec{x}_{CS}$  and  $\vec{y}_{CS}$  are rotated counterclockwise by  $(\alpha - \pi/2)$  about the  $\vec{z}_{CS}$ -axis. In II  $\vec{y}'$  and  $\vec{z}'$  are rotated counterclockwise by  $(\delta + \pi/2)$  about the  $\vec{x}'$ -axis. In III  $\vec{x}''$  and  $\vec{y}''$  are rotated counterclockwise by  $\psi$  about the  $\vec{z}''$ -axis. After the rotations performed by step I and II, the  $\vec{z}''$ -axis points into the opposite direction of the line of sight from the Earth to the neutron star. In III the here called lines *a* and *b* that define the polarisation angle  $\psi$  are pictured. Line *a* is the intersection of the gravitational wave plane (the plane transverse to the propagation direction) and the equatorial plane of the Earth. Line *b* is perpendicular to the neutron star's angular momentum and also lies in the gravitational wave plane.

$\vec{z}_{\text{CS}}$ . In the second step, the coordinate system  $(\vec{x}', \vec{y}', \vec{z}')$  is rotated counterclockwise about its  $\vec{x}'$ -axis by the angle  $\theta$ , where  $\theta = (\delta + \pi/2)$ . This leads to the intermediate coordinate system  $(\vec{x}'', \vec{y}'', \vec{z}'')$  in which  $\vec{x}''$  corresponds to  $\vec{x}'$ . After these two rotations  $\vec{z}''$  coincides with the  $z$ -axis of the gravitational wave coordinate system. The information about the position of the neutron star in the celestial equatorial coordinate system leads to the transformation of  $\vec{z}_{\text{CS}}$  to  $\vec{z}_{\text{GW}}$ . Thus, the  $z''$ -axis points in the opposite direction of the line of sight from the Earth to the neutron star. In the third and last step, the coordinate system  $(\vec{x}'', \vec{y}'', \vec{z}'')$  is rotated about its  $\vec{z}''$ -axis by the angle  $\psi$ , the polarisation angle. By definition of  $\psi$  this transforms  $(\vec{x}'', \vec{y}'', \vec{z}'')$  into the gravitational wave coordinate system  $(\vec{x}_{\text{GW}}, \vec{y}_{\text{GW}}, \vec{z}_{\text{GW}})$ . With the Euler angles  $(\delta + \pi/2, \alpha - \pi/2, \psi)$  according to Equation 4.46 and 4.47 in [50],  $M_1^T$  and  $M_1$  are given by

$$M_1^T = \begin{pmatrix} \sin \alpha \cos \psi - \cos \alpha \sin \delta \sin \psi & -\cos \alpha \cos \psi - \sin \alpha \sin \delta \sin \psi & \cos \delta \sin \psi \\ -\sin \alpha \sin \psi - \cos \alpha \sin \delta \cos \psi & \cos \alpha \sin \psi - \sin \alpha \sin \delta \cos \psi & \cos \delta \cos \psi \\ -\cos \alpha \cos \delta & -\sin \alpha \cos \delta & -\sin \delta \end{pmatrix} \quad (1.19)$$

and

$$M_1 = \begin{pmatrix} \sin \alpha \cos \psi - \cos \alpha \sin \delta \sin \psi & -\sin \alpha \sin \psi - \cos \alpha \sin \delta \cos \psi & -\cos \alpha \cos \delta \\ -\cos \alpha \cos \psi - \sin \alpha \sin \delta \sin \psi & \cos \alpha \sin \psi - \sin \alpha \sin \delta \cos \psi & -\sin \alpha \cos \delta \\ \cos \delta \sin \psi & \cos \delta \cos \psi & -\sin \delta \end{pmatrix}. \quad (1.20)$$

The matrix  $M_2$  transforms from the celestial equatorial coordinate system to the cardinal coordinate system located at the detector. It is defined in terms of the latitude,  $\lambda$ , of the detector's site, the total rotational angular velocity of the Earth,  $\Omega_r$ , and a deterministic phase,  $\phi_r$ , which defines the position of the Earth in its diurnal motion at  $t = 0$ . From Figure 1.5 it can be seen that the unit vectors of the cardinal coordinate system  $(\vec{x}_{\text{CD}}, \vec{y}_{\text{CD}}, \vec{z}_{\text{CD}})$  take the following form when expressed in the celestial equatorial coordinate system

$$\begin{aligned} \vec{x}_{\text{CD}} &= \begin{pmatrix} \sin \lambda \cos(\phi_r + \Omega_r t) \\ \sin \lambda \sin(\phi_r + \Omega_r t) \\ -\cos \lambda \end{pmatrix}, & \vec{y}_{\text{CD}} &= \begin{pmatrix} -\sin(\phi_r + \Omega_r t) \\ \cos(\phi_r + \Omega_r t) \\ 0 \end{pmatrix}, \\ \vec{z}_{\text{CD}} &= \begin{pmatrix} \cos \lambda \cos(\phi_r + \Omega_r t) \\ \cos \lambda \sin(\phi_r + \Omega_r t) \\ \sin \lambda \end{pmatrix}. \end{aligned} \quad (1.21)$$

Equations 1.10 and 1.21 yield the matrix  $M_2$

$$M_2(t) = \begin{pmatrix} \sin \lambda \cos(\phi_r + \Omega_r t) & \sin \lambda \sin(\phi_r + \Omega_r t) & -\cos \lambda \\ -\sin(\phi_r + \Omega_r t) & \cos(\phi_r + \Omega_r t) & 0 \\ \cos \lambda \cos(\phi_r + \Omega_r t) & \cos \lambda \sin(\phi_r + \Omega_r t) & \sin \lambda \end{pmatrix}. \quad (1.22)$$

The matrix  $M_3$  is defined in terms of the angle  $\gamma$  measured counterclockwise from East to the bisector of the interferometer arms and  $\zeta$  the angle between the interferometer arms.  $M_3$  can be derived in the same way as  $M_2$ . As can be seen in Figure 1.6, the unit vectors of the detector proper reference frame coordinate system  $(\vec{x}_{\text{DT}}, \vec{y}_{\text{DT}}, \vec{z}_{\text{DT}})$  have the following form when expressed in the cardinal coordinate system  $(\vec{x}_{\text{CD}}, \vec{y}_{\text{CD}}, \vec{z}_{\text{CD}})$

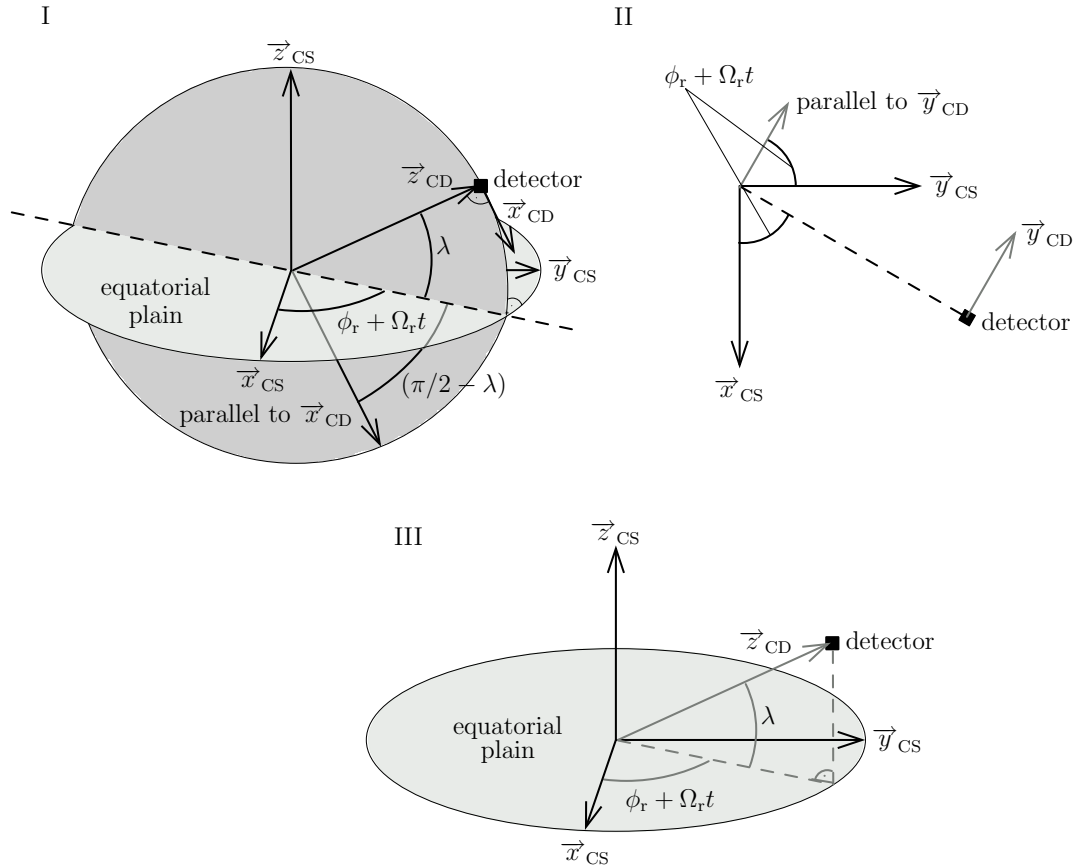


**Figure 1.5:** Presentation of the vectors spanning the cardinal coordinate system  $(\vec{x}_{CD}, \vec{y}_{CD}, \vec{z}_{CD})$  in the celestial equatorial coordinate system  $(\vec{x}_{CS}, \vec{y}_{CS}, \vec{z}_{CS})$ . The grey (light and dark) ellipses in I and III span a plane on which all vectors are situated, that end at the rim of an ellipse. The light grey ellipses represent the equatorial plane of the celestial equatorial coordinate system. For the representation of  $\vec{y}_{CD}$  in II, only the equatorial plane of the celestial equatorial coordinate system is pictured, because  $\vec{y}_{CD}$  is parallel to the equatorial plane. As an aid to directly read the coordinates of  $\vec{y}_{CD}$  in  $(\vec{x}_{CS}, \vec{y}_{CS}, \vec{z}_{CS})$  a vector parallel to  $\vec{y}_{CD}$  is drawn, starting in the origin of the celestial equatorial coordinate system. In III, the coordinates of  $\vec{z}_{CD}$  in  $(\vec{x}_{CS}, \vec{y}_{CS}, \vec{z}_{CS})$  can be seen.  $\vec{z}_{CD}$  is pointing by definition from the geocentre to the detector. If a plane that is spanned by  $\vec{x}_{CD}$  and  $\vec{z}_{CD}$  is added to picture III one receives picture I. This plane, presented by the dark grey ellipse, is perpendicular by definition to the equatorial plane of the celestial coordinate system. Again, as an aid to directly read the coordinates of  $\vec{x}_{CD}$  in  $(\vec{x}_{CS}, \vec{y}_{CS}, \vec{z}_{CS})$ , a vector parallel to  $\vec{x}_{CD}$  is drawn, starting in the origin of the celestial equatorial coordinate system.



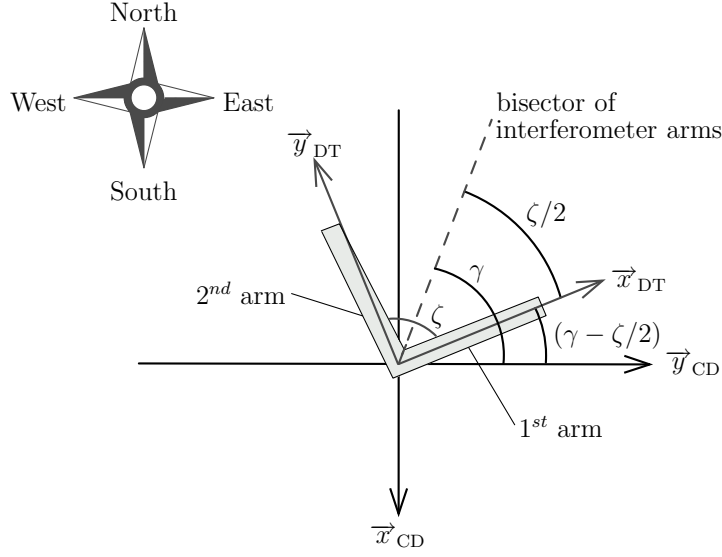


**Figure 1.6:** Presentation of the vectors spanning the detector proper reference frame coordinate system  $(\vec{x}_{DT}, \vec{y}_{DT}, \vec{z}_{DT})$  in the cardinal coordinate system  $(\vec{x}_{CD}, \vec{y}_{CD}, \vec{z}_{CD})$ . Only the plane tangent to the Earth surface is depicted.  $\vec{z}_{DT}$  which coincides with  $\vec{z}_{CD}$  points out of the page. The angle  $\gamma$  is measured counterclockwise from East to the bisector of the interferometer arms. In the picture GEO 600 with its proper orientation is drawn. At GEO 600  $\zeta$ , the angle between the interferometer arms, is  $94.33^\circ$ .

$$\vec{x}_{DT} = \begin{pmatrix} -\sin(\gamma - \zeta/2) \\ \cos(\gamma - \zeta/2) \\ 0 \end{pmatrix}, \vec{y}_{DT} = \begin{pmatrix} -\cos(\gamma - \zeta/2) \\ -\sin(\gamma - \zeta/2) \\ 0 \end{pmatrix}, \vec{z}_{DT} = \begin{pmatrix} 0 \\ 0 \\ 1 \end{pmatrix}. \quad (1.23)$$

Equations (1.10) and (1.23) yield the matrix  $M_3$ <sup>6</sup>

$$M_3 = \begin{pmatrix} -\sin(\gamma - \zeta/2) & \cos(\gamma - \zeta/2) & 0 \\ -\cos(\gamma - \zeta/2) & -\sin(\gamma - \zeta/2) & 0 \\ 0 & 0 & 1 \end{pmatrix}. \quad (1.24)$$

Now  $h(t)$  can be directly computed with

$$h(t) = \frac{1}{2} \vec{e}_1 [\tilde{H}(t) \vec{e}_1] - \frac{1}{2} \vec{e}_2 [\tilde{H}(t) \vec{e}_2], \quad (1.25)$$

where  $\vec{e}_1$  and  $\vec{e}_2$  denote the unit vectors parallel to the first and second arm of the interferometer, respectively. That means  $\vec{e}_1$  is always parallel to  $\vec{x}_{DT}$  and  $\vec{e}_2 = (\cos \zeta, \sin \zeta, 0)$ . For the case of an interferometer where the arms are perpendicular to each other,  $\vec{e}_2$  is parallel to  $\vec{y}_{DT}$ . Combining Equations 1.16 to 1.25 and extensive

<sup>6</sup>Please note that in [47] in Equation 8 the argument of all trigonometric functions should be  $(\gamma - \zeta/2)$  instead of  $(\gamma + \zeta/2)$ .

algebraic manipulations yield the expressions

$$F_+(t) = \sin \zeta [a(t) \cos 2\psi + b(t) \sin 2\psi] \quad (1.26)$$

$$F_\times(t) = \sin \zeta [b(t) \cos 2\psi - a(t) \sin 2\psi], \quad (1.27)$$

where

$$\begin{aligned} a(t) = & \frac{1}{16} \sin 2\gamma (3 - \cos 2\lambda) (3 - \cos 2\delta) \cos [2(\alpha - \phi_r - \Omega_r t)] \\ & - \frac{1}{4} \cos 2\gamma \sin \lambda (3 - \cos 2\delta) \sin [2(\alpha - \phi_r - \Omega_r t)] \\ & + \frac{1}{4} \sin 2\gamma \sin 2\lambda \sin 2\delta \cos [\alpha - \phi_r - \Omega_r t] \\ & - \frac{1}{2} \cos 2\gamma \cos \lambda \sin 2\delta \sin [\alpha - \phi_r - \Omega_r t] \\ & + \frac{3}{4} \sin 2\gamma \cos^2 \lambda \cos^2 \delta, \end{aligned} \quad (1.28)$$

$$\begin{aligned} b(t) = & \cos 2\gamma \sin \lambda \sin \delta \cos [2(\alpha - \phi_r - \Omega_r t)] \\ & + \frac{1}{4} \sin 2\gamma (3 - \cos 2\lambda) \sin \delta \sin [2(\alpha - \phi_r - \Omega_r t)] \\ & + \cos 2\gamma \cos \lambda \cos \delta \cos [\alpha - \phi_r - \Omega_r t] \\ & + \frac{1}{2} \sin 2\gamma \sin 2\lambda \cos \delta \sin [\alpha - \phi_r - \Omega_r t]. \end{aligned} \quad (1.29)$$

Thus it can be seen that the antenna response functions,  $F_+(t)$  and  $F_\times(t)$ , actually depend on eight angles, that is  $F_+(t, \psi, \alpha, \delta, \lambda, \phi_r, \Omega_r, \gamma, \zeta)$  and  $F_\times(t, \psi, \alpha, \delta, \lambda, \phi_r, \Omega_r, \gamma, \zeta)$ .

## Chapter 2

# Production of a simulated, continuous gravitational wave signal

In order to inject a simulated strain signal into the interferometer, an analog electronic signal proportional to the gravitational wave amplitude is generated. This electronic signal is used to produce a force that acts upon one of the interferometer main mirrors, thereby changing the differential length of the two arms and simulating the effect of a gravitational wave. Splitting the continuous gravitational wave signal into a slowly varying amplitude component and a sinusoidal phase component, as described below, allows us to generate these two components independently of each other. A Hitachi 3048F microcontroller with two on-chip D/A converters is used as a direct digital frequency synthesiser (DDS) to generate the signal. The sinusoidal component and the slowly varying amplitude factor are separately generated by the two D/A converters and are then combined by analog electronic multiplication. The complicated phase evolution of the signal is controlled by a PC running a C program that uses GPS timing signals and the LIGO/LSC algorithm library (LAL).

Our setup for the hardware injection aims for a phase error of less than 1 % of  $2\pi$  rad from the correct signal phase and an amplitude error below 1 % of the maximal amplitude for injection times of several months and signal frequencies between 100 Hz and 2 kHz. A phase error of 1 % will not affect the sensitivity of the search algorithms and an amplitude accuracy of 1 % is better than the accuracy of the actuators used for the hardware injection (see section 3.2).

For the first time a simulated, continuous gravitational wave signal was injected at GEO 600 during S3 II (second part of science run three lasting from 2003-12-30 15:00:00 UTC to 2004-01-13 16:00:00 UTC). Over this whole period the signal was applied to an actuator of the main interferometer and the signal was recorded directly with the data acquisition system. As it turned out later there was electronic cross-talk of the directly recorded signal to the interferometer channels. Therefore the injection during S3II could not be used for analysis. For convenience the directly recorded signal during S3II has been used to investigate the performance of the signal. Therefore most of the investigations of the generated signal are performed during time stretches of S3II.

In the first part of this chapter the simulated, continuous gravitational wave signal is converted into a form with only one amplitude and one oscillatory term. Then it is explained how this signal is generated on the software side. In the second part of this chapter the hardware used for the signal production is described in detail.

## 2.1 Signal generation software

The continuous gravitational wave signal from a non-axisymmetric, non-precessing, spinning neutron star, as given in Equations 1.4 to 1.6,

$$h(t) = F_+(t, \psi) \frac{1}{2} h_0 (1 + \cos^2 \iota) \cos 2\phi(t) + F_\times(t, \psi) h_0 \cos \iota \sin 2\phi(t), \quad (2.1)$$

can be rewritten (by expressing the continuous gravitational wave signal in terms of an amplitude  $a(t)$  and an oscillatory part  $\sin \varphi(t)$  only), according to section 2.5.2.1.4 of [51], as

$$h(t) = h_0 \underbrace{\sqrt{F_+^2(t, \psi) \frac{1}{4} (1 + \cos^2 \iota)^2 + F_\times^2(t, \psi) \cos^2 \iota}}_{a(t)} \times \sin \left[ \underbrace{2\phi(t) + \arctan \frac{F_+(t, \psi) (1 + \cos^2 \iota)}{2F_\times(t, \psi) \cos \iota}}_{\varphi(t)} \right]. \quad (2.2)$$

For the explanation of the quantities see subsection 1.2.2.  $h(t)$ ,  $a(t)$  and  $\varphi(t)$  can be determined numerically using the LIGO/LSC Algorithm Library (LAL) [52]. Equation 2.2 shows how the amplitude  $a(t)$  and the oscillatory part  $\sin \varphi(t)$  can be produced electronically independently of each other and then combined by analog electronic multiplication to give the full simulated signal.

### 2.1.1 Calculating the phase

The function  $\varphi(t)$  is the phase evolution of the continuous gravitational wave signal and, according to Equations 1.8 to 1.14, a function of  $f_0$ ,  $\dot{f}_0$ ,  $\ddot{f}_0$ ,  $\alpha$ ,  $\delta$ ,  $\varepsilon$ ,  $\phi_0$ ,  $\Omega_0(t)$ ,  $\lambda$ ,  $\phi_r$ ,  $\Omega_r$ ,  $R_{SE}(t)$ ,  $R_{ED}$ ,  $\iota$ ,  $\psi$ ,  $\gamma$ , and  $\zeta$ . The orbital angular velocity of the Earth,  $\Omega_0(t)$ , the deterministic phase,  $\phi_0$ , which defines the position of the Earth in its diurnal motion at  $t = 0$ , the rotational angular velocity of the Earth,  $\Omega_r$ , the deterministic phase,  $\phi_r$ , which defines the position of the Earth in its diurnal motion at  $t = 0$ , and the distance,  $R_{SE}(t)$ , from the SSB to the Earth centre are read within the LAL code from ephemeris data<sup>1</sup>. The phase  $\varphi(t)$  is calculated in a C program running on a control computer with the function `atan2` used for the arctan in Equation 2.2. This function makes phase jumps of  $2\pi$  when the denominator is negative and the numerator has a zero crossing as can be seen in Figure 2.1. These jumps are subtracted from the overall  $\varphi(t)$  yielding a continuous form of  $\varphi(t)$ , which is needed to control the phase as described in section 2.2.

The gravitational wave signal frequency at the detector is constantly changing due to the spin-down of the neutron star ( $\dot{f}_0$  and  $\ddot{f}_0$ ) and a Doppler shift caused by the detector motion relative to the neutron star. This relative motion can be split into a motion due to the Earth's diurnal motion and one due to the Earth's orbit around the sun. The

---

<sup>1</sup>Ephemerides contain the exact positions and velocities of celestial bodies at certain times, which are calculated and adjusted by observational data.

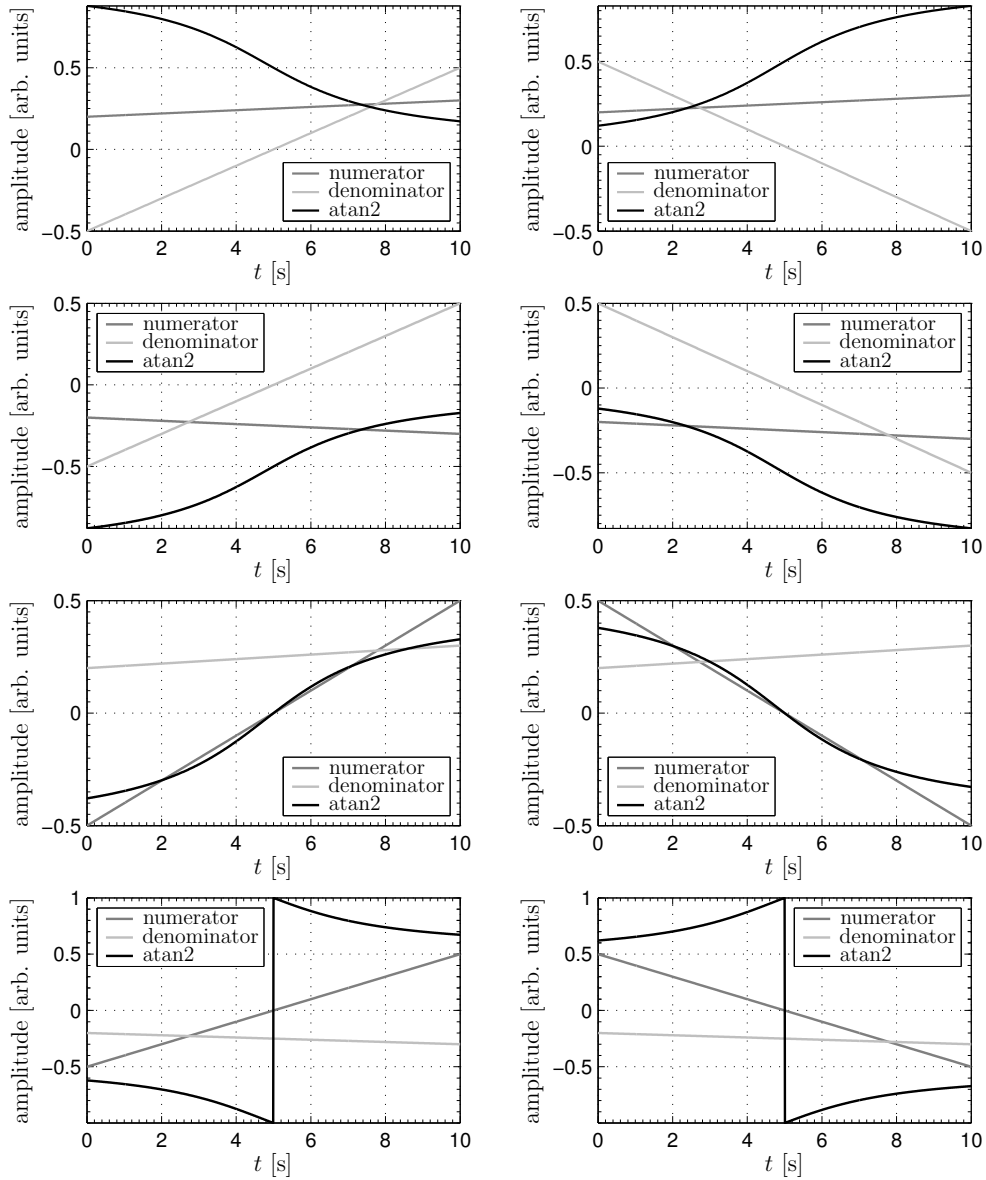


**Figure 2.1:** Behaviour of the `atan2` function in C. In the above graphs the numerator and denominator of the `atan2` function are plotted. The curve identified as `atan2` is the `atan2(numerator,denominator)`. Only if the denominator is negative and the numerator changes sign, phase jumps of  $2\pi$  rad occur. If the numerator changes from negative to positive a jump of  $+2\pi$  rad occurs. If the numerator changes from positive to negative a jump of  $-2\pi$  rad occurs.

absolute value of the upper limit of a relative frequency shift due to the Doppler shift caused by the Earth's motion is given by

$$\frac{|\Delta f_{\max}|}{f_{\text{SSB}}} = \frac{v}{c}, \quad (2.3)$$

where  $\Delta f_{\max}$  is the maximal frequency shift,  $f_{\text{SSB}}$  the gravitational wave signal frequency at the SSB (the spin-down is already taken into account),  $v$  the maximal velocity of the detector in the SSB reference frame, and  $c$  the velocity of light. The maximal frequency shift  $\Delta f_{\max}$  is defined such that the instantaneous signal frequency,  $f$ , always falls in the interval  $(f_{\text{SSB}} - \Delta f_{\max}, f_{\text{SSB}} + \Delta f_{\max})$ .

The maximal Doppler shift due to the diurnal motion can be estimated by calculating the maximal velocity at a point on the Earth's surface due to its rotation. With an equatorial radius of 6378 km and a mean sidereal day of 86164 s [53], the maximal velocity on the Earth's surface is  $v_{\oplus\text{rot}} = 465$  m/s. According to Equation 2.3 this gives a relative maximal frequency shift of  $\Delta f_{\max}/f_{\text{SSB}} = 1.6 \times 10^{-6}$  over one sidereal day. With a maximal orbital velocity of  $v_{\oplus\text{orb}} = 30290$  m/s the relative maximal frequency shift due to the orbital motion is given by  $\Delta f_{\max}/f_{\text{SSB}} = 1.0 \times 10^{-4}$  for one sidereal year. The gravitational wave signal frequency will therefore have a small modulation with a period of one sidereal day on top of a larger modulation with a period of one sidereal year.

In the following paragraph it is shown how the frequency of a gravitational wave signal of a neutron star can be calculated within LAL at any time given the neutron star parameters. This method allows for the determination of the effect of the spin-down and the Doppler shift on the frequency of the gravitational wave signal. According to Equation (8.47) of [54] the first derivative of a function  $g(x)$  is given by

$$g'(x_1) = \frac{g(x_2) - g(x_1)}{h} - \frac{h}{2} g''(x_1 + \vartheta h), \quad (2.4)$$

where  $h = x_2 - x_1$  and  $0 < \vartheta < 1$ . As

$$f(t) = \frac{1}{2\pi} \varphi'(t),$$

the gravitational wave signal frequency is to first order approximation

$$f(t_1) = \frac{\varphi(t_2) - \varphi(t_1)}{2\pi\Delta t}, \quad (2.5)$$

where  $\Delta t = t_2 - t_1 = \text{SR}$ , with SR being the sample rate of  $\varphi(t_n)$ . To estimate how good the first order approximation is, the error

$$f_{\text{err}} = \frac{\Delta t}{4\pi} \varphi''(t_1 + \vartheta\Delta t) \quad (2.6)$$

is estimated. To estimate the maximal error of  $f(t_n)$  the maximum of  $\varphi''(t_n)$  needs to be determined. Knowing the maximal relative frequency shift  $\Delta f_{\max}/f_{\text{SSB}}$  due to the orbital and diurnal motion and taking a sinusoidal approach for the orbital and

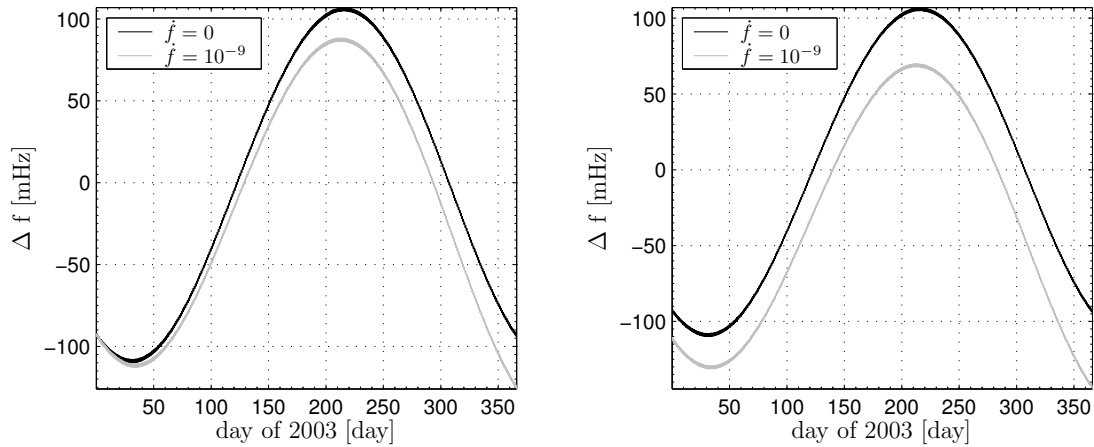
diurnal motion, the maximum of  $\varphi''(t_n)$  can be estimated. With the maximal relative frequency shift  $\Delta f_{\max}/f_{\text{SSB}}$  for the orbital motion being  $1.0 \times 10^{-4}$  over a period of one sidereal year the maximum of  $\varphi''(t_n)$  becomes  $2.0 \times 10^{-11} \text{ 1/s}^2$  for a signal at 1 Hz. With  $\Delta t = 400 \text{ s}$  the maximal error,  $f_{\text{err}}$ , is  $6.4 \times 10^{-8} \%$ . With the maximal relative frequency shift  $\Delta f/f_{\text{SSB}}$  for the diurnal motion being  $1.6 \times 10^{-6}$  over a period of one sidereal day the maximum of  $\varphi''(t_n)$  becomes  $1.2 \times 10^{-10} \text{ 1/s}^2$  for a signal at 1 Hz. With  $\Delta t = 1 \text{ s}$  the maximal error,  $f_{\text{err}}$ , is  $9.5 \times 10^{-10} \%$ . Thus Equation 2.5 is a very good approximation to determine the instantaneous signal frequency. The estimation of  $\varphi''(t_n)$  was made under the assumption that the frequency shift over a year due to spin-down is negligible compared to the frequency shift due to the orbital and diurnal Doppler shift. This is true for real spin-down values, i.e.  $\dot{f}_0 \leq 10^{-11} \text{ 1/s}^2$ .

Figure 2.2 shows the gravitational wave signal frequency offset to its original frequency,  $2f_0$ , for GEO 600 for the year 2003. The neutron star parameters were set to  $\psi = 0.372640504$ ,  $\delta = 0$ ,  $\alpha = 0.776235274$ ,  $\iota = 0.837452625$ , and  $2f_0 = 1125.647365 \text{ Hz}^2$ . All angles are given in radians. The sample rate was chosen to be  $\text{SR} = 0.0025 \text{ Hz}$ . In the black curves of both graphs the spin-down was set to  $\dot{f} = 0 \text{ Hz/s}$ . Thus the black curves show a frequency offset due to Doppler shift only. On the other hand, for the grey curves the spin-down was set to  $\dot{f} = 10^{-9} \text{ Hz/s}$  and they hence show a frequency offset due to Doppler shift and spin-down. It can be seen that the Doppler shift is periodic in one (sidereal) year. For the case of the negative spin-down this periodicity is overlaid by a constant drop of the gravitational wave signal frequency at the SSB. In the left-hand graph the epoch (a fiducial time at which the values  $f_0$ ,  $\dot{f}$ , and  $\ddot{f}$  are given) was chosen to coincide with the start of the data; therefore the curves with spin-down  $\dot{f} = 0 \text{ Hz/s}$  and  $\dot{f} = 10^{-9} \text{ Hz/s}$  start in the same point. In the right-hand graph the epoch was chosen to be half a year before the start of the data; therefore the curve with the negative spin-down  $\dot{f} = 10^{-9} \text{ Hz/s}$  starts at a larger negative offset than the one for  $\dot{f} = 0 \text{ Hz/s}$ .

Figure 2.3 shows the gravitational wave signal frequency offset to its original frequency,  $2f_0$ , for GEO 600 over two days. The neutron star parameters are set to the same values as in the previous example (Figure 2.2). The frequency epoch was chosen to be GPS second 725414413 (1 January 2003) and the spin-down was set to  $\dot{f} = 0 \text{ Hz/s}$ . So the frequency offset arises from the Doppler shift only. Figure 2.3 is a zoom of the black curve in Figure 2.2 at two different times in the year 2003. The periodicity of the Doppler shift in one (sidereal) day due to the effect of the Earth rotation about its axis can be seen. In the left-hand graph of Figure 2.3 the frequency offset is plotted for the days 30-31 of 2003. As can be seen in Figure 2.2 the Doppler shift due to the Earth's orbital motion is at this time largest for the chosen parameters and almost constant. In the right-hand graph of Figure 2.3 the frequency offset is plotted for the days 123-124 of 2003, when the Doppler shift due to the Earth's orbital motion is smallest and changes most rapidly. In the right-hand graph of Figure 2.3 it can be seen how the amplitude of the diurnal Doppler shift is distorted by the superposition of the orbital Doppler shift.

The spikes in both graphs of Figure 2.3 that occur every four hours are due to the

<sup>2</sup>LAL requires as one input the distance of the source, which was chosen to be 3600 pc for all calculations in this work. For distances above 1 kpc the signal values do not change for different distance values.



**Figure 2.2:** Gravitational wave signal frequency offset to  $2f_0$  for GEO 600 for the year 2003. The neutron star parameters were set to  $\psi = 0.372640504$ ,  $\delta = 0$ ,  $\alpha = 0.776235274$ ,  $\iota = 0.837452625$ , and  $2f_0 = 1125.647365$  Hz. All angles are given in radians. The epoch in the left-hand graph was chosen to coincide with the start time of the data. The epoch in the right-hand graph was chosen to be half a year ahead of the start time of the data. The periodicity of the Doppler shift in one (sidereal) year due to the Earth’s orbital motion can be seen. Also the effect of  $\dot{f} \neq 0$  and the epoch on the frequency offset are visible.

discretisation of the ephemeris data used by the LAL code. The ephemeris data are only updated every four hours, which can result in step-like changes of the phase when the ephemeris data are updated. The updates of the ephemeris data make the position of the Earth and thus of the detector used for calculating the signal “jump” every four hours. If the “jump” in velocity is along the propagation direction of the gravitational wave, it causes a maximal change of the signal frequency. It shows up only as a single spike in the frequency offset plots, as there is only a discontinuity between the adjacent times in between which the new ephemeris entry falls. If the “jump” in velocity is orthogonal to the propagation direction of the gravitational wave, it hardly effects the frequency of the signal. These two extremes can be seen in Figure 2.3 where the spikes in the left-hand graph are much larger than in the right-hand graph, 93 days later in the year. The maximal error in travel time  $\tau$  for the signal from the SSB to the detector can accumulate due to this effect up to  $\tau = 0.5 \mu\text{s}$ . This is of the order of the numerical errors of the LAL code [55]. It leads to a phase error of  $\Delta\phi = 3.14 \text{ mrad} \times [2f_0/1 \text{ kHz}] \times [\tau/0.5 \mu\text{s}]$ . In the case of  $2f_0 = 1125.647365$  Hz the discretisation of the ephemeris data can lead to a maximal phase error of 3.5 mrad which is 0.06 % of a full cycle and hence well below the target phase accuracy.

### 2.1.2 Mapping the amplitude envelope

The amplitude is produced with one of the D/A converters of the microcontroller, that is used for the signal generation. The continuous amplitude  $a(t)$  therefore needs to be



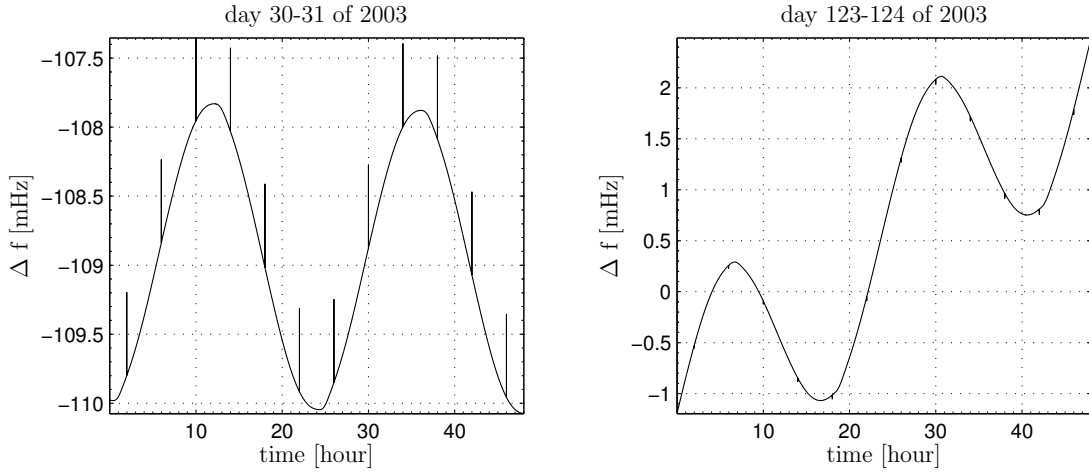


**Figure 2.3:** Gravitational wave signal frequency offset to  $2f_0$  for GEO 600 for four days of the year 2003. The neutron star parameters are set to  $\psi = 0.372640504$ ,  $\delta = 0$ ,  $\alpha = 0.776235274$ ,  $\iota = 0.837452625$ , and  $2f_0 = 1125.647365 \text{ Hz}$ . All angles are given in radians. The frequency epoch was chosen to be GPS second 725414413 (1 January 2003) and the spin-down was set to  $\dot{f} = 0 \text{ Hz/s}$ . The periodicity of the Doppler shift in one (sidereal) day due to the Earth rotation about its axis can be seen. In the left-hand graph the Doppler shift due to the Earth's orbital motion is largest and almost constant. In the right-hand graph the Doppler shift due to the Earth's orbital motion is smallest and at its most rapid change. It can be seen how the amplitude of the diurnal Doppler shift is distorted by the superposition of the orbital Doppler shift. The spikes in the both graphs are due to the discretisation of the ephemeris data used by the LAL code.

mapped onto one of the 8-bit D/A converters. This is achieved by digitising the function  $a(t)$ .

The amplitude  $a(t)$  is the absolute value of the envelope of the continuous gravitational wave signal and, according to Equation 2.2 and subsection 1.2.2, a function of  $h_0, \iota, \psi, \alpha, \delta, \lambda, \phi_r, \Omega_r, \gamma$ , and  $\zeta$  (for the definition of these parameters see subsection 1.2.2). The function  $a(t)$  describes the signal amplitude modulation due to the changing orientation of the detector towards the neutron star as the detector rotates with the Earth. It is periodic in time with a period of one sidereal day.

During the design of the electronics in which the microcontroller is embedded, the signal that represents the amplitude envelope  $a(t)$  was chosen to be bipolar, in order to allow phase shifts of  $\pi$  of the oscillatory signal. Out of the 256 possible 8-bit integers 0-255, the integer 255 stays unused, and the range 0-254 is used for the signal. To make it bipolar, integer 127 is mapped to 0 V. The non-negative amplitude envelope  $a(t)$  can then be mapped onto the integers 127-254 or 0-127 of the 8-bit D/A converter of the microcontroller. This allows a positive or negative sign of the amplitude or in other words a phase shift of  $\pi$ . The maximal amplitude is mapped onto integer 0 or integer 254, depending on the sign.

Thus the full amplitude is spread over 128 integers exploiting 50% of the full dynamic

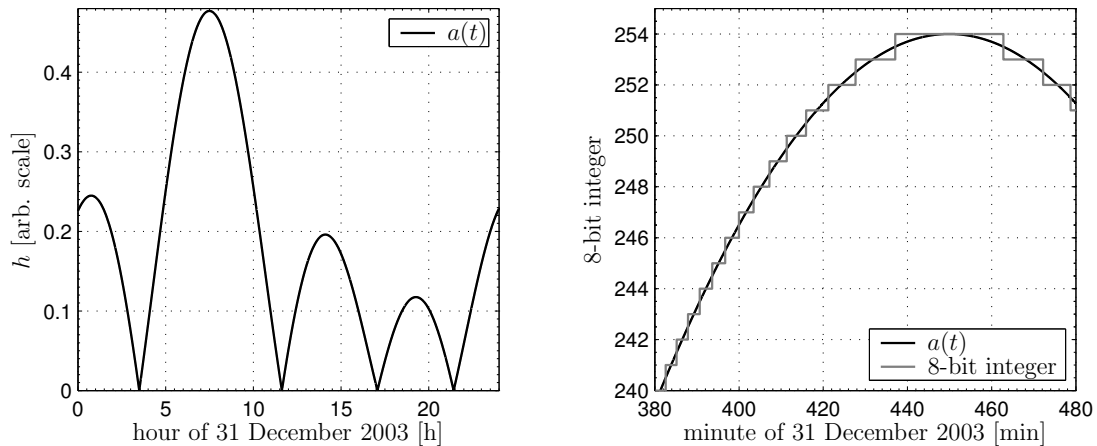


**Figure 2.4:** The left graph shows the gravitational wave signal amplitude envelope  $a(t)$  of a neutron star scaled to  $h_0 = 1$ ,  $\iota = \pi/2$ ,  $\psi = 0.372640504$ ,  $\alpha = 0.776235274$  and  $\delta = -0.616383646$  for GEO 600 on 31 December 2003. All angles are given in radians. The right graph shows how the amplitude envelope  $a(t)$  of the left graph is mapped onto an 8-bit D/A converter for minutes 380 to 480 on 31 December 2003 (corresponding to the time from 6:20:00 to 8:00:00).

range of the 8-bit D/A converter. In Table 2.1 the  $a(t)$  signal range for the according integer and analog output is listed for the 8-bit D/A converter. In this table

$$\Delta a = \frac{a_{\max}}{127}, \quad (2.7)$$

where  $a_{\max}$  is the maximum of  $a(t)$ .  $V_{\max}$  is the maximal output of the D/A converter, which is 10 V for the Hitachi 3048F. The digitisation error referred to the maximal amplitude is then below 0.8% and hence better than the amplitude accuracy of the injection hardware (see section 3.2).

Figure 2.4 gives the gravitational wave signal amplitude envelope  $a(t)$  of a neutron star scaled to  $h_0 = 1$ ,  $\iota = \pi/2$ ,  $\psi = 0.372640504$ ,  $\alpha = 0.776235274$ , and  $\delta = -0.616383646$  for GEO 600 on 31 December 2003 with a sample rate of 1 Hz. For all calculations in this subsection 2.1.2 the gravitational wave signal frequency  $2f_0$  was set to 1125.647365 Hz, the spin-down to 0 Hz/s, the phase epoch to GPS second 751680013, and the phase offset to 1.993746459. The left-hand graph shows the gravitational wave signal amplitude envelope  $a(t)$  determined with LAL. In the right-hand graph the gravitational wave signal amplitude envelope  $a(t)$  of the left graph is mapped onto the 8-bit D/A converter for minutes 380 to 480 for 31 December 2003. The amplitude is mapped into the bins 127-254. For this signal over a whole day the time period over which the amplitude is set to the same 8-bit integer is 78 seconds at the steepest slope and 1541 seconds at the shallowest slope. A sample rate of 1 Hz was used for these calculations.

Figure 2.5 shows the gravitational wave signal amplitude envelopes  $a(t)$  of neutron stars scaled to  $h_0 = 1.0$ ,  $\alpha = 0.776235274$  and  $\psi = 0.372640504$  for GEO 600 on 31 December 2003 (UTC). The parameters  $\iota$  and  $\delta$  are varied;  $\iota$  is given the value  $\pi/2$  or 0.837452625 and  $\delta$  is given the value  $\pi/2$  or  $-0.616383646$ . As can be seen in Figure 2.5

Mapping of the amplitude		
$a(t)$	integer	analog output
$(\frac{253}{2}\Delta a, 127\Delta a]$	254	$V_{\max}$
$(\frac{251}{2}\Delta a, \frac{253}{2}\Delta a]$	253	$\frac{126}{127}V_{\max}$
...	...	...
$(\frac{1}{2}\Delta a, \frac{3}{2}\Delta a]$	128	$\frac{1}{127}V_{\max}$
$(-\frac{1}{2}\Delta a, \frac{1}{2}\Delta a]$	127	0
$(-\frac{3}{2}\Delta a, -\frac{1}{2}\Delta a]$	126	$-\frac{1}{127}V_{\max}$
...	...	...
$(-\frac{253}{2}\Delta a, -\frac{252}{2}\Delta a]$	1	$-\frac{126}{127}V_{\max}$
$[-127\Delta a, -\frac{253}{2}\Delta a]$	0	$-V_{\max}$

**Table 2.1:** This table shows which  $a(t)$  range is mapped onto which integer and what the according analog output is for an 8-bit D/A converter ( $\Delta a = a_{\max}/127$ ).  $V_{\max}$  is the maximal output of the D/A converter, which is 10 V for the Hitachi 3048F.

the resulting gravitational wave signal amplitude envelope is usually not sinusoidal.

### 2.1.3 Software comparison of the time-domain search algorithm and the hardware injection code

In this section the signal produced by the time-domain search algorithm and the signal produced by the hardware signal injection code are compared against each other. Both signals can differ, as the search algorithm calculates the signal according to Equation 2.1 and the hardware injection code according to Equation 2.2.

For the software comparison the signal parameters of the recorded simulated gravitational wave signal during S3 II<sup>3</sup> at GEO 600 were used. The signal parameters are listed in Table 2.2. The signals generated with the hardware injection code and the time-domain search algorithm are compared at the maximal and minimal amplitude of the signal on 31 December 2003. In the lower left graph of Figure 2.6 the amplitude of this signal is plotted over the whole day. It can be seen that the maximal amplitude is around 7:35:00 of that day and the minimal amplitude around 21:24:00. The signals generated with the two different codes are plotted in the left graphs of Figure 2.7 over a few  $\mu\text{s}$ . In the right graphs of Figure 2.7 their difference is expressed in percentage of the maximal amplitude of the signal in the second the data is taken from. The upper

<sup>3</sup>S3II stands for science run 3 part II, that lasted from 2003-12-30 15:00:00 UTC until 2004-01-13 16:00:00 UTC. The hardware injection performed during S3 II is invalid, as electronic cross-talk in the data acquisition system from a direct recording of the electronic simulated signal occurred by various interferometer channels. For convenience the data of the directly recorded signal is used for investigations on the signal generation hardware. Therefore the software tests are done as well in this time period.

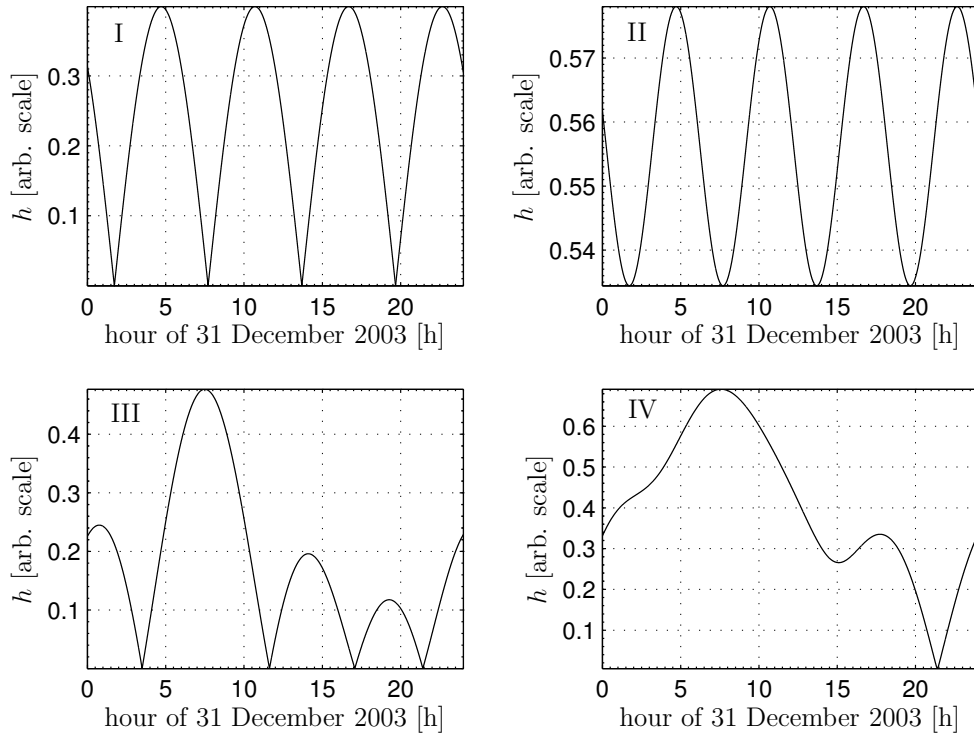


**Figure 2.5:** Gravitational wave signal amplitude envelopes of neutron stars scaled to  $h_0 = 1.0$ ,  $\alpha = 0.776235274$  and  $\psi = 0.372640504$  for GEO 600 on 31 December 2003 (UTC). In graph I  $\iota = \pi/2$  and  $\delta = \pi/2$ ; in graph II  $\iota = 0.837452625$  and  $\delta = \pi/2$ ; in graph III  $\iota = \pi/2$  and  $\delta = -0.616383646$ ; in graph IV  $\iota = 0.837452625$  and  $\delta = -0.616383646$ . All angles are given in radians.

plots of Figure 2.7 correspond to times of maximal amplitude around 7:35:00 and the lower plots correspond to times of minimal amplitude around 21:24:00 on 31 December 2003. It can be seen that the difference stays well below 0.001%.

The timing routines used within LAL to compute the phase of the signal were checked against the widely-used radio astronomy package TEMPO [46, 57, 58].

In the upper left graph of Figure 2.6 the signal frequency offset to the neutron star spin frequency is plotted for the continuous gravitational wave signal at GEO 600 on 31 December 2003 (for the neutron star parameters see Table 2.2). It can be seen that there is a dip around 21:20:00 of that day. This occurs when both antenna response functions,  $F_+(t)$  and  $F_\times(t)$ , are around 0 at the same time. As the absolute error of the beam pattern functions (determined within LAL) is up to  $6 \times 10^{-4}$  [59], the relative error of the phase  $\varphi(t)$  increases when both  $F_+(t)$  and  $F_\times(t)$  are around 0 at the same time. Under these conditions the amplitude  $a(t)$  is also around 0. Therefore the effect of this inaccuracy in the phase  $\varphi(t)$  of the signal is negligible for the overall signal.

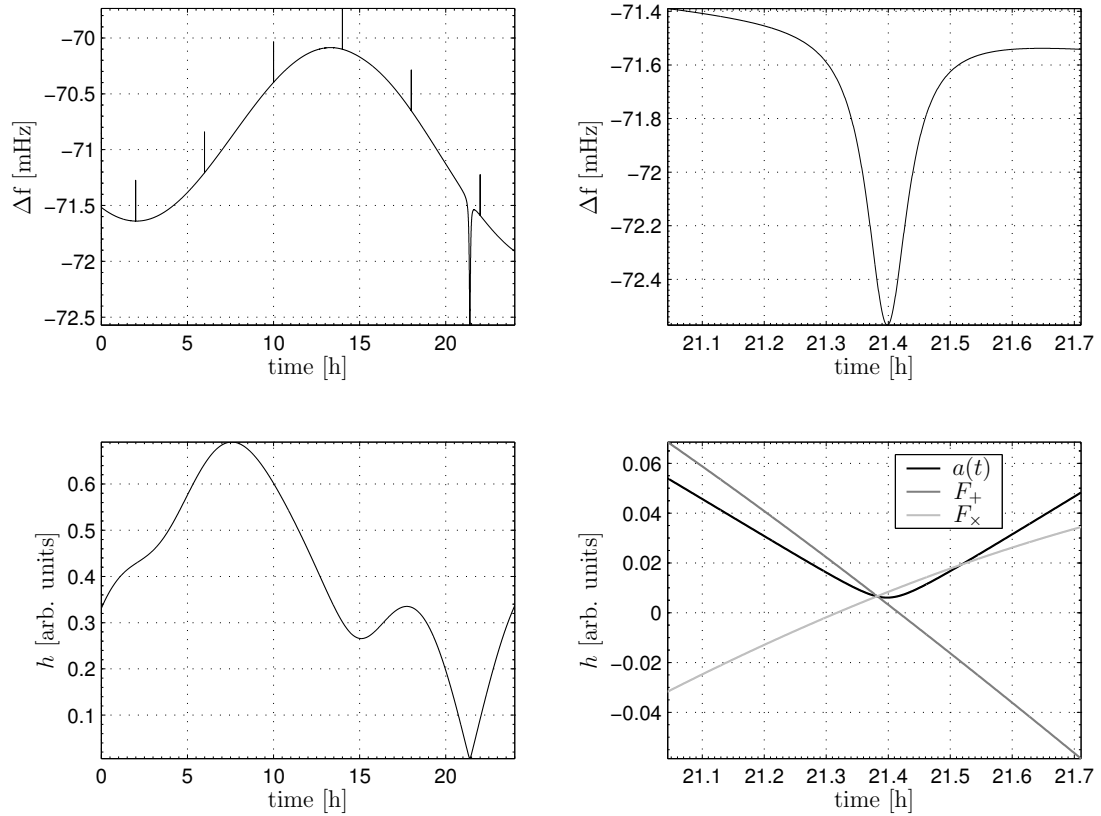


**Figure 2.6:** The upper left graph shows the signal frequency offset to its original frequency for the continuous gravitational wave signal recorded at GEO 600 on 31 December 2003 (for the neutron star parameters see Table 2.2). The dip in the phase of the signal around 21:24:00 occurs when both antenna response functions,  $F_+(t)$  and  $F_\times(t)$ , are around 0 at the same time, as can be seen in the upper right and lower right graph. By definition (see Equation 2.2) the amplitude of the signal is around 0 during these times, as can be seen in the lower left graph.

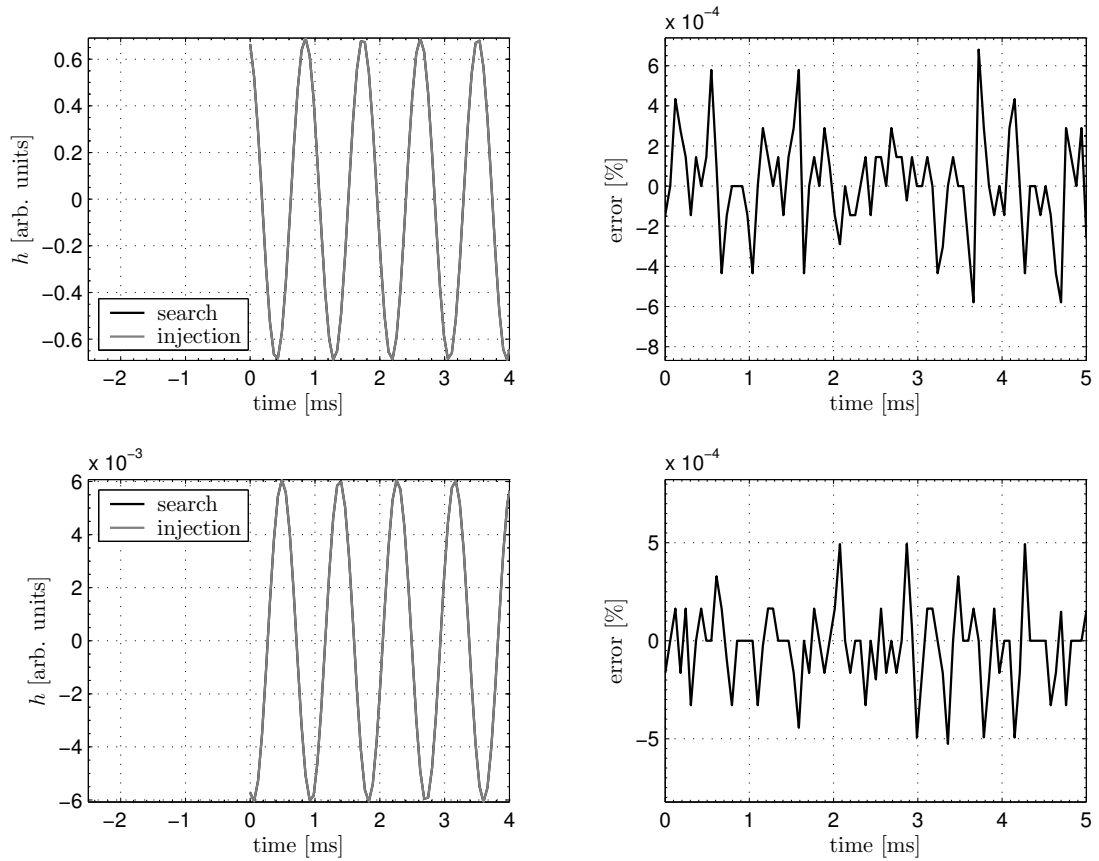


**Figure 2.7:** The left graphs show the signal generated with the time-domain search algorithm and the hardware injection code for GEO 600 at maximal amplitude around 7:35:00 and minimal amplitude around 21:24:00 on 31 December 2003. The parameters for the neutron star are given in Table 2.2. A difference is not visible by eye. The right graphs show the difference of the two signals expressed in percent of the maximal amplitude of the seconds from which the time stretches are taken.

S3 II pulsar parameters		
$h_0$	$7.52231 \times 10^{-22}$	
$2f_0$	1125.647365	[Hz]
$\dot{f}$	$-2.87 \times 10^{-11}$	[Hz/s]
$\ddot{f}$	0.0	[Hz/s <sup>2</sup> ]
$\alpha$	0.776235274	[rad]
$\delta$	-0.616383646	[rad]
$\psi$	0.372640504	[rad]
$\iota$	0.837452625	[rad]
$\phi_0$	1.993746459	[rad]
epoch	751680013	[s] (November 1, 2003, 00:00:00 UTC)

**Table 2.2:** Pulsar parameters of the recorded, simulated gravitational wave signal during S3 II at GEO 600. The same parameters were used for the software comparison and the hardware injection performed in June 2004.

## 2.2 Signal production hardware

In the following section the hardware used to generate the simulated, continuous gravitational wave signal is described in detail. A Hitachi 3048F microcontroller with two on-chip D/A converters is used as a direct digital frequency synthesiser (DDS) to generate the continuous gravitational wave signal. The DDS produces the sinusoidal part of the signal under control of a PC running a LAL-based program. First a description of how a DDS functions is given followed by what determines the accuracy of a DDS. Then the DDS running on the microcontroller is specified and how the instantaneous frequency of the simulated, continuous gravitational wave signal is controlled via a phase-locked loop (PLL). Also the timing of the signal production via GPS is explained and the performance of the phase accuracy is given. In addition the setting of the amplitude on the microcontroller is described. Figure 2.8 shows an overview of the principle hardware signal injection setup.

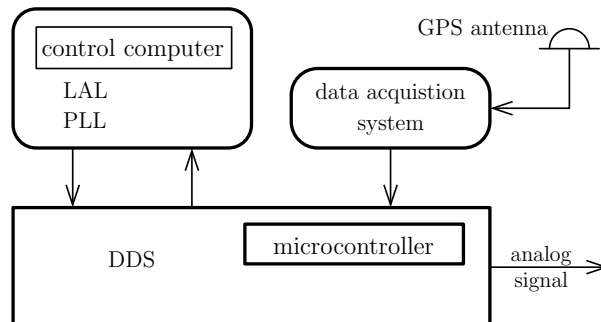


**Figure 2.8:** Schematic of the hardware signal injection setup

### 2.2.1 Operating mode of a direct digital synthesiser

While in general a DDS can produce arbitrary waveforms, it is used here to generate a sinusoidal signal with the help of a phase accumulator, a phase increment register, a sine look-up table, and an external clock. Figure 2.9 shows the schematic of a DSS producing a sinusoidal signal. The phase accumulator holds at all times the instantaneous phase of the signal,  $\varphi_{\text{ACC}}(t)$ . This phase, modulo  $2\pi$ , is used as an index into a sine look-up table, the output of which is fed to the D/A converter. The external clock of a constant frequency,  $f_{\text{CL}}$ , increments the phase accumulator by the contents of the phase increment register (PIR) once per cycle. The fundamental frequency of the signal,  $f_{\text{DDS}}$ , at the D/A converter output is then given by

$$f_{\text{DDS}} = \frac{f_{\text{CL}} \text{PIR}}{2\pi}, \quad (2.8)$$

where the contents of PIR is interpreted as a number measured in radians. Figure 2.10 shows how a sinusoidal signal is mapped onto a D/A converter with a resolution of 3-bit. In Table 2.3 the corresponding sine look-up table for a PIR resolution of

$$\Delta\text{PIR} = \frac{2\pi}{2^3} \quad (2.9)$$

is given.

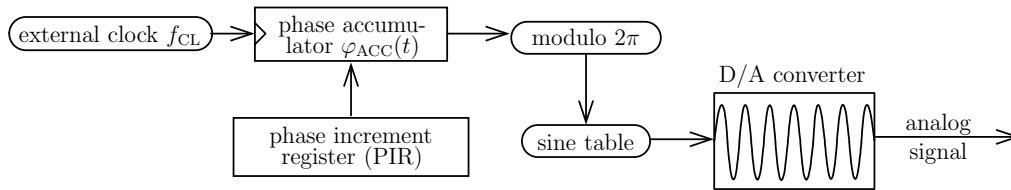


**Figure 2.9:** Schematic of a DDS, which generates a sinusoidal signal. The phase accumulator, holding the instantaneous phase of the signal,  $\varphi_{\text{ACC}}(t)$ , is incremented by the contents of the phase increment register (PIR) at each pulse of an external clock,  $f_{\text{CL}}$ . The phase, modulo  $2\pi$ , is used as an index into a sine look-up table, the output of which is given to the D/A converter thus generating a sinusoidal signal.

The phase accuracy of the sinusoidal DDS signal depends on the frequency stability of the external clock,  $f_{\text{CL}}$ , and the resolution of the phase increment register,  $\Delta\text{PIR}$ . If the frequency standard of the external clock,  $f_{\text{CL}}$ , drifts, the DDS signal follows these drifts. The PIR resolution determines which exact frequencies can be produced with the DDS. In other words it sets the minimal frequency step,  $\Delta f_{\text{step}}$ , between two adjacent frequencies, which can be exactly produced by Equation 2.8. The minimal frequency steps are given by

$$\Delta f_{\text{step}} = \frac{f_{\text{CL}}}{2\pi} \Delta\text{PIR}. \quad (2.10)$$

If a frequency needs to be produced that falls in the middle of two possible adjacent frequencies, the phase error,  $\varphi_{\text{error}}(t)$ , in radians that accumulates over time is given by



$$\varphi_{\text{error}}(t) = 2\pi \frac{\Delta f_{\text{step}}}{2} t = \frac{f_{\text{CL}}}{2} \Delta \text{PIR} t. \quad (2.11)$$

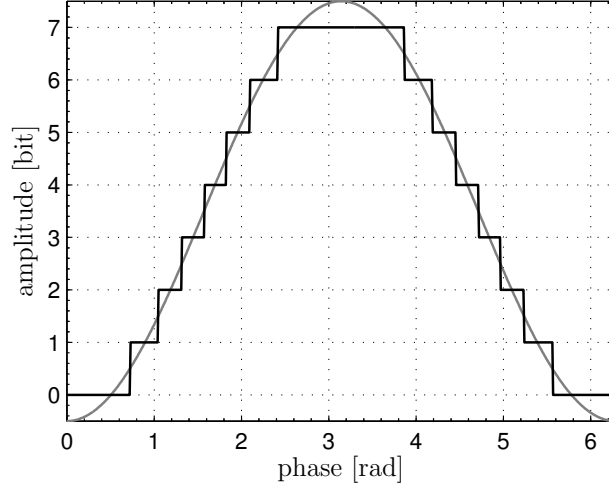


**Figure 2.10:** Graphical illustration of a sine look-up table in which a sinusoidal signal is mapped onto 3-bit against the phase. In the sine look-up table the bit integer values and their correspondent phase intervals are given. Table 2.3 lists the values of the sine look-up table displayed here.

### 2.2.2 The use of the microcontroller

On the microcontroller with two on-chip D/A converters, one D/A converter is run as a DDS producing the sinusoidal part,  $\sin \varphi(t)$ , of the simulated gravitational wave signal and the other is used to produce the amplitude envelope,  $a(t)$ , of the signal. Both D/A converters have a resolution of 8-bit. The parameters of the DDS and the amplitude values are set by a control computer (an office-type PC running Linux). On the control computer,  $\varphi(t)$  and  $a(t)$  are calculated using LAL. In the following, the parameters of the DDS are specified, as well as how the correct frequency of the signal is achieved via a phase-locked loop<sup>4</sup> (PLL) running on the control computer. The timing of the signal injection is described as well as how the amplitude setting is achieved. Precautions taken to ensure a stable performance are described and the performance of the PLL is investigated.

In the microcontroller for the DDS the phase accumulator is implemented as a 64-bit fixed-point number with a 32-bit integer part and a 32-bit fractional part. Thus the PIR resolution,  $\Delta \text{PIR}$ , is  $2\pi/2^{32}$ . The clock frequency is 32768 Hz. The step between two adjacent possible output frequencies of the microcontroller is then  $\Delta f_{\text{step}} \approx 7.6 \mu\text{Hz}$ . The external clock frequency is produced by dividing a  $2^{22}$  Hz signal ( $\approx 4$  MHz) from the GPS-locked data acquisition system by 128 [61]. Thus the DDS and the recording

<sup>4</sup>For an introduction to PLLs see [60] section 9.27.

Sine look-up table	
phase [rad]	binary value
[0,0.723]	0
(0.723,1.047]	1
(1.047,1.318]	2
(1.318,1.571]	3
(1.571,1.823]	4
(1.823,2.094]	5
(2.094,2.418]	6
(2.418,3.864]	7
(3.864,4.188]	6
(4.188,4.459]	5
(4.459,4.712]	4
(4.712,4.965]	3
(4.965,5.236]	2
(5.236,5.560]	1
(5.560,2 $\pi$ ]	0

**Table 2.3:** Sine look-up table which corresponds to the projection of a sinusoidal signal onto 3-bit as illustrated in Figure 2.10

of the signal use synchronised clocks. The external clock, which increments the phase accumulator, is used as a non-maskable interrupt on the microcontroller. An interrupt causes a microcontroller to temporarily halt the execution of the current commands in order to perform immediately some other commands, that are initiated by the interrupt. A non-maskable interrupt is the interrupt with the highest priority. Initiating the incrementation of the phase accumulator with a non-maskable interrupt ensures the immediate processing of the phase accumulator incrementation with highest priority.

As shown in subsection 2.1.1, the frequency of the gravitational wave signal is constantly and continuously changing. As the DDS cannot follow the exact frequency of the signal, the DDS frequency needs to be controlled such that the overall phase error between the phase of the DDS produced sinusoidal signal and the simulated gravitational wave signal stays below 1% of one full cycle of the signal. This is achieved by forcing the phase accumulator of the microcontroller to follow the desired signal phase by a digital PLL running on the control computer. A schematic of the PLL is depicted in Figure 2.11. The difference between the phase accumulator,  $\varphi_{\text{ACC}}(t)$ , and the correct signal phase from LAL,  $\varphi(t)$ , provides the error signal for the control loop. A digital filter is used in the loop to produce a suitable open loop gain, and its output changes the phase increment register in the microcontroller once per second. The parameters for the DDS are thus set by the control computer. Controlling the signal phase in such a closed-loop feedback system ensures that any glitches, e.g. on the clock line, are automatically detected and compensated, as opposed to feedforward systems. This feature is essential for a stable long-term operation.

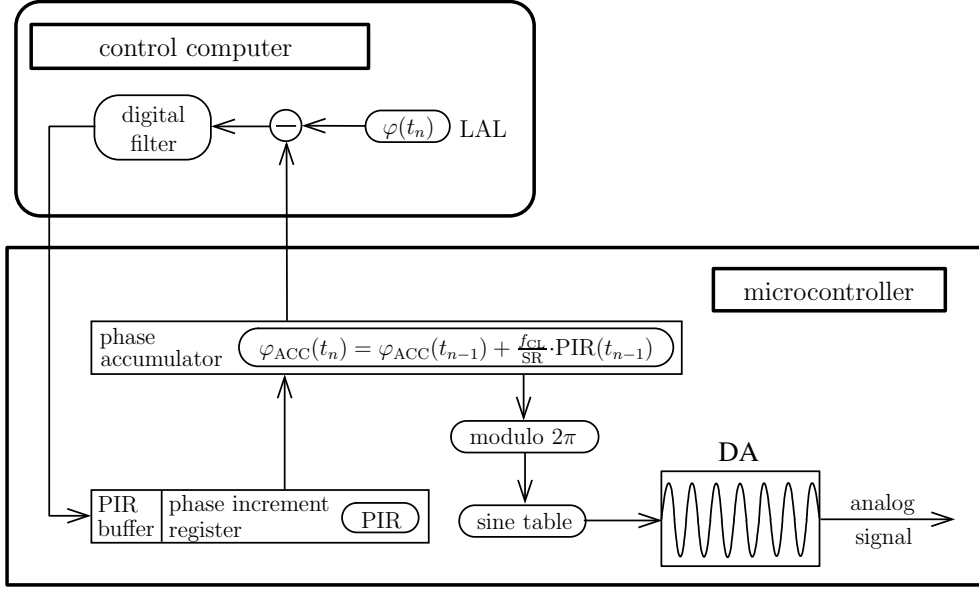


**Figure 2.11:** Schematic of the PLL running on the control computer which controls the phase accumulator  $\varphi_{ACC}(t)$  on the microcontroller. The phase accumulator value  $\varphi_{ACC}(t_n)$  is sent every GPS second to the control computer. The error signal of the PLL is determined by taking the difference between the correct simulated gravitational wave signal phase,  $\varphi(t_n)$ , calculated within LAL and the phase accumulator value,  $\varphi_{ACC}(t_n)$ . The error signal is converted with the help of a digital filter into a phase increment register value to correct for the phase error. This phase increment register value is then sent to the microcontroller and stored in a buffer. With the next GPS second the value is written to the phase increment register of the microcontroller. The sample rate (SR) of the digital loop is 1 Hz, as the start of the GPS seconds are used for the timing of the PLL.

The absolute timing of the signal injection is controlled by pulses from the data acquisition system coinciding with the start of a GPS second. These pulses increment an internal counter of the microcontroller which provides the current GPS second. They are also used as a low priority interrupt to the microcontroller, which initiates an update of the PIR and reads out the phase accumulator for the current GPS second. The phase accumulator value and the current GPS second are then sent to the control computer. The control computer computes the phase error between the phase accumulator and the correct signal phase determined within LAL for that GPS second. Then it determines with the help of the digital filter of the PLL the new value of the PIR for the next GPS second to correct for the phase error. This value is then sent to the microcontroller and written to a buffer, from where it is copied to the PIR at the next GPS interrupt. Thus the phase increment register value computed with the help of  $\varphi_{ACC}(t_n)$  will be applied in second  $n + 1$ . The PIR value applied in second  $n + 1$  will be called  $\text{PIR}(t_{n+1})$ . The sample rate (SR) of the digital loop is hence 1 Hz, as the GPS second pulses are used to read the phase accumulator value  $\varphi_{ACC}(t)$  and update the PIR. The timing of the PLL is illustrated in Figure 2.12.

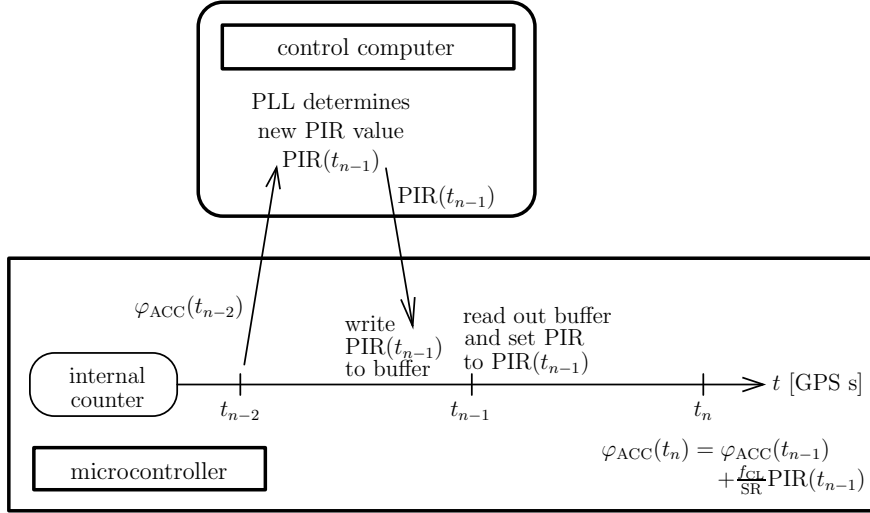


**Figure 2.12:** Timing of the PLL

Letting the control computer write the new phase increment register value first into a buffer instead of directly to the phase increment register increases the performance of the PLL. As the time which the control computer needs to determine the phase increment register value varies as well as the time the microcontroller needs to read the sent new PIR value, the times at which the phase increment register would be set would fluctuate, if the control computer was writing directly to the phase increment register. By writing into a buffer first and then copying the buffer into the real PIR at the GPS second interrupt, the time intervals between the setting of the phase increment register are well defined. The additional time delay does not affect the PLL open loop design, but still allows satisfactory performance.

The microcontroller clock was originally a 16 MHz crystal, which is also the specification limit. It was changed to a GPS-derived  $2^{24}$  Hz ( $\approx 16.78$  MHz) clock, which is thus coherent with the (DDS) update clock and the 1 PPS signal. This increases the performance of the PLL, as now the frequency at which the computing steps of the microcontroller are performed does not drift against the frequency  $f_{\text{CL}}$  with which the DDS increments the phase accumulator. With this setup the PLL suppresses the deviation of the phase accumulator value,  $\varphi_{\text{ACC}}(t)$ , from the gravitational wave signal phase,  $\varphi(t)$ , determined within LAL below 0.007% of a full cycle for the continuous gravitational wave signal recorded during S3 II and later used for injection. As the step-like changes in the phase  $\varphi(t)$  due to the discretisation of the ephemeris data can lead to a phase error of up to 0.06% (as described in subsection 2.1.1), the error in the PLL can be dominated by this effect. In Figure 2.13 in the upper graph the difference between the phase  $\varphi(t)$  calculated within LAL and the phase of the microcontroller phase accumulator,  $\varphi_{\text{ACC}}(t)$ , is plotted for 1 January 2004. In the lower graph the signal frequency offset to  $2f_0$  is plotted for the S3 II neutron star parameters (see Table 2.2) for GEO 600. Whenever a step-like change due to the discretisation of the ephemeris data occurs, the

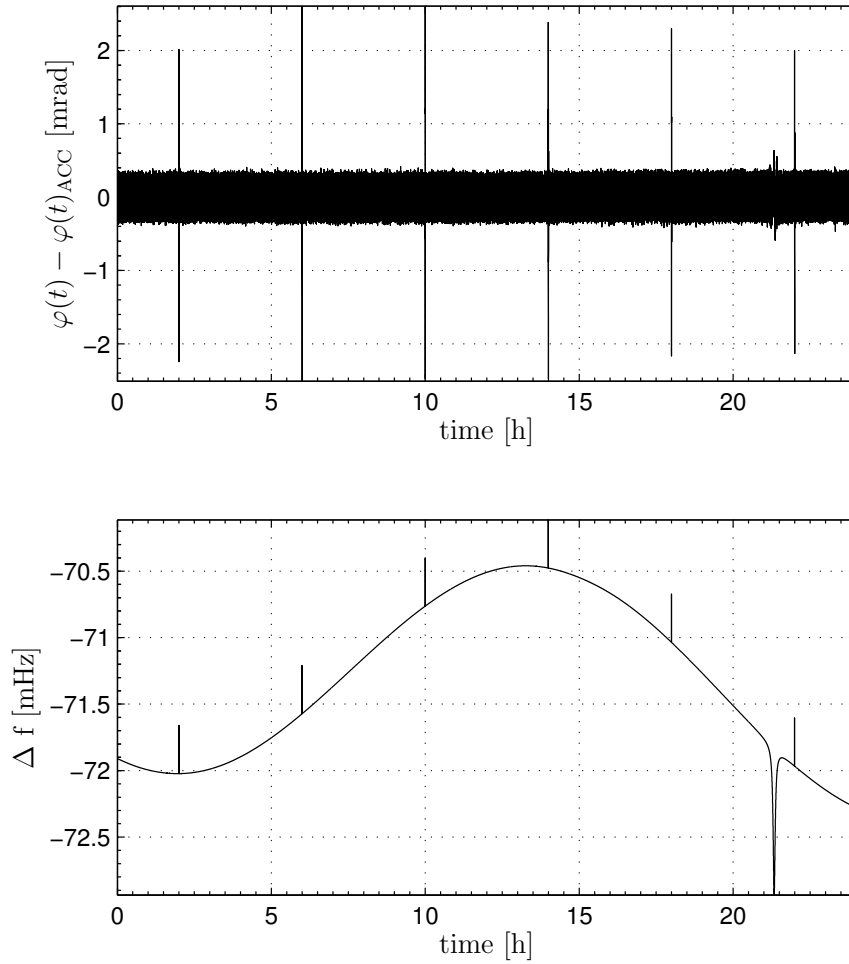


**Figure 2.13:** The graphs show the PLL performance on 1 January 2004. In the upper graph the difference between the gravitational wave signal phase,  $\varphi(t)$ , calculated within LAL and the microcontroller phase accumulator value,  $\varphi_{ACC}(t)$ , is plotted for the neutron star parameters given in Table 2.2. In the lower graph the frequency offset to  $2f_0$  for that signal is plotted. It can be seen that the performance of the PLL is better than the phase error due to the discretisation of the ephemeris data.

error in the PLL rises. In Figure 2.14 a zoom of the second spike in the upper graph of Figure 2.13 is plotted. From this plot it can be seen that it takes the PLL about 30 s to regain its original suppression.

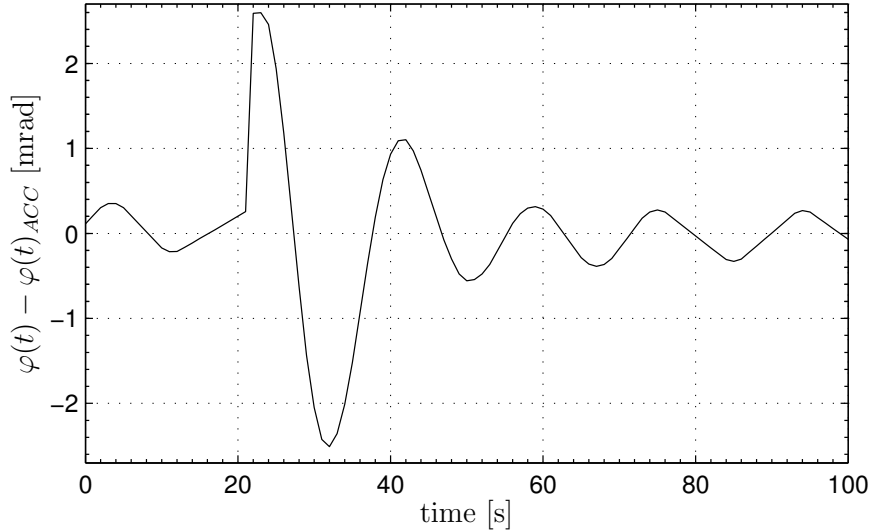


**Figure 2.14:** Settling of the PLL after a phase jump in the reference signal  $\varphi(t)$  calculated within LAL due to the discretisation of the ephemeris data. This is a zoom of the second spike in the upper graph of Figure 2.13.

Figure 2.15 shows the open-loop transfer function of the PLL. It was calculated by multiplying the transfer function of the digital filter with the transfer function of the numerically-controlled oscillator (NCO) of the PLL. The digital filter consists of four infinite impulse response (IIR) filters, which are sequentially applied to the data. The IIR filter tabs are given in Table 2.4. The sign convention for the filter tabs is such, that the transfer function,  $H(s)$ , can be calculated from the IIR filter tabs by

$$H(s) = \frac{\sum_{n=0}^N a_n z^{-1}}{\sum_{m=0}^M b_m z^{-1}}, \quad (2.12)$$

where  $N$  is the number of the filter tabs,  $a_n$ , in the nominator,  $M$  is the number of the filter tabs,  $b_m$ , in the denominator, and  $z = \exp sT$ , where  $s = i2\pi f$  is the complex angular frequency and  $T$  is the sampling interval of the digital filter. The tabs of the IIR filters have been determined by making a fit with LISO to the desired transfer function for the IIR filter [62]. The first IIR filter,  $H_1$ , is an integrator with a single zero at 0.01 Hz and gain 10 dB in the flat region of the filter. The second IIR filter,  $H_2$ , is a two pole low-pass filter with a double pole at 0.2 Hz and gain -20 dB. The last two IIR filters,  $H_3$  and  $H_4$ , are identical integrators with a single zero at 5 mHz and gain 0 dB. These integrators are implemented to increase the gain of the PLL at lower frequencies. The NCO is an integrator with the gain 0 dB. The transfer function has a unity gain frequency of 50 mHz, a gain margin of 34 dB, and a phase margin of 42°.

filter	$a_n$	$b_m$
$H_1$	$a_0 = 3.35209774035$ $a_1 = -3.14785301656$	$b_0 = 1$ $b_1 = -0.9999371431082$
$H_2$	$a_0 = 0.0151660663611$ $a_1 = 0.0373858357061$	$b_0 = 1$ $b_1 = -0.5310582131773$ $b_2 = 0.0145882760949$ $b_3 = 0.0400884182877$
$H_3$	$a_0 = 1.0157083294$ $a_1 = -0.984291794$	$b_0 = 1$ $b_1 = -0.9999937091$
$H_4$	$a_0 = 1.0157083294$ $a_1 = -0.984291794$	$b_0 = 1$ $b_1 = -0.9999937091$

**Table 2.4:** Tabs of the four IIR filters that form the digital filter in the PLL. Filters  $H_3$  and  $H_4$  are identical integrators with a single zero at 5 mHz.

On the control computer it is calculated within LAL from the amplitude envelope,  $a(t)$ , to which binary value the D/A converter should be set on the microcontroller for the current GPS second. This value is compared to the value that had been calculated for the previous GPS second. If the two values differ, the new binary value to which the amplitude D/A converter should be set is sent to the microcontroller. The amplitude is then immediately changed. To produce the full signal the amplitude envelope signal,  $a(t)$ , from the amplitude D/A converter is then multiplied by analog electronic multiplication with the sinusoidal signal from the DDS D/A converter. Figure 2.16 shows a detailed schematic of the microcontroller and control computer setup, which produces the simulated, continuous gravitational wave signal.

The control computer is connected to the microcontroller through an optically isolated serial link (RS-232). This allows to keep the electrical grounds of the microcontroller, the control computer, and the data acquisition system separate, which prevents ground loops. The data between the microcontroller and the control computer is transferred in hexadecimal representation to reduce the possibility of errors in the transmission.

The control computer can send four different commands to the microcontroller. Three of the four commands write to a buffer on the microcontroller. Their actual execution is synchronised with the 1 PPS indicating the start of a GPS second. These commands are setting the internal GPS counter, setting a new PIR value, and initialising the phase accumulator value. The fourth command sets the amplitude D/A converter value and is not synchronised with the 1 PPS, but executed immediately. The commands sent from the control computer to the microcontroller all start with a capital letter and end with a “\n”. The first letter of the command identifies the type of command sent to the microcontroller. In Table 2.5 the commands are listed along with their identification letter, size, and the physical quantity they transmit. Here an example is given for a command send from the control computer to the microcontroller: The command “K07D00000\n” sets the PIR to a new value. The first letter, a “K”, indicates that the following eight ASCII characters contain the new PIR value. The characters “07D00000” are the hexadecimal notation for the decimal number “131072000”, which is the new PIR

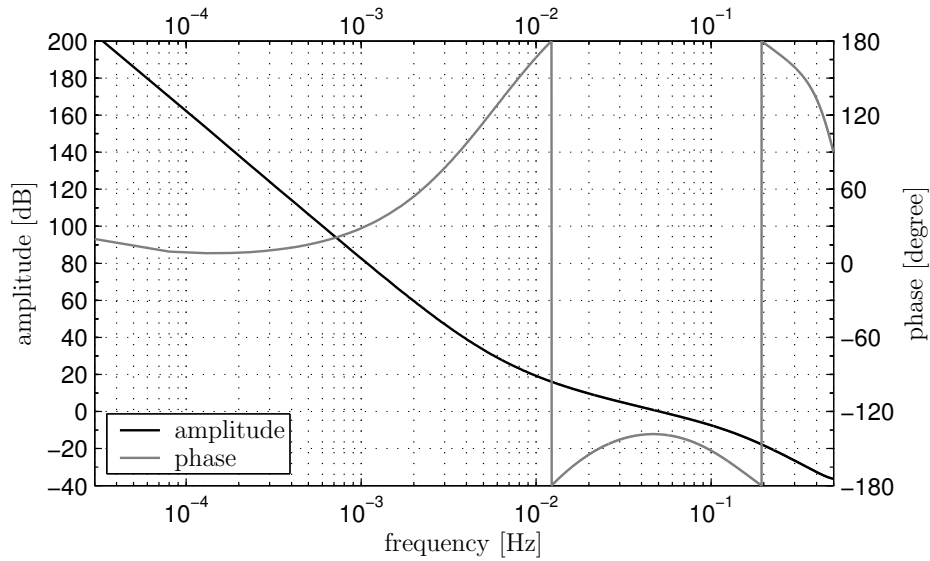


**Figure 2.15:** Open-loop transfer function of the PLL running on the control computer.

value. This value is written to a buffer on the microcontroller, which is copied with the next 1 PPS to the PIR. With this PIR value the DSS produces a sinusoidal signal of 1 kHz.

The microcontroller sends only one type of string to the control computer. This string consist of 28 characters and is sent once per second initiated by the 1 PPS to the control computer. The string contains the values of the internal GPS counter and the phase accumulator value at the start of the GPS second when it had been sent. The start of the values are indicated by lower case letters. The first character of the string, a “g”, indicates the start of the current internal GPS counter value. The next eight characters represent this GPS second in hexadecimal notation. The tenth character, an “h”, indicates the start of the phase accumulator value at the last 1 PPS. The next 16 characters represent that phase accumulator value in hexadecimal notation. The 27th character, an “i”, represents the end of the phase accumulator value. The 28th and last character is a “\n”. Here an example is given for a string sent from the microcontroller to the control computer: The string “g2DF7AD0hDA135FE2C7A1CF6Ei\n” contains the information that at GPS second 771206413 (in hexadecimal notation “2DF7AD0D”) the phase increment accumulator contained the value 15714008952442310511 (in hexadecimal notation “DA135FE2C7A1CF6E”). This phase increment accumulator value corresponds to  $15714008952442310511 \times 2\pi/2^{32}$  rad.

In Table 2.6 all characters are listed that are used in the data transfer between the control computer and the microcontroller. Their hexadecimal and ASCII notation is presented. All characters are 4-bit in size. It is described how each character is interpreted by the programs running on the control computer and the microcontroller. It is also indicated if the character is used for communication from the control computer to the microcontroller and/or from the microcontroller to the control computer.



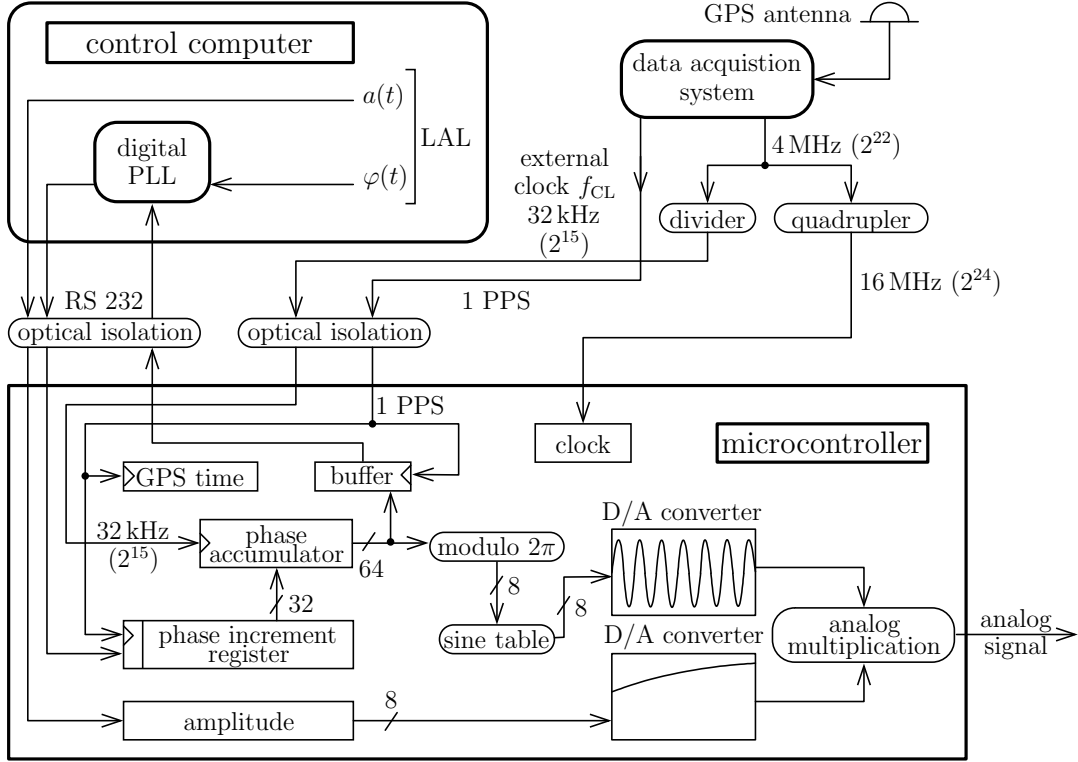


**Figure 2.16:** Schematic of the electronic signal production for the hardware injection of continuous gravitational waves. A microcontroller with two D/A converters is used to produce the amplitude envelope,  $a(t)$ , and the oscillatory part of the gravitational wave signal via its phase,  $\varphi(t)$ . Before injection into the interferometer they are combined by analog electronic multiplication. The control computer maps the amplitude envelope,  $a(t)$ , onto one of the D/A converters and controls the phase evolution of the signal by a phase-locked loop (PLL).

As can be seen in Figure 2.10 the amplitude envelope of the sinusoidal signal produced by the DDS has steps due to the finite amplitude resolution (8-bit) and sampling clock and therefore the full simulated electronic gravitational wave signal has frequency components at frequencies higher than the fundamental frequency. In particular the frequency  $f_{CL}$  ( $\approx 32$  kHz) at which the phase accumulator is incremented, shows up strongly in the electronic signal. As for the signal injection at GEO 600 only frequencies between 100 Hz and 2 kHz are of interest, the signal is band pass filtered behind the electronic multiplication (see Figure I.6 in Appendix I for a schematic of the electronics). A measurement of the transfer function of this band pass filter on the microcontroller module is shown in Figure 2.17. At the continuous gravitational wave frequency 1125.647365 Hz (the gravitational wave signal frequency used for the simulation and recording during S3 II, which was later also used for the injection) the phase lag due to the bandpass filter is  $-11.9^\circ$ . Therefore when calculating the phase  $\varphi(t)$  of the signal on the control computer within the LAL code a constant phase of 0.207 rad is added to the constant phase  $\phi_0$  of the signal to compensate for the bandpass filter.

physical quantity	size	transfer size	command string	transferred string size	synchronised to 1 PPS
GPS time	32 bit	8 byte	$IX_7X_6\dots X_0\backslash n$	10 byte	yes
amplitude	8 bit	2 byte	$JX_1X_0\backslash n$	4 byte	no
PIR value	32 bit	8 byte	$KX_7X_6\dots X_0\backslash n$	10 byte	yes
phase accumulator value	64 bit	16 byte	$LX_{15}X_{14}\dots X_0\backslash n$	18 byte	yes

**Table 2.5:** List of possible commands from the control computer to the microcontroller. Each command can be sent individually and independently and is terminated by a new line character (“\n”) which initiates its interpretation on the microcontroller.

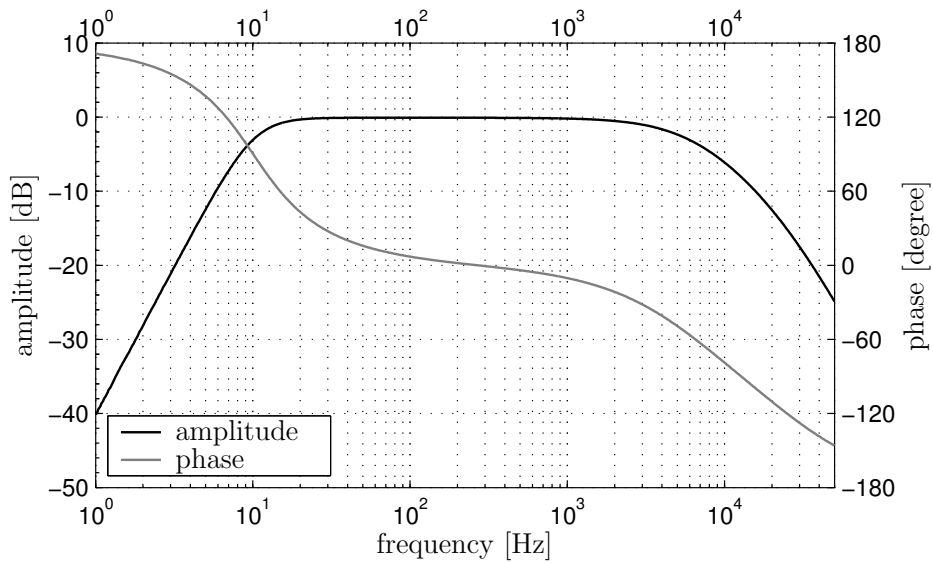


**Figure 2.17:** Measured transfer function of the analog bandpass filter behind the multiplication of the two D/A converter signals.

hexa- decimal notation	ASCII notation	interpretation	control PC ↓ microcontroller	microcontroller ↓ control PC
49	“I”	set GPS time	×	
4A	“J”	set amplitude	×	
4B	“K”	set PIR	×	
4C	“L”	set phase accumulator	×	
67	“g”	start of GPS second		×
68	“h”	start of phase accumulator value		×
69	“i”	end of string		×
0A	“\n”	end of command	×	×
30	“0”	hexadecimal digit	×	×
31	“1”	hexadecimal digit	×	×
32	“2”	hexadecimal digit	×	×
33	“3”	hexadecimal digit	×	×
34	“4”	hexadecimal digit	×	×
35	“5”	hexadecimal digit	×	×
36	“6”	hexadecimal digit	×	×
37	“7”	hexadecimal digit	×	×
38	“8”	hexadecimal digit	×	×
39	“9”	hexadecimal digit	×	×
41	“A”	hexadecimal digit	×	×
42	“B”	hexadecimal digit	×	×
43	“C”	hexadecimal digit	×	×
44	“D”	hexadecimal digit	×	×
45	“E”	hexadecimal digit	×	×
46	“F”	hexadecimal digit	×	×

**Table 2.6:** All characters used for data transfer between the control computer and the microcontroller. The hexadecimal and ASCII notation of each character is given and how it is interpreted on the control computer and/or the microcontroller. The last two columns indicate whether the character is used in the communication from the control computer (control PC) to the microcontroller and/or from the microcontroller to the control computer.



## Chapter 3

### Hardware signal injection

As mentioned in chapter 2, to inject a strain signal into the interferometer an analog electronic signal proportional to the gravitational wave amplitude is used to produce a force that acts upon one (or two) mirrors of the interferometer, thereby changing the differential length of the two arms and simulating the effect of a gravitational wave.

In the first part of this chapter the analog signal produced at the GEO 600 site is investigated in detail. Before turning to the actual hardware injection, the analog output of the direct digital frequency synthesiser (DDS) at the GEO 600 site is investigated for its accuracy in phase and amplitude. Here the correct timing of the signal generation and recording will be explained, which is essential for producing a signal with correct phase.

In the second part of this chapter the actuators are described, which convert an analog electronic signal into a force that acts directly on one or two main mirrors of the interferometer. At GEO 600 two different actuators can be used for signal injection: the electrostatic drive and a photon pressure actuator. The electrostatic drive produces a force on the two inboard mirrors by applying an inhomogeneous electric field next to them, thus pulling the dielectric mirror into the electric field. The photon pressure actuator produces a force on a main mirror by transferring the momentum of photons to it and thus pushing the mirror away from the light source of the photon pressure actuator. So far only the electrostatic drive has been used as an actuator to inject a simulated, continuous gravitational wave signal.

In the third part of this chapter the amplitude calibration of the hardware injected simulated gravitational wave signal is described.

#### 3.1 The simulated, continuous gravitational wave signal generated at the GEO 600 site

As mentioned in chapter 2, our setup for the hardware injection aims for a phase error of less than 1 % of  $2\pi$  rad of the correct signal phase and an amplitude error below 1 % for injection times of several months and signal frequencies between 100 Hz and 2 kHz. To achieve this an important feature of our system is that the phase-locked loop (PLL) that controls the signal phase automatically relocks to the correct signal phase after power-on and interruptions, once the internal time of the microcontroller is synchronised to GPS time. The signal has been measured to be stable over several months. Theoretically the setup allows injection times arbitrarily long. In order to keep the phase error below 1 % of  $2\pi$  rad of the correct signal phase, the timing of the signal injection needs to

be well controlled. For a 1 kHz signal the timing of the signal needs to be accurate to within 10  $\mu$ s. This timing accuracy needs to be fulfilled for the signal generation and the signal recording. In the following the timing accuracy of the signal is explained in detail. Then the simulated signal generated in software with the time-domain search algorithm is compared against the output of the direct digital frequency synthesiser (DDS).

### 3.1.1 Timing issues of the DDS output

There are three essential aspects to providing a good timing accuracy in our hardware setup: the synchronisation of the microcontroller to GPS time, the internal timing of the microcontroller interrupts, and the timing of the data acquisition system. In the following section it is described in detail how these three aspects are dealt with in the scope of this work.

#### Synchronisation of the microcontroller

As described in section 2.2 the microcontroller is synchronised to a pulse of the GPS-locked data acquisition system that coincides with the start of a GPS second. Among other things, this pulse increments an internal counter of the microcontroller which provides the current GPS second. The initialisation of this synchronisation is done manually. In the synchronisation process the current GPS second is read from the timing card of the data acquisition system [63], which shows the current GPS second on a digital display with nine digits in hexadecimal presentation. The first three digits give the current GPS week and the last six digits give the current GPS second of the week. The GPS week is held internally in the timing card as a 10-bit number; therefore, the maximum GPS week can be 1024. On 22 August 1999 00:00:00 UTC the 1025th GPS week started<sup>1</sup> [64]. This GPS roll over week is taken into account when converting the timing card display into the current GPS second.

A program has been written on the control computer with which the internal GPS second counter on the microcontroller can be set. When running this program one has to type in a GPS second in the format of the timing card display. This needs to be a GPS second in the future. In the second before the typed in GPS second, the command is sent by hitting a key on the control computer to the microcontroller. The microcontroller writes the GPS second to an internal buffer and with the next GPS pulse of the data acquisition system the buffer is read and written to the internal counter.

With another program it can be checked whether the synchronisation has been successful. This programme reads out the internal GPS second counter of the microcontroller and displays it immediately on the control computer in the timing card display format. If the values of the microcontroller and the timing card agree, the microcontroller is correctly synchronised.

Any additional pulse or spike on the cable providing the one pulse per second (PPS) from the data acquisition to the microcontroller can make the internal GPS counter of the microcontroller asynchronous. If this happens the generated analog gravitational wave signal from the DDS output for the hardware injection becomes asynchronous,

---

<sup>1</sup>The first GPS second was the first second of 6 January 1980 UTC.

too. In other words the phase of the signal would be behind by a second. Great care was taken with the design of the electronics in which the microcontroller is embedded to prevent such spikes. This includes the feature that the connections between the microcontroller and the data acquisition system, and the microcontroller and the control computer are optically isolated (see Figure 2.16 chapter 2). Despite these precautions, undesirable extra pulses on the 1 PPS can still occur. Since they cannot be entirely excluded, a feature has been built into the software on the control computer that can detect additional pulses. On the control computer the phase accumulator value at the beginning of the last GPS second,  $t_{n-1}$ , and the phase increment register value of that second are stored. Then the phase accumulator value at the beginning of the next second,  $t_n$ , is compared to the expected phase accumulator value derived from the stored phase accumulator value and the stored phase increment register. The expected phase accumulator is given by

$$\varphi_{\text{ACC}}(t_n) = \varphi_{\text{ACC}}(t_{n-1}) + \frac{f_{\text{CL}}}{\text{SR}} \text{PIR}(t_{n-1}), \quad (3.1)$$

where  $\varphi_{\text{ACC}}(t_n)$  is the expected phase accumulator value,  $\varphi_{\text{ACC}}(t_{n-1})$  the stored phase accumulator value,  $\text{PIR}(t_{n-1})$  the stored phase increment register,  $f_{\text{CL}}$  (32768 Hz) the external clock frequency of the direct digital synthesiser (DDS), and SR the sample rate of the PLL (1 Hz). A detailed description of this relation was given in section 2.2 and Figure 2.12. If the expected phase accumulator value deviates from the actual phase accumulator value by more than 30%, an error message is written. If desired, this error message can also be sent via the automated monitoring system of the data acquisition system as an SMS alarm to an operator on duty [63]. The expected phase accumulator value and the actual phase accumulator value can deviate by a certain amount. This is because the number of increments of the phase accumulator value can deviate between two adjacent times when the phase accumulator value is read out. They deviate when the number of non-maskable interrupts by the DDS clock at the frequency  $f_{\text{CL}}$  that occur between reading out the phase accumulator value varies. Allowing a deviation of 30% from the nominal phase accumulator difference ensures that additional pulses on the 1 PPS signal are detected and no false alarms occur. Since the installation of the microcontroller at the site of GEO 600 in December 2003 no additional pulses or spikes on the 1 PPS signal have been observed.

### **Internal microcontroller timing**

Two external interrupts are applied to the microcontroller (see Figure 2.16 section 2.2). One is a non-maskable interrupt running at 32768 Hz, the other, a 1 PPS, marks the start of a GPS second.

The non-maskable interrupt increments the phase accumulator, thus producing the sinusoidal signal. This means that the analog electronic simulated gravitational wave signal produced by the DDS is sampled with 32768 Hz. The generated signal consists of data points spaced approximately every 30.5  $\mu\text{s}$  in time.

With the 1 PPS interrupt the following three steps are performed immediately in this order: The phase increment register is set to its new value, the internal GPS second

is incremented, and the phase accumulator value is read out and sent together with the current GPS second and amplitude value to the control computer. For the timing accuracy of the DDS output it is essential to know at which time the phase accumulator is read out. In Figure 2.11 in subsection 2.2.2, it is shown and explained how the error signal of the digital PLL is gained. The difference of the phase accumulator value read at time  $t_n$  is compared to the phase calculated within LAL for that time. As the phase accumulator is not read out immediately with the 1 PPS interrupt, the time does not coincide exactly with the start of a GPS second. Instead it is delayed.

To determine this delay one line of the program running on the microcontroller was changed. Instead of reading the phase accumulator value, a certain value was written to the phase accumulator. The duration of the process of reading the phase accumulator value is approximately the same as writing to the phase accumulator. The value written to the phase accumulator was chosen in combination with the phase increment register such that, when the new phase accumulator value has been written to the microcontroller, the output signal changes from a low voltage signal to a high voltage signal. Later in the second, the output signal is changed to a low voltage signal again. On an oscilloscope the 1 PPS marking the start of a GPS second and the output of the microcontroller were simultaneously measured. The oscilloscope was triggered to the 1 PPS, where the start of a GPS second coincides with the falling edge of the signal. For the measurement, 64 averages were taken on the oscilloscope. In Figure 3.1 it can be seen that the change in the microcontroller output is delayed by approximately  $26 \mu\text{s}$ . For the production of the signal during S3II this offset was not taken into account. Therefore the signal recorded during S3II is delayed by  $26 \mu\text{s}$ . After S3II the code on the control computer was changed such that this time delay is automatically accounted for by calculating the correct gravitational signal phase  $\varphi(t)$  within LAL not at a full GPS second, but at a full GPS seconds  $+26 \mu\text{s}$ .

### Signal recording by the data acquisition system

The time stamps of the data acquisition system given to the recorded data points have an offset in time. This offset can be measured by comparing the time stamps given by the data acquisition system with a signal from a GPS-locked Rb clock that marks the beginning of a GPS second [63]. Thus the time stamps of the data acquisition system are compared to another GPS-locked reference clock. So far offsets have been measured varying between  $-53 \mu\text{s}$  and  $+16 \mu\text{s}$ . The sample rate with which the simulated gravitational wave signal is recorded by the data acquisition system is 16384 Hz. This is equivalent to a sample every  $61 \mu\text{s}$ . The offset of the time stamps is therefore smaller than one full sample. To correct this offset it needs to be subtracted from the time stamps given by the data acquisition.

The offset is permanently measured by an automated system [65]. The system immediately detects changes in the offset. So far it has not been completely understood what causes the offset and why it varies. During all of S3II the timing offset was  $+16 \mu\text{s}$ . As the reference signal of the Rb clock is permanently recorded, the offset of the timing stamps can be reconstructed at any given time. This timing stamp offset needs to be subtracted from the recorded simulated gravitational wave signal (the recorded DDS



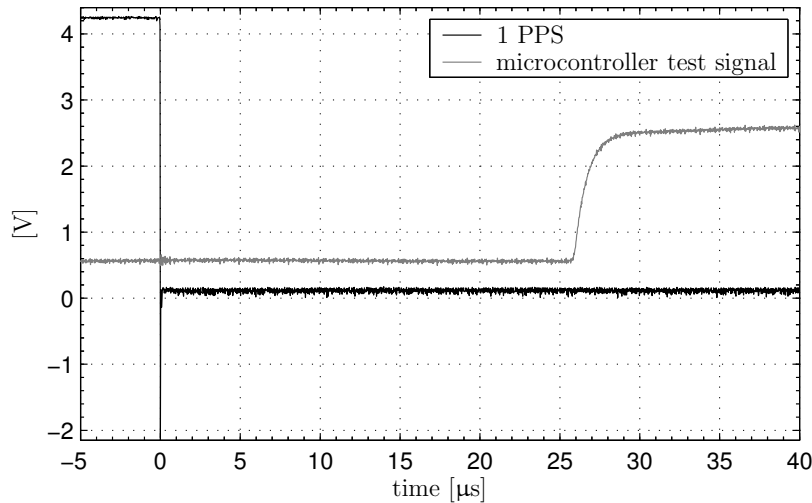


**Figure 3.1:** Measurement of the time delay with which the phase accumulator of the microcontroller is read out in reference to the 1 PPS coinciding with the start of a GPS second of the data acquisition system. For the measurement, the microcontroller was reprogrammed such that instead of reading out the phase accumulator value a new value was written to the phase accumulator. The values were chosen such that this lead to a steplike change of the microcontroller output from a low voltage to a high voltage signal. The start of a GPS second coincides with the falling edge of the 1 PPS to which the oscilloscope was triggered. For the above data 64 averages were taken. As can be seen, the setting of the phase accumulator value on the microcontroller has a delay of approximately  $26 \mu\text{s}$ .

output) when comparing it against the simulated signal generated in software.

In Table 3.1, the two timing inaccuracies concerning the recorded DDS output are given. These are the only known timing inaccuracies caused by inaccuracies in the signal production and the signal recording.

### 3.1.2 Test of the DDS output

In the following section, the simulated signal generated in software with the time-domain search algorithm, hereafter  $s_{\text{LAL}}(t)$ , is compared against the output of the direct digital frequency synthesiser (DDS), hereafter  $s_{\text{DDS}}(t)$ .  $s_{\text{LAL}}(t)$  is the simulated, continuous gravitational wave signal determined within LAL and exists only in software.  $s_{\text{DDS}}(t)$  is the simulated, continuous gravitational wave signal generated by the DDS in an analog electronic form used later for the hardware injection.  $s_{\text{DDS}}(t)$  was recorded for this test with the data acquisition system at the detector site. There are two different approaches to this test, one is the comparison of the signal in the frequency domain and the other in the time domain. The comparison in the frequency domain is very accurate but at the same time very complex. The comparison in the time domain is not so elaborate but easy to conduct. The comparison in the frequency domain was performed only once using data from a whole day, to check the accuracy of the generated signal. The comparison in the time domain is performed only over a few seconds of data at a

Timing inaccuracies			
cause	value [ $\mu\text{s}$ ]	measure	comment
1 PPS interrupt delay	+26	needs to be subtracted	during S3 II not undone, after S3 undone by software on control computer
inaccurate DAQS timing stamps	-54 to +16, usually +16	needs to be subtracted	varying, but measurable; +16 $\mu\text{s}$ during S3 II

**Table 3.1:** Timing inaccuracies of the recorded DDS output. Given are the causes of the timing inaccuracies, their actual value, and how they are undone.

time. The time domain comparison is used as a quick check to verify that the signal generation is running faultlessly at a certain time. The frequency domain comparison will be described in detail before the time domain comparison is introduced. For both comparisons  $s_{\text{DDS}}(t)$  is checked against  $s_{\text{LAL}}(t)$ .

### Frequency domain comparison

The comparison of the software generated signal,  $s_{\text{LAL}}(t)$ , and the DDS output,  $s_{\text{DDS}}(t)$ , in the frequency domain is performed by a single-bin discrete Fourier transform (SBDFT) [66]. For the SBDFT conducted every 0.5 s over one day of data, a Fourier transform was performed for one frequency bin over 2730 data points after applying a Hanning window to these data points. Thus a complex number is produced every 0.5 s from which an amplitude and a phase can be derived. The SBDFT was performed over the DDS output,  $s_{\text{DDS}}(t)$ , and the software produced data,  $s_{\text{LAL}}(t)$  (which was produced as the recorded DDS output with a sample rate of 16384 Hz). Then the amplitude and the phase of the two signals were compared. This test was performed for 1 January 2004 with the neutron star parameters used during the S3 II signal recording (see Table 2.2). As can be seen in Figure 2.6 in chapter 2,  $s_{\text{DDS}}(t)$  had a frequency offset of approximately 71.25 mHz during that time. The SBDFT was therefore performed at the frequency  $2f_0 - 0.07125$  Hz, which corresponds to 1125.576115 Hz with  $f_0$  being the spin frequency of the neutron star.

In Figure 3.2 the phase evolution of the two signals is compared. In the upper graph the phase of  $s_{\text{LAL}}(t)$  and  $s_{\text{DDS}}(t)$  is plotted for 1 January 2004. In the lower graph the difference of the two signals is taken and expressed in percent of a full cycle. In the lower graph the known time delay of 42  $\mu\text{s}$  is taken into account. The remaining 0.64% correspond to a delay of the recorded signal of approximately 5.7  $\mu\text{s}$ . Every four hours a spike occurs in the phase difference which is due to the discretisation of the ephemeris data (see subsection 2.1.1). During the most rapid change of the signal frequency (compare subsection 2.1.3) the phase difference deviates from the otherwise almost constant offset. The overall phase error stays below 1%.

In Figure 3.3 the amplitude envelope of the two signals is compared. In the upper graph the amplitude envelope of the recorded and software generated signals are plotted for 1 January 2004. In the lower graph the difference of the two signals is taken and

### 3.1 The simulated, continuous gravitational wave signal generated at the GEO 600 site

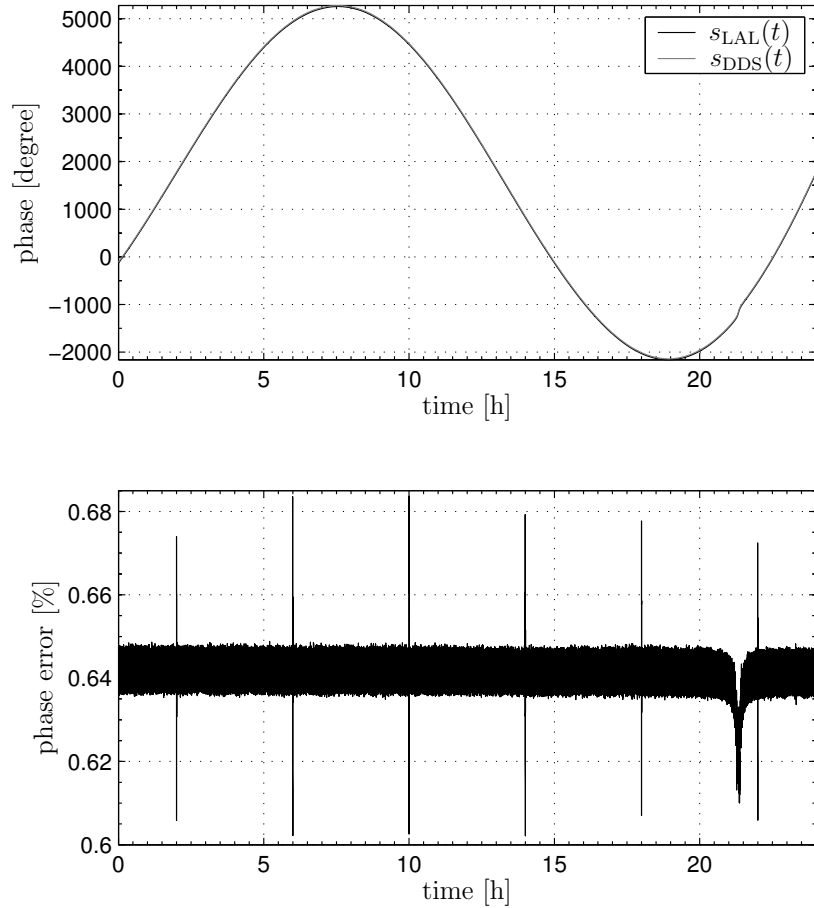


**Figure 3.2:** Frequency domain comparison of the phase of the simulated signal generated in software,  $s_{\text{LAL}}(t)$ , and the DDS output,  $s_{\text{DDS}}(t)$ , on 1 January 2004. Every 0.5 s a single-bin discrete Fourier transform around the expected frequency was performed from which the phase was derived. In the upper graph the phase evolution of  $s_{\text{LAL}}(t)$  and  $s_{\text{DDS}}(t)$  is plotted. In the lower graph the difference of the two signals is taken and expressed in percent of a full cycle. The 0.64% constant offset corresponds to a delay of approximately  $5.7 \mu\text{s}$  of the DDS output,  $s_{\text{DDS}}(t)$ . The spikes every four hours are due to the discretisation of the ephemeris data.

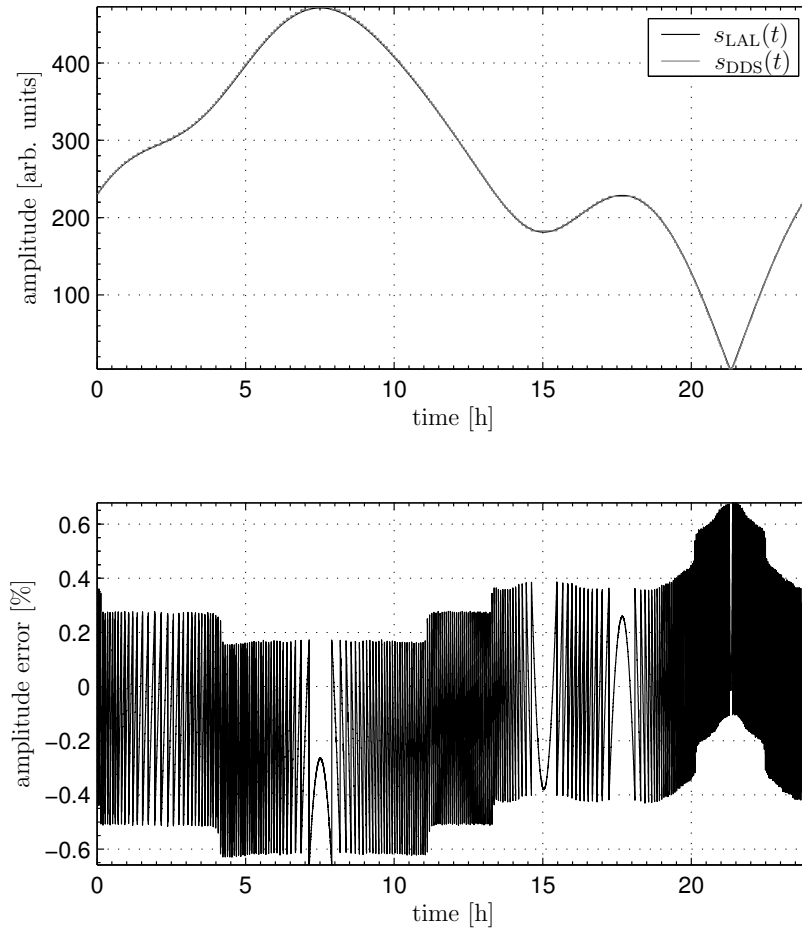


**Figure 3.3:** Frequency domain comparison of the amplitude envelope of the simulated signal generated in software,  $s_{LAL}(t)$ , and the DDS output,  $s_{DDS}(t)$ , on 1 January 2004. Every 0.5 s a single-bin discrete Fourier transform around the expected frequency was performed from which the amplitude was derived. In the upper graph the amplitude of  $s_{LAL}(t)$  and  $s_{DDS}(t)$  are plotted. In the lower graph the difference of the two signals is taken and expressed in percent of the maximal amplitude during that time stretch.

expressed in percent of the maximal signal amplitude on 1 January 2004. In the lower graph it can be seen that the steps in the amplitude envelope of the recorded signal lead to steps in the difference of the two signals. The overall amplitude error stays below 1 %.

### **Time domain comparison**

In the following section, the simulated signal generated in software,  $s_{\text{LAL}}(t)$ , is compared against the DDS output,  $s_{\text{DDS}}(t)$ . In principle this is the same test as performed in subsection 2.1.3 except that instead of the software part of the hardware injection now the recorded DDS output used for the hardware injection is compared against the time-domain search algorithm. The phase of the signal, as well as the amplitude envelope of the signal, will be compared. For the amplitude comparison, the discretisation of the amplitude envelope is investigated to see how it affects the amplitude error (see subsection 2.1.2 for the description of the amplitude envelope discretisation).

For the comparison of the simulated signal generated in software,  $s_{\text{LAL}}(t)$ , and the DDS output,  $s_{\text{DDS}}(t)$ , the following effect of the data acquisition system needs to be taken into account. Depending on the channel of the hardware of the data acquisition system on which the DDS output,  $s_{\text{DDS}}(t)$ , is recorded, a constant DC offset is introduced. This offset introduces an error to the amplitude envelope of the signal. When the phase difference between two sinusoidal signals is determined by comparing the difference between a zero crossings of the two signals in one point, an amplitude offset leads to an apparent phase offset. This relation is depicted in Figure 3.4. Therefore for a correct comparison of  $s_{\text{LAL}}(t)$  against  $s_{\text{DDS}}(t)$  this amplitude offset needs to be undone.

Since the installation of the microcontroller on the site of GEO 600, the DDS output was always directly recorded on channel 22 of the data collecting unit alchemist in the central building. The DDS output was recorded with 16-bit resolution covering a dynamic range of  $\pm 2$  V. The uncertainty in the amplitude of one sample due to the data acquisition system is thus approximately  $61 \mu\text{V}$ . The DC offset introduced by the data acquisition system is of the order of a few mV and varies over a day in the order of a few  $100 \mu\text{V}$  due to temperature drifts [67].

To determine the DC offset, the mean of the recorded DDS output is determined over a certain number of seconds. For high accuracy, not all of the data are used. Instead the starting sample is chosen to be the first positive sample of the first full cycle in those seconds. The last sample is chosen to be the last negative sample of the last full cycle in those seconds. Software simulations of this process show that the thus determined offset over 2 s has an error below  $\pm 5 \mu\text{V}$ . For this simulation a sinusoidal signal with a peak amplitude of 2 at the frequency of the recorded simulated, continuous gravitational wave signal was produced with a sample rate of 16384 Hz. This signal was digitised with 16-bit resolution. Then the DC offset of that sinusoidal signal was determined in the above described way. This was repeated for small shifts in time of the sinusoidal signal, until the first and the last samples had changed. In this simulation the maximal observed DC offset stayed below  $\pm 5 \mu\text{V}$ .

For each time interval over which a time domain comparison of  $s_{\text{LAL}}(t)$  and  $s_{\text{DDS}}(t)$

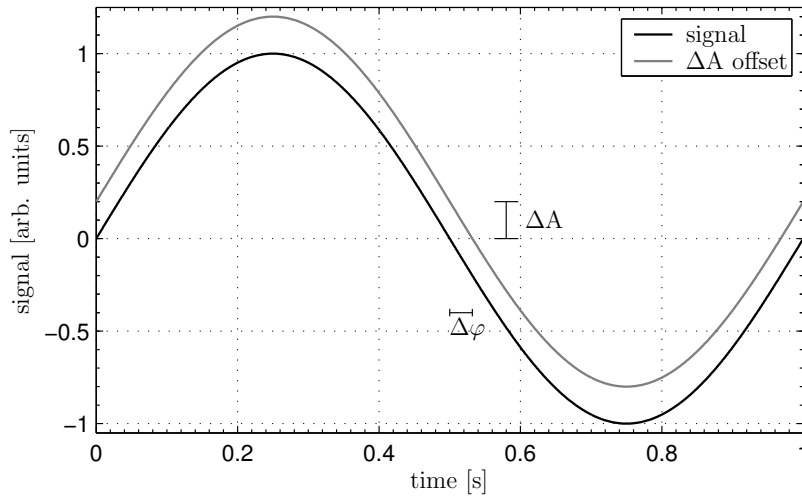


**Figure 3.4:** Graphical display of a positive DC offset in the amplitude leading to an apparent phase error at a zero crossing of a sinusoidal signal. Depicted is a pure sinusoidal signal and the same signal with a positive amplitude offset. At the zero crossing of the negative gradient of the two signals it looks like the signal with the positive amplitude offset is in phase behind the pure sinusoidal signal.

is made, the DC offset of the recorded DDS output,  $s_{\text{DDS}}(t)$ , is calculated in the way described above. These DC offsets also include asymmetries of the two D/A converters of the microcontroller.

For a direct comparison of the two signals in the time domain the different amplitude scaling of the signals needs to be taken into account. In the following paragraph it is explained, how the different scaling is undone to allow a direct comparison of the two signals. The simulated signal generated in software,  $s_{\text{LAL}}(t)$ , is in strain. In the code the amplitude has been set arbitrarily to  $h_0 = 1$ . Depending on the neutron star parameters the maximal amplitude of the software generated  $h(t)$  signal is a fraction of  $h_0$ . The DDS output recorded with the data acquisition system is in volts. The conversion factor to convert the DDS output into strain was determined in the following way. In subsection 2.1.2 it is shown how the amplitude envelope is mapped onto one of the D/A-converters of the microcontroller. The maximum of the signal falls exactly onto the 8-bit integer 0 or 254. The amplitude in the microcontroller was set to its maximum. The microcontroller was set to a fixed phase increment value producing a sinusoidal signal with a fixed frequency. The frequency was chosen such that it falls in the frequency range of the simulated, injected gravitational wave signal generated by the DDS during S3 and later injected. Then the DDS output was recorded with an oscilloscope and averaged 64 times. The maximum of the recorded signal and the maximum fractional part of  $h_0$  of the software generated  $h(t)$  signal were then used to compute the conversion factor from voltage to strain. For the neutron star parameters used for recording during the S3 II was determined to be  $0.41 \text{ V}^{-1} \pm 1.5\%$ .

When taking the timing effects, the DC offset of the recorded DDS output, and the

### 3.1 The simulated, continuous gravitational wave signal generated at the GEO 600 site

amplitude conversion factor into account, the simulated signal generated in software,  $s_{\text{LAL}}(t)$ , and the DDS output,  $s_{\text{DDS}}(t)$ , can be compared directly. To take the timing effects into account from the time stamps of the recorded DDS output,  $s_{\text{DDS}}(t)$ , the microcontroller delay, and the timing offset of the data acquisition system are subtracted. The DC offset introduced by the data acquisition system and the asymmetries in the microcontroller D/A converters is subtracted from the recorded DDS output and the conversion factor to transform the DDS output into strain is applied. The two simulated gravitational wave signals can then be compared directly to each other in the time domain.

In Figure 3.5 the software generated signal and the DDS output are plotted on 1 January 2004 at 07:30:56. At this time the amplitude envelope of the gravitational wave signal was maximal. It can be seen that the recorded DDS output data points are earlier in time than the software generated data points. This is due to the timing offset of the microcontroller and the data acquisition system. When zooming into the plot at a zero crossing, it can be seen that the recorded DDS output is approximately  $6\ \mu\text{s}$  behind the software generated signal. This is in good agreement with the 0.64% (corresponding to  $5.7\ \mu\text{s}$ ) phase offset discovered in the frequency domain comparison. With the signal frequency being 1125.647365 Hz the signal has a period of  $888\ \mu\text{s}$ . Thus the recorded DDS output has a phase error of less than 1% of  $2\pi$ .

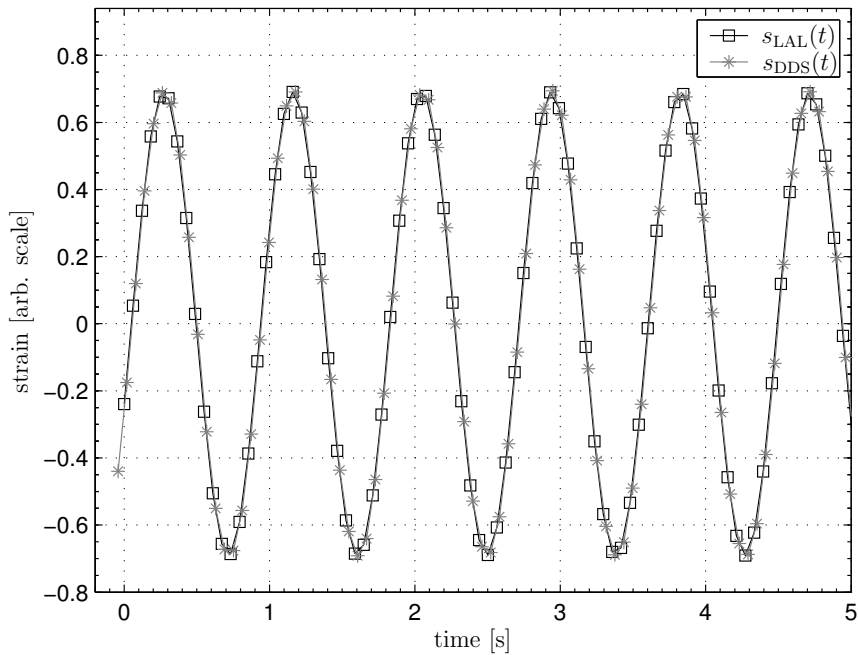


**Figure 3.5:** Direct comparison of the simulated signal generated in software,  $s_{\text{LAL}}(t)$ , and the recorded DDS output,  $s_{\text{DDS}}(t)$ . As the known timing effects are undone for the recorded DDS output, the data points of the DDS output appear earlier than the data points of the software generated signal. The software generated signal was calculated with a sample rate of 16384 Hz starting at a full GPS second.

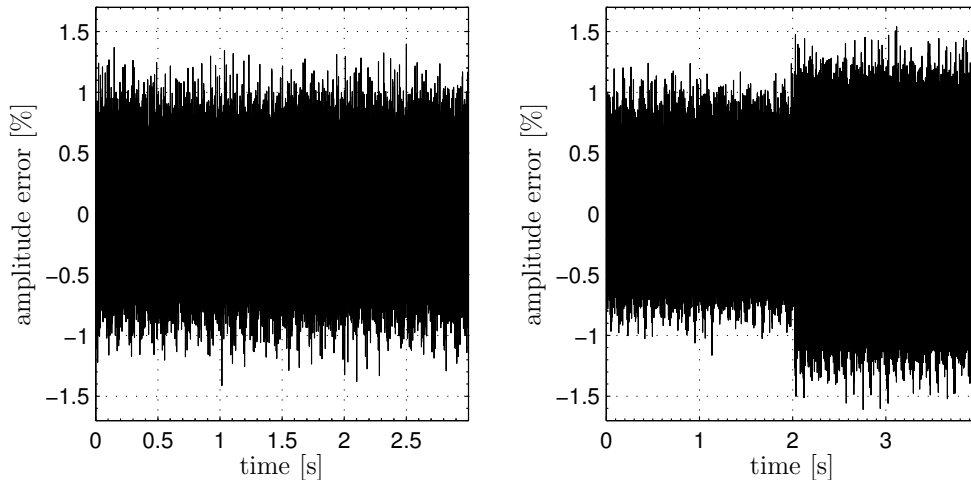


**Figure 3.6:** Difference between the DDS output,  $s_{\text{DDS}}(t)$ , and the simulated signal generated in software,  $s_{\text{LAL}}(t)$ , expressed in percent of the maximal amplitude of the time stretch from which the data is taken. In the left-hand graph the data is from 1 January 2004 from 07:30:55 onwards. At this time the amplitude envelope of the signal is maximal. In the right-hand graph the data is from 1 January 2004 from 07:08:25 onwards. During this time the D/A converter producing the amplitude envelope is changed by one integer. The software generated signal was calculated at times  $48 \mu\text{s}$  earlier than the time stamps given by the data acquisition system to the recorded DDS output. This takes the  $26 \mu\text{s}$  offset of the 1 PPS interrupt on the microcontroller, the  $16 \mu\text{s}$  offset of the data acquisition time stamps, and the observed phase error of approximately  $6 \mu\text{s}$  of unknown origin into account. The amplitude error is for both times of the order 1.5%, which corresponds to the error of the amplitude calibration for the recorded DDS output.

In subsection 2.1.3 in chapter 2 it was shown how a phase error can translate into an amplitude error. In order to estimate the error between the amplitude envelope of the software generated signals and the DDS output, the known phase offset of  $6 \mu\text{s}$  is taken into account. The software generated signal is generated at times  $-48 \mu\text{s}$  off the time stamps of the recorded DDS output ( $-26 \mu\text{s}$  for microcontroller interrupt offset,  $-16 \mu\text{s}$  data acquisition timing stamp offsets,  $-6 \mu\text{s}$  unknown, but measured offset). Then the difference of the two signals is expressed in percent in reference to the maximum of the signal in that time stretch. In Figure 3.6, the amplitude error between the software generated signal and the DDS output is plotted at two different times over a few seconds on 1 January 2004. In the left-hand graph the difference is plotted over three seconds from 07:30:55 onwards. During this time the amplitude envelope of the signal was maximal. In the right-hand graph the amplitude error is plotted over four seconds from 07:08:25 onwards. In the middle of this time stretch the value of the D/A converter producing the amplitude envelope is changed by one integer. At the time when the change occurs a step is visible in the amplitude error. In theory no change in the amplitude error should occur, as the amplitude is changed when the value is exactly between two 8-bit integer values onto which the amplitude envelope is mapped. But due to asymmetries in the D/A-converter and the signal recorded in the data acquisition



an effect is visible. It can be seen that the amplitude error is for both time stretches of the order 1.5%. This corresponds to the error of the amplitude calibration of the data acquisition system with which the DDS output is recorded.

## 3.2 Actuators for the hardware signal injection

At GEO 600 all main interferometer mirrors are suspended as triple pendulums [68]. To apply a force directly to a main mirror, an electrostatic drive or a photon pressure actuator can be used. The electrostatic drive can apply a force to the two so-called inboard mirrors East and North, MCE and MCN respectively (see the the optical layout of GEO 600 in Appendix G for their location). The photon pressure actuator is situated in the North end building and can apply a force to the so-called Mirror Far North, MFN. Figure 3.7 shows a schematic of the suspension of the main mirrors of the interferometer and the actuators by which a force can be applied to them. For both actuators, the transfer function needs to be considered, that describes the relation between an externally applied force to the mirror and the mirror displacement.

### Pendulum transfer function

In the following, the pendulum transfer function from a force,  $F_{\text{ex}}(t)$ , applied externally to the centre of a mirror suspended as a pendulum to its longitudinal displacement,  $s$ , will be derived. The parameter  $s$  is the distance on the circle described by the pendulum, the dashed curved line in Figure 3.8. The distance  $s$  of the mirror is given by  $s = l\varphi$ , where  $\varphi$  is the angle of excursion and  $l$  is the pendulum length. For small excursion angles  $\varphi$ ,  $s$  corresponds, to first order, to the displacement  $x$  along the optical axis of the mirror, as  $x = l \sin \varphi$ . At GEO 600 all excursion angles of the suspended mirrors are very small and therefore  $s$  can be regarded as displacement along the optical axis of the mirror.

The equation of motion for a pendulum is given by

$$F_{\text{ex}}(t) = m\frac{g}{l}s(t) + \gamma\dot{s}(t) + m\ddot{s}(t), \quad (3.2)$$

where  $m$  is the mass of the mirror,  $g$  the acceleration in the gravitational field of the Earth, and  $\gamma$  the coefficient of friction of a viscous damping. The restoring force  $F_{\text{r}} = mg \sin \varphi$  pictured in Figure 3.8 is approximated in Equation 3.2 to first order for small angles, yielding  $F_{\text{r}} = mgs/l$ .

If the externally applied force,  $F_{\text{ex}}$ , is harmonic, that is of the form

$$F_{\text{ex}} = F_{\text{ex}}(\omega) \exp(i\omega t),$$

$s(t)$  will follow this excitation with the same frequency due to the linearity of the equation of motion. Here  $\omega$  is the circular frequency connected with the frequency  $f$  of a signal by  $\omega = 2\pi f$ . Therefore the assumption

$$s(t) = s(\omega) \exp(i\omega t)$$

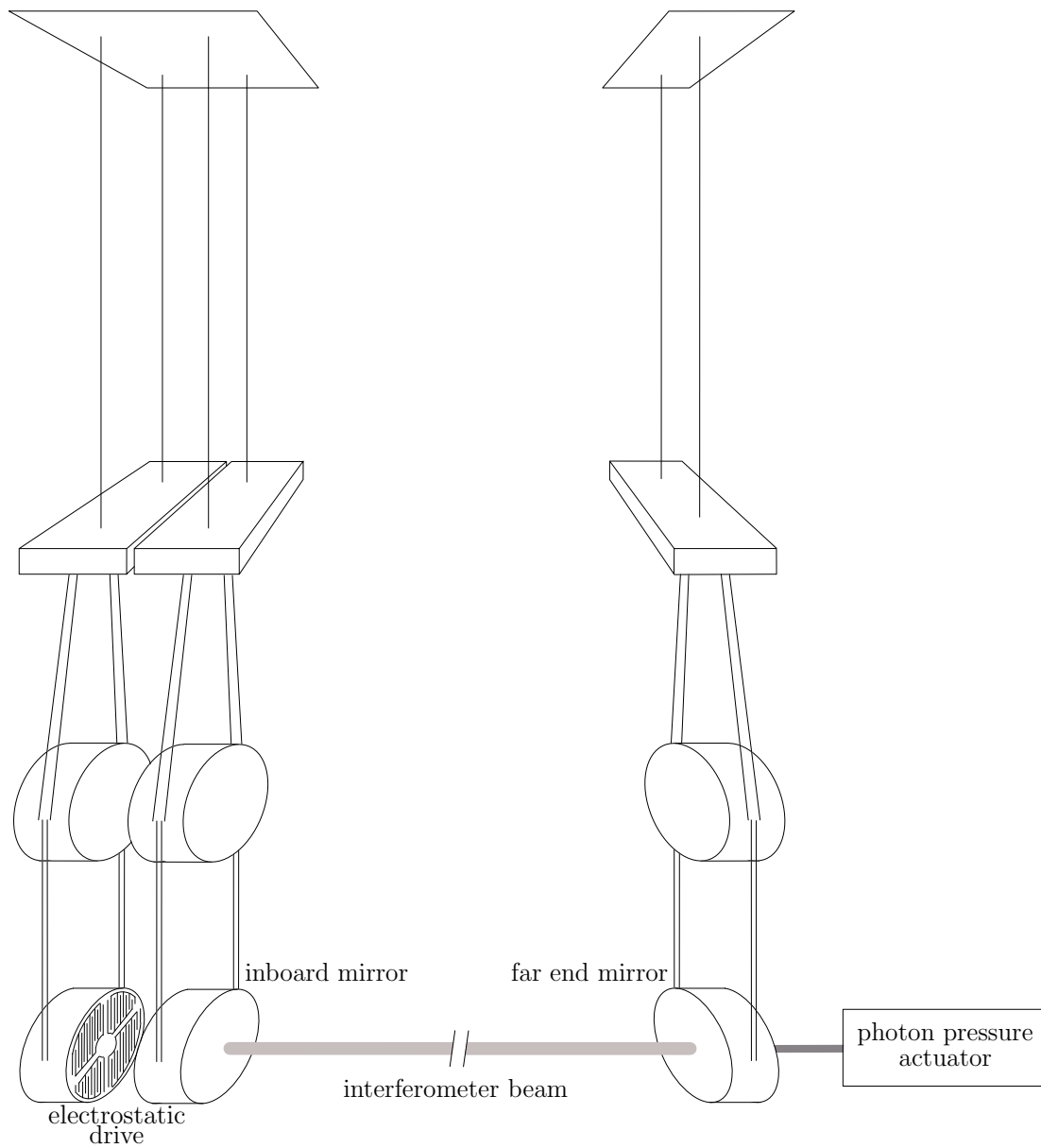


**Figure 3.7:** Schematic of the inboard and far end mirrors and their actuators. The main mirrors of the interferometer are suspended as triple pendulums. To allow an actuation with an electrostatic drive the inboard mirrors are suspended as so-called double triple pendulums, two triple pendulums hanging next to each other. The far end mirrors are suspended as single triple pendulums. These mirrors can be acted on using the photon pressure of an external light source.

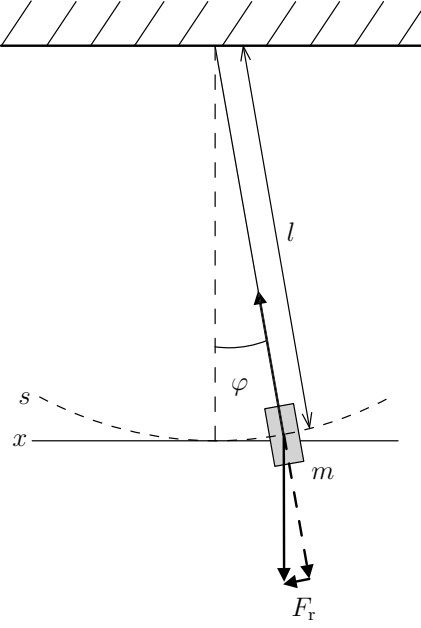


**Figure 3.8:** Schematic of a mirror suspended as a pendulum to show the relevant parameters for the determination of the pendulum transfer function from force applied to the centre of mass of the suspended mirror to its displacement.

can be made for the displacement  $s$ . With the angular resonance frequency  $\omega_0 = \sqrt{g/l}$ , Equation 3.2 can be rewritten giving the transfer function  $T_{\text{long}}(\omega)$  from externally applied force to longitudinal displacement

$$\begin{aligned} T_{\text{long}}(\omega) &= \frac{s(\omega)}{F_{\text{ex}}(\omega)} \\ &= \frac{1}{m[(\omega_0^2 - \omega^2) + i\frac{\gamma}{m}\omega]} \\ &= \frac{1}{m[(\omega_0^2 - \omega^2) + i\frac{\omega_0}{Q}\omega]} \end{aligned} \quad (3.3)$$

In the last step of Equation 3.3 the quality factor  $Q$  was introduced which is defined as

$$Q = 2\pi \frac{\text{stored energy}}{\text{energy dissipation per oscillation period}} = \frac{\omega_0 m}{\gamma} \quad (3.4)$$

If less energy is dissipated per oscillation period, the better is the quality factor  $Q$ , and the stronger is the resonance of the pendulum at its resonance frequency. In Figure 3.9 the pendulum transfer function from an externally applied force in Newtons to the mirror displacement in meters as given in Equation 3.3 is displayed in a Bode plot for a pendulum with a resonance frequency of  $\omega_0 = 1$  Hz, a  $Q$  of 10 and a mirror weight 5.6 kg. It can be seen that above the resonance frequency the amplitude of the transfer function drops with  $1/f^2$ .

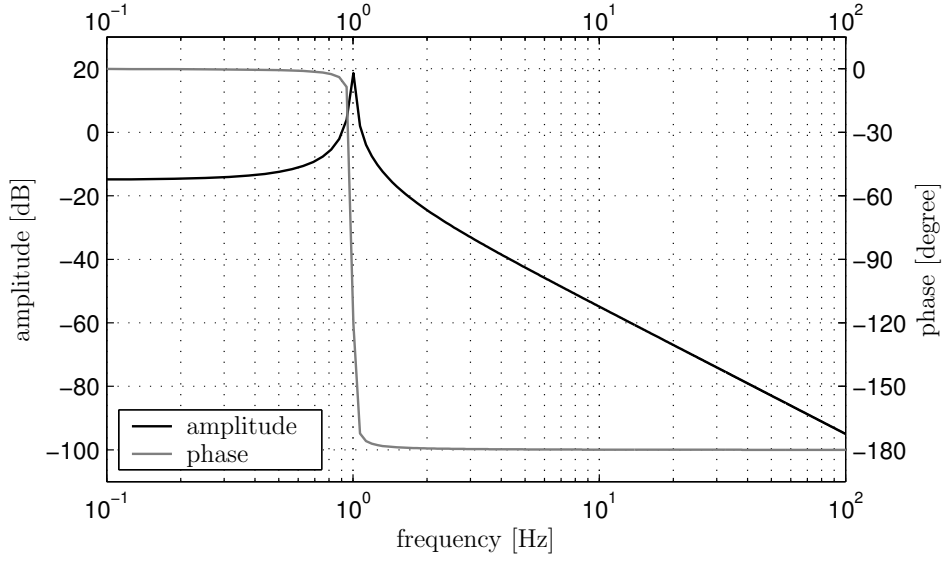


**Figure 3.9:** Bode plot of a pendulum transfer function from an externally applied force to the mirror displacement along the optical axis of the mirror, suspended as a pendulum. The transfer function is given for a resonance frequency  $\omega_0 = 1$  Hz, a  $Q$  of 10 and a mirror weight 5.6 kg.

If the external force,  $F_{\text{ex}}$ , is not directly applied to the centre of the mirror, a torque is present which leads to a rotation  $\theta$  of the main mirror in addition to the resulting longitudinal displacement. The torque depends on the distance  $d_c$  from the centre where the external force is applied. The equation of motion for the angular motion of a pendulum is given by

$$D_{\text{ex}}(t) = I\ddot{\theta}(t) + \gamma\dot{\theta}(t) + \kappa\theta(t), \quad (3.5)$$

where  $D_{\text{ex}} = |\vec{d}_c \times \vec{F}_{\text{ex}}|$  is the externally applied torque,  $I$  the moment of inertia, and  $\kappa$  the torque constant of the pendulum. The term  $\kappa\theta$  gives, according to Hooke's law, the restoring force of the pendulum when an external torque is applied.

Making the same assumption ( $s(t)$  is of the form  $s(\omega) \exp(i\omega t)$ ) that lead from Equation 3.2 to 3.3, Equation 3.5 can be rewritten giving the transfer function  $T_{\text{torque}}(\omega)$  from an externally applied force  $F_{\text{ex}}$  [N] perpendicular to the mirror surface at distance  $d_c$  from the centre to a rotation  $\theta$  [rad] as,

$$\begin{aligned} T_{\text{torque}}(\omega) &= \frac{\theta(\omega)}{F_{\text{ex}}(\omega)} \\ &= \frac{d_c}{I\omega^2 - i\gamma\omega - \kappa}. \end{aligned} \quad (3.6)$$

For simplicity the distance  $d_c$  is divided into a  $d_z$  and a  $d_y$  component. The  $d_z$  component is perpendicular to the optical axis of the main interferometer and parallel to the ground. A force impinging on the mirror at a non-zero  $d_z$  value leads to a yaw

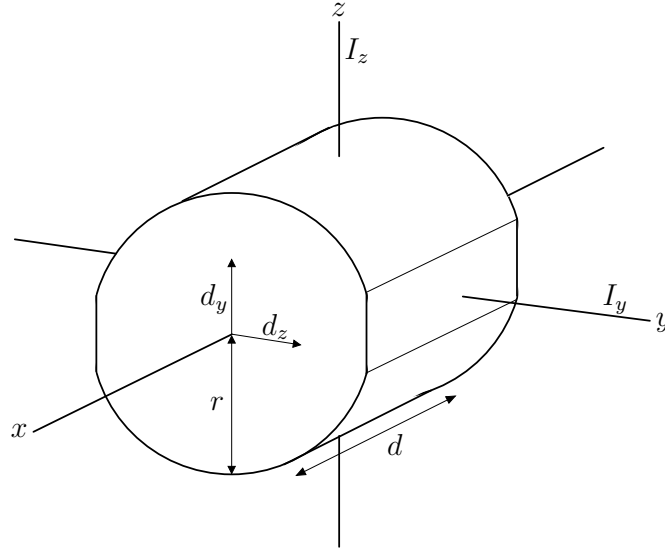


**Figure 3.10:** Schematic of a main mirror with its axis of rotation and moments of inertia.

around the  $z$ -axis depicted in Figure 3.10. Let the moment of inertia of the mirror around this rotation axis be  $I_z$ . At GEO 600 such a movement of a mirror is also referred to as rotation. The  $d_y$  component is perpendicular to the optical axis of the main interferometer and perpendicular to the ground. A force impinging the mirror at a non-zero  $d_y$  value leads to a pitch around the  $y$ -axis as depicted in Figure 3.10. Let the moment of inertia of the mirror around this rotation axis be  $I_y$ . At GEO 600 such a movement of a mirror is also referred to as tilt. Equation 3.6 can then be rewritten as

$$T_{\text{torque}}(\omega) = \frac{d_z}{I_z \omega^2 - i\gamma_z \omega - \kappa_z} + \frac{d_y}{I_y \omega^2 - i\gamma_y \omega - \kappa_y}. \quad (3.7)$$

According to [69] the moments of inertia of a solid cylinder are

$$I_z = I_y = \frac{1}{4}mr^2 + \frac{1}{12}md^2, \quad (3.8)$$

where  $r$  is the radius of the cylinder,  $d$  the thickness, and  $m$  the mass. As can be seen in Figure 3.10, the mirrors are not perfect cylinders. At both sides parallel to the  $z$ -axis, they are flattened. Therefore their actual moment of inertia will be smaller than the one given in Equation 3.8. As Equation 3.7 will be used only to determine what the maximal rotational movement for a given applied force is, the values of Equation 3.8 can be used for  $I_y$  and  $I_z$  to set this upper limit.

### 3.2.1 Electrostatic drive

A charge,  $q$ , in an electric field,  $E$ , experiences the force  $F$ , where,

$$\vec{F} = q\vec{E}. \quad (3.9)$$

If a dielectric is brought into an electric field, due to dielectric polarisation surface charges build up on the surface of the dielectric against the electric field. Inside the dielectric the electric field is reduced to  $E/\epsilon_r$ , where  $\epsilon_r$  is the (relative) dielectric constant of the dielectric. The energetic more favourable state is when the dielectric is between the capacitor plates. Thus the dielectric is pulled towards the capacitor as long as it is in the inhomogeneous part of the electric field. Figure 3.11 depicts this situation schematically for the special case of a parallel plate capacitor. The electric field is given by the voltage,  $U$ , that is applied to the capacitor. A dielectric brought close to the capacitor, and into the electric field of the capacitor, is polarised. If the dielectric is in the inhomogeneous part of the electric field, that is not between the two plates but next to them, it is then pulled as already stated towards the capacitor where the electric field is stronger. The force that acts on the dielectric is given by

$$F = \epsilon_r \epsilon_0 U^2 A , \quad (3.10)$$

where  $\epsilon_0$  is the dielectric constant of vacuum and  $A$  is a geometric factor depending on the electrode design and the distance between the plate capacitor. Depending on the applied voltage, the force on the dielectric can be changed, but the force can only pull the dielectric into the stronger part of the electric field of the capacitor.

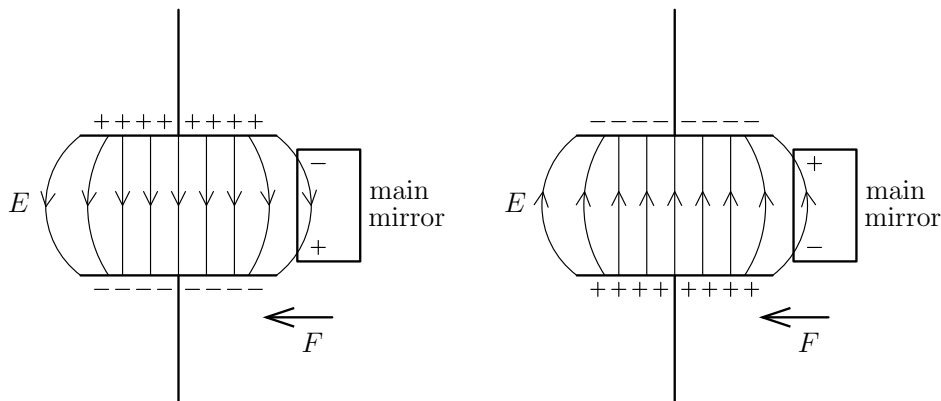


**Figure 3.11:** Sketch of the mechanism of the electrostatic drive. If an electric field is produced by a parallel plate capacitor next to a dielectric, the electric field produces surface charges on the dielectric due to polarisation. Here the dielectric is an interferometer main mirror. If the mirror is in the inhomogeneous part of the electric field it is pulled towards the capacitor where the electric field is stronger.

At GEO 600 this mechanism is utilised for the electrostatic drive. The two inboard mirrors MCE and MCN are suspended as double triple pendulums as depicted in Figure 3.7. Both triple pendulums are almost identical in suspension, shape and weight. The triple pendulum that suspends the actual mirror is further away from the beam splitter (see Appendix G for the optical layout of GEO 600). The distance between the two triple pendulums is fixed between 3 and 5 mm. The mirror is made of the dielectric, fused silica. The triple pendulum closer to the beam splitter is the so-called reaction

pendulum. The reaction pendulum suspends the reaction mass, a mass identical to the main mirrors, except that it is not coated with a reflective surface. Instead the reaction mass is coated on its surface closest to the main mirror with eight comb-like thin gold electrodes (see Appendix H). Between pairs of electrodes, forming a capacitor, a voltage of up to 1 kV can be applied, producing an inhomogeneous field in the area of the mirror. As the force applied to the mirrors is proportional to the square of the voltage applied to the capacitors, the force depends on the difference between the voltages applied to the two electrodes of one capacitor. To allow a bipolar displacement of the main inboard mirrors a constant bias force is applied to the mirrors. This is achieved by applying a constant DC voltage to all comb-pair capacitors. One electrode of the capacitor is put on ground and to the other a high voltage is applied (for example 500 V). Signals to the electrostatic drive are either directly applied or amplified by a high-voltage amplifier before being applied. If the signal is applied directly, the so-called low-voltage path of the actuator is used. The signal is applied to the electrode that is put on ground for producing a constant DC voltage. This path is used for very small signals such that the conversion of voltage to force is approximately linear. For signals like an injected simulated, continuous gravitational wave signal, the low-voltage path of the electrostatic drive is used. If a high gain is desired the so-called high-voltage path of the actuator is used. In this path, the signal is amplified by a high-voltage amplifier and passed through a square-root circuit before being applied to the electrode with the high-voltage offset. The square-root circuit transforms the quadratic proportionality between applied voltage and resulting force (as can be seen in Equation 3.10) into a linear proportionality.

In the following paragraph, it is shown that using the low-voltage path does not significantly affect the accuracy of the amplitude of the hardware injection, although in the low-voltage path the square-root of the applied voltage is not taken. For a sinusoidal signal with 200 mV peak amplitude being applied to the low-voltage path, a sinusoidal signal with 9.9 mV peak amplitude is applied to the electrodes of the ESD (see Appendix I Figure I.9 and Figure I.10). If at the same time the constant offset of the electrostatic drive is 500 V, the error in amplitude due to not taking the square-root of the voltage applied to the low-voltage path is less than 0.1 %. This is well below the overall accuracy of the electro static drive, which is approximately 5 %.

Each of the four capacitors of the electrostatic drive is situated on one quadrant of the surface of the reaction mass. By applying different combinations of voltages to the four capacitors different degrees of freedom of the mirror can be controlled, such as longitudinal displacement, yaw (rotation), and pitch (tilt). The force is then given by Equation 3.10. For details on the geometry of the electrodes of the capacitors and the correct geometric factor giving the capacitance, see Appendix H and [70]. In order to get a longitudinal displacement of the main inboard mirrors, the same signal needs to be applied to all four capacitors. In Appendix I in Figure I.8 through I.10 the electronics of the so-called low-voltage path for the various degrees of freedom can be found.

By using an electrostatic drive the masses remain free from any attachments. When using a standard coil-magnet system magnets are attached directly onto the main mirrors, thus degrading the Q of the masses and thereby its thermal noise properties. GEO 600 is currently the only large scale laser-interferometric gravitational wave detec-

tor that uses an electrostatic drive as actuators.

### 3.2.2 Photon pressure actuator

A photon of the wavelength  $\lambda$  has momentum,

$$p = \frac{h}{\lambda}, \quad (3.11)$$

where  $h$  is Planck's constant. If a photon impinges normally on a mirror and is reflected, twice the momentum of the photon is transferred to the mirror. If a laser beam with the power  $P$  is shone normally on a mirror with total reflection and no absorption the force,

$$F = 2 \frac{P}{c}, \quad (3.12)$$

is applied to the mirror, where  $c$  is the speed of light. This force applied to the mirror surface is called radiation pressure. It can be used to act on a mirror suspended as a pendulum. By modulating the laser power, the applied force is modulated. If Equation 3.12 is inserted into Equation 3.3, the mirror displacement due to the externally applied radiation pressure can be obtained as,

$$s(\omega) = \frac{2P(\omega)}{mc[(\omega_0^2 - \omega^2) + i\frac{\omega_0}{Q}\omega]}. \quad (3.13)$$

For modulation frequencies  $\omega \gg \omega_0$  and  $\omega \gg \omega_0/Q$ , Equation 3.13 can be approximated by

$$s(\omega) = -\frac{2P(\omega)}{mc\omega^2}. \quad (3.14)$$

At GEO 600, first experiments have been conducted with a photon pressure actuator with a light power of approximately 500 mW. The photon pressure actuator has not been used while the detector was running in science mode. No hardware signal injections have been performed with the photon pressure actuator so far.

### 3.2.3 Implications of the actuator transfer functions on the hardware signal injection

The electrostatic drive and the photon pressure actuator can be used for hardware signal injection. Both have a transfer function from applied force to a main interferometer mirror to its displacement proportional to  $1/f^2$  above the resonance frequency of the pendulum, formed by the suspended mirror.

The  $1/f^2$  dependency does not need to be taken into account for the hardware injection of simulated, continuous gravitational wave signals. In subsection 2.1.1 it has been shown that the maximal Doppler shift due to the orbital motion of the Earth around the Sun is  $\Delta f/f_{\text{SSB}} = 1.0 \times 10^{-4}$  in one sidereal year, where  $\Delta f$  is the frequency shift and  $f_{\text{SSB}}$  the gravitational wave signal frequency at the solar system barycentre. This leads to a maximal amplitude error of  $\pm 0.02\%$  for signal frequencies well above the resonance frequency of the main mirror suspension pendulums. Therefore the frequency dependency of the transfer function of the actuators does not need to be taken into account.



### 3.2.4 Noise of the microcontroller on the analog simulated gravitational wave signal

The simulated gravitational wave signal generated by the microcontroller is directly applied to the actuators of the main mirrors of the interferometer. This signal is directly translated into a longitudinal displacement of the interferometer mirrors. Therefore the signal must not contain noise in the detection band that reduces the interferometer sensitivity. Figure 3.12 gives the spectrum of the microcontroller signal when the injected signal was about one third of its maximal amplitude and the PLL was running on the microcontroller. The neutron star parameters for the signal generation are those of the recorded signal during S3II (see Table 2.2). In the same plot the spectrum of the microcontroller signal is plotted for a zero amplitude and the PLL being turned off. During this measurement the phase increment register was fixed and had a value producing a sinusoidal signal with a frequency as in the other plot. It can be seen that the actual signal is at least three orders of magnitude above the noise. As the signal shows up in the spectrum of the output of the interferometer only after integration times of several 100 seconds with a signal-to-noise ratio below 10, no significant noise is introduced into the interferometer by the hardware injection.

## 3.3 Amplitude of the injected simulated, continuous gravitational wave signal

The simulated, continuous gravitational wave signal produced by the microcontroller simulates all neutron star parameters correctly except the absolute amplitude of the signal. On the control computer the signal amplitude is set arbitrarily to  $h_0 = 1$ . To determine the amplitude  $h_0$  of the signal which is actually being injected, one needs to take the amplitude factors of the microcontroller and the calibration factor of the actuator into account. As so far only the low-voltage path of the electrostatic drive has been used for the injection of a simulated, continuous gravitational wave signal, only the calibration factor of the low-voltage electrostatic drive is of relevance. In the following, the calibration factors for the performed hardware signal injection are described.

### Amplitude factors of the microcontroller

To determine the amplitude of the injected signal on the microcontroller side, two factors need to be taken into account. The first is the maximal possible amplitude for  $h(t)$  expressed in fractions of  $h_0$  at the detector site for given neutron star parameters. The second is the maximal voltage of the signal provided by the microcontroller.

On the control computer the amplitude of the simulated gravitational wave signal is set arbitrarily to  $h_0 = 1$ . Before the signal injection is started and the amplitude envelope is mapped into the D/A converter (see subsection 2.1.2), the maximal possible amplitude of the signal at the detector site is determined. As can be seen in Equation 2.2, this is not necessarily  $h_0$  due to the inclination of the neutron star and the beam pattern functions. The effects due to the inclination and the beam pattern functions are combined in the factor called  $F_{bp}$ . As the amplitude envelope is mapped onto the D/A converters such

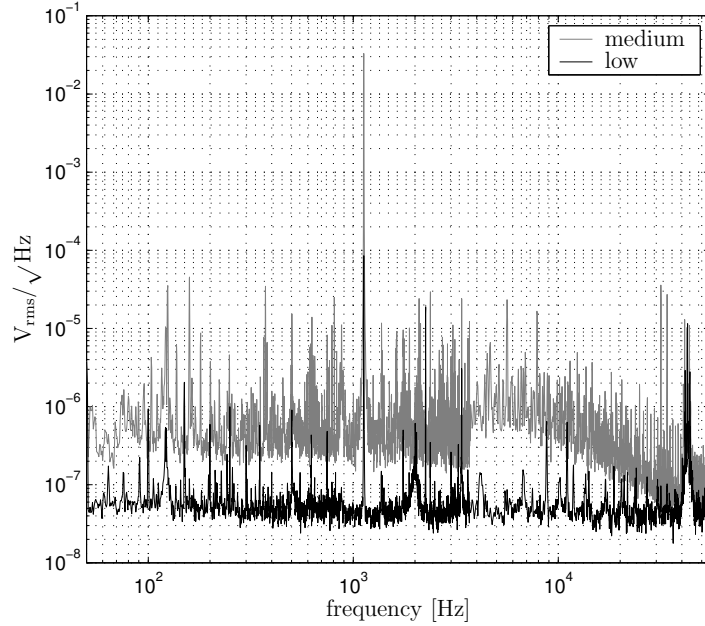


**Figure 3.12:** Amplitude spectral density of the microcontroller signal with an effective noise bandwidth of 0.75 for 50 to 850 Hz, 3.0 for 850 to 3700 Hz, and 48 for 37 to 54.9 kHz (the effective noise bandwidth is defined by Equation C.4). The line “medium” gives the spectrum of the analog simulated gravitational wave signal while the signal was about one third of its maximal amplitude. While the spectrum was taken, the PLL was running on the microcontroller and the neutron star parameters were set to the same values as the recorded signal during the S3 II. The line “low” gives the spectrum of the microcontroller signal when the amplitude was set to zero and the PLL was turned off. The phase increment register was set to a value producing a signal at the frequency of the signal recorded during S3 II without taking Doppler shifts into account.

that the dynamic range is optimally used, the maximal amplitude value produced by the microcontroller does not correspond to  $h_0$  but  $F_{bp}$ . Therefore the signal provided by the microcontroller needs to be divided by  $F_{bp}$  to determine  $h_0$  of the injected signal.

The maximal voltage of the signal is frequency dependent due to the band pass filter after the electronic combination of the signal amplitude envelope and oscillatory part (see Figure I.6). To determine the maximal voltage, the phase increment register on the microcontroller is set to the value of the gravitational wave signal, not taking any Doppler shifts into account, and the PLL is turned off. Then the maximal voltage of the signal at the output used for the injection is determined on a digital oscilloscope. This was done averaging 64 times over one cycle of the signal. This factor will be called  $V_{max}$ . The calibration factor of the low-voltage electrostatic drive needs to be multiplied by  $V_{max}$  to determine the mirror movement caused by the injected signal.

### Amplitude factors of the low-voltage electrostatic drive

The frequency dependent calibration factor of the high-voltage path of the electrostatic drive,  $F_{\text{hv}}(f)$  [m/V], that relates applied voltage to mirror displacement has been determined several times [70, 71]. It is used for the calibration of the interferometer data to produce  $h(t)$  data [25]. With the knowledge of the calibration factor of the high-voltage path the calibration factor of the low-voltage path can be determined. For this, only the ratio between the low and high-voltage paths,  $R_{\text{lh}}$ , needs to be measured.

Before determining the ratio between the low and high-voltage paths of the electrostatic drive, the calibration factor of the North and East electrostatic drive need to be balanced. The distance between the inboard East and North mirrors to their reaction mass have the largest effect on the calibration factor. At GEO 600 a signal can be applied to the East and North high-voltage path or the East high-voltage path only. To balance the East and North electrostatic drive, a sinusoidal signal at a fixed frequency is applied to the East high-voltage path only. In the Michelson differential error point in-phase of the high-power photodiode, the height of the injected signal is determined in an amplitude spectrum. Then the same signal is applied to the East and North high-voltage path. If the signal applied to East and North yields a value in the spectrum more than twice the size of the same signal applied to East only, the North mirror and its reaction mass are closer to each other than the East mirror and its reaction mass. Then the North mirror needs to be moved away from the reaction mass. If the signal applied to East and North yields a value in the spectrum less than twice the size of the same signal applied to East only, the North mirror and its reaction mass are further apart from each other than the East mirror and its reaction mass. Then the North mirror needs to be moved closer to its reaction mass. After moving the inboard mirror the procedure needs to be repeated until the North and East electrostatic drives are balanced.

When the East and North electrostatic drives are balanced, the ratio between the low and high-voltage path of the electrostatic drive,  $R_{\text{lh}}$ , can be determined. For this, a sinusoidal signal at a fixed frequency with a fixed amplitude is applied to the high-voltage path and the amplitude of the signal is determined in the amplitude spectrum of the Michelson differential error point in-phase on the high-power photodiode. Then a sinusoidal signal at the same frequency is applied to the low-voltage electrostatic drive. As the low-voltage electrostatic drive is much more sensitive than the high-voltage electrostatic drive the amplitude needs to be lower than the one injected into the high-voltage electrostatic drive (the high-voltage drive has a gain approximately 2150 times larger than the gain of the low-voltage drive). The signal amplitude is determined again in the amplitude spectrum of the Michelson differential error point. The amplitudes should be chosen such that the signal in the amplitude spectrum has a signal-to-noise ratio of at least 10. From these numbers the ratio  $R_{\text{lh}}$  can be determined.

The last step in determining the amplitude  $h_0$  of the injected signal is to convert the mirror displacement into strain sensitivity. This relation is given for a Michelson interferometer in Equation 1.1 as

$$h = 2\Delta L/L ,$$

where  $L$  is the length of one arm and  $\Delta L$  is the length change in one arm. This yields for  $h_0$ ,

$$h_0 = 2 \frac{1}{F_{\text{bp}}} V_{\text{max}} R_{\text{lh}} F_{\text{hv}}(f)/L. \quad (3.15)$$

As  $F_{\text{hv}}$  gives mirror displacement of one mirror per applied voltage,  $V_{\text{max}} \times R_{\text{lh}} \times F_{\text{hv}}$  gives the mirror displacement of one mirror for the applied voltage to the low-voltage electrostatic drive. The same voltage is applied to the East and North electrostatic drive.

### 3.3.1 Signal amplitude of 11-12 June 2004 injection

During 11-12 June 2004 a successful hardware injection of a simulated, continuous gravitational wave signal was performed. The injection parameters of the neutron star were those of the signal recorded during S3 II. For the parameters see Table 2.2. The maximal amplitude of  $h(t)$  on the control computer for  $h_0 = 1$  was 0.691. The maximal voltage of the signal around 1125.647365 Hz on the microcontroller was 0.1828 V. The ratio  $R_{\text{lh}}$  between the low and high-voltage electrostatic drives was determined to be  $4655 \times 10^{-7}$ . The mirror displacement of one mirror per applied voltage of the high-voltage electrostatic drive was 48 fm/V. This yields an injected signal amplitude  $h_0$  of

$$h_0 = 2 \times \frac{1}{0.691} \times 0.1828 \text{ [V]} \times 4655 \times 10^{-7} \times 48 \left[ \frac{\text{fm}}{\text{V}} \right] / 1200 \text{ [m]} = 9.9 \times 10^{-21}. \quad (3.16)$$

The error on the amplitude, which is dominated by the error of  $R_{\text{lh}}$ , is approximately 10% [72]. As already mentioned in chapter 2, the amplitude error of the signal injection is dominated by the error of the actuator used for the injection.

In chapter 4 the results of the successfully injected continuous gravitational wave signals are presented. For the injection the electrostatic drives with the above given signal amplitude were used.

## Chapter 4

### Results of the hardware injection experiment

From 11 June until 12 June 2004 a simulated, continuous gravitational wave signal was successfully hardware injected at GEO 600 and subsequently extracted from the  $h(t)$  data with the continuous wave time-domain search algorithm. In this chapter, the extraction of the injected signal is described. The time-domain search algorithm for continuous gravitational waves will be described briefly. The time domain algorithm is restricted due to the nature of the signal on small frequency ranges in the data. Frequency bands that are contaminated with so-called “line noise” (noise that appears as a line in the frequency spectrum of the data) is not optimal for continuous gravitational wave searches. To collect the knowledge of existing line noise in the detector, a database of all known line noise has been created. This database will be described. At the end of this chapter the detection of the hardware injected simulated, continuous gravitational wave signal with the time-domain search algorithm is presented.

#### 4.1 The time-domain search algorithm

The time-domain search algorithm for continuous gravitational waves was written to conduct targeted searches for continuous gravitational waves emitted by spinning neutron stars. The search algorithm has been developed at the University of Glasgow by Réjean Dupuis and Graham Woan and was the first that produced astrophysical results on GEO 600 and LIGO data [73]. The advantage of this algorithm is that it needs comparatively small computational power in contrast to the frequency-domain search algorithm for continuous gravitational waves. This is because the time-domain search algorithm performs a targeted search, while the frequency-domain search algorithm does an all-sky search. For a detailed description of the time-domain search algorithm for continuous gravitational waves see [74].

A targeted search looks for signals from a known source. In the case of continuous gravitational waves, known sources are spinning neutron stars which are pulsars. From the electromagnetic emission of the pulsar, several parameters that are believed to determine the shape of the gravitational wave signal are known. As described in chapter 1 the continuous gravitational wave signal from a non-axisymmetric, non-precessing, spinning neutron star depends on nine parameters of the neutron star. These are the position of the neutron star given by its right ascension  $\alpha$  and declination  $\delta$ , spin frequency  $f_0$  and spin-down parameters  $\dot{f}$  and  $\ddot{f}$  for a certain epoch, amplitude  $h_0$  and constant phase  $\phi_0$  of the gravitational wave signal, the angle  $\iota$  between the neutron star’s spin direction and the propagation direction of the gravitational wave, and the polarisation angle  $\psi$  of

the wave. The position  $\alpha$  and  $\delta$ , and the spin-down parameters  $f_0$ ,  $\dot{f}$ , and  $\ddot{f}$  of a pulsar are known very accurately from electromagnetic observations. This knowledge is used in a targeted search, leaving only four unknown parameters for the gravitational wave signal, which are  $h_0$ ,  $\phi_0$ ,  $\iota$ , and  $\psi$ .

The time-domain search algorithm consists out of two steps. In the first step, the intrinsic frequency of the pulsar is removed from the data. This is achieved by heterodyning the data. The data is multiplied in the time domain with the cosine and sine of the phase evolution of the gravitational wave pulsar signal given by Equation 1.8. Thus the knowledge of  $f_0$ ,  $\dot{f}$ , and  $\ddot{f}$  for a certain epoch is made use of. After filtering and resampling, a complex data set is obtained. The data volume is significantly reduced leaving the antenna response functions of the interferometer as the only remaining time-varying quantity of the signal template in the complex data set.

In the second step, the complex data set is fitted to the remaining set of signal templates. These signal templates are a function of the position  $\alpha$  and  $\delta$  of the neutron star, the position of the detector, moving with the rotation of the Earth, and the four unknown neutron star parameters  $h_0$ ,  $\phi_0$ ,  $\iota$ , and  $\psi$ . The different combinations of the unknown parameters form the set of remaining signal templates. A fit is made to these four unknown parameters. In this step a Bayesian approach is taken [75]. A Gaussian distribution is chosen as the likelihood function. The standard deviation of the data is calculated before the fit and enters the likelihood function as a known parameter. For the noise, the assumption is made that it is stationary over 30 minutes worth of data. A uniform prior for the parameters  $\phi_0$ ,  $\cos \iota$ , and  $\psi$  is chosen as the prior probabilities. For  $h_0$  a uniform prior with an upper limit is chosen. The posterior probability is marginalised over the other parameters to gain the probability density function of one of the parameters.

In the past months a more sophisticated statistical approach had been developed. In that approach a Student's-t distribution is chosen as the likelihood function. This approach does not assume stationary noise, but weighs the noise. As the coding of this new statistical approach had not been publicly available within LAL at the time when the analysis of the hardware signal injection was performed, only the Gaussian distribution approach was used to extract the hardware injected signal from the data.

The maximum of the probability density function of one parameter yields the so-called best fit of that parameter; the form of the function is a measure of the belief that the parameter lies in the neighbourhood of a particular point. The best fit of a Bayesian data analysis approach should not be mistaken with the fitted value from a conventional  $\chi^2$ -fit. The result of a Bayesian data analysis approach yields the probability density function over a certain range of the parameter which is fitted. From this the degree of belief with which the parameter lies in a certain range can be derived.

Thus the result of the time-domain continuous gravitational wave search algorithm is therefore the degree of belief with which a detection is obtained for a certain parameter range. For the case of the continuous gravitational wave time-domain search algorithm no detection is made when the probability density function of  $h_0$  does not drop to near zero close to  $h_0 = 0$ . Then the degree of belief can be given with which no detection for a certain signal amplitude of the gravitational wave was made for a signal from a neutron star with known parameters. A detection is made when most of the probability

density function is displayed away from  $h_0 = 0$  and the function is near zero close to  $h_0 = 0$ . Then the degree of belief can be given with which a detection for a certain amplitude range was made.

## 4.2 Noise

Non-Gaussian noise such as line noise close to the expected continuous gravitational wave frequencies reduces the effectiveness of the search algorithm to identify possible continuous gravitational wave signals from pulsars. This noise usually arises from excited resonances in the detector hardware. In the first part of this section sources for known line noise of GEO 600 are described.

In the case of the hardware injection of a simulated, continuous gravitational wave signal, the analog electronic signal can be picked up electronically. In that case the signal enters the interferometer data as noise. A blind test was performed to ensure that the signal is only entering the interferometer data via the actuation of the main mirrors. In the second part of this section the blind test is presented.

### 4.2.1 Line noise

As mentioned above, line noise in the vicinity of the frequency band where a continuous gravitational wave signal is expected, can reduce the effectiveness of the search algorithm. One effect is that using a Gaussian distribution for the likelihood function is not any longer a good estimate, therefore leading to a faulty posterior probability. When performing a search the knowledge of the spectrum of the investigated data is, therefore, of great importance. Once lines are identified, it can be investigated if they are avoidable, hence if a change in the hardware of the detector can avoid their emergence. If they are not avoidable, it can be considered whether they should be removed in software by filtering certain frequency bands or applying a line removal algorithm [76, 77]. To have an overview on the known and identified sources of line noise, a detector frequency database was built.

#### Detector frequency database

In the scope of this work the GEO 600 frequency database was set up. This database contains information about known resonance frequencies of the GEO 600 detector hardware. It is written in mysql and allows mysql-based search commands through a web interface [78]. The database contains measured and modelled resonance frequencies. For each frequency, the physical component that exhibits the resonance is given. A distinction is made between mechanical and electronic resonances. Besides information about the location of the physical component, references to the measurements and models are given. The resonance frequencies are listed with their  $Q$  value and errors if available (see Equation 3.4 for the definition of  $Q$ ). Currently there are 577 entries to the database out of which about a third are modelled values.

Typical resonance frequencies of the detector are pendulum resonances of the suspended mirrors, violin modes of the suspension fibres, internal mirror modes, and inter-

nal modes of the mechanical parts of the suspension and the vacuum system. Environmental line noise which can couple into the interferometer data such as vacuum pump frequencies and power lines are also included.

The violin modes of the suspension fibres contribute the largest line noise in the frequency band of interest for continuous gravitational wave searches at GEO 600, which is 100 Hz to 2 kHz. The pendulum resonances are of the order 1 Hz and the internal mirror modes are above 2 kHz. On the data of the second science run S2 of LIGO, an upper limit was set on the gravitational wave emission from 28 pulsars [79]. In the database, it can be seen that of these 28 pulsars twice the spin frequencies of the pulsars B0021-72N and B1821-24 are close to the fundamental violin mode of the fused silica suspension of MFE (mirror far East, for its location see the optical layout of GEO 600 Appendix G). In the future the fundamental violin modes should be monitored to see if they drift closer to the spin frequencies of the pulsars [80].

#### 4.2.2 Blind test

As the simulated, continuous gravitational wave signal for the hardware injection is first produced electronically and then applied to the actuator for injection, one needs to be sure that the signal only couples into the interferometer via the actuator. Other paths such as electronic coupling into other interferometer channels or electronic pick up in the data acquisition system need to be excluded. During the investigations of electronic coupling and pick up, it became clear that under certain setups the simulated signal couples into  $h(t)$  in undesired ways. In particular, electronic pick up in the data acquisition was observed when the simulated, continuous gravitational wave signal was recorded directly with the data acquisition during injection at the same time. When the signal was only directly recorded and not injected, it appeared in the interferometer channels and  $h(t)$ .

The valid setup found for signal injections without undesired coupling or pick up into  $h(t)$  is the following. The microcontroller producing the simulated, continuous gravitational wave signal is situated in rack C in the control room. Only the signal of the microcontroller used for the injection is connected. No signal is directly recorded during injections. The signal can be tested by direct recording shortly before the injection and after the injection to ensure that the microcontroller behaved correctly during the injection.

For the blind test, the microcontroller was run in this setup, except that the signal from the microcontroller to the actuator had been removed. The microcontroller was running producing a simulated gravitational wave signal with the signal parameters used for the hardware injection given in Table 4.1 (these are the same parameters as used for the S3II recordings). The blind test was performed from 14 June 2004 19:30:00 UTC until 15 June 2004 8:30:00 UTC. The detector was in lock during the whole time of the blind test. No signal with the neutron star parameters at which the microcontroller had been running during this time could be found. Figure 4.1 gives the probability density functions for the fitted parameters  $h_0$ ,  $\phi_0$ ,  $\cos \iota$ , and  $\psi$ . The probability density functions do not promote a particular value for the fitted parameters. From the probability density function for  $h_0$ , it can be seen that, with 95% confidence, no signal with an



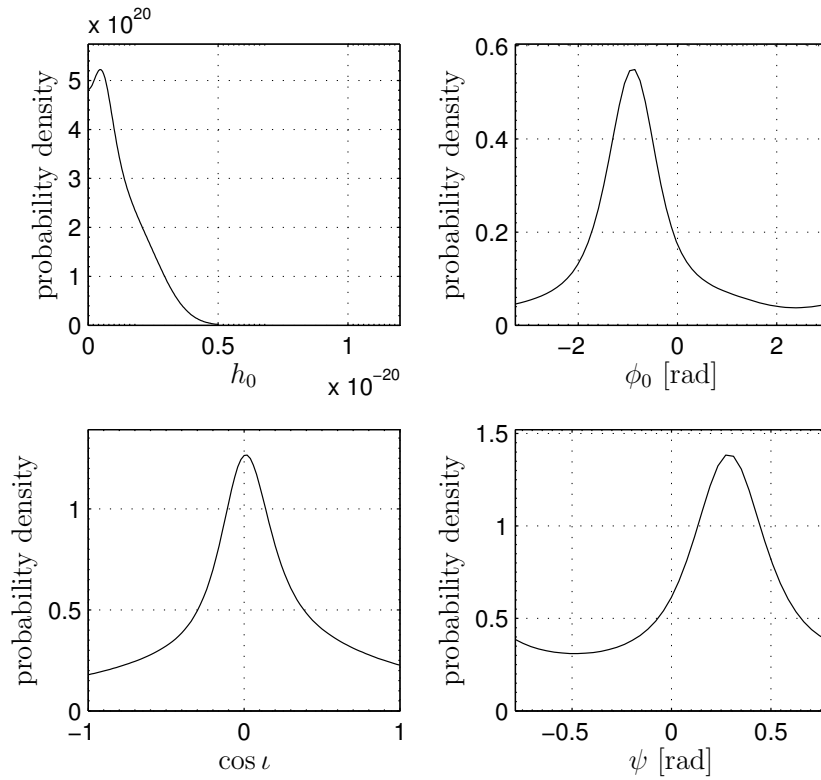


**Figure 4.1:** Probability density functions of the data of the blind test of the simulated, continuous gravitational wave hardware signal injection. To show that no undesired electronic coupling or pickup occurs, the microcontroller was producing a signal with the hardware injection parameters (see Table 4.1) with no signal being connected to the actuator or data acquisition system. It can be seen from the  $h_0$  plot that by the time-domain search algorithm no signal could be found.

Injected and extracted pulsar parameters			
	injected	best fit	unit
$\alpha$	0.776235274	-	[rad]
$\delta$	-0.616383646	-	[rad]
$2f_0$	1125.647365	-	[Hz]
$\dot{f}$	$-2.87 \times 10^{-11}$	-	[Hz/s]
$\ddot{f}$	0.0	-	[Hz/s <sup>2</sup> ]
epoch	751680013	-	GPS second
$h_0$	$9.9 \times 10^{-21} \pm 10\%$	$9.3 \times 10^{-21}$	[1]
$\phi_0$	1.993746459	2.29	[rad]
$\psi$	0.372640504	0.23	[rad]
$\cos \iota$	0.669357543	0.675	[1]

**Table 4.1:** Parameters used to produce the simulated, continuous gravitational wave signal for the hardware injection and the best fits for the reconstructed values. The best fits are the maximal values of the probability density functions plotted in Figure 4.3. They cannot be considered as fitted values.

amplitude of  $h_0 = 3.1 \times 10^{-21}$  or smaller and the neutron star parameters position  $\alpha = 0.776235274$ ,  $\delta = -0.616383646$ , spin-down parameters  $2f_0 = 1125.647365$  Hz,  $\dot{f} = -2.87 \times 10^{-11}$  Hz/s,  $\ddot{f} = 0.0$  Hz/s<sup>2</sup> at epoch GPS second 751680013 is present in the data.

### 4.3 Extraction of the continuous gravitational wave signal

From 11 June 2004 18:00:00 UTC to 12 June 2004 21:05:06 UTC, a continuous gravitational wave signal was injected of a neutron star with position  $\alpha = 0.776235274$ ,  $\delta = -0.616383646$ , at the frequency  $2f_0 = 1125.647365$  Hz, spin-down parameters  $\dot{f} = -2.87 \times 10^{-11}$  Hz/s,  $\ddot{f} = 0.0$  Hz/s<sup>2</sup> at epoch GPS second 751680013, amplitude  $h_0 = 9.9 \times 10^{-21}$ ,  $\phi_0 = 1.993746459$ , and  $\psi = 0.372640504$ . The interferometer was in lock over the entire period. Figure 4.2 shows the amplitude spectral densities of  $h(t)$  starting at 11 June 2004 20:50:00 UTC. At this time the amplitude of the injected signal was maximal. The left-hand plot is over 10 s worth of data over the full frequency range. The sharp lines with a signal-to-noise ratio of about 100 in that plot are calibration lines which are permanently injected into the interferometer for calibrating the interferometer data. Around the injected frequency the noise is of the order  $10^{-20} h_{\text{rms}}/\sqrt{\text{Hz}}$ . In the right-hand plot of Figure 4.2, the amplitude spectral density of  $h(t)$  is given over 100 s worth of data between the frequencies 1110-1140 Hz. For an integration of 100 s the injected signal becomes distinguishable from the noise if the signal is at its maximal amplitude. For the determination of the amplitude spectral densities, a Hanning window was used.

Figure 4.3 gives the probability density functions for the fitted parameters  $h_0$ ,  $\phi_0$ ,  $\cos \iota$ , and  $\psi$ . The vertical dashed lines indicate the parameter values used for the injection.

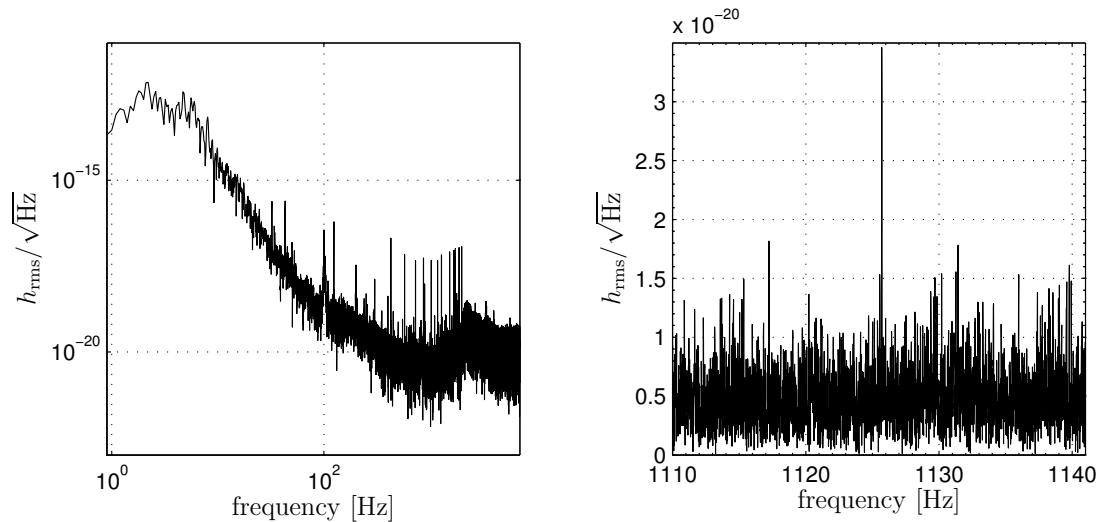


**Figure 4.2:** Amplitude spectral density of  $h(t)$  on data starting at 11 June 2004 20:50:00 UTC. At this time the amplitude of the injected signal was maximal. The left graph gives the spectrum over 10s worth of data over the full frequency range. The sharp lines with a signal-to-noise ratio of about 100 in that plot are calibration lines which are permanently injected into the interferometer for calibrating the interferometer data. The right graph gives the spectrum over 100s worth of data around the injected signal frequency. The injected signal is clearly visible. For the determination of the amplitude spectral density a Hanning window was used.

Figure 4.4 shows the probability density functions for the parameters  $(h_0, \phi_0)$ ,  $(h_0, \psi)$ , and  $(h_0, \cos \iota)$ . The left-hand graphs show colourmaps of the probability density function over the full parameter space used for the calculation. In the right-hand graphs the contours for 33 %, 10 %, and 3 % of the maximum of the probability density function are plotted. As in the contour plots two parameters are estimated, the error of a contour corresponds to its maximal  $y$ - and  $x$ -range. These errors are indicated by the vertical and horizontal lines for one of the three contours in each right-hand graph. The asterisks indicate the parameter values used for the injected signal. It can be seen that for  $(h_0, \phi_0)$  and  $(h_0, \psi)$  the injected parameter values fall within the area where the values of the contour are well above 10 % of its maximum. For  $(h_0, \cos \iota)$  the injected parameter values falls within the area where the values of the contour are well above 33 % of its maximum. As the parameters  $(h_0, \cos \iota)$  are strongly correlated the contours are elliptical.

Table 4.1 lists the parameters used to produce the simulated, continuous gravitational wave signal for the hardware injection along with the best fits for the reconstructed values of  $h_0, \phi_0, \cos \iota$ , and  $\psi$ . The best fits are the maximal values of the probability density functions plotted in Figure 4.3. As the probability density functions describe the degree of belief with which a fitted parameter lies in a certain value range, the best fits should not be mistaken as fitted values. Instead of giving a single value with an error margin as the result, the probability density functions are given.

A simulated, continuous gravitational wave signal was hardware injected into the in-

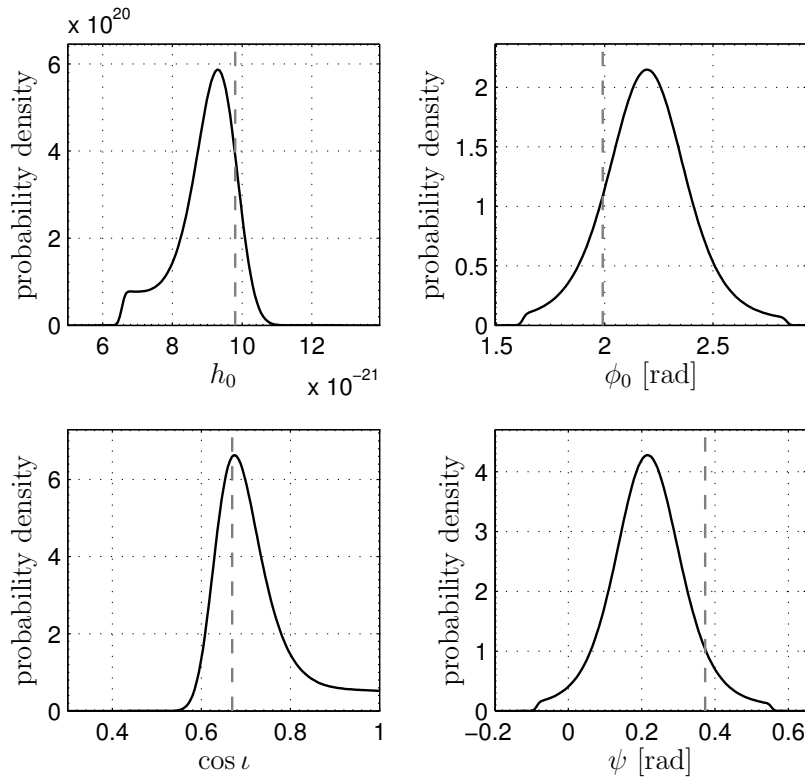


**Figure 4.3:** Probability density functions of the hardware injection for the injected signal parameters  $h_0$ ,  $\phi_0$ ,  $\cos \iota$ , and  $\psi$ . The vertical dashed lines indicate the parameter values used for the injection.

terferometer by actuating on the two end mirrors of the interferometer arms, thereby changing the differential length of the two arms and simulating the effect of a gravitational wave. The injected signal was successfully recovered from the data with the time-domain search algorithm for continuous gravitational waves. In particular, the amplitude and the phase were recovered with values consistent with the parameters of the injected signal, thus proving the full detection chain for continuous gravitational waves at GEO 600.

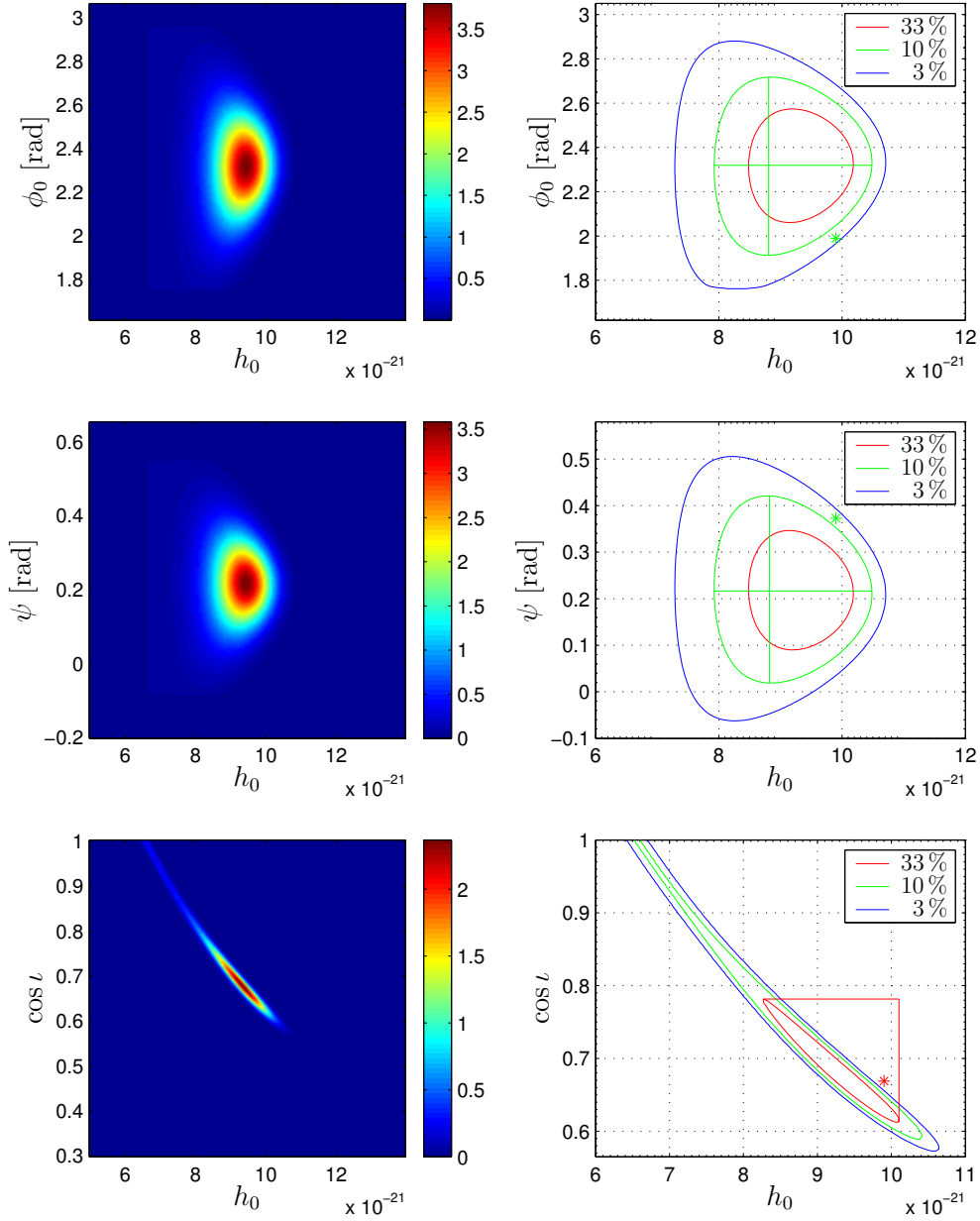


**Figure 4.4:** Probability density functions for the parameters  $(h_0, \phi_0)$ ,  $(h_0, \psi)$ , and  $(h_0, \cos \iota)$ . The left-hand graphs show colourmaps of the probability density function over the full parameter space used for the calculation. In the right-hand graphs the contours for 33%, 10%, and 3% of the maximum of the probability density function are plotted. The errors on the two parameters are indicated by the vertical and horizontal lines for one of the three contours in each right-hand graph. The asterisks indicate the parameter values used for the injected signal.



## Chapter 5

### Increasing the calibration accuracy - A photon pressure actuator

As mentioned before, the accuracy of the electrostatic drives used for the hardware signal injection and the injection of the calibration lines for an online calibration is about 5%. The overall absolute calibration of  $h(t)$  is accurate to within 10%. When moving from the first direct detections of gravitational waves to gravitational wave astronomy, it is of great interest to improve the accuracy of the amplitude calibration of the measured gravitational wave signals. One application where high accuracy is needed is the determination of the Hubble constant by using inspiraling neutron star binaries as standard candles. The accuracy with which the Hubble constant can be determined depends partly on the accuracy with which the amplitude of the gravitational wave signals of such an event is measured [81, 82]. Some scientists point out that the component of the gravitational wave driving the test mass back and forth in the propagation direction of the gravitational wave (also referred to as the gravitational Lorentz force) needs to be taken into account, in order to prevent misestimation of the parameters of the radiating system [83]. The gravitational Lorentz force will lead to corrections of the order of up to 10%. Therefore to be able to distinguish the gravitational Lorentz force corrections an accuracy better than 10% is needed. Besides these two examples, a good calibration has always been essential in astronomy conducted in the electromagnetic spectrum to draw correct physical conclusions from the observations [84]. This argument can be directly applied to gravitational wave astronomy. Overall, it is desirable to have a calibration that is as accurate as possible.

The GEO 600 goal is a calibration accuracy of the order of 1%. In this chapter the theoretically achievable accuracy for an online calibration using a photon pressure actuator (PPA) is investigated. To use the radiation pressure from a periodic light source for the external excitation of an interferometer mirror has been first suggested by Albrecht Rüdiger [85]. The requirements on the minimal actuation force, and hence the minimal power of the PPA, are presented. Then the possible theoretical accuracy of a PPA is investigated taking into account the error in the pendulum transfer function of the suspended main mirrors not knowing the correct resonance frequency and quality factor  $Q$  of the pendulum, the accuracy of absolute power measurements, the light power reflected by the interferometer main mirror, apparent longitudinal displacement of the main mirror due to mirror rotation and thermally induced longitudinal length changes in the interferometer main mirror. In the next section the current setup of the PPA is described. The accuracy of the current setup is estimated and first measurements with the current PPA at GEO 600 on the main interferometer are presented. At the end a

possible setup for an advanced PPA is given.

## 5.1 Power needed for online calibration

To do an online calibration of the GEO 600 detector, a permanent injection of at least five calibration lines is necessary. A calibration line is produced by a defined longitudinal displacement of one or two main mirrors of the interferometer at a fixed frequency leading to a differential length change of the interferometer at that frequency. The calibration converts the measured differential length change of the interferometer to the corresponding apparent gravitational wave strain. The GEO 600 calibration scheme samples the injected lines once per second. As the signal-to-noise ratio (SNR) of the lines contributes to the overall calibration accuracy, the SNR of the lines needs to be chosen to allow the desired calibration accuracy. For a calibration accuracy of the order of 1%, an SNR of approximately 100 in a 1 s long fast Fourier transform (fft) is necessary. For a detailed description of the calibration process see [25].

As described in section 3.2, a PPA can be used to apply a force directly to one or two of the main mirrors at GEO 600. The force, and thus the displacement of the mirrors, is proportional to the power reflected by the mirror (see Equation 3.12). As a light source for the PPA, a current pumped laser diode is used. To produce a calibration line at a certain frequency, the pump current of the laser diode is modulated at that frequency. For a mirror suspended as a pendulum the force applied to the mirror is proportional to  $1/\omega^2$  for excitation frequencies well above the pendulum resonance frequency. Here  $\omega = 2\pi f$ , where  $f$  is the excitation frequency (see Equation 3.14). For calibration lines at high frequencies, more power is needed to achieve the same longitudinal displacement as for calibration lines at lower frequencies.

In the following, the power needed to produce five calibration lines at 200, 400, 600, 800, and 1000 Hz with a SNR of 100 is determined for a PPA applied to one of the far mirrors under normal incidence for the GEO 600 design sensitivity [86]. For this calculation, various factors need to be taken into account. First of all, the noise at the design sensitivity needs to be converted from amplitude spectral density to amplitude spectrum (see Appendix C). The factor for this transformation depends on the sample rate (SR) with which the data is taken, the length  $N$  of the data segment over which one fft is performed for the online calibration, and the window  $\text{win}_n$  that is used to obtain the amplitude spectral density. The factor needed for the transformation from amplitude spectral density to amplitude spectrum is given by the square root of Equation C.4, which corresponds to

$$\frac{\sqrt{\text{SR} \sum_{n=1}^N \text{win}_n^2}}{\sum_{n=1}^N \text{win}_n}.$$

It also needs to be considered that the fft gives the rms-value (which is equivalent to the DC power in a signal, see section C.2) of each Fourier component. To determine the power needed for a peak-to-peak (pp) excursion by the PPA, the noise spectrum needs to be multiplied by  $2\sqrt{2}$  (see section C.2). Then the gravitational wave amplitude strain,  $h$ , is converted into mirror displacement according to Equation 1.1 for a Michelson inter-



ferometer. For the far mirrors, an additional factor of 2 needs to be taken into account, as the laser beam is folded in the interferometer arms and hits the far end mirrors twice per round trip (see Appendix G for the optical layout of GEO 600). The actual power needed to achieve the desired mirror displacement is then given by Equation 3.14.

In Appendix D, the matlab script is given that was used to calculate the needed power for the described online calibration. One input to the calculation is the design sensitivity curve of GEO 600 [87]. When GEO 600 reaches its design sensitivity, a reflected modulated laser power of 2.9 W is needed to produce the calibration lines described above. For this calculation a mirror mass of 5.32 kg, a SR of 16384 Hz, an integration of 1 s for the fft, and the usage of a Hanning window were assumed. Due to a necessary threshold current and nonlinearities for high modulation depths, the total power of a laser diode cannot be used for modulation. Therefore it is assumed that approximately 80% of the total power of the laser diode can be used for modulation. Thus, a laser diode with at least 3.5 W is needed. This does not take into account the fact that not all of the power will be reflected at the interferometer main mirror. If the phase relation between the calibration lines is chosen in an advantageous way, the total maximal power that needs to be modulated at one time can be reduced. The factor that can be gained from a defined fixed phase between the calibration lines is of the order two.

The high reflectivity of the interferometer main mirrors is specified for wavelengths from approximately 980 nm to 1190 nm for light under normal incidence. The current PPA is a laser diode with 980 nm wavelength. Due to the availability of laser diodes and high-power fibre-coupled laser diodes at 980 nm, the wavelength for an advanced PPA is also chosen to be 980 nm.

## 5.2 Theoretical accuracy

In this section the theoretically achievable accuracy of a PPA is investigated. First it is shown that Equation 3.14 is a very good approximation for the pendulum transfer function when using a PPA. Thus, the accuracy of the PPA depends on how well the parameters in Equation 3.14 can be determined. These are the reflected power,  $P$ , at the interferometer main mirror, the mirror mass,  $m$ , and the modulation frequency,  $f$ . As the modulation frequency of the injected lines is locked to the same frequency standard as that used to drive the acquisition process of signals, the error on  $f$  is negligible. Therefore only the reflected power,  $P$ , and the mirror mass,  $m$ , are investigated in detail. For the accuracy of the PPA it also needs to be considered if shining a power-modulated laser beam onto an interferometer main mirror leads only to longitudinal displacement and if so, whether it is only via the transferred photon impulse. The effect of apparent longitudinal displacement due to rotation (pitch and yaw) excited by photon pressure is investigated. Also the effect of thermally induced length changes by a power modulated laser beam is estimated. At the end of this section the various effects are compared quantitatively.

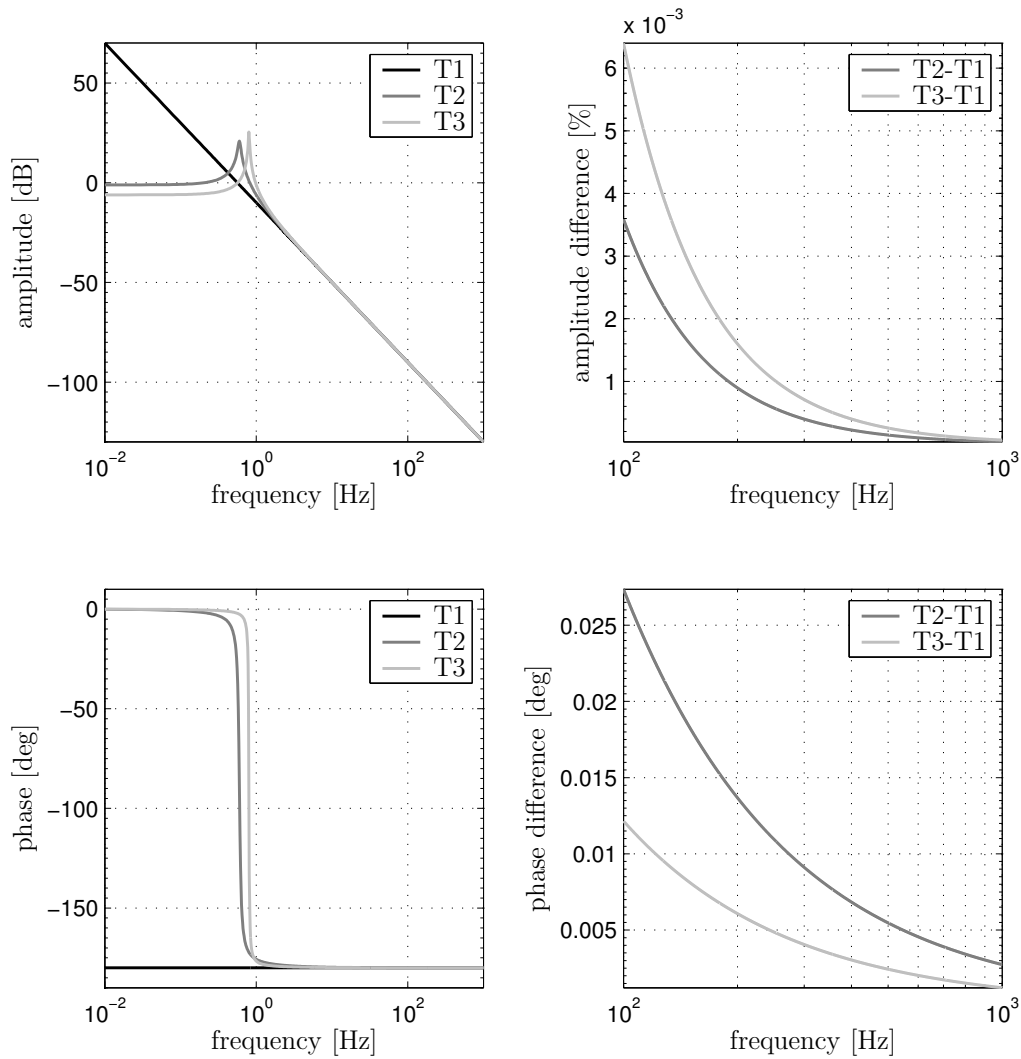


**Figure 5.1:** Graphical display of the investigation of the approximated transfer function accuracy from applied light power to the centre of a mirror to its longitudinal displacement. T1 is calculated according to Equation 3.14. T2 and T3 are calculated according to Equation 3.13, where T2 has a resonance frequency of  $f_0=0.6$  Hz and a quality factor of  $Q=2$ . T3 has a resonance frequency of  $f_0=0.8$  Hz and a quality factor of  $Q=6$ . For all transfer functions the mass, the laser power and the speed of light were set to 1 kg, 1 W, and 1 m/s respectively. In the upper left-hand graph the amplitude is plotted for all three transfer functions. In the upper right-hand graph the difference between the amplitudes of T2 and T1, and T3 and T1 is plotted and expressed in percent of the amplitude of T1. In the lower left-hand graph the phase is plotted for all three transfer functions. In the lower right-hand graph the difference between the phases of T2 and T1, and T3 and T1 is plotted in degree. The phase of T1 was chosen to be  $-180^\circ$  to compare with the pendulum response phase, which approaches  $180^\circ$  well above the resonance frequency  $f_0$ .

### 5.2.1 Pendulum transfer function

In subsection 3.2.2, the transfer function from externally applied radiation pressure to the centre of a mirror (suspended as a pendulum), to its longitudinal displacement, is given. In Equation 3.13 the transfer function is given for all frequencies. In Equation 3.14, the transfer function is approximated for frequencies well above the resonance frequency of the pendulum. The transfer function for the PPA will only be needed for frequencies well above the resonance frequency. This is the frequency range over which the calibration lines are injected (200 Hz to 1 kHz). The PPA cannot be used to move one of the main mirrors through at least two adjacent dark fringes (for this a longitudinal displacement of 266 nm for the far mirrors is necessary), as this would require a total power of at least 125 W. Therefore the exact knowledge of the DC gain of the transfer function and thus of the resonance frequency of the pendulum does not play a role for the accuracy of the PPA, as it is not used at low frequencies. Nevertheless, Equation 3.13 and Equation 3.14 differ. In the following paragraph, the difference between the two transfer functions is calculated for different resonance frequencies,  $f_0$ , and quality factors,  $Q$ , of the pendulum.

The difference is estimated in the following way. One transfer function, T1, is computed with Equation 3.14. Two other transfer functions, T2 and T3, are computed according to Equation 3.13, where T2 has the parameters  $f_0=0.6$  Hz and  $Q=2$ , and T3,  $f_0=0.8$  Hz and  $Q=6$ . The upper and lower limits of  $f_0$  and  $Q$  correspond to how well those parameters of the inboard mirrors are currently known [67]. The mass, the power, and the speed of light are set to 1 kg, 1 W, and 1 m/s respectively. Then the difference between the amplitudes and the phases of T2 and T1, and of T3 and T1 is taken. The difference above 200 Hz stays below 0.0065 % for the amplitude and below 0.03 degree for the phase, as can be seen in Figure 5.1. Therefore the error due to the approximation of the pendulum transfer function is negligible.

The end mirrors are actually suspended as triple pendulums with multiple wires. It is unknown if the coupling between the different pendulum modes of the suspension play a role at frequencies above 200 Hz. It is also not clear if the transfer function of the actual suspension deviates from the transfer function of a simple pendulum. Currently there is no appropriate simulation to model this aspect of the suspensions [88]. Therefore all considerations concerning the accuracy of the PPA due to the simplification of the mirror suspension are neglected.

### 5.2.2 Absolute intensity measurement

To measure the power reflected by the interferometer main mirror with an accuracy of 1 %, it needs to be made sure that no power is lost in the beam path due to cutting off the beam, and also that the photodiode used for the absolute intensity measurement has an accuracy of 1 % or better. A Gaussian laser beam has more than 99.5 % of its total power in the area where the intensity of the beam reduces to 1 %. If an absolute intensity measurement better than 1 % is aimed for, it needs to be made sure that the beam is not cut off within the area where the beam is equal or above 1 % of its maximal intensity. Therefore the aperture of the beam path needs to be chosen carefully.

At the PTB<sup>1</sup> in Braunschweig, a method based on Fourier transform spectroscopy has been developed to calibrate silicon photodiodes from 200 nm to 1000 nm with an uncertainty of 0.05 % within 10 minutes [89]. It needs to be checked whether this is also possible with InGaAs photodiodes, which might be used instead of silicon photodiodes. As the response of a photodiode is temperature and wavelength dependent, the photodiode and laser diode need to be temperature stabilised.

It is known that the response of a photodiode is not perfectly flat over its active area [90]. Therefore, the accuracy of the absolute power calibration of a photodiode given above as 0.05 % can only be reproduced if a beam with the same size hitting the same area on the photodiode is used as the one with which the calibration was performed. This is typically not possible. To estimate the effect of the changing response of the photodiode over its active area a simulation with measured data was done.

The measured data were provided by Michael Tröbs from the Laser Zentrum Hannover. The data give the response of a photodiode over its active area with a resolution of  $10\ \mu\text{m} \times 10\ \mu\text{m}$  at the wavelength 1058.25 nm. The beam diameter on the photodiode was approximately  $20\ \mu\text{m}$  for the measurement. Possible photodiodes for the PPA with a wavelength of 980 nm are the G8605-15 InGaAs photodiode from Hamamatsu with a diameter of 5 mm and the IPL10050 silicon photodiode from Integrated Photomatrix Ltd. with an active area of approximately  $6\ \text{mm} \times 6\ \text{mm}$  [91, 92]. In Figure 5.2 the measured intensity response of these photodiodes over their active area is given in percent of their maximal response. It can be seen that the response decreases significantly towards the edges of the active area. Although the measurement was done at 1058.25 nm, the data can be used to simulate the error for an absolute power measurement at 980 nm, as the slope of the photo sensitivity of silicon and InGaAs is approximately the same at 1058.25 nm and 980 nm.

From Figure 5.2 it is clear that if a Gaussian laser beam changes its position on the active area of the photodiode the total measured power changes. The intensity profile of a simulated Gaussian laser beam was convoluted with the measured response of the photodiodes. The position of the laser beam was changed in steps of  $100\ \mu\text{m}$  on the surface of the photodiode. The simulation was done for beam diameters of 0.92 mm, 1.84 mm, and 3.04 mm. The beam diameter here is defined by the points where the intensity of the beam dropped to below 1 % of its maximal intensity. In Figure 5.3, the results of the simulation with the measured data are presented for the silicon and InGaAs photodiode. The plots show the differences between the simulated measured power for the laser beam position at position (0,0) and the simulated measured power for the laser beam at positions  $(x, y)$ . Above a certain threshold the differences were set to zero in order to use the full dynamic range of the colour plot for differences of the order 1 %. For the silicon photodiode roughly over a range of  $4\ \text{mm} \times 3\ \text{mm}$  into the  $x$ - or  $y$ -direction, respectively, the absolute power changes by less than 1 %. For the InGaAs photodiode roughly over a range with the diameter 2 mm the absolute power changes by less than 1 %.

It can be seen that the beam diameter can be optimised to allow maximal offsets in the  $x$ - and  $y$ -direction while staying below the 1 % deviation in absolute power mea-

---

<sup>1</sup>The PTB is the German national metrology institute.

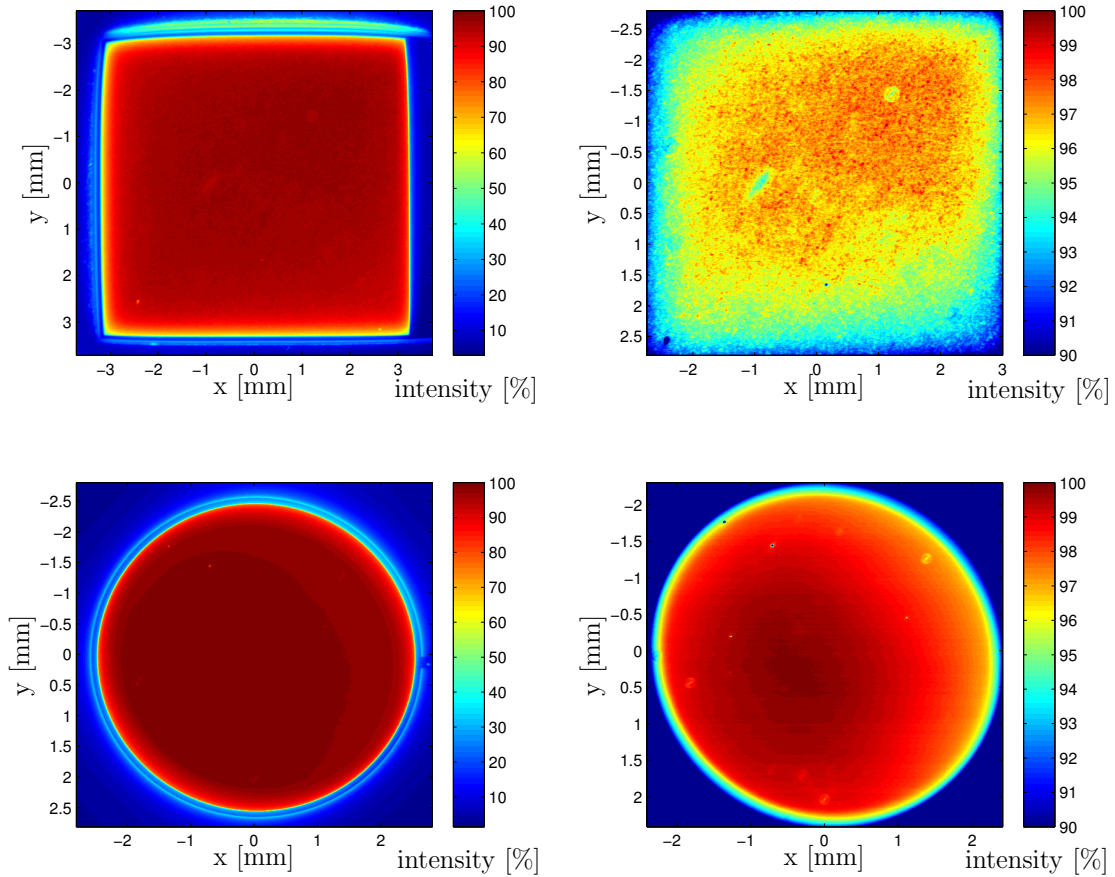


**Figure 5.2:** Measured response of a photodiode over its active area. The response is given in percent, where 100% correspond to the maximal measured response of the photodiode. The measurements were done with a resolution of  $10\ \mu\text{m} \times 10\ \mu\text{m}$  at the wavelength  $1058.25\ \text{nm}$  with a beam diameter of approximately  $20\ \mu\text{m}$  on the photodiode. The upper graphs give the response of an IPL10050 silicon photodiode from Integrated Photomatrix Ltd. with a quadratic active area of approximately  $6\ \text{mm} \times 6\ \text{mm}$ . The lower graphs give the response of a G8605-15 InGaAs photodiode from Hamamatsu with a circular active area with a diameter of  $5\ \text{mm}$ . In the right-hand graphs a zoom of the area where the intensity is between 90-100 % is given. For these plots the intensity was set to 90 % for all values below 90 %, to use the full dynamic range of the colour bar for the 90-100 % response range. The measured data were provided by Michael Tröbs from the Laser Zentrum Hannover.

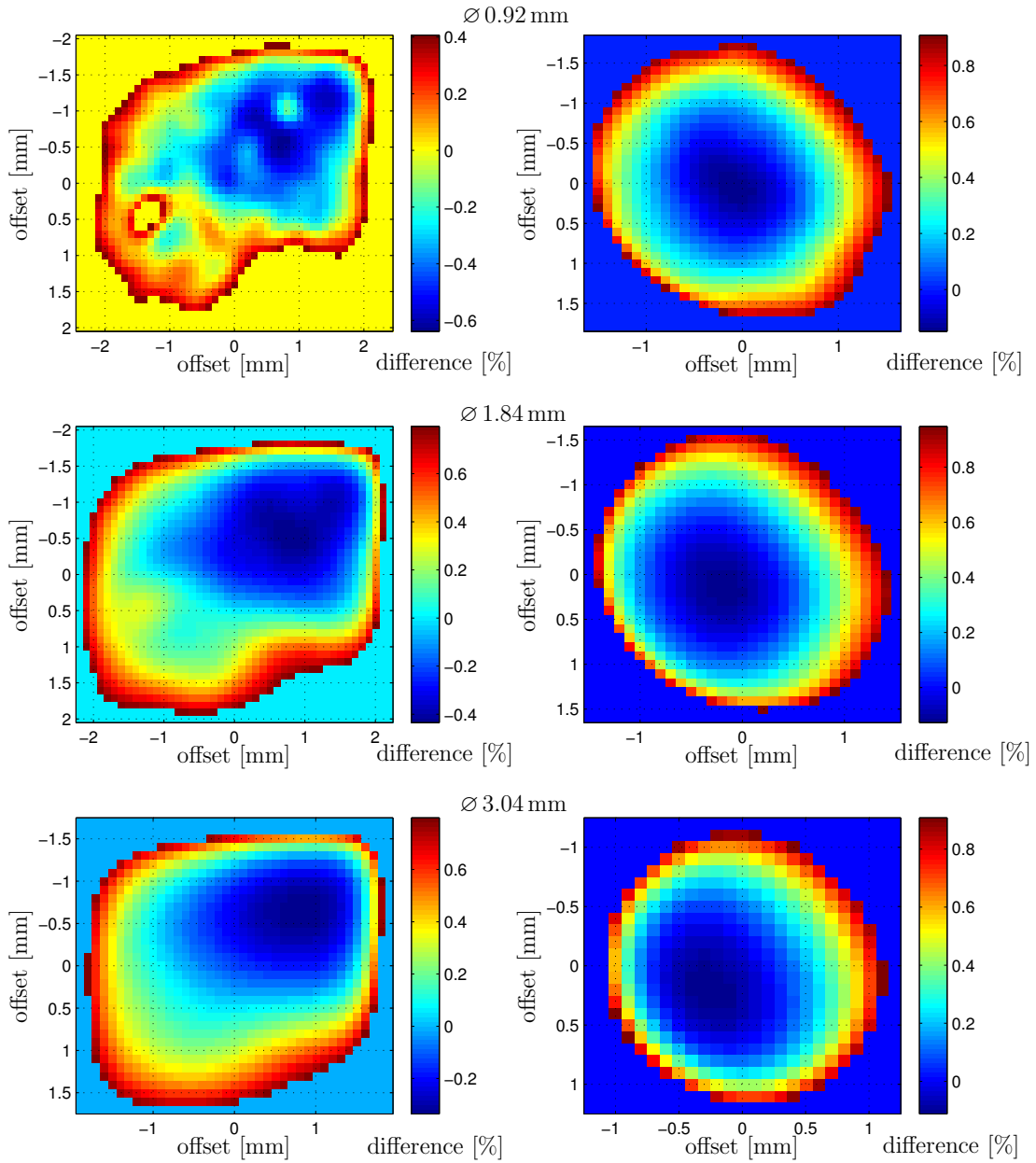


**Figure 5.3:** Differences between the expected measured power of a laser beam at position (0,0) and positions varied in the  $x$ - and  $y$ -direction on the active area of a photodiode. The plots were produced by convolving a simulated Gaussian laser beam with the measured data given in Figure 5.2. Above a certain threshold the differences were set to zero in order to use the full dynamic range of the colour plot for differences of the order 1%. In the upper graphs the laser beam had a diameter of 0.92 mm, the graphs in the middle 1.84 mm, and in the lower graphs 3.04 mm. The beam diameter refers to a drop in intensity below 1% of its maximal power. The left graphs show the results for the IPL10050 silicon photodiode. The right graphs show the results for the G8605-15 InGaAs photodiode.

surement. This is expected as a laser beam with a very small diameter can still resolve the graininess of the response of the photodiode. A laser beam with a large diameter covers with relatively small offsets in the  $x$ - and  $y$ -direction areas of the photodiode, where the response is changing rapidly. It is assumed that in principle an absolute power measurement with an accuracy of 1% should be possible if great care is taken in the whole setup and calibration process [93].

### 5.2.3 Determining the amount of reflected power

As mentioned before, only the photons reflected transfer their momentum to the mirror (actually, the photons that are absorbed also transfer their momentum, but with an absorption of 6 ppm/cm in the mirror substrate this effect is negligible [94]). At GEO 600, the main mirrors are situated in a vacuum system. To determine the amount of light reflected by a mirror, the light power leaving the vacuum and the transmittance of the vacuum viewports need to be known.

To measure the light power leaving the vacuum, a fixed amount of light power should be split off from the beam leaving the vacuum. For this, preferably a cube beam splitter or a prism should be used to prevent influences from second-order surface reflections. The ratio with which the beam splitter or prism reflects and transmits can be determined in a relative intensity measurement. For this, an attenuated laser beam can be used. The full dynamic range of the photodiode should not be used for this measurement to prevent a change in temperature of the photodiode through high power dissipation (a ratio of the order of 99:1 is desired). The more robust solution is probably a prism, as its temperature dependence should be smaller than that of a cube beam splitter.

Besides the light power leaving the vacuum, the transmittance of the vacuum viewport needs to be known. Theoretically the transmittance of the viewport can be measured very accurately with a relative intensity measurement. The accuracy of such a measurement is assumed to be 0.1%. Thus the absolute light power reflected at the interferometer main mirror is theoretically measurable with an accuracy of at least 1.1%. This includes an error of 0.1% for passing of the viewport and 1% for the absolute intensity measurement.

### 5.2.4 Mirror mass

The accuracy of the PPA also depends on how accurate the mass of the main mirror is known, to which the photon pressure is applied. Theoretically, the mirror mass can be determined with a commercially available scale to an accuracy of 0.1%. None of the currently suspended far mirrors (see mirror far North (MFN) and mirror far East (MFE) in Appendix G), were weighed before their installation.

### 5.2.5 Effect of mirror rotation on the mirror's longitudinal displacement

If the beam of the PPA does not hit the main optic exactly centred, a torque is applied. This leads to a rotation,  $\theta$ , of the mirror. The rotation of a cylindrical mirror can lead to apparent longitudinal displacement of the mirror. The axis perpendicular to the surface of a cylindrical mirror through its centre of mass is referred to as the optical

axis (the equivalent to the  $x$ -axis in Figure 3.10). Movements along this axis are called longitudinal displacements  $x_d$ . In the following paragraphs, the relationship between mirror rotation,  $\theta$ , and apparent longitudinal displacement,  $x_d$ , is derived. A rotation,  $\theta$ , of the mirror around its axis of symmetry, parallel to the flat surfaces of the cylindrical mirror, leads to a longitudinal displacement,  $x_d$ , if the thickness,  $d$ , of the mirror is non-zero. From Figure 5.4 one can see that

$$\begin{aligned} \cos \theta &= \frac{\frac{d}{2}}{\frac{d}{2} + x_d} \\ \Leftrightarrow x_d &= \frac{d}{2} \frac{1 - \cos \theta}{\cos \theta} \\ \text{for } \theta \ll 1 \quad \Rightarrow \quad x_d &\approx \frac{d}{4} \theta^2 . \end{aligned} \tag{5.1}$$

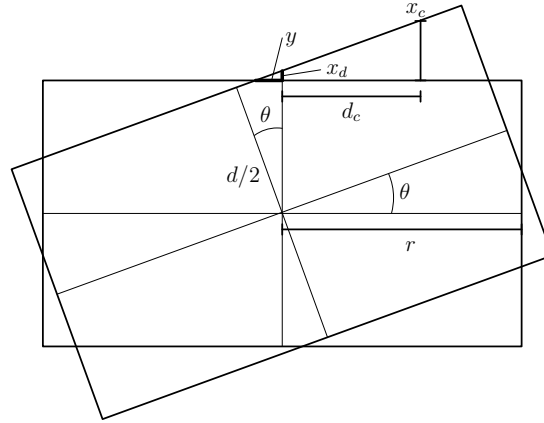


**Figure 5.4:** Schematic of the effect of rotation on the longitudinal displacement of a cylindrical mirror.

This formula is only valid for

$$\theta \leq \arccos \left( \frac{d}{\sqrt{2r^2 + d^2}} \right) , \tag{5.2}$$

where  $r$  is the radius of the mirror. Figure 5.5 shows the longitudinal displacement  $x_d$  in dependence of  $\theta$  for a GEO 600 main optic with thickness  $d = 10$  cm and radius  $r = 9$  cm.

As the longitudinal displacement,  $x_d$ , due to the thickness of the mirror scales with  $\theta^2$ , the effect is very small. As can be seen in Figure 5.4, the longitudinal displacement,  $x_c$ , at distance,  $d_c$ , away from the centre of the mirror due to rotation is larger than  $x_d$ . With  $y = x_d / \tan \theta$ , the longitudinal displacement,  $x_c$ , at the distance,  $d_c$ , away from



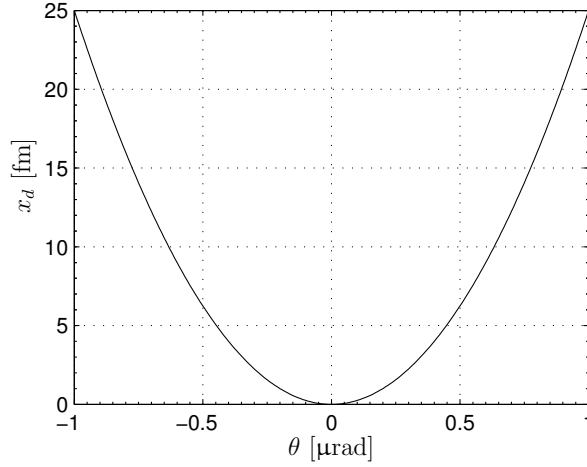


**Figure 5.5:** Plot of apparent longitudinal displacement of a GEO 600 main mirror as a function of its rotation. The mirrors have a thickness of  $d = 10$  cm and a radius of  $r = 9$  cm. The apparent longitudinal displacement is the displacement of the mirror centre along its optical axis.

the centre is given by

$$\begin{aligned} \tan \theta &= \frac{x_c}{d_c + y} \\ \Leftrightarrow x_c &= d_c \tan \theta + x_d \\ \text{for } \theta \ll 1 \quad \Rightarrow \quad x_c &\approx d_c \theta + \frac{d}{4} \theta^2. \end{aligned} \quad (5.3)$$

Since for  $x_c$ , the longitudinal displacement scales with  $\theta$ , the effect is much bigger than for  $x_d$ .

The rotation  $\theta$  that is induced by the beam of the PPA if the beam does not hit the main optic exactly centred, can be quantitatively described with the calculations performed in chapter 3. When inserting Equation 3.12 into Equation 3.6 the angle  $\theta$  is given by

$$\theta(\omega) = \frac{2Pd_c}{c(I\omega^2 - i\gamma\omega - \kappa)}. \quad (5.4)$$

Here it can be seen that the further away from the centre the beam hits the main mirror, the bigger is the resulting rotation. How big the apparent longitudinal displacement is, as seen by the main interferometer due to this rotation, depends on how well the interferometer beam is centred on the main mirror.

In the above calculation, the assumption was made that if a main mirror experiences a torque produced by the PPA, the resulting rotation can be split into a rotation about the mirror's axis of symmetry, perpendicular to the ground, and parallel to the ground (which correspond to the  $z$ - and  $y$ -axis in Figure 3.10, respectively). Thus the distance  $d_c$  at which the mirror is hit away from its centre is split into a distance parallel and perpendicular to the ground. It is unclear if this is a good approximation. The main

main mirrors (fused silica)			
$\rho$	$2.2 \times 10^3$	$[\text{kg m}^{-3}]$	density
$C$	772	$[\text{J kg}^{-1}\text{K}^{-1}]$	specific heat capacity
$\kappa$	1.4	$[\text{W m}^{-1}\text{K}^{-1}]$	conductivity
$\alpha_{\text{ab}}$	6	$[\text{ppm/cm}]$	absorption coefficient
$\alpha_{\text{ex}}$	$5 \times 10^{-7}$	$[\text{K}^{-1}]$	expansion coefficient
$d$	10	$[\text{cm}]$	mirror thickness

**Table 5.1:** Material properties of the main mirrors, which are made of fused silica.

mirrors are suspended by wires that break off at the mirror 1 mm above its centre of mass (see section 3.6 [80]). As already mentioned for the case of the longitudinal transfer function in subsection 5.2.1, in particular no appropriate simulation to model this aspect of the suspension exists.

### 5.2.6 Temperature distribution in a mirror illuminated by a modulated laser beam

At GEO 600 the modulated laser light is applied to one of the far mirrors through the viewport (see Figure 5.8). As the high reflective coating of the mirror is on the inside of the interferometer, the light of the PPA passes twice through the mirror substrate. By modulating the light, the heat deposited in the optic is also modulated. This can lead to a time-dependent temperature distribution and thus a time-dependent length change due to the temperature dependent expansion. In the following paragraphs, a rough estimation of the order of magnitude of this length change (which is indistinguishable from longitudinal displacements) is made.

For the calculations, the assumption was made that the vacuum and the mirror extend infinitely in the radial direction. Therefore, the calculation is applicable when the laser beam is much smaller than the radial dimension of the mirror, and the thermal length of the mirror substrate is less than the mirror dimension for the used modulation frequencies. The estimation is based on the theory of photothermal deflection spectroscopy [95].

The temperature distribution can be derived via the diffusion equation

$$\nabla^2 T(\mathbf{r}, t) - \frac{1}{k} \frac{\partial T(\mathbf{r}, t)}{\partial t} = -\frac{Q(\mathbf{r}, t)}{\kappa}, \quad (5.5)$$

with the thermal diffusivity  $k$

$$k = \frac{\kappa}{\rho C}. \quad (5.6)$$

Here,  $T(\mathbf{r}, t)$  gives the temperature rise above the ambient temperature at  $\mathbf{r} = (x, y, z)$ ,  $\kappa$  is the conductivity,  $\rho$  the density,  $C$  the specific heat capacity,  $z$  the propagation direction of the laser beam, and  $Q(\mathbf{r}, t)$  the heat deposited per unit volume and time in the absorbing medium. In the vacuum, no heat is deposited, therefore  $Q(\mathbf{r}, t)$  is zero in

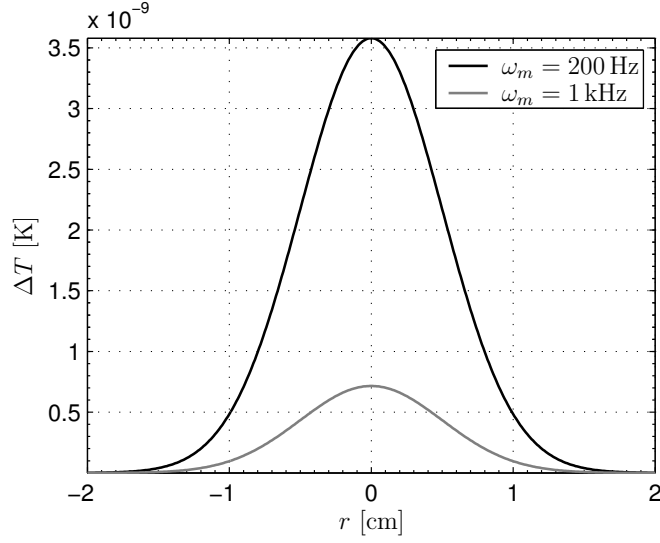


**Figure 5.6:** Temperature change induced in a main mirror by a modulated laser beam traversing orthogonally back and forth. The graphs for two different modulation frequencies are given. It is assumed that the input laser beam has a radius of  $1/e^2$  of 1 cm and is modulated with 1 W peak-to-peak change in light power. The material properties given in table 5.1 were used for the calculation.

this region. In the substrate, for a sinusoidally power modulated Gaussian laser beam,  $Q(\mathbf{r}, t)$  is given by

$$Q(\mathbf{r}, t) = 2 \frac{P}{\pi a^2} \exp\left(-\frac{2r^2}{a^2}\right) \cos(\omega_m t) \exp(-\alpha_{ab} z), \quad (5.7)$$

where  $P$  is the modulated power,  $r = \sqrt{x^2 + y^2}$ ,  $\alpha_{ab}$  is the absorption coefficient,  $\omega_m$  the angular modulation frequency and  $a$  is the  $1/e^2$  radius of the Gaussian laser beam. As  $z$  is the propagation direction of the laser beam, the term  $\exp(-\alpha_{ab} z)$  describes the absorption along the propagation. The term  $\cos(\omega_m t)$  gives the modulation depth at time  $t$ . The remaining term describes the Gaussian power distribution. With 1.1.3.4 (3.) of [51] it can be seen that

$$\begin{aligned} & \int_{-\infty}^{\infty} dx \int_{-\infty}^{\infty} dy \ 2 \frac{P}{\pi a^2} \exp\left(-\frac{2(x^2 + y^2)}{a^2}\right) \\ &= 8 \frac{P}{\pi a^2} \int_0^{\infty} dx \int_0^{\infty} dy \ \exp\left(-\frac{2(x^2 + y^2)}{a^2}\right) \\ &= 8 \frac{P}{\pi a^2} \left(\frac{\sqrt{\pi}}{2} \frac{a}{\sqrt{2}}\right)^2 \\ &= P. \end{aligned} \quad (5.8)$$

In [95], a special case is considered where the distribution is decomposed into distributions that act independently of each other and show a radially uniform temperature

distribution. The effective thermal length,  $l_{\text{th}}$ , of that distribution is given by

$$l_{\text{th}} = \sqrt{\frac{\kappa}{\rho C} \frac{2}{\omega_m}}. \quad (5.9)$$

With the properties for fused silica listed in Table 5.1, this gives an effective thermal length for the main mirrors of  $3.6 \times 10^{-5}$  m for modulations at 200 Hz and  $1.6 \times 10^{-5}$  m for modulations at 1 kHz. If the heat diffusion into the vacuum is neglected and the thermal length,  $l_{\text{th}}$ , is much smaller than the beam profile, the temperature distribution integrated along the  $z$  direction can be described by (Equation (13) of [95])

$$\int_0^d dz T(\mathbf{r}, t) = 2P \frac{[1 - \exp(-\alpha_{\text{ab}} d)]}{\pi \omega_m \rho C a^2} \exp\left(\frac{-2r^2}{a^2}\right) \sin(\omega_m t), \quad (5.10)$$

where  $d$  is the thickness of the mirror. The temperature distribution follows the beam profile because there is no diffusion of heat. The maximal difference in temperature,  $\Delta T$ , is then given by

$$\Delta T = \frac{4}{d} P \frac{[1 - \exp(-\alpha_{\text{ab}} d)]}{\pi \omega_m \rho C a^2} \exp\left(\frac{-2r^2}{a^2}\right). \quad (5.11)$$

In Figure 5.6, the temperature change in a mirror with the material properties given in Table 5.1, for a modulation frequency of  $f_m = 200$  Hz and  $f_m = 1$  kHz, are plotted for a PPA beam with a modulated power of  $P = 1$  W and a beam radius  $a = 1$  cm, where  $f_m = 2\pi\omega_m$ . In the case of the lower modulation frequency, the effective thermal length is larger, which leads to the situation that the area over which a temperature change against the ambient temperature takes place, is larger. This temperature change can be transformed into a length change of the (by the PPA beam) illuminated part of the mirror

$$\Delta L = \alpha_{\text{ex}} d \Delta T, \quad (5.12)$$

where  $\alpha_{\text{ex}}$  is the expansion coefficient of the mirror substrate. This is only an approximated value, as it is assumed that the cylindrical part in the mirror that is illuminated by the PPA beam can expand independently of the surrounding material (see Figure 5.7). The generated stress in the material due to the expansion is neglected. The approximated maximal length change on one side of a far mirror, for  $P = 1$  W of modulated laser power and a beam radius  $a = 1$  cm, is then  $8.9 \times 10^{-17}$  m at 200 Hz and  $1.8 \times 10^{-17}$  m at 1 kHz. This is of an order which is significantly larger than the relative length change detectable by GEO 600 [86]. It should be kept in mind though, that this maximal longitudinal displacement due to temperature changes is an upper limit and the length change is only at a single point on the mirror surface. The displacement drops to zero over the area which is illuminated by the PPA beam and is zero outside the illuminated area (see Figure 5.7). The area illuminated by the PPA beam is significantly smaller than the total area of the mirror surface. Thus the wave front of the interferometer laser beam will average over this single, maximal, longitudinal displacement. In contrast to this the longitudinal displacement due to the momentum transfer by the PPA displaces the total mirror and not only a single point on the mirror surface. This should be

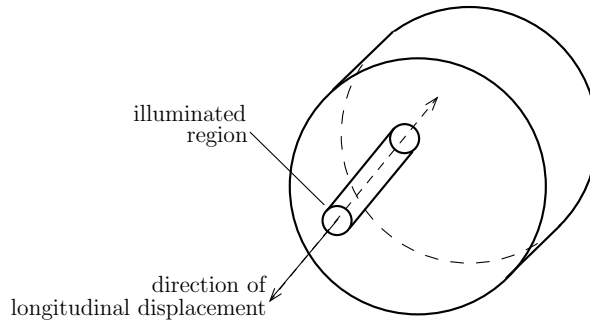


**Figure 5.7:** Example for a region of a main mirror which is illuminated by the PPA. The small cylinder within the mirror is the area where time dependent temperature change will take place due to the modulated laser beam of the PPA. This temperature change can result in an expansion of this area in the direction along the optical axis of the main interferometer, and thus lead to an undesired longitudinal displacement of the mirror surface.

kept in mind when comparing the values given for the longitudinal displacement due to momentum transfer by the PPA and thermally induced length changes.

When comparing Equation 3.14 with Equation 5.11 it can be seen that the longitudinal displacement due to the photon pressure is proportional to  $1/\omega^2$  and the longitudinal displacement due to temperature changes is proportional to  $1/\omega$ . Therefore the portion of the longitudinal displacement due to temperature changes of the total longitudinal displacement becomes larger for higher frequencies.

### 5.2.7 Quantitative comparison of photon pressure actuator accuracy

If great care is taken with the setup of the PPA, an accuracy of the order of a few percent should be possible. For a setup with high accuracy, the following points need to be taken care of. The optical properties of all optical components involved in the PPA, such as the main optics and viewports, need to be measured independently of each other at the PPA wavelength. The photodiodes used in an advanced setup (see Figure 5.13), need to be calibrated with high accuracy. Then their response over their active area needs to be measured and it needs to be determined in which area the Gaussian laser beam of the PPA should hit the photodiode so that the error of the absolute power measurement stays below 1%. The photodiodes need to be temperature stabilised. A laser diode with high power (of the order of a few Watts) should be used to allow high signal-to-noise ratios at high frequencies. The laser diode should be temperature stabilised, to guarantee a constant wavelength of the PPA laser beam. The mass of the interferometer main mirror to which the PPA is applied needs to be measured. For high accuracy the pendulum transfer function of the main optic, suspended as a triple pendulum, should be studied in detail to investigate if modes other than the longitudinal displacement are excited by the PPA. Also a finite element analysis should be made to determine the thermally excited expansion of the coating material at the excitation frequencies of the PPA, as the upper limit for the longitudinal displacement due to

a thermal length change is only one order of magnitude below the direct longitudinal displacement (see Table 5.3). The remaining crucial issue is how well the PPA can be centred on the main mirror to prevent rotational excitation which leads to apparent longitudinal displacement.

For the previously described effects of apparent longitudinal displacement due to rotation and thermally excited length change, values were calculated. For the PPA, a modulated laser beam with 1 W peak-to-peak change in light power was assumed and a  $1/e^2$  beam radius of 1 cm on the mirror surface. The material properties of the mirror are given in Table 5.1. The geometric mirror properties and the mass used for the calculation are given in Table 5.2. The calculations were done for 200 and 1000 Hz. In Table 5.3, the direct longitudinal displacement and the upper limit of the thermally induced expansion is given. Also listed is the rotational excitation of the mirror if it is hit by the PPA 1 cm away from its centre. The resulting rotation is converted into apparent longitudinal displacement of the mirror at the centre and 1 cm away from the centre.

main mirrors		
$d$	10 cm	mirror thickness
$r$	9 cm	mirror radius
$d$	5.32 kg	mirror mass

**Table 5.2:** Geometric properties and mass of main mirrors.

### 5.3 Current photon pressure actuator

The current PPA is setup in the North end building. As a light source a multi-mode, 1 W laser diode from Thorlabs with wavelength 980 nm is used. The laser diode is a single-stripe emitter with a beam divergence of  $8^\circ$  and  $40^\circ$  which is collimated with a cylindric lens. 2 m away from the emitter the beam size is approximately  $5 \times 5 \text{ mm}^2$  (the beam size was estimated by eye using an IR viewing card). The total power in the collimated laser beam is approximately 500 mW. The laser beam is shone under an angle of approximately  $4^\circ$  onto the mirror far North (MFN) (see Figure 5.8). The incoming power to the interferometer main mirror is measured on a photodiode behind the first mirror redirecting the laser beam. The light power returning from the interferometer main mirror is shone directly onto a power meter.

In the following sections, the accuracy of the current PPA is estimated. Then first measurements with the PPA are presented and some conclusions to these measurements are drawn.

#### 5.3.1 Accuracy of the current photon pressure actuator

The transmittance of the viewport and the reflectivity of the main mirror were not measured with high accuracy at 980 nm before they were built into the vacuum system.

frequency	longitudinal displacement			rotational excitation due to radiation pressure torque if the mirror is hit 1 cm off its centre		
	momentum transfer	upper limit of thermally induced length change		apparent displacement due to rotational excitation		
		substrate	coating	centre	1 cm off centre	
200 Hz	$7.9 \times 10^{-16}$ [m]	$1.8 \times 10^{-17}$ [m] (2.3 %)	$2.1 \times 10^{-17}$ [m] (2.7 %)	$3.9 \times 10^{-32}$ [m]	$2.8 \times 10^{-17}$ [m] (3.5 %)	$2.8 \times 10^{-15}$ [rad]
1 kHz	$3.2 \times 10^{-17}$ [m]	$3.6 \times 10^{-18}$ [m] (11 %)	$4.3 \times 10^{-18}$ [m] (13 %)	$6.2 \times 10^{-35}$ [m]	$1.1 \times 10^{-18}$ [m] (3.4 %)	$1.1 \times 10^{-16}$ [rad]

**Table 5.3:** Quantitative comparison of the effects that lead to longitudinal displacement and apparent longitudinal displacement. All values were calculated with the material properties of the mirror given in Table 5.1 and the geometric mirror properties and mass given in Table 5.2 for 1 W of modulated laser power and a beam radius of 1 cm on the mirror surface. The rotational excitation due to radiation pressure torque is calculated for the case where the PPA hits the main mirror 1 cm off its centre. The apparent longitudinal displacement due to rotational excitation is given at the centre off the mirror and 1 cm off its centre for the case that the PPA hits the mirror 1 cm off its centre. The given longitudinal displacement due to a thermally induced length change is a conservative upper limit for the expected longitudinal displacement. This upper limit gives the displacement where the laser beam of the PPA is at its maximal power. The numbers in brackets are the upper limits in percent of the momentum transfer.

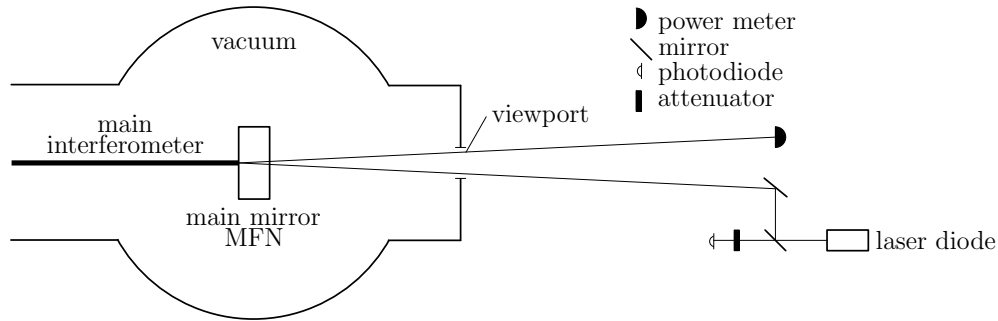


**Figure 5.8:** Current setup of the PPA measurement.

Therefore the largest uncertainty of the current PPA setup lies in the reflected light power at the main mirror. To estimate this uncertainty the error of the reflectivity of the main mirror and the losses at the viewport need to be determined. 980 nm fall on the edge of the wavelength range of the highly reflective coating of the main mirrors for normal incidence. For the main mirrors, measured data for the wavelength dependent reflectivity of the coatings provided by the coating company are available. From that data, the reflectivity at 980 nm of the far end mirrors is  $0.998 \pm 0.5\%$ .

For the current viewports (which have an anti reflective coating), only a measurement of the reflectivity of one viewport is available from the batch when the currently used viewports were coated by the company LASEROPTIK (see Appendix E). According to this measurement the reflectivity of the coated viewport at 980 nm is approximately 0.2%. The anti-reflective coating of the viewports was designed for 1064 nm. No measurements of the losses at 980 nm exist for the viewports. To estimate the transmittance of the viewport for the current setup, the following approach is taken. We assume that the same fraction of light power is lost when entering the vacuum as it is when leaving the vacuum. Here the loss at the viewport (reflectivity and absorption) is called  $\alpha_{vp}$ . Then the light power,  $I_{in}$ , entering the vacuum and the light power,  $I_{out}$ , leaving the vacuum is measured. The light power after entering the vacuum is  $(1 - \alpha_{vp}) \times I_{in}$ . With a reflectivity of 0.998 of the main optic the light power is  $0.998 \times I_{in} (1 - \alpha_{vp})^2$  after leaving the vacuum. From this, it can be estimated that the loss at the viewport is

$$\alpha_{vp} = 1 - \sqrt{\frac{1}{0.998} \frac{I_{out}}{I_{in}}}. \quad (5.13)$$

At the beginning of the measurements, the incoming and outgoing absolute power were measured. A loss of 27% on the first day and 28% on the second day between the ingoing and outgoing beam was determined. According to Equation 5.13, this gives a loss of  $\alpha_{vp} = 0.148$  at the viewport. These values suggest that the losses are not only due to reflectivity and absorption of the viewport. Additionally scattering and perhaps too small apertures are suspected to contribute to the losses. Nevertheless for these first measurements the approach is taken in which it is assumed that the same amount of light is lost on the way from entering the vacuum to the main mirror as it is on the way



from the main mirror to leaving the vacuum. This is equivalent to assuming a loss of  $\alpha_{vp} = 0.148$  at the viewport. The absolute power of the outgoing light was measured with a power meter, and the ingoing power was measured with a photodiode which was calibrated with the power meter. The accuracy of the power meter is of the order 5%. Thus the transmittance at the viewports for the current setup is only known with an error of approximately 10%.

The modulated power was determined by looking at the amplitude of the photodiode signal on an oscilloscope. The laser diode was modulated over a range of about 95%. From earlier measurements in Hannover, it is known that approximately 10% of the modulation at such a modulation depth are in the first harmonic. During all measurements the power level on the photodiode and the power meter were observed by eye. Thus it was made sure that the power stayed about the same. It was seen that there is scattered light on the viewport. This was not taken into account to estimate the error of the measurement.

The currently used main mirror MFN in the setup of the PPA was not weighed before its installation. To determine its approximate mass two spare mirrors were weighed [96], one inboard mirror and one far mirror. Both weighed 5.32 kg. It is not clear with which accuracy a mass of 5.32 kg can be assumed for MFN. The measurement of the spares had an error of  $\pm 20$  g. We assume an error of 1% for the main mirror mass excited in the current setup of the PPA.

The overall error of the current setup of the PPA is assumed to be  $\pm 20\%$ . It is not clear where exactly the PPA beam hits the mirror and how well the interferometer beam was centred on the mirror at that time. As described in subsection 5.2.5 an offset of the main interferometer beam can lead to an additional apparent longitudinal displacement, if rotation is excited by the PPA. Please be aware that neither scattered light nor rotational excitation errors were taken into account. Errors due to this effect are not included in the error bars of the graphs of Figure 5.11 and Figure 5.12, representing the results of the measurements graphically. The error due to the SNR of the injected signal is taken into account. Therefore, the error bars increase with higher frequencies, as the SNRs become lower.

### 5.3.2 First Measurements with the photon pressure actuator

First measurements with the PPA were performed on 17 February 2004 and 19 February 2004 [97]. On 17 February 2004, one measurement was performed at seven frequencies between 161 and 1387 Hz. On 19 February 2004, three measurements were performed, measurement I at seven frequencies between 161 and 1387 Hz and measurement II/III at nine frequencies between 161 and 1815 Hz.

During the measurement on 17 February 2004 and measurement I on 19 February 2004, the beam was approximately parallel to the ground. During measurement I on 19 February 2004 the beam was slightly aligned upwards compared to the beam alignment on 17 February 2004. For measurements II and III on 19 February 2004, the beam was tilted a little upwards and downwards, respectively. When tilting it up for measurement II, the outgoing laser beam was about 5 cm higher than for measurement I approximately 1.20 m away from the viewport (at the the large lens, which images the

interferometer beam onto a CCD camera). When tilting the beam downwards the outgoing beam was about 2.2 cm lower than for measurement I. Tilting the beam further down was not possible as then it was already visibly clipped somewhere. The beam positions on the vacuum viewport were approximately like those given in Figure 5.9.

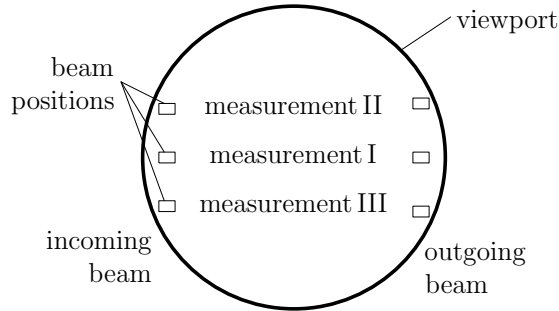


**Figure 5.9:** Positions of the laser beam of the PPA on the vacuum viewport during the measurements on 19 February 2004. The view is directly onto the viewport.

In the  $h(t)$  data, the height of the peaks produced by the PPA were compared to the expected peaks due to the measured power,  $P$ . The  $h(t)$  data had been calibrated with the calibration lines injected by the electrostatic drive (ESD). The error of the ESD is  $\pm 5\%$ . The absolute overall error of the calibration with the ESD is  $\pm 10\%$  for calibration lines with a SNR of approximately 100. For lower SNRs an additional error was added. For this it was assumed that a line with a SNR of 100 has an error of 1%.

In Table 5.4, the measured values of the lines in the  $h(t)$  amplitude spectrum are given. The SNRs are also given for the lines. This table is good for comparing how the signal heights and SNRs varied from measurement to measurement for the different modulation frequencies. The SNR was calculated by determining the average noise around the peak in the spectrum by taking 21 data points below and above the peak into account starting at the third data point away from the peak centre. Shortly before the injection of the line at 1387 Hz during measurement I on 19 February 2004, a small line appeared at 1387.09 Hz with about half the SNR of the later injected line (see Figure 5.10). The injected line is not optimally centred around 1387 Hz as the injection lines are for the other injections. It can be seen that the frequency content of the lower adjacent frequency bin is much higher than the frequency content of the higher adjacent frequency bin. It is unclear if spurious line noise affected the determination of the values of the injected lines in the amplitude spectrum of  $h(t)$ .

In Table 5.5 and Table 5.6, the calculated longitudinal displacements,  $\Delta L$ , due to the applied photon pressure are compared with the measured longitudinal displacements gained with the ESD calibration for 17 February and 19 February, respectively. The measurement on 17 February 2004 was done within 14 minutes. On 19 February 2004 the measurement I was done within 14 minutes, measurement II within 37 minutes and measurement III within 63 minutes. The time stretches for the injections from 161 Hz to 1387 Hz were about the same for all measurements. Between measurement II and measurement III the operating conditions of the interferometer changed (the interferometer

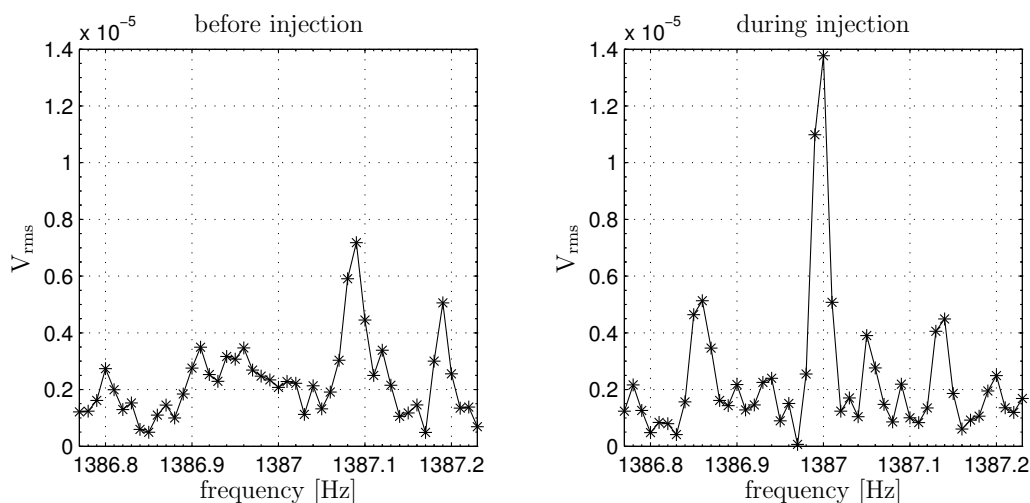


**Figure 5.10:** The left graph shows the amplitude spectrum of the Michelson differential error point around 1387 Hz at 14:07:30 on 19 February 2004. This is shortly before the injection of a line with the PPA at 1387 Hz. The right graph shows the amplitude spectrum around 1387 Hz at 14:09:40, during the injection. In the right graph it can be seen that the injected line is not symmetric about 1387 Hz. This fact was observed during measurement I.

unlocked and the offset of the  $2f$  signal for the locking process was changed).

For alignment behind the North end mirror a quadrant diode and a CCD camera are installed. During the measurements, interference filters were put in front of the quadrant diode and the CCD camera in the North end building to avoid the light from the PPA affecting the signals of the quadrant diode and camera. These interference filters have a transmittance of approximately 0.8 at 1064 nm and  $10^{-6}$  at 980 nm.

### 5.3.3 Conclusion

In Table 5.5 and Table 5.6 it can be seen that for low frequencies the longitudinal displacement determined by the PPA and by the ESD agree very well. In Figure 5.11 it can be seen that at low frequencies the measured values for PPA and ESD agree within their errors. For the measurement on 17 February 2004 and measurement I and II on 19 February 2004 the longitudinal displacement determined with the PPA becomes significantly smaller than the longitudinal displacement determined with the ESD at higher frequencies. For measurement II the longitudinal displacement determined with the ESD even looks like it turns into a  $1/f$  dependency at high frequencies. This behaviour is not understood. For measurement III the longitudinal displacement determined with the ESD follows the expected  $1/f^2$  dependency up to 1571 Hz. The different behaviour of the different measurements is not understood either. It should be kept in mind, that the SNRs at high frequencies are very poor for the PPA (see Table 5.4). As already mentioned, between measurement II and III on 19 February 2004 the operating conditions of the interferometer changed.

f [Hz]	17.2.2004		19.2.2004 I		19.2.2004 II		19.2.2004 III	
	$h_{\text{rms}}$	SNR	$h_{\text{rms}}$	SNR	$h_{\text{rms}}$	SNR	$h_{\text{rms}}$	SNR
161	$2.3 \times 10^{-18}$	24	$2.6 \times 10^{-18}$	26	$2.6 \times 10^{-18}$	28	$2.6 \times 10^{-18}$	18
310	$5.3 \times 10^{-19}$	18	$6.4 \times 10^{-19}$	22	$6.1 \times 10^{-19}$	21	$6.2 \times 10^{-19}$	22
580	$2.0 \times 10^{-19}$	29	$2.1 \times 10^{-19}$	27	$2.3 \times 10^{-19}$	38	$1.7 \times 10^{-19}$	23
765	$1.3 \times 10^{-19}$	28	$1.4 \times 10^{-19}$	35	$1.7 \times 10^{-19}$	42	$1.1 \times 10^{-19}$	24
925	$9.6 \times 10^{-20}$	22	$9.9 \times 10^{-20}$	31	$1.3 \times 10^{-19}$	33	$7.8 \times 10^{-20}$	17
1182	$7.5 \times 10^{-20}$	14	$7.2 \times 10^{-20}$	13	$1.1 \times 10^{-19}$	16	$5.2 \times 10^{-20}$	6
1387	$6.5 \times 10^{-20}$	10	$5.4 \times 10^{-20}$	8	$8.5 \times 10^{-20}$	12	$3.9 \times 10^{-20}$	5
1571	-	-	-	-	$7.4 \times 10^{-20}$	7	$2.7 \times 10^{-20}$	3
1815	-	-	-	-	$6.2 \times 10^{-20}$	6	$3.1 \times 10^{-20}$	4

**Table 5.4:** Results of the first measurements done on the interferometer main mirror far North (MFN) with a PPA. Given are the heights of the injected signal in the amplitude spectrum of  $h(t)$ . The first set of measurements was done on 17 February 2004, the next three sets of measurements were done on 19 February 2004. For the last two sets of measurements on 19 February 2004 the PPA laser beam was moved upwards and downwards, respectively, with respect to the laser beam during measurement I.

17.2.2004		
f [Hz]	PPA <sub>rms</sub> [m]	ESD <sub>rms</sub> [m]
161	$1.66 \times 10^{-16}$	$1.69 \times 10^{-16}$
310	$4.47 \times 10^{-17}$	$3.89 \times 10^{-17}$
580	$1.28 \times 10^{-17}$	$1.47 \times 10^{-17}$
765	$7.34 \times 10^{-18}$	$9.55 \times 10^{-18}$
925	$5.02 \times 10^{-18}$	$7.05 \times 10^{-18}$
1182	$3.07 \times 10^{-18}$	$5.51 \times 10^{-18}$
1387	$2.23 \times 10^{-18}$	$4.78 \times 10^{-18}$

**Table 5.5:** Longitudinal displacements  $\Delta L$  of the measurement on 17 February 2004. Compared are the expected longitudinal displacements due to the applied PPA excitation and the longitudinal length changes measured with the interferometer calibrated with the electrostatic drive (ESD).

19.2.2004				
f [Hz]	PPA <sub>rms</sub> [m]	ESD <sub>rms</sub> [m] I	ESD <sub>rms</sub> [m] II	ESD <sub>rms</sub> [m] III
161	$1.80 \times 10^{-16}$	$1.93 \times 10^{-16}$	$1.87 \times 10^{-16}$	$1.90 \times 10^{-16}$
310	$4.87 \times 10^{-17}$	$4.72 \times 10^{-17}$	$4.46 \times 10^{-18}$	$4.52 \times 10^{-17}$
580	$1.39 \times 10^{-17}$	$1.51 \times 10^{-17}$	$1.71 \times 10^{-18}$	$1.27 \times 10^{-17}$
765	$7.99 \times 10^{-18}$	$1.02 \times 10^{-17}$	$1.22 \times 10^{-17}$	$7.79 \times 10^{-18}$
925	$5.47 \times 10^{-18}$	$7.24 \times 10^{-18}$	$9.41 \times 10^{-18}$	$5.72 \times 10^{-18}$
1182	$3.35 \times 10^{-18}$	$5.31 \times 10^{-18}$	$7.86 \times 10^{-18}$	$3.78 \times 10^{-18}$
1387	$2.43 \times 10^{-18}$	$3.95 \times 10^{-18}$	$6.25 \times 10^{-18}$	$2.87 \times 10^{-18}$
1571	$1.90 \times 10^{-18}$	-	$5.45 \times 10^{-18}$	$2.00 \times 10^{-18}$
1815	$1.42 \times 10^{-18}$	-	$4.57 \times 10^{-18}$	$2.27 \times 10^{-18}$

**Table 5.6:** Longitudinal displacements  $\Delta L$  of the measurements on 19 February 2004. Compared are the expected longitudinal displacements due to the applied PPA excitation and the longitudinal length changes measured with the interferometer calibrated with the electrostatic drive (ESD). Three sets of measurements were made. During measurement I the actuator beam was about parallel to the ground hitting the viewport on the left side approximately in the middle with respect to its vertical position. For measurements II and III the beam was pointed upwards and downwards, respectively, approximately 2 cm away from its position during measurement I.

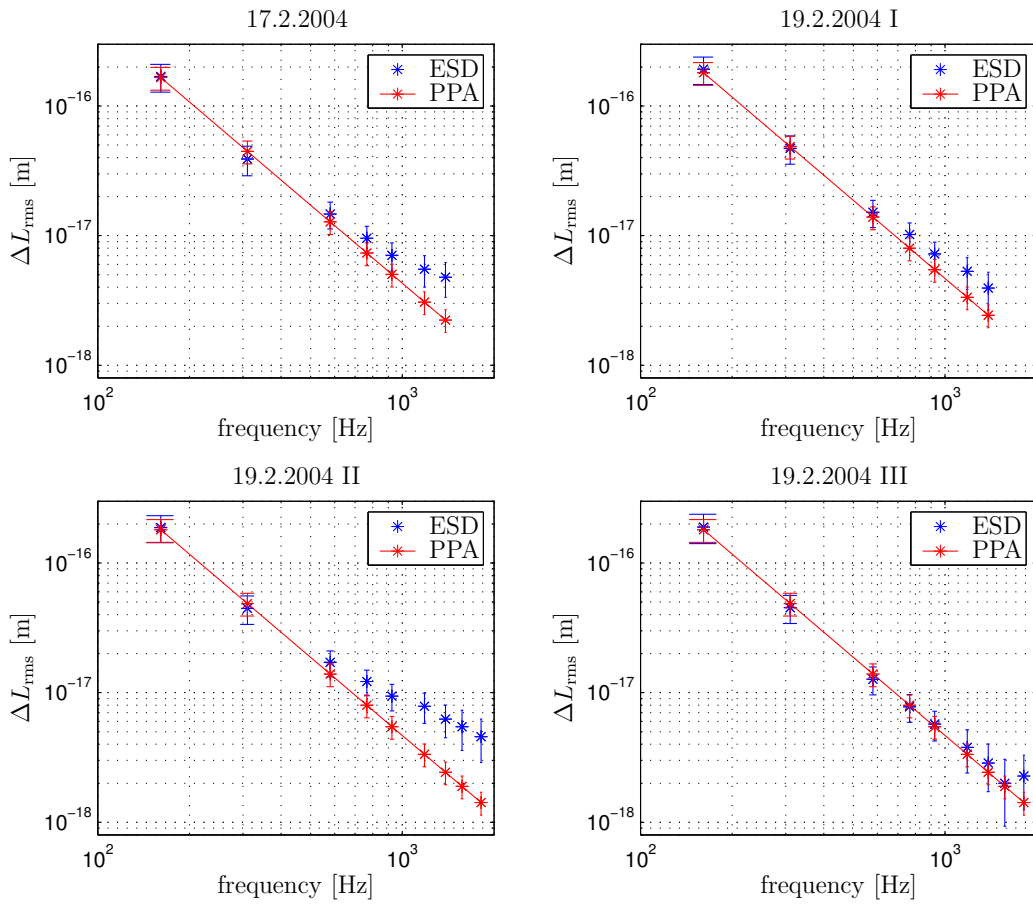


**Figure 5.11:** Four measurements done with a PPA; the blue dots represent the longitudinal displacement measured with the interferometer and calibrated with the electrostatic drive (ESD). The red dots and lines represent the expected longitudinal displacement due to the PPA. The error bars on the PPA values do not take thermally induced length changes and apparent longitudinal displacement due to rotation into account. Also the effect of scattered light at the viewport is not treated. The red lines follow the expected  $1/f^2$  dependence.

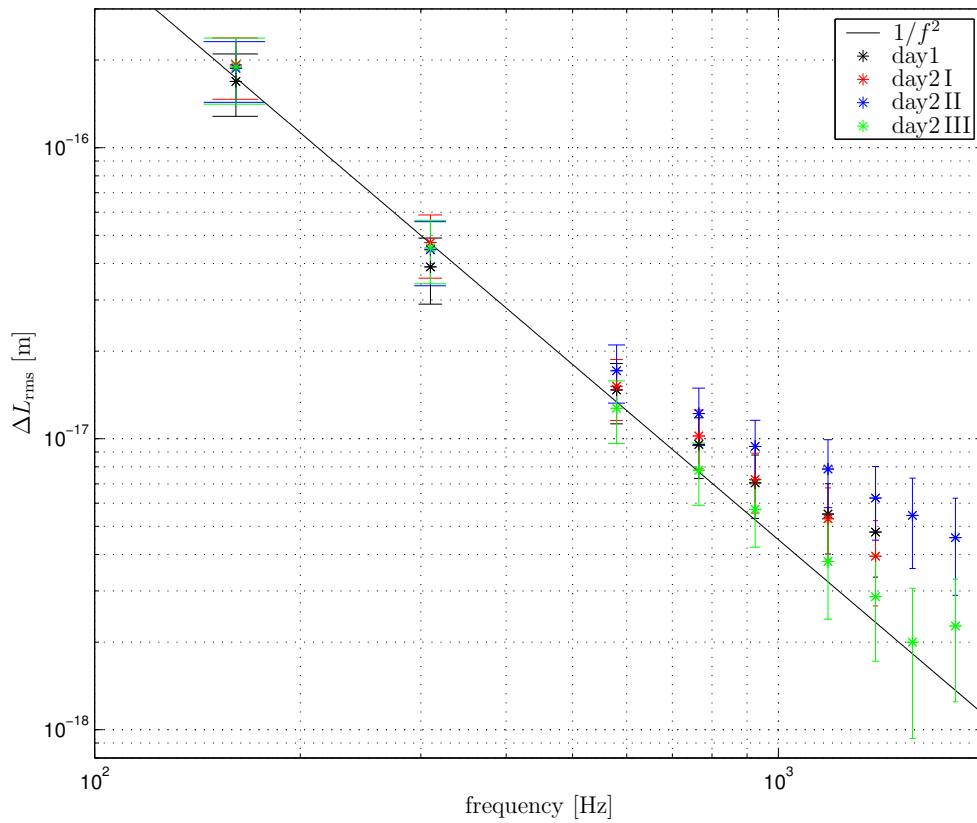


**Figure 5.12:** Graphical display of all measured data and one arbitrarily chosen  $1/f^2$  curve

For a better understanding of the behaviour of the PPA the measurements should be repeated with more laser power to get better signal-to-noise ratios, particularly at high frequencies. At the same time the position of the laser beam of the PPA should be centred with great care on the main mirror of the interferometer. This is, on the one hand, to reduce the effect of apparent longitudinal displacement due to mirror rotation and, on the other hand, to minimise possible excitation of other modes. With the current setup of the PPA it is not expected to reach an accuracy better than  $\pm 10\%$ . In the next section a possible setup for an advanced PPA is given which can reach an accuracy better than  $\pm 10\%$ .

## 5.4 Possible setup for an advanced photon pressure actuator

A possible setup for an advanced PPA is given in Figure 5.13. The advantages compared to the old setup are a higher laser power and the usage of a dichromatic mirror. At the beginning of the optical path of the laser beam, a small amount of the light power is split off at a beam splitter to monitor the input light power. Then the beam is shone via the dichromatic mirror under an angle of approximately  $0.5^\circ$  onto a far mirror of the interferometer. The dichromatic mirror reflects at 980 nm and transmits at 1064 nm. Thus it can separate the laser beam of the PPA with a wavelength of 980 nm and the laser beam of the interferometer with a wavelength of 1064 nm leaving the vacuum. The dichromatic mirror allows almost normal incidence of the PPA laser beam onto the interferometer main mirror. With such a setup the position of the PPA laser beam on the interferometer main mirror can be well controlled.

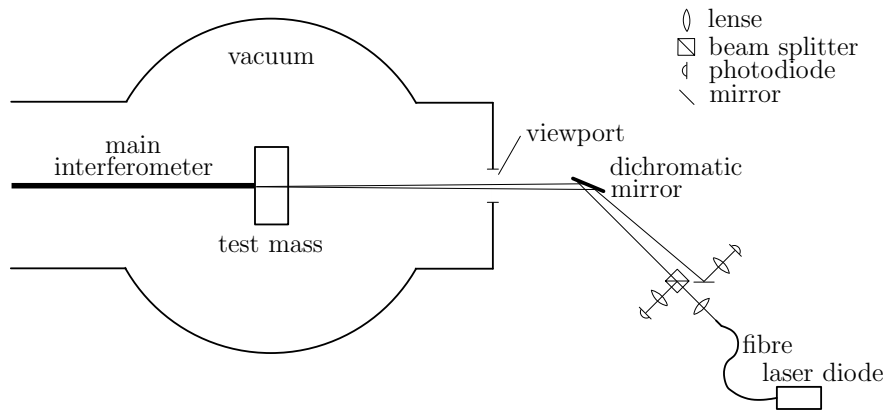


**Figure 5.13:** Suggested setup for an advanced PPA with a fibre coupled laser diode at 980 nm, 30 W cw and a fibre diameter of 600  $\mu\text{m}$ .

As has been described in subsection 5.2.2 it needs to be made sure that the beam is not cut off where the intensity is above or equal to 1% of the total intensity. In Figure 5.14 the radius of the beam (here, the radius indicates where the intensity of the beam has dropped to 1%) has been plotted for a possible setup. The propagation of a laser beam of a multi-mode fibre coupled laser diode was calculated with a set of equations for



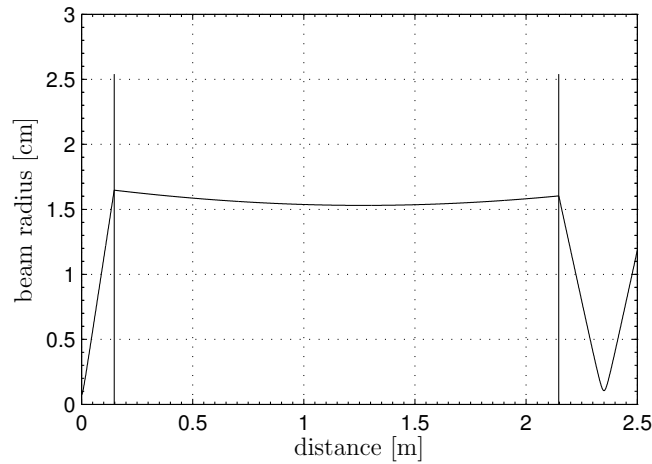


**Figure 5.14:** Laser beam radius of the suggested advanced PPA; as a laser source a fibre coupled laser diode at wavelength 980 nm with a fibre diameter 600  $\mu\text{m}$ ,  $\text{NA}=0.22$  is used. The beam radius refers to where the intensity of the beam has dropped to 1%. The NA refers to the beam radius where the intensity has dropped to 5%. The first lens, indicated by a vertical line, at approximately 0.15 m collimates the beam of the fibre. The second lens, also indicated by a vertical line, at approximately 2.15 m focuses the beam onto a photodiode. The distances are chosen as in the possible advanced setup for a PPA given in Figure 5.13.

Gaussian beam propagation where the so-called  $M^2$  factor is added [98]. The calculation was done for a commercially available fibre coupled laser diode with wavelength 980 nm, 30 W cw power, a fibre diameter of 600 nm and a numerical aperture (NA) of 0.22 (the NA refers to the beam radius where the intensity has dropped to 5%). With this setup the PPA beam can be moved at least 2 cm away from the centre of the viewport without cutting the beam off. The viewport has a diameter of 10 cm, but it is assumed that the coating is uniform over 8 cm only. Entering the vacuum under normal incidence allows a better control of the laser beam position of the PPA on the interferometer main mirror, than entering the vacuum under a fixed input and output angle. In the later case it is as well harder to make sure that the beam is not cut off. As described in subsection 5.2.5 the laser beam of the PPA should hit the interferometer main mirror at its centre. As the viewport and the interferometer main mirror are not perfectly aligned with respect to each other, a change in the position of the laser beam of the PPA on the interferometer main mirror allows this misalignment to be compensated for.

With such an advanced setup a PPA accuracy of the order 1% should be realisable. This is only possible if great care is taken with the setup and the improvements already mentioned in subsection 5.2.7 are implemented. These include:

- A laser diode with high power (of the order of a few Watts) needs to be used to allow high signal-to-noise ratios at all frequencies. The laser diode needs to be temperature stabilised.
- The pendulum transfer function of the main optic, suspended as a triple pendulum,

needs to be studied carefully to investigate if modes other than the longitudinal displacement are excited by the PPA.

- At least one photodiode needs to be calibrated with high accuracy and also needs to be temperature stabilised. Its response over its active area needs to be measured. Then it needs to be determined which area can be reproducibly hit with the laser beam of the PPA and in which error this results for an absolute power measurement.
- The optical properties of the viewport should be measured very accurately at the PPA wavelength.
- For the case of monitoring also the light power injected into the vacuum the optical properties of the main optic should be measured very accurately at the PPA wavelength.
- The mass of the interferometer main mirror to which the PPA is applied needs to be measured.
- The relative position of the main mirror and the viewport needs to be determined to be able to centre the laser beam of the PPA as well as possible on the main mirror.
- A finite element analysis should be made to determine the thermally excited expansion of the mirror substrate and the coating material at the excitation frequencies of the PPA.

The remaining crucial issue, that might very well dominate the accuracy of the PPA, is how well the laser beam of the PPA can be centred on the main mirror to prevent rotational excitation which leads to apparent longitudinal displacement.

## Appendix A

### Gravitational waves emitted by a non-axisymmetric non-precessing spinning neutron star

In this appendix the special case of gravitational waves emitted by a non-axisymmetric, non-precessing spinning neutron star is calculated. First the neutron star shape and orientation of spin are described. Then the second (or quadrupole) moment of the mass distribution of the neutron star is calculated which yields the tensor of the metric perturbation in the far field linear approximation. From this tensor the plus- and cross-polarisations of the gravitational waves seen by an observer in the far field are determined. The result is used in chapter 1 in Equation 1.5 to 1.7.

A neutron star is considered which deviates from a perfect sphere by elongation along an axis of symmetry. In other words the neutron star is an ellipsoid with one semi-major axis of size  $a$  and two semi-minor axes of size  $b$ , where  $a > b$ . The geometry of the neutron star is depicted in Figure A.1. Let the  $z$ -axis be the axis of rotation, then the so-called wobble angle is  $\pi/2$ . The wobble angle is the angle between the total angular momentum vector of the star and the star's axis of symmetry.

The tensor  $h_{jk}^{TT}$  describing the metric perturbations due to a time dependent quadrupole moment is according to equation (36.47) of [24] given by<sup>1</sup>

$$h_{jk}^{TT} = \frac{G}{c^4} \frac{2}{R} \ddot{I}_{jk}^{TT}, \quad (\text{A.1})$$

where  $R$  is the distance from the neutron star,  $G$  is the gravitational constant,  $c$  is the velocity of light and  $\ddot{I}_{jk}^{TT}$  is the second time derivative of the trace-free part of the second moment of the mass distribution of the neutron star. To determine  $h_{jk}^{TT}$  first the trace-free part of the second moment of the mass distribution of the non-rotating neutron star  $I_{jk}^{TT}$  as depicted in Figure A.1 is calculated. According to Equation (36.3) of [24] it is defined as

$$I_{jk} = \int d^3x \rho (x_j x_k - \frac{1}{3} \delta_{jk} x_i x_i), \quad (\text{A.2})$$

where  $\rho$  is the density and the volume integral  $\int d^3x$  corresponds in Figure A.1 to  $\int dx dy dz$ . Introducing the stretched spherical coordinates  $x = b r \sin \vartheta \cos \varphi$ ,  $y = a r \sin \vartheta \sin \varphi$ , and  $z = b r \cos \vartheta$  with  $0 \leq r$ ,  $0 \leq \vartheta \leq \pi$ , and  $0 \leq \varphi < 2\pi$  turns the volume integral in Equation A.2 into

$$\int d^3x = \int_0^1 dr \int_0^\pi d\vartheta \int_0^{2\pi} d\varphi ab^2 r^2 \sin \vartheta, \quad (\text{A.3})$$

---

<sup>1</sup>Please note that in Equation (36.47) of [24]  $c$  and  $G$  have been set to 1.

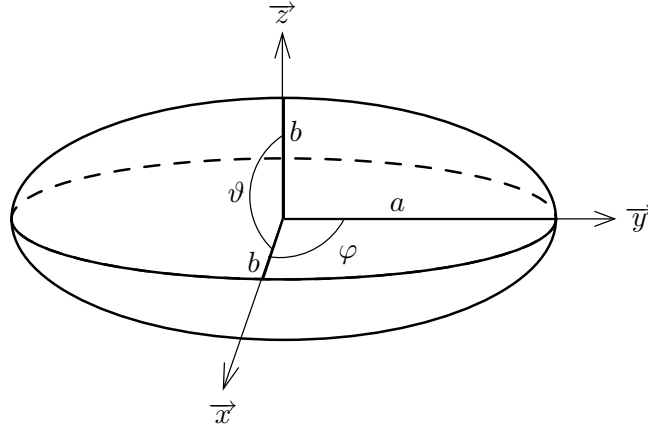


**Figure A.1:** Neutron star with one semi-major axis of size  $a$  and two semi-minor axes of size  $b$ .

as  $\rho = 0$  outside the neutron star. Equation A.2 then yields for a homogeneous density  $\rho$  the trace-free part of the second moment of the mass distribution

$$\begin{aligned} I_{yy} &= \frac{2}{15} M(a^2 - b^2) , \\ I_{xx} = I_{zz} &= \frac{1}{15} M(b^2 - a^2) , \end{aligned} \quad (\text{A.4})$$

where  $M$  is the total mass of the neutron star and all other components of  $I_{jk}$  are zero. If the neutron star is now rotating counterclockwise around the  $z$ -axis with the angular velocity  $\Omega$ , the time dependent second moment of the mass distribution is given by

$$I_{\text{rot}} = D I D^T , \quad (\text{A.5})$$

where  $D$  is the matrix of rotation

$$D = \begin{pmatrix} \cos \Omega t & -\sin \Omega t & 0 \\ \sin \Omega t & \cos \Omega t & 0 \\ 0 & 0 & 1 \end{pmatrix} . \quad (\text{A.6})$$

This gives

$$I_{\text{rot}} = \frac{M}{5} \begin{pmatrix} a^2 \cos^2 \Omega t + b^2 \sin^2 \Omega t & -(b^2 - a^2) \sin \Omega t \cos \Omega t & 0 \\ -(b^2 - a^2) \sin \Omega t \cos \Omega t & a^2 \sin^2 \Omega t + b^2 \cos^2 \Omega t & 0 \\ 0 & 0 & b^2 \end{pmatrix} - \frac{M}{5} (a^2 + 2b^2) \mathbf{1} . \quad (\text{A.7})$$

The second time derivative  $\ddot{I}_{\text{rot}}$  yields

$$h^{TT} = \frac{G}{c^4} \frac{M}{R} \frac{4}{5} \Omega^2 (b^2 - a^2) \begin{pmatrix} \cos 2\Omega t & \sin 2\Omega t & 0 \\ \sin 2\Omega t & -\cos 2\Omega t & 0 \\ 0 & 0 & 0 \end{pmatrix} . \quad (\text{A.8})$$

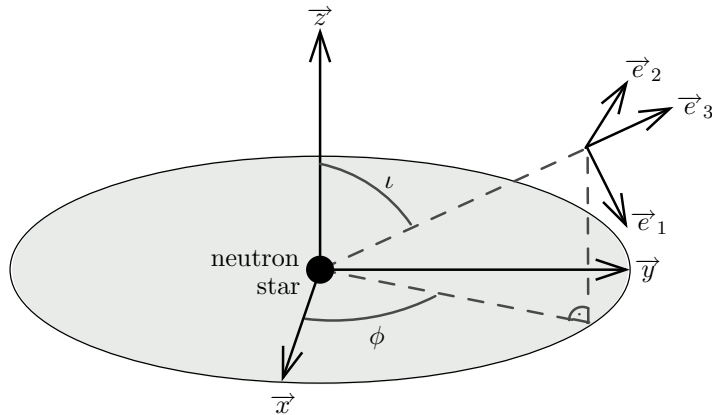


**Figure A.2:** Relative orientation of the neutron star's reference frame system spanned by  $\vec{x}$ ,  $\vec{y}$ , and  $\vec{z}$  with the neutron star in its origin and the observer's reference system spanned by  $\vec{e}_1$ ,  $\vec{e}_2$ , and  $\vec{e}_3$ .

In the far field an observer sees the cross- and plus-polarisation,  $h_+(t)$  and  $h_\times(t)$  depending on his relative position to the neutron star. Let the  $\vec{e}_3$ -axis of the observer's reference frame be along the propagation direction of the gravitational wave and the  $h_+(t)$  polarisation be along the  $\vec{e}_1$ - and  $\vec{e}_2$ -axis. The  $\vec{e}_2$ -axis of the observer's reference frame is perpendicular to the  $\vec{e}_3$ -axis and parallel to the  $xy$ -plane of the neutron star's reference frame. The neutron star's reference system and the observer's reference system are depicted in Figure A.2. From this it can be seen that  $\vec{e}_1 = \cos \iota \cos \phi \vec{x} + \cos \iota \sin \phi \vec{y} - \sin \iota \vec{z}$  and  $\vec{e}_2 = -\sin \phi \vec{x} + \cos \phi \vec{y}$ . The  $h_+(t)$  and  $h_\times(t)$  in the observer's reference frame are then given by<sup>2</sup>

$$\begin{aligned} h_+ &= \frac{1}{2} [\vec{e}_1^T h^{TT} \vec{e}_1 - \vec{e}_2^T h^{TT} \vec{e}_2], \\ h_\times &= \vec{e}_1^T h^{TT} \vec{e}_2 = \vec{e}_2^T h^{TT} \vec{e}_1. \end{aligned} \quad (\text{A.9})$$

Solving Equation A.9 yields the two polarisations of a gravitational wave in the far field

$$\begin{aligned} h_+ &= \frac{16\pi^2 G f^2 M}{c^4 R 5} (b^2 - a^2) \frac{1}{2} (1 + \cos^2 \iota) \cos(2\Omega t - 2\phi), \\ h_\times &= \frac{16\pi^2 G f^2 M}{c^4 R 5} (b^2 - a^2) \cos \iota \sin(2\Omega t - 2\phi). \end{aligned} \quad (\text{A.10})$$

<sup>2</sup>For a description of the polarisations of a gravitational wave see [24] section §35.6.



## Appendix B

### Coordinate systems

#### B.1 Celestial equatorial coordinate system

In the celestial equatorial coordinate system [53], also referred to as the celestial sphere coordinate system, the origin is at the Earth centre. The  $z$ -axis coincides with the Earth rotation axis and points towards the North pole. The  $x$ - and  $y$ -axes lie in the Earth's equatorial plane defining the celestial equator. As the Earth's equatorial plane is inclined towards the orbital plane of the Earth, the Sun describes an apparent annual path in the sky. When the Sun lies on the intersection line of the celestial equator (the Earth's equatorial plane) and the orbital plane of the Earth, the Sun is crossing in its apparent path the celestial equator. This event occurs two times during one orbit of the Earth. When the Sun crosses the celestial equator moving northward, the sun is at the point of the vernal equinox (spring). The  $x$ -axis of the celestial equatorial coordinate system points towards the vernal equinox.

In the celestial equatorial coordinate system, the position of a celestial body is specified by its declination  $\delta$  (DEC) and right ascension  $\alpha$  (R.A.) (see Figure B.1). Declination is the analogue of terrestrial latitude. By convention, positions between the celestial equator and the north celestial pole have positive declination, and those between the celestial equator and the south celestial pole negative declination; hence, declination ranges from  $-\pi/2$  (the south celestial pole) to  $\pi/2$  (the north celestial pole). Right ascension is the analogue of terrestrial longitude measured eastward. The point of origin of right ascension is the vernal equinox. Usually right ascension is given in hours, minutes, and seconds of time, thus ranging from  $0^{\text{h}}0^{\text{min}}0^{\text{s}}$  to  $23^{\text{h}}59^{\text{min}}59^{\text{s}}$ .

Since the orientation of the Earth's equator and pole are continuously changing, it must be specified to which particular epoch the celestial equatorial coordinates refer to [99]. In radio pulsar astronomy the coordinate systems B1950 and J2000 are commonly used [100]. The B1950 and J2000 equatorial coordinate systems are defined by the mean orientation of the Earth's equator and ecliptic at the beginning of the years 1950 and 2000. They are also tied to the sky by star coordinates. In addition the J2000 system is also tied to radio sources. The assumed orientation of the Earth on these two dates is more a matter of definition than actual, since the "mean" orientation does not include short term motions of the Earth's spin axis (nutations and smaller effects). The coordinates of celestial objects in B1950 and J2000 differ by many arc minutes.

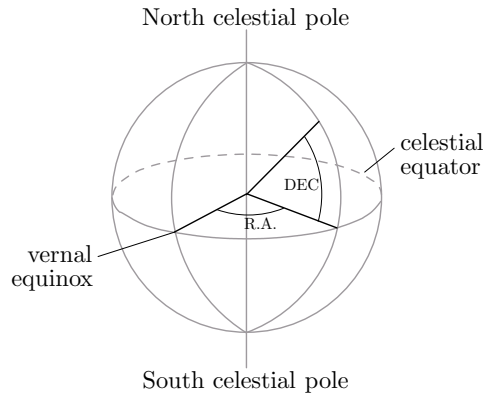


**Figure B.1:** Schematic of the celestial equatorial coordinate system where the position of a celestial body is specified by its declination and right ascension.

## B.2 Cardinal coordinate system

The cardinal coordinate system describes a coordinate system which's origin coincides with a point on the surface of the Earth. The  $xy$ -plane is tangent to the surface of the Earth at this point with the  $x$ -axis in the North-South direction and the  $y$ -axis in the West-East direction. The  $z$ -axis is along the Earth radius pointing toward the zenith [47]. Figure B.2 shows a cardinal coordinate system for an arbitrarily chosen point on the Earth's surface. In the cardinal coordinate system of a gravitational wave detector the beam splitter is chosen as the origin of the coordinate system.

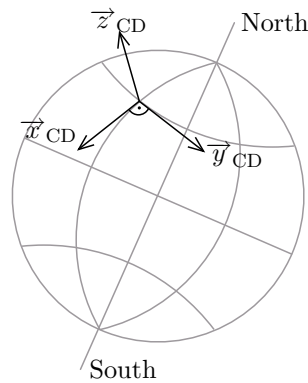


**Figure B.2:** Schematic of the Earth with meridians and parallels of latitude. A cardinal coordinate system at the crossing of a meridian and parallel of latitude is depicted.



### B.3 Detector proper reference frame coordinate system

In the detector proper reference frame coordinate system the  $\vec{z}_{\text{DT}}$  axis coincides with the  $z$ -axis of the cardinal coordinate system at the detector location. The  $\vec{x}_{\text{DT}}$  axis is along the first arm of the interferometer. The first arm is defined such that the vector  $\vec{e}_1 \times \vec{e}_2$  points outward from the Earth<sup>1</sup>, where  $\vec{e}_1$  is parallel to the first arm of the interferometer and  $\vec{e}_2$  is parallel to the second arm. At GEO 600 the first interferometer arm is the so-called East arm, pointing to  $21.61^\circ$  measured counterclockwise from the East.

The  $\vec{y}_{\text{DT}}$  axis of the detector proper reference frame coordinate system is perpendicular to the  $\vec{x}_{\text{DT}}$  and  $\vec{z}_{\text{DT}}$  axes forming a right-hand coordinate system. Only for detectors where the second interferometer arm is perpendicular on the first arm the  $\vec{y}_{\text{DT}}$  axis coincides with the second interferometer arm. Otherwise the second arm is parallel to the unity vector  $\vec{e}_2 = (\cos \zeta, \sin \zeta, 0)$ , where  $\zeta$  is the angle between the interferometer arms. At GEO 600 the angle between the two interferometer arms is  $94.33^\circ$ [101]; this is graphically displayed in Figure 1.6 of chapter 1.

---

<sup>1</sup>This definition of first and second interferometer arm does not correspond to the one used in [101], but it is consistent with the matrix of transformation given in 5 to derive the antenna response functions.



# Appendix C

## Power spectral densities

In the frequency domain noise and signals are described by power spectral densities and power spectra, respectively. The definition for the normalisation of power spectral densities and power spectra is given below which corresponds to the normalisation performed by a spectrum analyser. Then the existing vocabulary on power spectral densities and power spectra used by individuals in the GEO 600 community is summarised.

### C.1 Normalisation

#### C.1.1 Normalised power spectral density

The following normalisation of a power spectral density corresponds to the normalisation used by the matlab function `pwelch` [102], which is equivalent to the normalisation a spectrum analyser performs.

Let the discrete Fourier transform be defined as

$$X_k = \sum_{n=1}^N x_n e^{-i2\pi(n-1)(k-1)/N}, \quad 1 \leq k \leq N, \quad (\text{C.1})$$

where  $N$  is the number of sample points and  $x_n$  with  $n \in N$  corresponds to the sample values, which all together form the sample set represented by  $[x_n]$ . Then  $X_k$  with  $k \in N$  are the Fourier components of  $[x_n]$ . This corresponds to the definition of the discrete Fourier transform in the matlab function `fft` [102].

The discrete Fourier transform of a sample set  $[x_n]$  to which a window has been applied is then

$$Y_k = \sum_{n=1}^N \text{win}_n x_n e^{-i2\pi(n-1)(k-1)/N}, \quad 1 \leq k \leq N, \quad (\text{C.2})$$

where  $\text{win}_n$  is the value of the window applied at the sample  $x_n$  with  $n \in N$ .

For the case of a real sample set  $[x_n]$  the normalised one sided power spectral density PSD is then

$$\text{PSD}_k = \frac{2 |Y_k|^2}{\text{SR} \sum_n \text{win}_n^2}, \quad 1 < k < \frac{N}{2}, \quad (\text{C.3})$$

where SR corresponds to the sample rate of the sample set  $[x_n]$ .

For  $k = 1$  the factor of two in Equation C.3, due to converting the two sided power spectral density to the one sided power spectral density, has to be omitted. In the case

of  $N$  being even the matlab function `pwelch` calculates the Fourier components  $Y_k$  for  $k \in [1, N/2 + 1]$  and does not apply the factor 2 to the first and last Fourier components of the one sided power spectral density, when converting the two sided power spectral density into the one sided power spectral density. In the case of  $N$  being odd `pwelch` calculates the Fourier components  $Y_k$  for  $k \in [1, (N + 1)/2]$  and does not apply the factor 2 to the first and last Fourier components of the one sided power spectral density, when converting the two sided power spectral density into the one sided power spectral density. As the value of the last Fourier component is not crucial in a plain power spectral density plot, it is in this context dispensable to give an unequivocal definition of that very component.

If the physical unit of the sample set  $x_n$  is measured in [V], the units of the normalised power spectral density PSD in Equation C.3 are  $[V_{\text{rms}}^2/\text{Hz}]^1$ .

### C.1.2 Normalised power spectrum

To obtain the normalised power spectrum (NPS) from the normalised power spectral density (PSD), Equation C.3 needs to be multiplied with the factor

$$\frac{\frac{1}{N} \sum_n \text{win}_n^2}{\frac{1}{N^2} (\sum_n \text{win}_n)^2} \frac{\text{SR}}{N} . \quad (\text{C.4})$$

This leads to the normalised one sided power spectrum

$$\text{NPS}_k = \frac{2 |Y_k|^2}{(\sum_n \text{win}_n)^2} , \quad 1 < k < \frac{N}{2} . \quad (\text{C.5})$$

The discussion of the factor 2 for converting the two sided power spectral density to the one sided power spectral density in section subsection C.1.1 applies for converting the two sided power spectrum to the one sided power spectrum as well.

If the physical unit of the sample set  $[x_n]$  is measured in [V], the unit of the normalised power spectrum is  $[V_{\text{rms}}^2]$ . The conversion from power spectral density to the power spectrum is consistent with [103]. Please be aware that in equation (9) through (11) and (15) of reference [103] factors of  $1/N$  have been omitted.

## C.2 Vocabulary

If PSD is the normalised power spectral density as defined in Equation C.3 with the units  $[V_{\text{rms}}^2/\text{Hz}]$  and if NPS is the normalised power spectrum as defined in Equation C.5 with the units  $[V_{\text{rms}}^2]$ , the names and units listed in Table C.1 apply.

The expression  $V_{\text{rms}}$  corresponds to the equivalent DC power in a signal. If a signal  $f(t)$  is measured in [V] the relation between the equivalent DC power  $f_{\text{rms}}$   $[V_{\text{rms}}]$  and  $f(t)$  [V] is given by

$$\int_0^T f^2(t) dt = f_{\text{rms}}^2 T , \quad (\text{C.6})$$

---

<sup>1</sup>The expression  $V_{\text{rms}}$  does not mean the root mean square of  $V$ . For the definition of  $V_{\text{rms}}$  see section C.2 Equation C.6

expression	name	units
$\sqrt{\text{PSD}}$	amplitude spectral density	$[\text{V}_{\text{rms}}/\sqrt{\text{Hz}}]$
$\sqrt{\text{PSD}}$	linear spectral density	$[\text{V}_{\text{rms}}/\sqrt{\text{Hz}}]$
$\sqrt{\text{NPS}}$	amplitude spectrum	$[\text{V}_{\text{rms}}]$
$\sqrt{\text{NPS}}$	linear spectrum	$[\text{V}_{\text{rms}}]$

**Table C.1:** Vocubular of spectral densities and spectra.

where  $T$  is the length of the time interval in which the signal is regarded. For a signal that is sinusoidal and periodic in  $T$  the relation between  $V$  and  $V_{\text{rms}}$  becomes  $V = \sqrt{2}V_{\text{rms}}$ . Therefore this relation applies for the units of Fourier components obtained by a discrete Fourier transform. The values  $V_{\text{pp}}$  for value peak-to-peak,  $V_{\text{pk}}$  for value peak, and  $V_{\text{rms}}$  for value rms for normalised amplitude spectra are related in the following way

$$V_{\text{pp}} = 2 V_{\text{pk}} = 2 \sqrt{2} V_{\text{rms}} . \quad (\text{C.7})$$

Taking the amplitude spectrum as defined in Equation C.5 of only a pure sinusoidal signal with amplitude  $\pm 1$  [V] at the frequency  $f_0$  and multiplying the result with  $\sqrt{2}$  gives the value 1 [ $V_{\text{pk}}$ ] in the amplitude spectrum at the frequency  $f_0$ , if the frequency  $f_0$  falls exactly into a frequency bin of  $Y_k$ .



## Appendix D

### Matlab script to determine power needed for online calibration with a photon pressure actuator

```
% radiation pressure actuator values
c = 2.997e8; % speed of light [m/s]
m = 5.32; % mirror mass [kg]
combF = [200; 400; 600; 800; 1000]; % calibration line frequencies [Hz]
SNR = 100; % signal-to-noise ratio of comb lines

% fft conversion factors
SR = 16384; % sample rate of data acquisition system [Hz]
T = 1; % length of data segment over which fft is taken in [s]
N = T*SR; % length of data segment over which fft is taken in samples
rms_to_pp = (2*sqrt(2)); % transfers noise Delta x_rms into Delta x_PP

% conversion factor to transform amplitude spectral density to
% amplitude spectrum; it is assumed the measurement of the amplitude
% spectrum was done with a Hanning window
dens_to_spec=sqrt(sum(hanning(N).*hanning(N))/sum(hanning(N)).^2*SR)

% load design sensitivity and current noise detector noise level
% noise given in h_rms/sqrt(Hz)
design_sens = load('design_sens.txt');

% convert noise into mirror motion of a far mirror
design_mov = 600*design_sens(:,2);

% calculate necessary actuation in [m] for design sensitivity curve
design_combF = combF-design_sens(1,1)+1;
design_combX = SNR*dens_to_spec*design_mov(design_combF);

% calculate power needed for this actuation
design_combP = rms_to_pp*m*c*(2*pi*combF).^2.*design_combX/2;
design_Ptotal = sum(design_combP) % [W]
```





## Appendix E

### Reflectivity of viewport

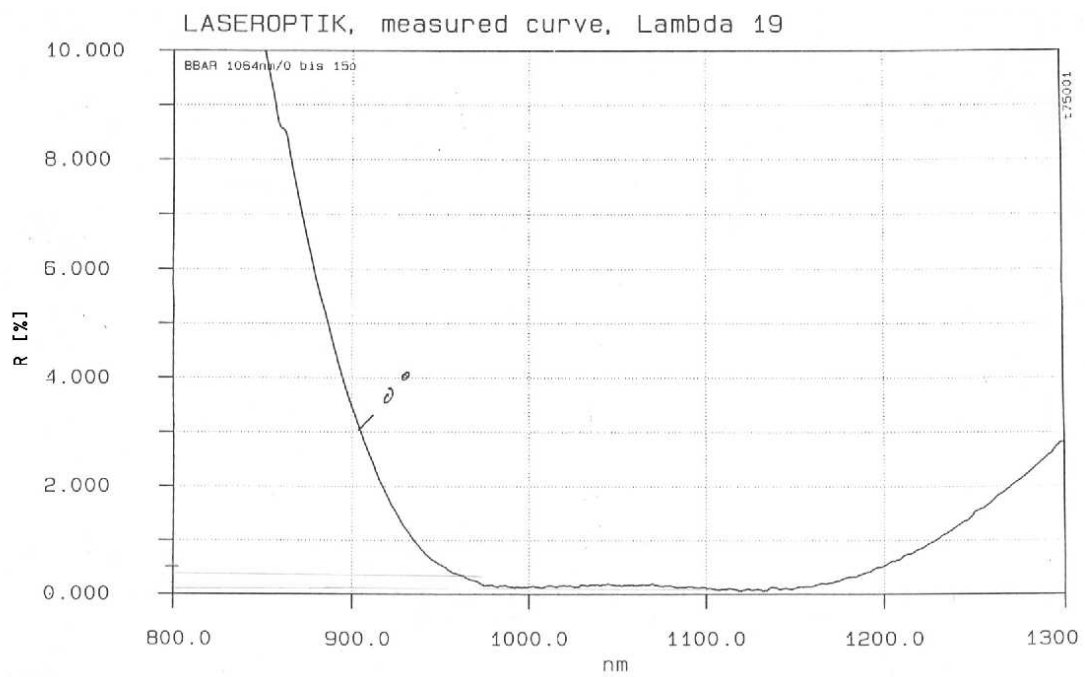


**Figure E.1:** Graphical display of the measured reflectivity of a coated viewport under normal incidence; the data has been provided by the coating company LASEROPTIK.



# Appendix F

## Transformation between transfer function notations

The following sections describe how to convert the parameters of two different notations of transfer functions into each other. The two notations are the single-complex zero and pole notation as given in Equation F.1 used in the GEO 600 Detector Data Base [104] and the frequency Q-value notation as given in Equation F.2 used by LISO [62].

### F.1 Notations

#### F.1.1 Single-complex zero pole notation

The following notation is the single-complex zero and pole notation used in the GEO 600 Detector Data Base

$$H(s) = k_{\text{DB}} \frac{\prod_{n=1}^k (s - z_n)}{\prod_{m=1}^l (s - p_m)}, \quad (\text{F.1})$$

where  $s$  is the complex angular frequency  $s = i\omega = i2\pi f$  with  $f$  being the frequency in Hz,  $k_{\text{DB}}$  is the gain factor of this notation,  $z_n$  are the zeros and  $p_m$  are the poles of the transfer function. If the zeros  $z_n$  or poles  $p_m$  are real numbers they represent single zeros or single poles, respectively. If a zero  $z_n$  is a complex number it represents together with its complex conjugate value a double zero. That is  $z_n$  together with  $z_{n+1} = z_n^*$  forms a double zero. If a pole  $p_m$  is a complex number it represents together with its complex conjugate value a double pole.

#### F.1.2 Frequency/Q-value notation

The following notation is the frequency/Q-value notation used in LISO. It corresponds to the more intuitive notation where the frequency of a pole and zero and a double pole or zero can roughly be read directly from a plot of the transfer function. For a Q of 0.5 this is approximately at the frequency where the amplitude dropped to -6dB or rose to 6dB, respectively.

$$H(s) = k_{\text{LISO}} \frac{\prod_{n=1}^k (1 + \frac{s}{\omega_{Zn}})}{\prod_{m=1}^l (1 + \frac{s}{\omega_{Pm}})} \frac{\prod_{n=1}^v (1 + \frac{s}{Q_n \omega_{Zn}} + \frac{s^2}{\omega_{Zn}^2})}{\prod_{m=1}^w (1 + \frac{s}{Q_m \omega_{Pm}} + \frac{s^2}{\omega_{Pm}^2})}, \quad (\text{F.2})$$

where  $s$  is the complex angular frequency,  $k_{\text{LISO}}$  is the gain factor of this notation (called factor in LISO \*.fil files),  $\omega_{Zn} = 2\pi f_{Zn}$  with  $f_{Zn}$  being the frequency of the zero in Hz and  $\omega_{Pm} = 2\pi f_{Pm}$  with  $f_{Pm}$  being the frequency of the pole in Hz.

A single zero appears in this notation only as a  $f_{Zn}$ . A single pole appears in this notation only as a  $f_{Pm}$ . Single zeros and poles are represented in the first fraction of Equation F.2. A double zero or pole appears in this notation as a pair  $(f_{Zn}, Q_n)$  or  $(f_{Pm}, Q_m)$  respectively. Double zeros and poles are represented in the second fraction of Equation F.2.

## F.2 Transformation between the two notations

When changing from the one to the other notation, the values of the single and complex zeros and poles and the gain factors need to be converted to the values of the other notation.

### F.2.1 Transformation from single-complex zero pole notation to f/Q-value notation

Single zeros transform in the following way:

$$\begin{aligned} f_{Zn} &= -\frac{\operatorname{Re}(z_n)}{2\pi}, \\ k_{\text{LISO}} &= k_{\text{DB}} (-\operatorname{Re}(z_n)). \end{aligned} \quad (\text{F.3})$$

Complex zero pairs transform like this to a  $(\omega_{Zn}, Q_n)$  pair:

$$\begin{aligned} f_{Zn} &= \frac{\sqrt{\operatorname{Re}(z_n)^2 + \operatorname{Im}(z_n)^2}}{2\pi}, \\ Q_n &= -\frac{\sqrt{\operatorname{Re}(z_n)^2 + \operatorname{Im}(z_n)^2}}{2\operatorname{Re}(z_n)}, \\ k_{\text{LISO}} &= k_{\text{DB}} (\operatorname{Re}(z_n)^2 + \operatorname{Im}(z_n)^2). \end{aligned} \quad (\text{F.4})$$

Single poles transform in the following way:

$$\begin{aligned} f_{Pm} &= -\frac{\operatorname{Re}(p_m)}{2\pi}, \\ k_{\text{LISO}} &= \frac{k_{\text{DB}}}{(-\operatorname{Re}(p_m))}. \end{aligned} \quad (\text{F.5})$$

Complex pole pairs transform like this to a  $(\omega_{Pm}, Q_m)$  pair:

$$\begin{aligned} f_{Pm} &= \frac{\sqrt{\operatorname{Re}(p_m)^2 + \operatorname{Im}(p_m)^2}}{2\pi}, \\ Q_m &= -\frac{\sqrt{\operatorname{Re}(p_m)^2 + \operatorname{Im}(p_m)^2}}{2\operatorname{Re}(p_m)}, \\ k_{\text{LISO}} &= \frac{k_{\text{DB}}}{(\operatorname{Re}(p_m)^2 + \operatorname{Im}(p_m)^2)}. \end{aligned} \quad (\text{F.6})$$

For single or complex poles with the value 0 in the data base notation one needs to add poles in LISO at very low frequencies, that is frequencies well below frequencies from which onwards the transfer function is supposed to be valid.

The next equation shows how the gain factor accumulates for more than one single or complex zero or pole. As single and complex zeroes, both denoted earlier as  $z$ , appear in the same equation, the notation  $z_{SG}$  is introduced for a single zero and  $z_{CP}$  for a complex zero. For single and complex poles, both denoted earlier as  $p$ , the notation  $p_{SG}$  is introduced for a single pole and  $p_{CP}$  for a complex pole. This is how the gain factor is transformed for more than one single or complex zeroes or poles:

$$k_{LISO} = k_{DB} \prod_{n=1}^k (-\text{Re}(z_{SGn})) \prod_{n=1}^v (\text{Re}(z_{CPn})^2 + \text{Im}(z_{CPn})^2) \prod_{m=1}^l \frac{1}{(-\text{Re}(p_{SGm}))} \prod_{m=1}^w \frac{1}{(\text{Re}(p_{CPm})^2 + \text{Im}(p_{CPm})^2)} . \quad (\text{F.7})$$

### F.2.2 Transformation from f/Q-value notation to single-complex zero pole notation

To convert from f/Q-value notation to single-complex zero pole notation the equations in subsection F.2.1 need to be solved to determine the Re and Im parts of the single or complex poles and zeros and  $k_{DB}$ .

This yields for complex zeros

$$z_{1,2} = -\frac{2\pi f_{Zn}}{2Q_n} \pm i \frac{2\pi f_{Zn}}{2Q_n} \sqrt{4Q_n^2 - 1} , \quad (\text{F.8})$$

$$k_{DB} = \frac{k_{LISO}}{2\pi f_{Zn}} .$$

For complex poles one obtains

$$p_{1,2} = -\frac{2\pi f_{Pm}}{2Q_m} \pm i \frac{2\pi f_{Pm}}{2Q_m} \sqrt{4Q_m^2 - 1} , \quad (\text{F.9})$$

$$k_{DB} = k_{LISO} 2\pi f_{Pm} .$$

## F.3 Example

A transfer function with a double pole at 100 Hz and 0 gain at DC is represented in the two different notations in the following way:

LISO	$f_{P1} = 100, Q_1 = 0.5, k_{LISO} = 1$
DB	$p_1 = -628.3185, p_2 = -628.3185, k_{DB} = 3.9478 \times 10^5$

For a graphical representation of this transfer function see Figure F.1.

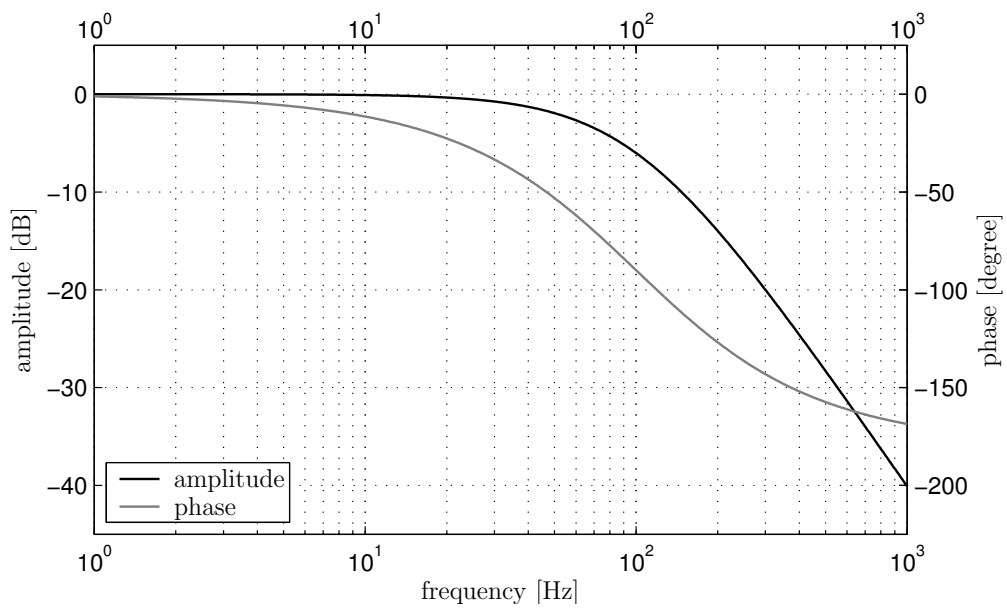


**Figure F.1:** Bode plot of a transfer function with the parameters  $f_{P1} = 100$ ,  $Q_1 = 0.5$ , and  $k_{LISO} = 1$  in LISO notation and the parameters  $p_1 = -628.3185$ ,  $p_2 = -628.3185$ , and  $k_{DB} = 3.9478 \times 10^5$  in single-complex zero pole notation.

## Appendix G

### Optical layout of GEO 600

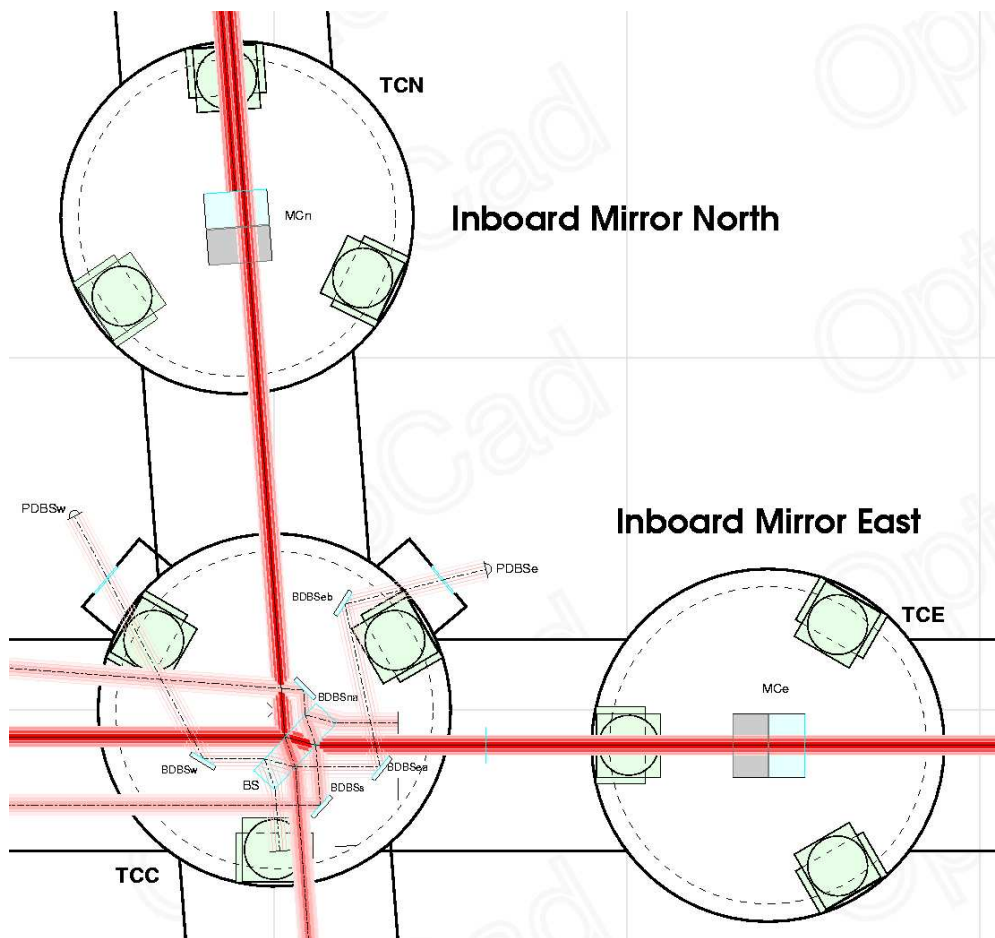


**Figure G.1:** Inboard mirrors (MCN, MCE) of the optical layout of GEO 600

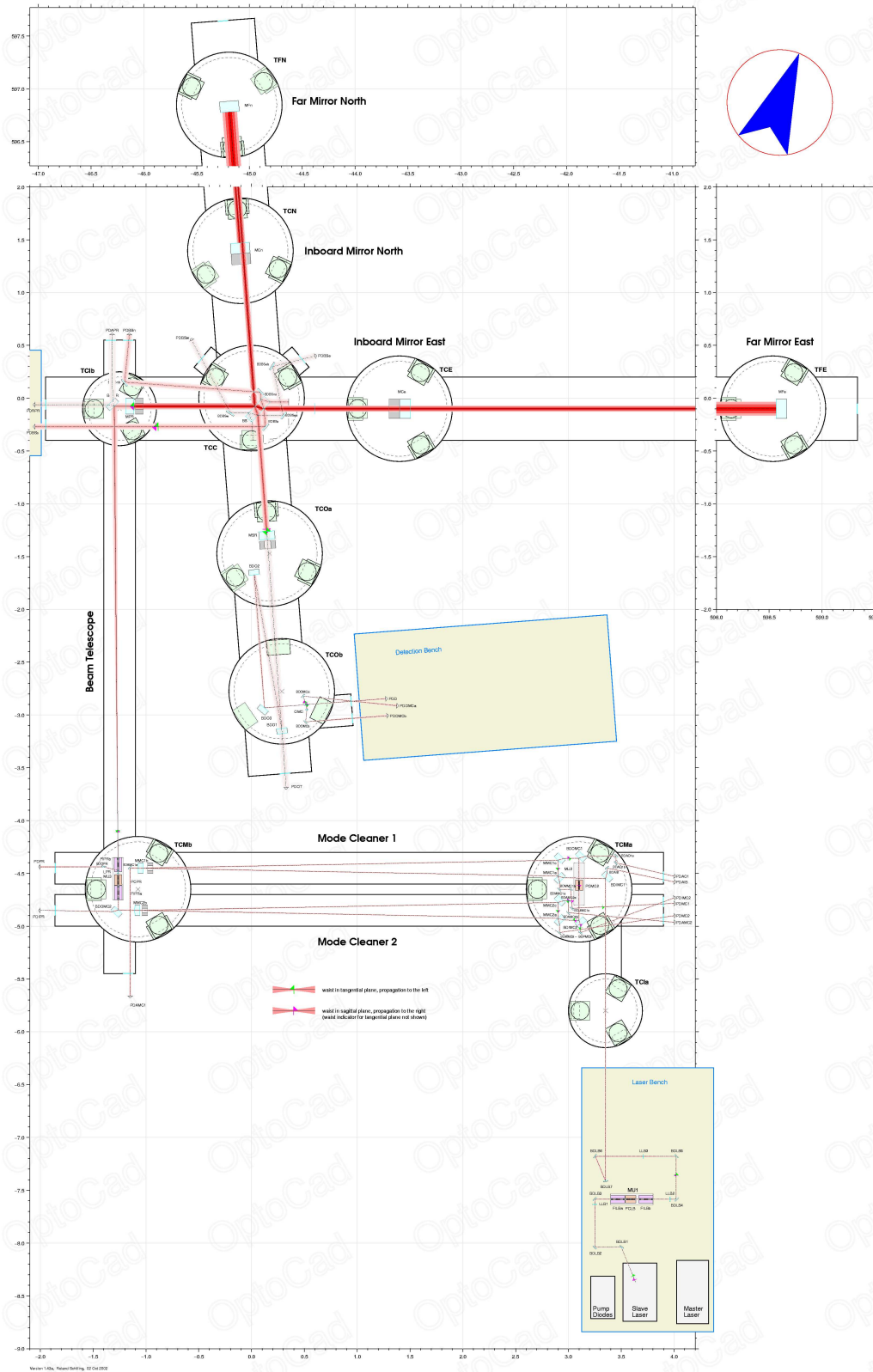
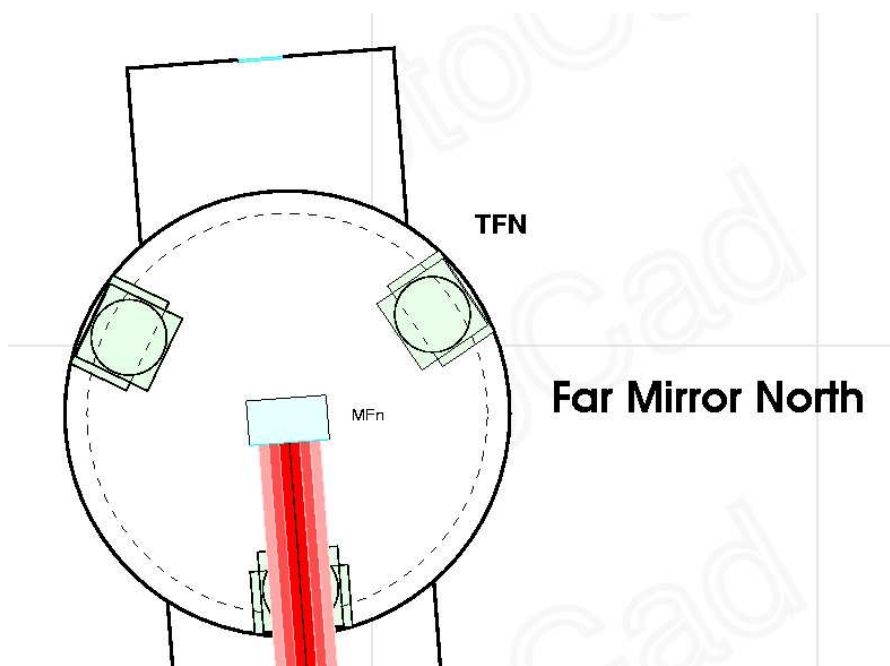


Figure G.2: Complete optical layout of GEO 600





**Figure G.3:** Mirror far north (MFN) of the optical layout of GEO 600



# Appendix H

## The electrostatic drive

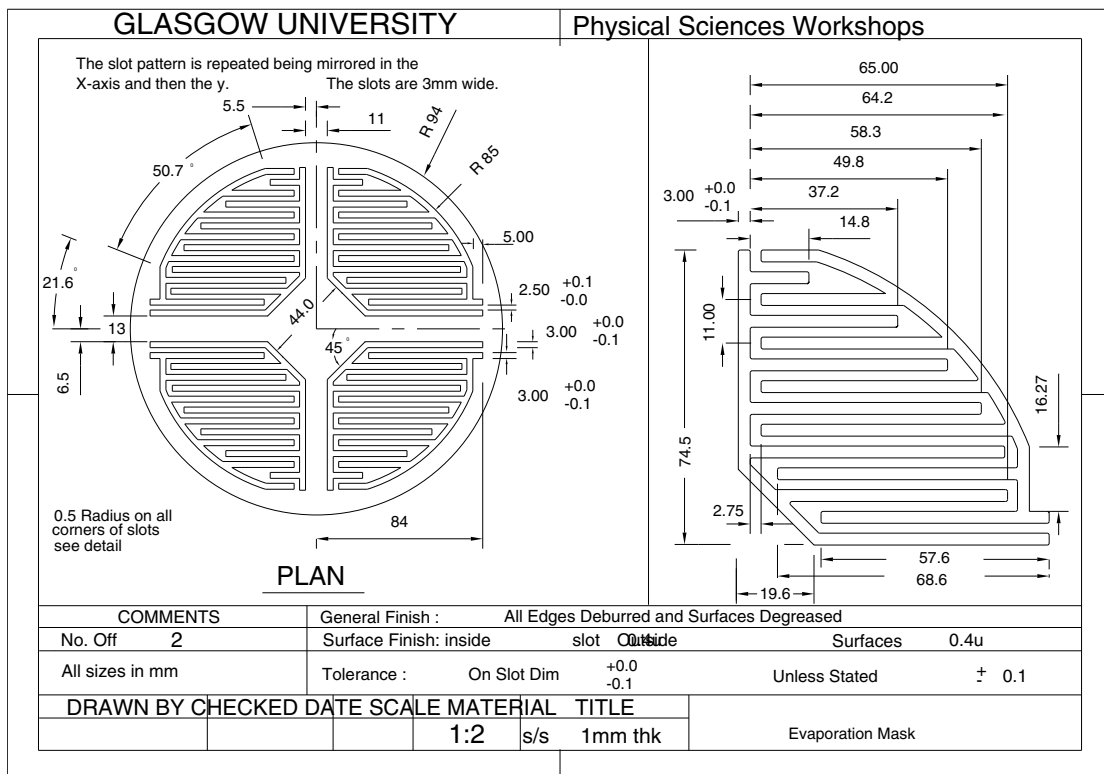


**Figure H.1:** Schematic of the electrostatic drive showing details of the capacitor quadrants



# **Appendix I**

## **Electronics**













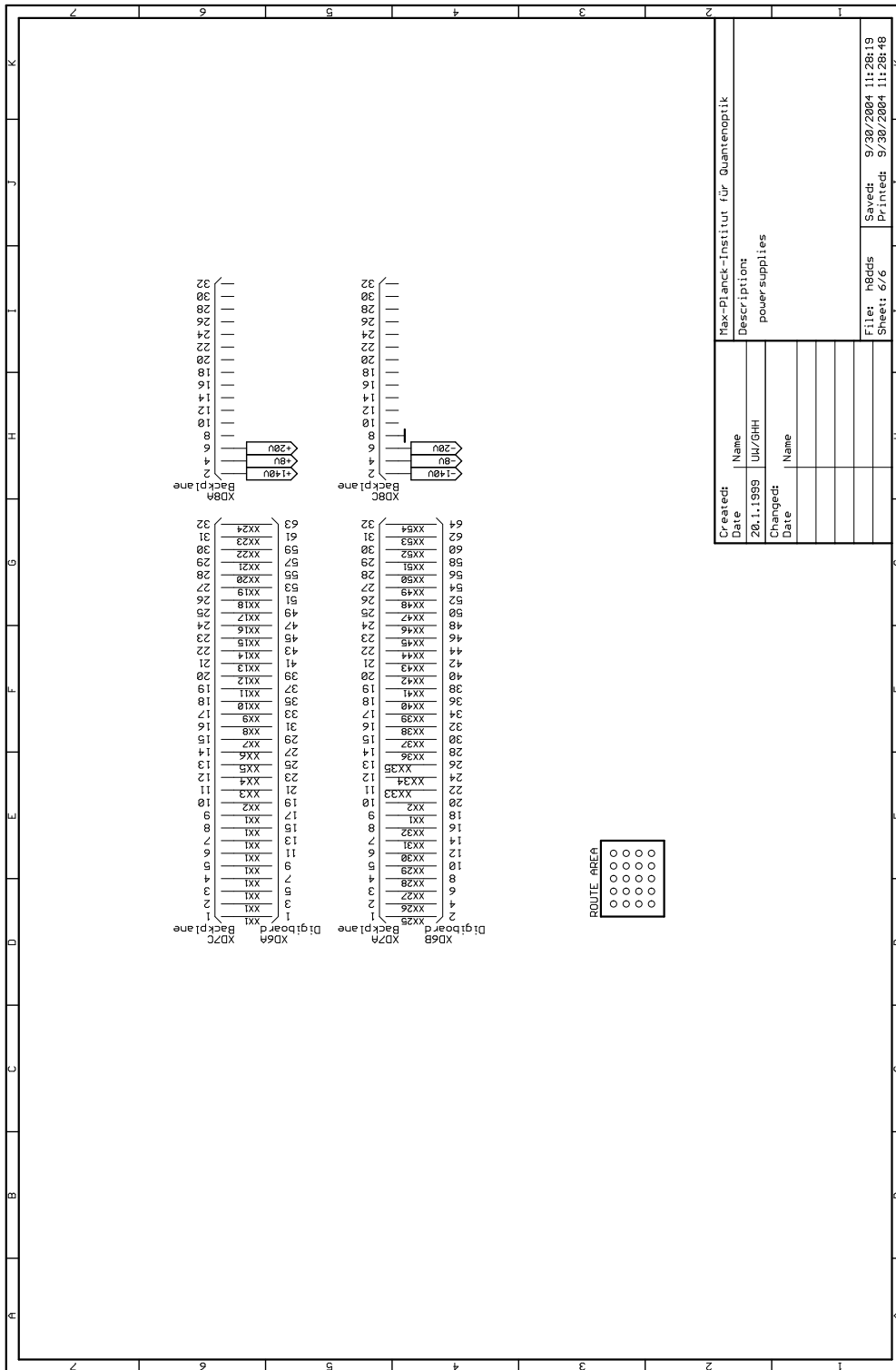
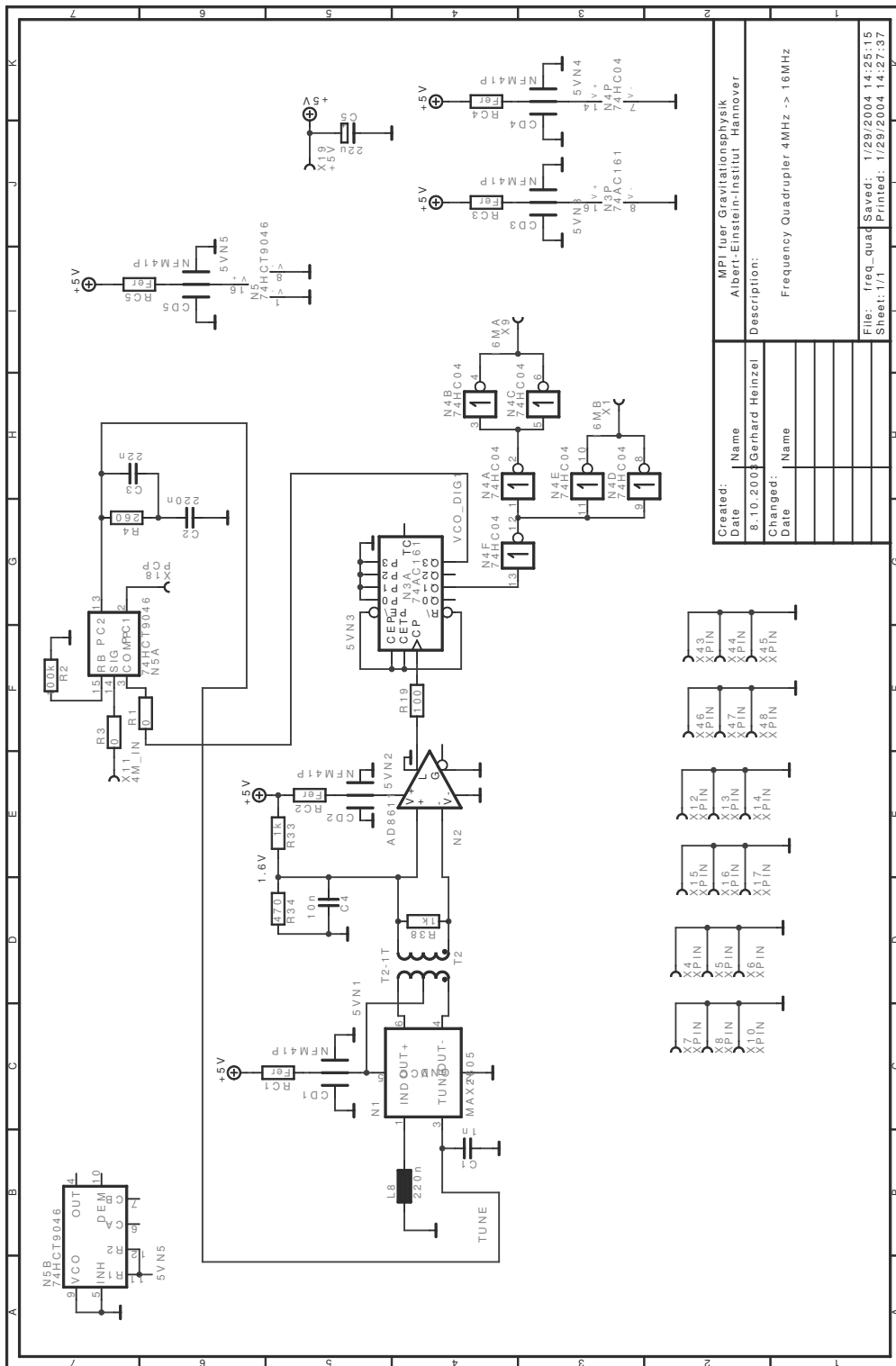


Figure I.6: Power supplies of the microcontroller electronics



Created:	Name	Description:
8.10.2004	Gerhard Heinzel	Frequency Quadrupler 4MHz -> 16MHz
Changed:	Name	
Date		

File: freq\_quad Saved: 1/29/2004 14:25:15  
 Sheet: 1/1 Printed: 1/29/2004 14:27:37

Figure I.7: Circuit to quadruplicate the 222 Hz signal of the data acquisition system

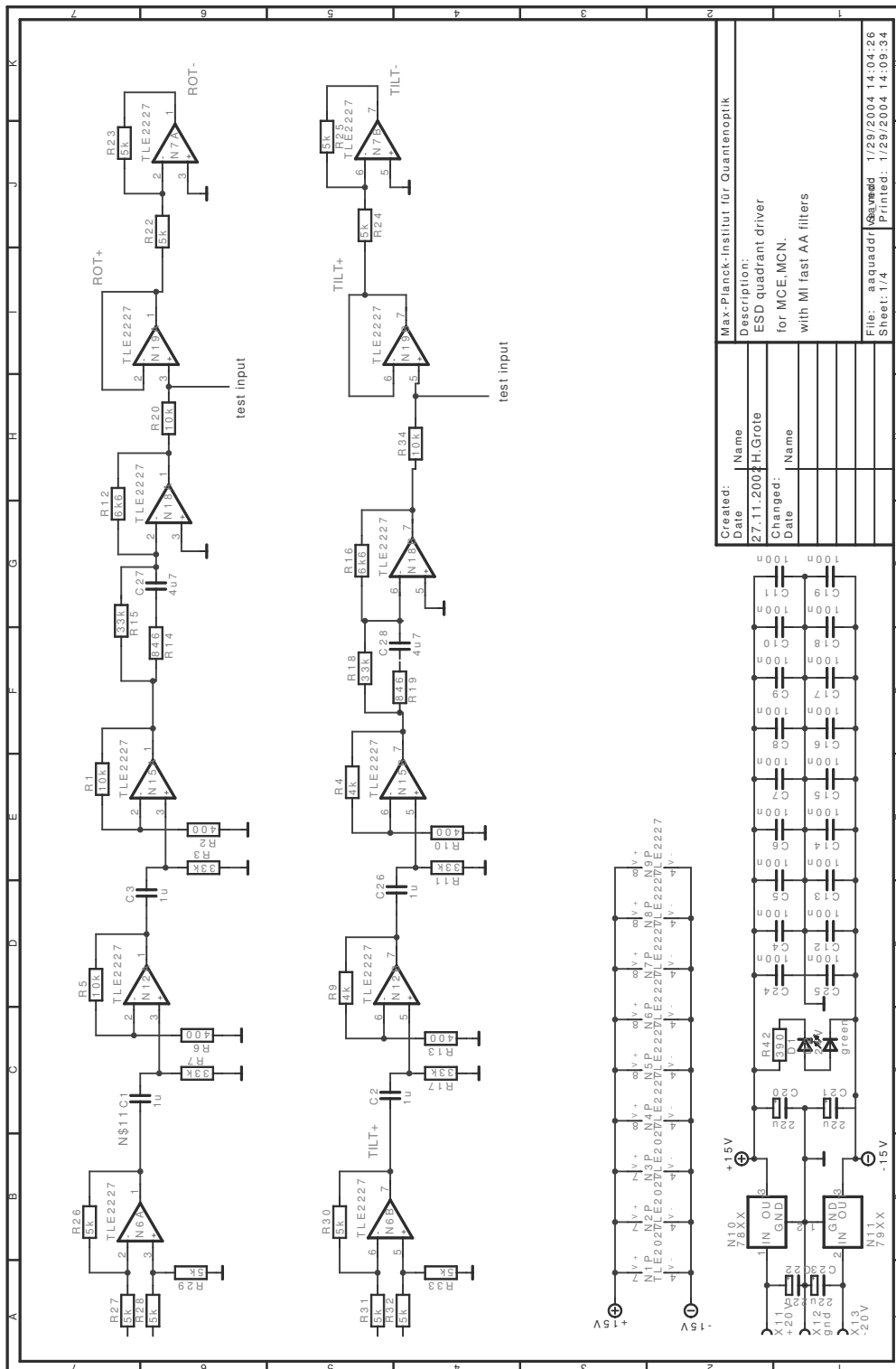


Figure I.8: Auto alignment quadrant driver of the electro static drive

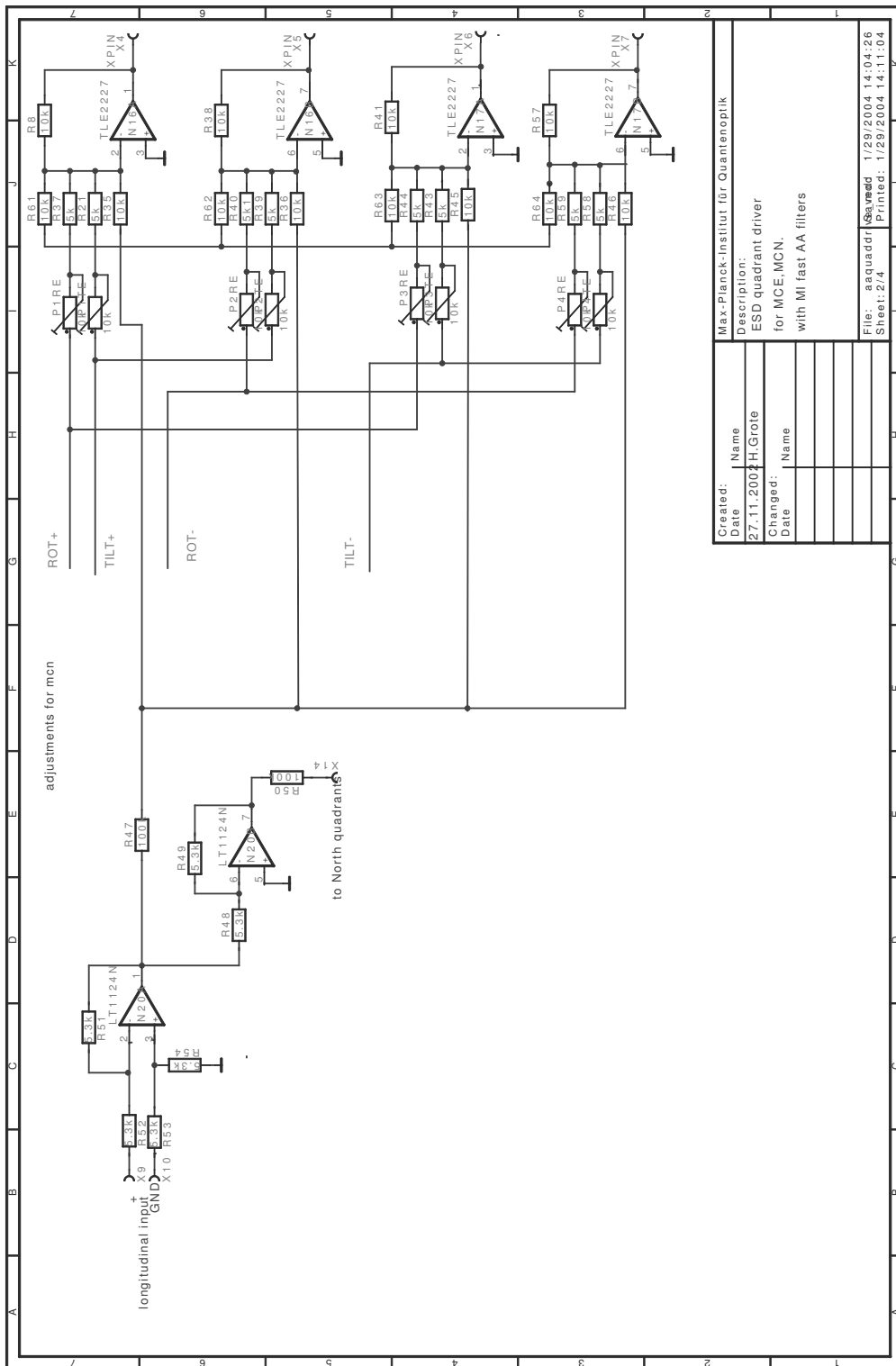


Figure I.9: MCE electro static drive quadrant driver.







## Bibliography

- [1] A. Einstein: *Die Grundlage der allgemeinen Relativitätstheorie* Annalen der Physik, Band **49**, Heft 7, 169-822 (1916).
- [2] H. Bondi, M.G.J. van der Burg, A.W.K. Metzner: *Gravitational waves in general relativity* Proc. Roy. Soc. Lond. **A 269**, 21 (1962).
- [3] R.A. Hulse, J.H. Taylor: *Discovery of a pulsar in a binary system* Astroph. Jour. (Letters) **195**, L51-L53 (1975).
- [4] J.H. Taylor, L.A. Fowler, P.M. McCulloch: *Measurements of general relativistic effects in the binary pulsar PSR 1913 + 16* Nature **277**, 437-440 (1979).
- [5] B.F. Schutz: *Gravitational Radiation - Encyclopedia of Astronomy and Astrophysics* Institute for Physics Publishing/ Nature publishing group, **Vol. 2**, 1030-1042 (Bristol, Philadelphia, London 2001).
- [6] Z.K. Geng, W.O. Hamilton, W.W. Johnson, E. Mauceli, S.M. Merkowitz, A. Morse, N. Solomonson: *Operation of the ALLEGRO Detector at LSU* First Edoardo Amaldi Conference on Gravitational Wave Experiments, edited by E. Coccia, G. Pizella, and F. Ronga (World Scientific Publishing Co., Singapore, 1995).
- [7] J. P. Zendri et al.: *Status report of the gravitational wave detector AURIGA* in “Gravitational waves”, Proceedings of the 3rd Amaldi Conference, (CalTech - California, 1999), edited by S.Meshkov, AIP Conference Proceedings, New York, 421-422 (2000).
- [8] P. Astone: *Long-term operation of the Rome Explorer cryogenic gravitational wave detector* Phys. Rev. **D 47**, No.2, 362-375 (1997).
- [9] P. Astone et al.: *The next science run of the g.w. detector Nautilus* Proceedings of the 4th Amaldi Conference on gravitational waves, Class. Quantum Grav. **19**, 1911-1917 (2002).
- [10] D. Coward, D. Blair, R. Clay, G. Mazzitelli: *Improved sensitivity of NIOBE in 2001 and the search for anomalous cosmic ray events* Proceedings of the 4th Amaldi Conference on gravitational waves, Class. Quantum Grav. **19**, 1871-1875 (2002).
- [11] V. Fafone: *Resonant-mass detectors: status and perspectives* Proceedings of the 5th Edoardo Amaldi Conference on Gravitational waves, Tirrenia (Pisa), Class. Quantum Grav. **21**, No.5, 377-383 (2004).
- [12] A. de Waard et al.: *Cooling down MiniGRAIL to milli-Kelvin temperatures* Proceedings of the 5th Edoardo Amaldi Conference on Gravitational waves, Tirrenia (Pisa), Class. Quantum Grav. **21** No.5 465-471 (2004).
- [13] O.D. Aguiar et al.: *The Brazilian spherical detector: progress and plans* Proceedings of the 5th Edoardo Amaldi Conference on Gravitational waves, Tirrenia (Pisa), Class. Quantum Grav. **21**, No.5 457-463 (2004).
- [14] M. Cerdonio, L. Conti, J.A. Lobo, A. Ortolan, L. Taffarello, J.P. Zendri: *Wideband Dual Sphere Detector of Gravitational Waves* Phys. Rev. Lett. **87**, 031101 (2001).

- [15] R. Takahashi et al.: *Status of TAMA300* Class. Quantum Grav. **21**, No.5, 403-408 Sp. Iss. SI MAR 7 (2004).
- [16] B. Willke et al.: *Status of the GEO 600* Class. Quantum Grav. **21**, 417-423 (2004).
- [17] D. Sigg et al.: *Commissioning of LIGO detectors* Class. Quantum Grav. **21**, 409-415 (2004).
- [18] A. Freise and the VIRGO Collaboration: *Status of VIRGO* <http://arxiv.org/abs/gr-qc/0406123>
- [19] H. Tagoshi, T. Tanaka, N. Kanda, et al.: *Searching for gravitational waves from inspiraling compact binaries using TAMA300 data* Int. J. Mod. Phys. **D 9** (3), 319-323 JUN (2000).
- [20] H. Grote, A. Freise, M. Malec, G. Heinzel, B. Willke, H. Lück, K.A. Strain, J. Hough, K. Danzmann: *Dual recycling for GEO 600* Class. Quantum Grav. **21**, 473-480 (2004).
- [21] B. Abbott and the LIGO Scientific Collaboration: *Detector Description and Performance for the First Coincidence Observations between LIGO and GEO* Nucl. Instr. Methods **A 517**, 154-179 (2004).
- [22] P. Fritschel: *Second generation instruments for the laser interferometer gravitational wave observatory (LIGO)* Proceedings of the society of photo-optical instrumentation engineers (SPIE) **4856**, 282-291 (2003).
- [23] S. Braccini: *The VIRGO suspensions* Proceedings of the 4th Amaldi Conference on gravitational waves Class. Quantum Grav. **19**, 1623-1629 (2002).
- [24] C. Misner, K. Thorne, J.A. Wheeler: *Gravitation* W.H. Freeman and Company (1973).
- [25] M. Hewitson: *On aspects of characterising and calibrating the interferometric gravitational wave detector, GEO 600* Ph.D. thesis University of Glasgow (2004).
- [26] C. Cutler, K. S. Thorne: *An overview of gravitational-wave sources* World Scientific, Proceedings of the 16th International Conference on General Relativity and Gravitation (2002).
- [27] B. Allen, M.A. Papa, B.F. Schutz: *Optimal Strategies for Sinusoidal Signal Detection* Phys. Rev. **D 66**, 102003 (2002).
- [28] A.G. Lyne, F. Graham-Smith: *Pulsar astronomy* Cambridge University press (1990).
- [29] <http://www.atnf.csiro.au/research/pulsar/psrcat/> *ATNF Pulsar Catalogue*
- [30] D.R. Lorimer: *Binary and Millisecond Pulsars at the New Millennium* Living Rev. Relativity **4**, (2001), 5. [Online article]: cited on 22 Jul 2004.
- [31] F. Verbunt: *Origin and evolution of X-ray binaries and binary radio pulsars* Annu. Rev. Astron. Astrophys. **31**, 93-127 (1993).
- [32] D.C Backer, S.R. Kulkarni, C. Heiles, M.M. Davis, W.M. Goss: *A Millisecond Pulsar* Nature **300**, 615-618 (1982).
- [33] M. van der Klis: *Millisecond oscillations in x-ray binaries* Annu. Rev. Astron. Astrophys. **38**, 717-60 (2000).
- [34] R. Wijnands, M. van der Klis, J. Homan, D. Chakrabarty, C.B. Markwardt, E.H. Morgan: *Quasi-periodic X-ray brightness fluctuations in an accreting millisecond pulsar* Nature **424**, 44-47 (2003).
- [35] D. Chakrabarty, E.H. Morgan, M.P. Muno, D.K. Galloway, R. Wijnands, M. van der Klis, C.B. Markwardt: *Nuclear-powered millisecond pulsars and the maximum spin frequency of neutron stars* Nature **424**, 42-44 (2003).

- 
- [36] G.B. Cook, S.L. Shapiro, S.A. Teukolsky: *Recycling pulsars to millisecond periods in general relativity* Astrophys. J. **423**, L117-L120 (1994).
- [37] R.V. Wagoner: *Heartbeats of a neutron star* Nature **424**, 27-28 (2003).
- [38] L. Bildsten: *Gravitational Radiation and rotation of accreting neutron stars* Astrophys. J. **501**, L89-L93 (1998).
- [39] L. Bildsten: *Arresting Accretion Torques with Gravitational Radiation* Astronomical society of the pacific conference series **302**, 289-294 (2003).
- [40] D.I. Jones, N. Andersson: *Gravitational waves from freely precessing neutron stars* Mon. Not. R. Astron. Soc. **331**, 203-220 (2002).
- [41] N. Andersson: *A new class of unstable modes of rotating relativistic stars* Astrophys. J. **502**, 708-713 (1998).
- [42] J.L. Friedman, S.M. Morsink: *Axial instability of rotating relativistic stars* Astrophys. J. **502**, 714-720 (1998).
- [43] P. Arras, E.E. Flanagan, S.M. Morsink, A.K. Schenk, S.A. Teukolsky, I. Wasserman: *Saturation of the r-mode instability* Astrophys. J. **591**, 1129-1151 (2003).
- [44] G. Ushomirsky, C. Cutler, L. Bildsten: *Deformations of accreting neutron star crusts and gravitational wave emission* Mon. Notic. Roy. Astron. Soc. **319** (3), 902-932 (2000).
- [45] C. Cutler: *Gravitational waves from neutron stars with large toroidal B-Fields* Phys. Rev. **D 66**, 084025 (2002).
- [46] B. Abbott et al.: *Setting upper limits on the strength of periodic gravitational waves from PSR J1939+2134 using the first science data from the GEO 600 and LIGO detectors* Phys. Rev. **D 69**, 082004 (2004).
- [47] P. Jaranowski, A. Królak, B. F. Schutz: *Data analysis of gravitational-wave signals from spinning neutron stars: The signal and its detection* Phys. Rev. **D 58**, 063001 (1998).
- [48] H. Schulz: *Physik mit Bleistift* Springer Verlag second edition (1993).
- [49] S. Bonazzola, E. Gourgoulhon: *Gravitational waves from pulsars: emission by the magnetic field induced distortion* Astron. Astrophys. **312**, 675 (1996).
- [50] H. Goldstein, C. Poole, J. Safko: *Classical mechanics* Addison Wesley third edition (2002).
- [51] I. Bronstein, K. Semendjajew: *Taschenbuch der Mathematik* B.G. Teubner Verlagsgesellschaft, 25. durchgesehene Auflage (1991).
- [52] <http://www.lsc-group.phys.uwm.edu/lal/>
- [53] M. Zeilik, E. v. P. Smith: *Introductory Astronomy and Astrophysics* Saunders College Publishing second edition (1987).
- [54] A. Fetzner, H. Fränkl: *Mathematik* VDI Verlag, Volume 1, 4. Auflage (1995).
- [55] C. Cutler: private communication.
- [56] R. Dupuis: private communication.
- [57] <http://pulsar.princeton.edu/tempo/index.html>
- [58] W. Graham: private communication.
- [59] K. Riles, D. Chin: private communication.

- [60] P. Horowitz, W. Hill: *The art of electronics* Cambridge University Press second edition (1989).
- [61] K. Kötter et al.: *Data acquisition and detector characterisation of GEO 600* Class. Quantum Grav. **19**, 1399-1407 (2002).
- [62] G. Heinzel: *LISO - Program for Linear Simulation and Optimization of analog electronic circuits* GEO DC logbook page 35.
- [63] K. Kötter: *Data Acquisition and Data Analysis for the Gravitational-Wave Detector GEO 600* Ph.D. thesis, Universität Hannover (2004).
- [64] R.B. Langley: *The GPS End-of-Week Rollover* GPS World **9** No.11, 40-47 (1998).
- [65] K. Kötter, M. Hewitson, H. Ward: *Timing accuracy of the GEO 600 data acquisition system* Class. Quantum Grav. **21**, 493-500 (2004).
- [66] G. Heinzel, V. Wand, A.F. García Marín, O. Jennrich, C. Braxmaier, D. Robertson, K. Middleton, D. Hoyland, A. Rüdiger, R. Schilling, U. Johann, K. Danzmann: *The LTP interferometer and phasemeter* Class. Quantum Grav. **21**, 581-587 (2004).
- [67] M. Hewitson: private communication.
- [68] S. Goßler, G. Cagnoli, D.R.M. Crooks, H. Lück, S. Rowan, K.A. Strain, J.R. Smith, J. Hough, K. Danzmann: *Damping and tuning of the fiber violin modes in monolithic silica suspensions* Class. Quantum Grav. **21**, 923-933 (2004).
- [69] E. Hering, R. Martin, M. Stohrer: *Physik für Ingenieure* VDI-Verlag GmbH (1988).
- [70] H. Grote: *Making it Work: Second Generation Interferometry in GEO 600!* Ph.D. thesis, Universität Hannover (2003).
- [71] GEO logbook page 1206
- [72] H. Grote: private communication.
- [73] R. Dupuis: *Known pulsar search* talk at the LSC meeting March 20-23, 2002 (2002).
- [74] R. Dupuis: *Bayesian searches for gravitational waves from pulsars* Ph.D. thesis, University of Glasgow (2004).
- [75] D.S. Sivia: *Data Analysis - A Bayesian Tutorial* Oxford Science Publication (1996).
- [76] A.M. Sintes, B.F. Schutz: *Coherent Line Removal: Filtering out harmonically related line interference from experimental data, with application to gravitational wave detectors* Phys. Rev. **D 58**, 122003 (1998).
- [77] A.M. Sintes, B.F. Schutz: *Removing non-stationary, non-harmonic external interference from gravitational wave interferometer data* Phys. Rev. **D 60**, 062001 (1999).
- [78] <https://info.geo600.uni-hannover.de/frequencies/>
- [79] B. Abbott and the LIGO Scientific Collaboration: *Limits on the gravitational wave strength from isolated radio pulsars using data from the second science run of LIGO* in preparation
- [80] S. Goßler: *The suspension system of the interferometric gravitational-wave detector GEO 600* Ph.D. thesis, Universität Hannover (2004).
- [81] B.F. Schutz: *Determining the Hubble constant from gravitational wave observations* Nature **323**, 310-311 (1987).

- 
- [82] B.F. Schutz: *Lighthouses of Gravitational Wave Astronomy* Proceedings of the MPA ESO MPE USM Joint Astronomy Conference, 207-224 (2002).
- [83] D. Baskarant, L.P. Grishchuk: *Components of the gravitational force in the field of a gravitational wave* <http://xxx.lanl.gov/abs/gr-qc/0309058>
- [84] L.P. Grischuk: private communication.
- [85] A. Rüdiger: private communication and internal GEO 600 documentation *Excitation of interferometer mirror by light pressure*
- [86] J. Smith et. al.: *Comissioning, characterization and operation of the dual-recycled GEO 600 Class*. Quantum Grav. **21** 1737-1745 (2004).
- [87] J. Smith: private communication.
- [88] M. Plissi, K.A. Strain: personal communication.
- [89] [www.ptb.de/en/publikationen/news/pdf/news982e.pdf](http://www.ptb.de/en/publikationen/news/pdf/news982e.pdf)
- [90] F. Seifert: *Entwicklung einer quantenrauschbegrenzten Leistungsstabilisierung für ein Präzisionslasersystem* Diploma thesis, Universität of Hannover (2002).
- [91] Hamamatsu product description.
- [92] Integrated Photomatrix Ltd. RS product description.
- [93] G. Heinzl: private communication.
- [94] W. Winkler: private communication.
- [95] W. B. Jackson, N. M. Amer, A. C. Boccara, D. Fournier: *Photothermal deflection spectroscopy and detection* Appl. Optics **20** No.8, 1333-1344 (1981).
- [96] GEO logbook page 1319
- [97] GEO logbook pages 1290 and 1294.
- [98] H. Sun: *Thin lense equation for a Real Laser Beam with Weak Lense Aperture Truncation* Opt. Eng. **37** No.11, 2906-2913 (1998).
- [99] [http://www.gb.nrao.edu/~rfisher/Ephemerides/ephem\\_use.html](http://www.gb.nrao.edu/~rfisher/Ephemerides/ephem_use.html)
- [100] <http://www.atnf.csiro.au/research/pulsar/psrcat/>
- [101] B. Allen: *Gravitational Wave Detector Sites*. <http://arxiv.org/pdf/gr-qc/9607075>
- [102] Matlab Help, Version 6.5.0.180913a Release 13.
- [103] F. J. Harris: *On the use of Windows for Harmonic Analysis with the Discrete Fourier Transform* Proceedings of the IEEE **66** No. 1, 51-74 (1978).
- [104] <https://info.geo600.uni-hannover.de/GEOStatus/Main>



## Acknowledgements

First of all I would like to thank Prof. Karsten Danzmann for giving me the opportunity to participate in the GEO 600 project. He has provided me with very motivating and valuable input whenever needed.

Without Gerhard Heinzl's guidance and invaluable support this work would not have been possible in its present form. I was often amazed at how simple a seemingly unsolvable problem could suddenly become when looking at it from the right perspective. I would like to thank him for his help and guidance during the past years.

It is my pleasure to thank Harald Lück and Benno Willke for advice, support and interesting discussions. I thank Kasem Mossavi for his cooperation in working on the photon pressure actuator. Many thanks go to Martin Hewitson who always had an open ear for calibration issues and data processing. As well I would like to thank Andreas Freise for the belligerent discussions we had, which always proved to be fruitful in the end. Substitutionally for all the others I would like to thank Hartmut Grote, Antonio García Marín, Stefan Goßler, Siong Heng, Michèle Heurs, Stefan Hild, Volker Leonhardt, Luciano Ribichini, Karsten Kötter, Michaela Malec, Frank Seifert, Joshua Smith, Konrad Mors, Johanna Bogenstahl, Andreas Weidner, and Walter Grass for making the Max-Planck-Institute for gravitational physics a place where one enjoys to work at.

I would like to thank Jim Hough, Henry Ward, and Graham Woan for their support during my stays in Glasgow. I would like to thank Graham Woan for the introduction to pulsars and very useful discussions on gravitational wave signals from pulsars. Ken Strain had always been the source of deep knowledge and pragmatic approaches to problem solving. I have enjoyed working with him not only in Glasgow. For answering numerous questions on suspensions I would like to thank Mike Plissi and Ken Strain. In particular I enjoyed the valuable discussions I have had with Oliver Jenrich and Malik Rakhmanov. Substitutional for all the others I would like to thank Geppo Cagnoli, Morag Casey, Alastair Grant, Christian Krillow, Valerie Nadeau, and Gail Penny for making me feel welcome in Glasgow.

For his unrelenting dedication for the European Graduate College on "Interference and Quantum Applications" I would like to thank Prof. Tiemann. Substitutionally for everybody I would like to thank Olivier Allard, Cristina Figl, André Grimpe, Kirsten Jaspers, Michaela Malec, and Nils Rehbein who put life into the Graduate College.

My thanks goes to Glasgow once more to Réjean Dupuis and Matthew Pitkins for their support in learning the usage of the continuous gravitational wave time-domain search algorithm. At this point I would also like to thank the many authors of the LIGO Algorithm Library, who were always very patient and gave useful advice in using LAL. Many thanks also goes to Golm to Steffen Grunewald and Bernd Machenschalk, who had to put up with constant requests for extra storage of data and sudden panic attacks

## *Acknowledgements*

---

about lost data.

For proofreading I would like to thank Andreas Freise, Jan Harms, Gerhard Heinzl, Siong Heng, Martin Hewitson, Stefan Hild, Oliver Jennrich, Harald Lück, Michaela Malec, Albrecht Rüdiger, Roland Schilling, Joshua Smith, Benno Willke and Graham Woan.

Last but not least I would like to thank my family, in particular my grandmother for her inspiring interest she had always been showing in my work and the pleasure she took in women pursuing a career in science.



# Curriculum Vitae

Uta Anne Weiland  
Glünderstr. 7  
30167 Hannover

Born 14 June 1974 in Hannover, Germany

2004	Max-Planck-Institut für Gravitationsphysik, Albert-Einstein-Institut, Teilinstitut Hannover
2002 - 2003	two and three months long visits at the Institute for Gravitational Research, University of Glasgow, Great Britain
2000 - 2003	scholarship holder at the European Graduate College “Interference and Quantum Applications”
2000 - 2004	PhD student at the University of Hannover
1998	DESY summer student, Hamburg
1997 - 1998	Technical University of St. Petersburg, Russia
1995	internship at CALTECH, USA
1994 - 2000	Physics Diploma, University of Hannover
1991 - 1994	Allgemeine Hochschulreife, Matthias-Claudius-Gymnasium Gehrden
1990 - 1991	High School Diploma, Centerville High School, Dayton OH, USA; scholarship holder of the German Bundestag
1986 - 1990	Matthias-Claudius Gymnasium Gehrden
1984 - 1986	Orientierungsstufe Wennigsen
1980 - 1984	Grundschule Wennigsen



## List of publications

J.R. Smith, B. Allen, P. Aufmuth, C. Albert, S. Babak, R. Balasubramanian, B.W. Barr, S. Berukoff, A. Bunkowski, C. Cagnoli, C.A. Cantley, M.M. Casey, S. Chelkowski, D. Churches, T. Cokelaer, C.N. Colacino, D.R.M. Crooks, C. Cutler, K. Danzmann, R. Davies, R.J. Dupuis, E. Elliffe, C. Fallnich, A. Franzen, A. Freise, S. Goßler, A. Grant, H. Grote, S. Grunewald, J. Harms, G. Heinzl, I.S. Heng, A. Heptonstall, M. Heurs, M. Hewitson, S. Hild, J. Hough, Y. Itoh, L. Jones, S.H. Hutter, K. Kawabe, C.J. Killow, K. Kötter, B. Krishnan, V. Leonhardt, H. Lück, B. Machenschalk, M. Malec, R.A. Mercer, C. Messenger, S.D. Mohanty, K. Mossavi, S. Mukherjee, P. Murray, S. Nagano, G.P. Newton, M.A. Papa, M. Perreux-Lloyd, M. Pitkin, M. Plissi, V. Quetschke, V. Re, S. Reid, L. Ribichini, D.I. Robertson, N.A. Robertson, J.D. Romano, S. Rowan, A. Rüdiger, B.S. Sathyaprakash, R. Schilling, R. Schnabel, B.F. Schutz, F. Seifert, A.M. Sintes, P. Sneddon, K.A. Strain, I. Taylor, R. Taylor, A. Thüring, C. Ungarelli, H. Vahlbruch, A. Vecchio, J. Veitch, H. Ward, U. Weiland, H. Welling, P. Williams, B. Willke, W. Winkler, G. Woan, I. Zawischa: *Commissioning, characterization, and operation of the dual-recycled GEO 600 Class*. *Quantum Grav.* **21** 1737-1745 (2004).

The LIGO Scientific Collaboration: B. Abbott, R. Abbott, R. Adhikari, A. Ageev, B. Allen, R. Amin, S. B. Anderson, W. G. Anderson, M. Araya, H. Armandula, F. Asiri, P. Aufmuth, C. Aulbert, S. Babak, R. Balasubramanian, S. Ballmer, B. C. Barish, D. Barker, C. Barker-Patton, M. Barnes, B. Barr, M. A. Barton, K. Bayer, R. Beausoleil, K. Belczynski, R. Bennett, S. J. Berukoff, J. Betzwieser, B. Bhawal, I. A. Bilenko, G. Billingsley, E. Black, K. Blackburn, B. Bland-Weaver, B. Bochner, L. Bogue, R. Bork, S. Bose, P. R. Brady, V. B. Braginsky, J. E. Brau, D. A. Brown, S. Brozek, A. Bullington, A. Buonanno, R. Burgess, D. Busby, W. E. Butler, R. L. Byer, L. Cadonati, G. Cagnoli, J. B. Camp, C. A. Cantley, L. Cardenas, K. Carter, M. M. Casey, J. Castiglione, A. Chandler, J. Chapsky, P. Charlton, S. Chatterji, Y. Chen, V. Chickarmane, D. Chin, N. Christensen, D. Churches, C. Colacino, R. Coldwell, M. Coles, D. Cook, T. Corbitt, D. Coyne, J. D. E. Creighton, T. D. Creighton, D. R. M. Crooks, P. Csatorday, B. J. Cusack, C. Cutler, E. D'Ambrosio, K. Danzmann, R. Davies, E. Daw, D. DeBra, T. Delker, R. DeSalvo, S. Dhurandhar, M. Díaz, H. Ding, R. W. P. Drever, R. J. Dupuis, C. Ebeling, J. Edlund, P. Ehrens, E. J. Elliffe, T. Etzel, M. Evans, T. Evans, C. Fallnich, D. Farnham, M. M. Fejer, M. Fine, L. S. Finn, E. Flanagan, A. Freise, R. Frey, P. Fritschel, V. Frolov, M. Fyffe, K. S. Ganezer, J. A. Giaime, A. Gillespie, K. Goda, G. González, S. Goßler, P. Grandclément, A. Grant, C. Gray, A. M. Gretarsson, D. Grimmer, H. Grote, S. Grunewald, M. Guenther, E. Gustafson, R. Gustafson, W. O. Hamilton, M. Hammond, J. Hanson, C. Hardham, G. Harry, A. Hartunian, J. Heefner, Y. Hefetz, G. Heinzl, I. S. Heng, M. Hennessy, N. Hepler, A. Heptonstall, M. Heurs, M. Hewitson, N. Hindman, P. Hoang, J. Hough, M. Hrynevych, W. Hua, R. Ingley, M. Ito, Y. Itoh, A. Ivanov, O. Jennrich, W. W. Johnson, W. Johnston, L. Jones, D. Jungwirth, V. Kalogera, E. Katsavounidis, K. Kawabe, S. Kawamura, W. Kells, J. Kern, A. Khan, S. Killbourn, C. J. Killow, C. Kim, C. King, P. King, S. Klimenko, P. Klovekorn, S. Koranda, K. Kötter, J. Kovalik, D. Kozak, B. Krishnan, M. Landry, J. Langdale, B. Lantz, R. Lawrence, A. Lazzarini, M. Lei, V. Leonhardt, I. Leonor, K. Libbrecht, P. Lindquist, S. Liu, J. Logan, M. Lormand, M. Lubinski, H. Lück, T. T. Lyons, B. Machenschalk, M. MacInnis, M. Mageswaran, K. Mailand, W. Majid, M. Malec, F. Mann, A. Marin, S. Märka, E. Maros, J. Mason, K. Mason, O. Matherny, L. Matone, N. Mavalvala, R. McCarthy, D. E. McClelland,

M. McHugh, P. McNamara, G. Mendell, S. Meshkov, C. Messenger, V. P. Mitrofanov, G. Mitselmakher, R. Mittleman, O. Miyakawa, S. Miyoki, S. Mohanty, G. Moreno, K. Mossavi, B. Mours, G. Mueller, S. Mukherjee, J. Myers, S. Nagano, T. Nash, H. Naundorf, R. Nayak, G. Newton, F. Nocera, P. Nutzman, T. Olson, B. O'Reilly, D. J. Ottaway, A. Ottewill, D. Ouimette, H. Overmier, B. J. Owen, M. A. Papa, C. Parameswariah, V. Parameswariah, M. Pedraza, S. Penn, M. Pitkin, M. Plissi, M. Pratt, V. Quetschke, F. Raab, H. Radkins, R. Rakhola, M. Rakhmanov, S. R. Rao, D. Redding, M. W. Regehr, T. Regimbau, K. T. Reilly, K. Reithmaier, D. H. Reitze, S. Richman, R. Riesen, K. Riles, A. Rizzi, D. I. Robertson, N. A. Robertson, L. Robison, S. Roddy, J. Rollins, J. D. Romano, J. Romie, H. Rong, D. Rose, E. Rothhoff, S. Rowan, A. Rüdiger, P. Russell, K. Ryan, I. Salzman, G. H. Sanders, V. Sannibale, B. Sathyaprakash, P. R. Saulson, R. Savage, A. Sazonov, R. Schilling, K. Schlaufman, V. Schmidt, R. Schofield, M. Schrempel, B. F. Schutz, P. Schwinberg, S. M. Scott, A. C. Searle, B. Sears, S. Seel, A. S. Sengupta, C. A. Shapiro, P. Shawhan, D. H. Shoemaker, Q. Z. Shu, A. Sibley, X. Siemens, L. Sievers, D. Sigg, A. M. Sintes, K. Skeldon, J. R. Smith, M. Smith, M. R. Smith, P. Sneddon, R. Spero, G. Stapfer, K. A. Strain, D. Strom, A. Stuver, T. Summerscales, M. C. Sumner, P. J. Sutton, J. Sylvestre, A. Takamori, D. B. Tanner, H. Tariq, I. Taylor, R. Taylor, K. S. Thorne, M. Tibbits, S. Tilav, M. Tinto, K. V. Tokmakov, C. Torres, C. Torrie, S. Traeger, G. Traylor, W. Tyler, D. Ugolini, M. Vallisneri, M. van Putten, S. Vass, A. Vecchio, C. Vorvick, S. P. Vyachanin, L. Wallace, H. Walther, H. Ward, B. Ware, K. Watts, D. Webber, A. Weidner, U. Weiland, A. Weinstein, R. Weiss, H. Welling, L. Wen, S. Wen, J. T. Whelan, S. E. Whitcomb, B. F. Whiting, P. A. Willems, P. R. Williams, R. Williams, B. Willke, A. Wilson, B. J. Winjum, W. Winkler, S. Wise, A. G. Wiseman, G. Woan, R. Wooley, J. Worden, I. Yakushin, H. Yamamoto, S. Yoshida, I. Zawischa, L. Zhang, N. Zotov, M. Zucker, and J. Zweizig: *Analysis of LIGO data for gravitational waves from binary neutron stars* Phys. Rev. **D 69** No.12 122001 (2004).

The LIGO Scientific Collaboration: *Analysis of first LIGO science data for stochastic gravitational waves* Phys. Rev. **D 69** No.12 122004 (2004).

The LIGO Scientific Collaboration: *First upper limits from LIGO on gravitational wave bursts* Phys. Rev. **D 69** No.10 102001 (2004).

The LIGO Scientific Collaboration: *Setting upper limits on the strength of periodic gravitational waves from PSR J1939+2134 using the first science data from the GEO 600 and LIGO detectors* Phys. Rev. **D 69** No.8 (2004).

B. Willke, P. Aufmuth, C. Aulbert, S. Babak, R. Balasubramanian, B. Barr, G. Cagnoli, C.A. Cantley, S. Chelkowski, D. Churches, C.N. Colacino, D.R.M. Crooks, C. Cutler, K. Danzmann, R. Davies, R.J. Dupuis, E.J. Elliffe, C. Fallnich, A. Freise, S. Goßler, A. Grant, H. Grote, S. Grunewald, J. Harms, G. Heinzl, I.S. Heng, A. Heptonstall, M. Heurs, M. Hewitson, S. Hild, R. Ingley, Y. Itoh, O. Jennrich, L. Jones, S.H. Hutter, K. Kawabe, C.J. Killow, K. Kötter, B. Krishnan, V. Leonhardt, H. Lück, B. Machenschalk, M. Malec, R.A. Mercer, S.D. Mohanty, K. Mossavi, S. Mukherjee, S. Nagano, G. Newton, M.A. Papa, M. Perreux-Lloyd, M. Pitkin, M. Plissi, V. Quetschke, V. Re, S. Reid, L. Ribichini, D.I. Robertson, N.A. Robertson, S. Rowan, A. Rüdiger, B. Sathyaprakash, R. Schilling, R. Schnabel, B.F. Schutz, F. Seifert, A.M. Sintes, J.R. Smith, P. Sneddon, K.A. Strain, I. Taylor, C.I. Torrie, C. Ungarelli, A. Vecchio, H. Ward, U. Weiland, H. Welling, L. Wen, P. Williams, W. Winkler, G. Woan, I. Zawischa: *Status of GEO 600* Class. Quantum Grav. **21** 417-423 (2004).

B. Allen, G. Woan and the LIGO Scientific Collaboration: *Upper limits on the strength of*

---

*periodic gravitational waves from PSR J1939+2134* Class. Quantum Grav. **21** 671-676 (2004).

A. J. Weinstein and the LIGO Scientific Collaboration: *First upper limits from LIGO on gravitational wave bursts* Class. Quantum Grav. **21** 677-684 (2003).

J. T. Whelan and the LIGO Scientific Collaboration: *First upper limit analysis and results from LIGO science data: stochastic background* Class. Quantum Grav. **21** 685-690 (2004).

G. González and the LIGO Scientific Collaboration: *Search for inspiralling neutron stars in LIGO S1 data* Class. Quantum Grav. **21** 691-696 (2004).

U. Weiland, G. Heinzel, H. Ward, G. Woan: *Hardware injection of simulated continuous gravitational wave signals for GEO 600* Class. Quantum Grav. **21** 861-865 (2004).

The LIGO Scientific Collaboration: *Detector description and performance for the first coincidence observations between LIGO and GEO* Nucl. Instr. Meth. Phys. Res. A **517** 154-179 (2004).

G. Woan, P. Aufmuth, C. Aulbert, S. Babak, R. Balasubramanian, B.W. Barr, S. Berukoff, S. Bose, G. Cagnoli, M. Casey, D. Churches, C.N. Colacino, D.R.M. Crooks, C. Cutler, K. Danzmann, R. Davis, R.J. Dupuis E. Elliffe, C. Fallnich, A. Freise, S. Goßler, A. Grant, H. Grote, G. Heinzel, A. Hepstonstall, M. Heurs, M. Hewitson, J. Hough, O. Jennrich, K. Kawabe, K. Kötter, V. Leonhardt, H. Lück, M. Malec, P. McNamara, K. Mossavi, S. Mohanty, S. Mukherjee, S. Nagano, G.P. Newton, B.J. Owen, M.A. Papa, M.V. Plissi, V. Quetschke, D.I. Robertson, N.A. Robertson, S. Rowan, A. Rüdiger, B.S. Sathyaprakash, R. Schilling, B.F. Schutz, R. Senior, A.M. Sintes, K.D. Skeldon, P. Sneddon, F. Stief, K.A. Strain, I. Taylor, C.I. Torrie, A. Vecchio, H. Ward, U. Weiland, H. Welling, P. Williams, W. Winkler, B. Willke, I. Zawischa: *The GEO 600 Gravitational Wave Detector: Pulsar Prospects* M. Bailes, D. Nice, S. Thorsett (eds.) Radio Pulsars. ASP Conference Series **CS-302** 351-355 (2003).

M. Hewitson, P. Aufmuth, C. Aulbert, S. Babak, R. Balasubramanian, B.W. Barr, S. Berukoff, G. Cagnoli, C.A. Cantley, M.M. Casey, S. Chelkowski, D. Churches, C.N. Colacino, D.R.M. Crooks, C. Cutler, K. Danzmann, R. Davis, R.J. Dupuis E. Elliffe, C. Fallnich, A. Freise, S. Goßler, A. Grant, H. Grote, G. Heinzel, S. Heng, A. Hepstonstall, M. Heurs, J. Hough, Y. Itoh, O. Jennrich, R. Jones, S. Hutter, K. Kawabe, C. Killow, K. Kötter, B. Krishnan, V. Leonhardt, H. Lück, B. Machenschalk, M. Malec, K. Mossavi, S. Mohanty, S. Mukherjee, S. Nagano, G.P. Newton, B.J. Owen, M.A. Papa, M. Perreux-Lloyd, M. Pitkin, M.V. Plissi, V. Quetschke, S. Reid, L. Ribichini, D.I. Robertson, N.A. Robertson, S. Rowan, A. Rüdiger, B.S. Sathyaprakash, R. Schilling, R. Schnabel, B.F. Schutz, F. Seifert, A.M. Sintes, J. Smith, P. Sneddon, K.A. Strain, I. Taylor, C.I. Torrie, A. Vecchio, H. Ward, U. Weiland, H. Welling, P. Williams, B. Willke, W. Winkler, G. Woan, I. Zawischa: *A report on the status of the GEO 600 gravitational wave detector* Class. Quantum Grav. **20** No.17 581-592 (2003).

A.M. Sintes, P. Aufmuth, C. Aulbert, S. Babak, R. Balasubramanian, B.W. Barr, S. Berukoff, S. Borger, G. Cagnoli, C.A. Cantley, M.M. Casey, S. Chelkowski, D. Churches, C.N. Colacino, D.R.M. Crooks, C. Cutler, K. Danzmann, R. Davies, R. Dupuis, E. Elliffe, C. Fallnich, A. Freise, S. Goßler, A. Grant, H. Grote, S. Grunewald, J. Harms, G. Heinzel, I.S. Heng, A. Hepstonstall, M. Heurs, M. Hewitson, J. Hough, R. Ingley, Y. Itoh, O. Jennrich, R. Jones, S. Hutter, K. Kawabe, C. Killow, K. Kotter, B. Krishnan, V. Leonhardt, H. Luck, B. Machenschalk, M. Malec, C. Messenger, K. Mossavi, S. Mohanty, S. Mukherjee, S. Nagano, G.P. Newton, M.A. Papa, M. Perreux-Lloyd, M. Pitkin, M.V. Plissi, V. Quetschke, S. Reid, L. Ribichini, D.I.

Robertson, N.A. Robertson, S. Rowan, A. Rudiger, B.S. Sathyaprakash, .R Schilling, R. Schnabel, B.F. Schutz, F. Seifert, J. Smith, P. Sneddon, K.A. Strain, I. Taylor, C.I. Torrie, A. Vecchio, H. Ward, U. Weiland, H. Welling, P. Williams, B. Willke, W. Winkler, G. Woan, I. Zawischa: *Detector characterization in GEO 600* Class. Quantum Grav. **20** No.17 731-740 (2003).

M. Hewitson, H. Grote, G. Heinzel, K.A. Strain, H. Ward, U. Weiland: *Calibration of GEO 600 for the S1 science run* Class. Quantum Grav. **20** No.17 885-894 (2003).

M. Hewitson, H. Grote, G. Heinzel, K.A. Strain, H. Ward, U. Weiland: *Calibration of the power-recycled gravitational wave detector, GEO 600* Rev. Sci. Instr. **74** No.9 4184-4190 (2003).

S. Goßler, M.M. Casey, A. Freise, A. Grant, H. Grote, G. Heinzel, M. Heurs, M.E. Husman, K. Kötter, V. Leonhardt, H. Lück, M. Malec, K. Mossavi, S. Nagano, P.W. McNamara, M.V. Plissi, V. Quetschke, D.I. Robertson, N.A. Robertson, A. Rüdiger, R. Schilling, K.D. Skeldon, K.A. Strain, C.I. Torrie, H. Ward, U. Weiland, B. Willke, W. Winkler, J. Hough, K. Danzmann: *Mode-cleaning and injection optics of the gravitational-wave detector GEO 600* Rev. Scientific Instr. **74** No.8 3787-3796 (2003).

B. Willke, P. Aufmuth, C. Aulbert, S. Babak, R. Balasubramanian, B.W. Barr, S. Berukoff, S. Bose, G. Cagnoli, M.M. Casey, D. Churches, C.N. Colacino, D.R.M. Crooks, C. Cutler, K. Danzmann, R. Davies, R. Dupuis, E. Elliffe, C. Fallnich, A. Freise, S. Goßler, A. Grant, H. Grote, J. Harms, G. Heinzel, S. Herden, A. Hepstonstall, M. Heurs, M. Hewitson, J. Hough, O. Jennrich, K. Kawabe, K. Kötter, V. Leonhardt, H. Lück, M. Malec, P.W. McNamara, K. Mossavi, S. Mohanty, S. Mukherjee, S. Nagano, G.P. Newton, B.J. Owen, M.A. Papa, M.V. Plissi, V. Quetschke, L. Ribichini, D.I. Robertson, N.A. Robertson, S. Rowan, A. Rüdiger, B.S. Sathyaprakash, R. Schilling, B.F. Schutz, F. Seifert, A.M. Sintes, S.K. Skeldon, P. Sneddon, K.A. Strain, I. Taylor, C.I. Torrie, A. Vecchio, H. Ward, U. Weiland, H. Welling, P. Williams, W. Winkler, G. Woan, I. Zawischa: *Status of the GEO 600 gravitational wave detector* Editors: M. Cruise, P. Saulson; Proceedings of the society of photo-optical instrumentation engineers (SPIE), 4856 238-246 (2003).

B. Willke, P. Aufmuth, C. Aulbert, S. Babak, R. Balasubramanian, B. W. Barr, S. Berukoff, S. Bose, G. Cagnoli, M. M. Casey, D. Churches, D. Clubley, C. N. Colacino, D. R. M. Crooks, C. Cutler, K. Danzmann, R. Davies, R. Dupuis, E. Elliffe, C. Fallnich, A. Freise, S. Goßler, A. Grant, H. Grote, G. Heinzel, A. Heptonstall, M. Heurs, M. Hewitson, J. Hough, O. Jennrich, K. Kawabe, K. Kötter, V. Leonhardt, H. Lück, M. Malec, P. W. McNamara, S. A. McIntosh, K. Mossavi, S. Mohanty, S. Mukherjee, S. Nagano, G. P. Newton, B. J. Owen, D. Palmer, M.A. Papa, M. V. Plissi, V. Quetschke, D. I. Robertson, N.A. Robertson, S. Rowan, A. Rüdiger, B. S. Sathyaprakash, R. Schilling, B. F. Schutz, R. Senior, A. M. Sintes, K. D. Skeldon, P. Sneddon, F. Stief, K. A. Strain, I. Taylor, C. I. Torrie, A. Vecchio, H. Ward, U. Weiland, H. Welling, P. Williams, W. Winkler, G. Woan and I. Zawischa: *The GEO 600 gravitational wave detector* Class. Quantum Grav. **19** 1377-1387 (2002).

K. Kötter, C. Aulbert, S. Babak, R. Balasubramanian, S. Berukoff, S. Bose, D. Churches, C.N. Colacino, C. Cutler, K. Danzmann, R. Davies, R. Dupuis, A. Freise, H. Grote, G. Heinzel, M. Hewitson, J. Hough, H. Lück, M. Malec, S.D. Mohanty, S. Mukherjee, S. Nagano, M.A. Papa, D. Robertson, B.S. Sathyaprakash, B.F. Schutz, A.M. Sintes, K.A. Strain, I.J. Taylor, A. Vecchio, H. Ward, U. Weiland, B. Willke, G. Woan: *Data acquisition and detector characterisation of GEO 600* Class. Quantum Grav. **19** 1399-1407 (2002).

---

U. Weiland: *Positions- und Orientierungsregelung von als Pendel aufgehängten Resonatorspiegeln* Diplomarbeit Universität Hannover (2000).